Mount Meager, a glaciated volcano in a changing cryosphere : hazards and risk challenges

Gioachino Roberti

Mount Meager, a glaciated volcano in a changing cryosphere: hazard and risk challenges

by

Gioachino Roberti

M.Sc, University of Turin, 2014

B.Sc, University of Turin, 2011

Thesis Submitted in Partial Fulfillment of the
Requirements for the
Joint Degree (Cotutelle)

Doctor of Philosophy in the Department of Earth Sciences
Faculty of Science at Simon Fraser University (Canada)
and
Doctor of Philosophy in the Laboratoire Magmas et Volcans, École Doctorale des Sciences Fondamentales
Université Clermont Auvergne (France)

SIMON FRASER UNIVERSITY

UNIVERISTE CLERMONT AUVERGNE

Defended October 24, 2018

Directeur de thèse: Prof. Benjamin van Wyk de Vries

Approval

Name:	**Gioachino Roberti**
Degree:	**Doctor of Philosophy (Earth Sciences)**
Title:	**Mount Meager, a glaciated volcano in a changing cryosphere: hazard and risk challenges**
Examining Committee:	**Chair:** Marta Chiarle Researcher
Benjamin van Wyk de Vries Supervisor Professor Laboratoire Magmas et volcans, Université Clermont Auvergne	
Brent Ward Supervisor Professor and Chair	
Glyn Williams-Jones Supervisor Professor	Via Teleconference / Skype
Kelly Russell External Examiner Professor Department of Earth, Ocean and Atmospheric Sciences, University of British Columbia	Via Teleconference / Skype
Marta Chiarle External Examiner Researcher Istituto di Ricerca per la Protezione Idrogeologica, Consiglio Nazionale delle Ricerche	
Irene Manzella External Examiner Lecturer School of Geography, Earth and Environmental Sciences, Plymouth University	Via Teleconference / Skype
Anja Dufresne External Examiner Senior Scientist Department of Engineering Geology and Hydrogeology RWTH Aachen University	Via Teleconference / Skype
Susan Conway External Examiner Chargé de recherche Laboratoire de Planétologie et Géodynamique, Université de Nantes	
Date Defended/Approved:	October 24, 2018

Abstract

Mount Meager is a glacier-clad volcanic complex in British Columbia, Canada. It is known for its landslides, of which the 2010 is the largest Canadian historical landslide. In this thesis we investigated slope instability processes at Mount Meager volcano and the effects of ongoing deglaciation. We used a variety of methods including field and remote, geological, geomorphological and structural mapping to characterize glacial and landslide activity at Mount Meager. We used Structure from Motion photogrammetry (SfM) and Lidar to produce digital surface models and InSAR to monitor slope deformation. We applied SfM to historic photography to document glacier and landslide activity at Mount Meager. We discussed a model of growth and erosion of a volcano in glacial and interglacial periods, and the scientific and dissemination value of historic 3D topographic reconstruction. We described the 2010 Mount Meager landslide deposit to interpret emplacement dynamics and kinematics. The 2010 landslide separated in water-rich and water-poor phases that had different runout and distinct deposits. We analyzed historic airphotos to constrain the slope deformation prior to the 2010 collapse. The glacier near the toe of the slope retreated in the failure lead up, the collapse evolved in four subfailures involving the whole volcanic sequence and some basement rocks. We estimated 6×10^6 m^3 of water in the slope, that allowed the separation of the frontal water-rich phase. The total failure volume was $53 \pm 3.8 \times 10^6$ m^3. We identified 27 large ($>5\times10^5$ m^2) unstable slopes at Mount Meager and calculated ~1.3 km^3 of ice loss since 1987. The west flank of Plinth peak and Devastation Creek valley moved up to -34±10 mm and -36±10 mm, respectively, over a 24-day period during the summer of 2016. The failure of these slopes could impact infrastructures and communities downstream of the volcano. The resulting decompression on the volcanic edifice after the failure of Plinth peak would affect the stress field to a depth of 6 km and up to 4 MPa. This sudden decompression could lead to hydrothermal or magmatic eruptions.

Keywords: Mount Meager volcano; Landslide; Glacier retreat; Climate change; Structure from Motion; Debris avalanche

Résumé

Mount Meager est un complexe volcanique glaciaire en British Columbia (Canada). Il est connu pour ses glissements de terrain, dont celui de 2010 étant le plus grand glissement de terrain historique au Canada. Dans cette thèse, nous avons étudié les processus d'instabilités du volcan Mont Meager ainsi que les effets de la déglaciation en cours. Nous avons utilisé une approche pluridisciplinaire, intégrant la cartographie géologique, géomorphologique et structurelle, du terrain et de la télédétection, pour caractériser l'activité glaciaire et les glissements de terrain au Mount Meager. Nous avons utilisé la photogrammétrie Structure from Motion (SfM) et la technologie Lidar pour produire des modèles numériques de terrain, et techniques InSAR pour surveiller le mouvement et la déformation des pentes du volcan. Nous avons appliqué la technique SfM à des photographies aériennes historiques pour documenter les activités des glaciers et des glissements de terrain au Mount Meager. Nous avons discuté un modèle de croissance et d'érosion d'un volcan en période glaciaire et interglaciaire, ainsi que la valeur scientifique et de vulgarisation de la reconstruction topographique 3D. Nous avons décrit les dépôts de glissement de terrain de 2010 à Mount Meager pour interpréter la dynamique de leur mise en place. Le glissement de terrain de 2010 s'est divisé en phases riches en eau et pauvres en eau, ayant des distances d'écoulement différentes et des dépôts distincts. Nous avons analysé des photographies aériennes historiques remontant à 1948, afin de documenter la déformation de la pente avant l'effondrement de 2010. Le glacier situé a proximité du pied de la pente a reculé durant les années précédents la rupture. Cette effondrement a évolué en quatre sous-effondrements, impliquant toute la séquence volcanique et le socle. Nous avons estimé 6×10^6 m^3 d'eau dans la pente, ce qui a permis la séparation de la phase frontale riche en eau. Le volume total d'effondrement est $53 \pm 3.8 \times 10^6$ m^3. Nous avons identifié 27 grands ($>5\times10^5$ m^2) flancs instables au Mount Meager et calculé a ~1.3 km^3 de récession des glaciers depuis 1987. Le flanc ouest de Plinth Peak et de la vallée de Devastation Creek se sont déplacés de -34±10 mm -36±10 mm, respectivement, dans un période de 24 jours pendant l'été 2016. L'effondrement de ces flancs pourrait avoir un impact important sur les infrastructures et les communautés en aval du volcan. La décompression résultant de l'édifice volcanique après l'effondrement du flanc ouest de Plinth Peak affecterait le champ de contrainte à une profondeur de 6 km et jusqu'à 4 MPa. Cette décompression soudaine pourrait

mener des éruptions hydrothermales et magmatiques. Un important glissement de terrain pourrait donc avoir joué un rôle dans le déclenchement de l'éruption de 2360 cal BP.

Mot clés Volcan Mount Meager; Glissement de terrain; Font de glace; Changement climatique; Structure from Motion; Avalanche de débris

Synthèses des travaux

Synthèses

Mount Meager est un complexe volcanique glaciaire en British Columbia, Canada. Il est connu pour ses nombreux glissements de terrain et une éruption en 2360 cal yr BP. Le lien entre les glaciers, les glissements de terrain, et l'activité volcanique a été mal contraint, malgré les aléas et les risques possibles pour les communautés locales. Cette thèse a intégré les approches de géologie Quaternaire, volcanologie, géotechnique, et l’étude des aléas naturels pour mieux comprendre l'interaction des processus à Mount Meager et améliorer l'évaluation des dangers et des risques géologiques.

L'importance de la photographie aérienne historique et un demi-siècle de changements géomorphologiques du Mount Meager

Chapitre 1 est un analyse bibliographique, où nous avons exploré la problématique d'un volcan dans une cryosphère en mutation. Les volcans sont des systèmes complexes auxquels les glaciers ajoutent un degré de complexité. Les dangers des volcans glaciaires sont parmi les plus meurtriers de la planète. Les changements climatiques entraînent un recul des glaciers, contribuant à conditionner les flancs à l’effondrement. Les effondrements des édifices volcaniques se transforment en avalanches de débris qui voyagent de longues distances, avec des effets dévastateurs en aval.

Chapitre 2 documente la recherche sur des données d’archives de photographies aériennes sur le Mount Meager. L’approche innovante du traitement de ces photos aériennes avec photogrammétrie Structure from Motion (SfM) a permis une reconstruction topographique rapide en 3D du Mount Meager de 1947 à 2006. La possibilité d'analyser plus de 50 ans de changements géomorphologiques au Mount Meager a permis d'identifier les mouvements des glaciers et des glissements de terrain. Chacun des glaciers a des tendances, des morphologies et une couverture de débris différentes. Les pentes se sont déformées et se sont effondrées, générant des glissements de terrain qui ont voyagé de longues distances. Afin d'expliquer la

fréquence élevée des glissements de terrain au Mount Meager, nous présentons un modèle conceptuel de l'évolution d'un édifice volcanique associée à des glaciations régionales multiples. L'activité volcanique pendant les périodes glaciaires construit des édifices plus instables qui sont susceptibles de s'effondrer pendant les périodes interglaciaires. Les glaciers influencent la forme du volcan pendant les périodes glaciaires, mais, lors les périodes interglaciaires, les glaciers sont influencés par l'activité volcanique. Outre la valeur scientifique de la photographie historique, la contribution de la visualisation de données 3D multi temporelle aux services de vulgarisation a une valeur inestimable. Des exemples de ce travail sont des images 3D par intervalles, faciles à comprendre et intéressantes aussi pour le public non scientifique (voir ici le Glacier Mosaic et ici le flanc sud de Mount Meager avant l'effondrement en 2010).

Le dépôt de glissement de terrain de Mount Meager 2010

Le 6 août 2010, le flanc sud du Mount Meager s’est effondré, provoquant le plus grand glissement de terrain de l'histoire canadienne. Dans le Chapitre 3, nous décrivons les dépôts de glissement de terrain, la dynamique de mise en place et de l'évolution rhéologique. Lorsque le flanc sud du Mount Meager s’est effondré, la masse fracturée et liquéfiée, se séparent en un flux frontal, plus rapide, riche en eau et un noyau plus lent et pauvre en eau. Les deux phases ont suivi des trajectoires différentes laissant des dépôts différents. La phase riche en eau a laissé un dépôt dispersé distal et a provoqué les fortes remontées observées sur les flancs des vallées.La phase pauvre en eau est restée confinée dans la vallée, laissant un dépôt épais avec des monticules. Le zonage lithologique brut dans le gisement respecte la structure originale du flanc de la source, avec le matériau avec l'altération hydrothermale de la base de la pente trouvée dans le dépôt distal. La teneur en argile dans le gisement indique qu'au moins 12% de la pente a été altérée par voie hydrothermale. Les différentes rhéologies et trajectoires ont des impacts différents sur les côtés des vallées (voir ici le modèle de la phase riche en eau de glissement de terrain de 2010), cela montre l'importance de considérer de multiples rhéologies et la transformation des flux lors de la modélisation des avalanches de débris et de la production de cartes de danger.

La pente avant le glissement de terrain du Mount Meager en 2010

Pour comprendre la dynamique de la mise en place de glissement de terrain 2010, nous avons déplacé notre attention sur l'état de la pente avant la rupture (Chapitre 4). En utilisant les photographies aérienne historiques nous avons documenté la déformation des pentes et l'activité des glaciers de 1948 à 2006. Avec le travail de terrain, nous avons amélioré les contraintes sur la géologie et les structures de la cicatrice d'effondrement. Nous avons recalculé le volume d'effondrement, et nous discutons du volume et du rôle de l'eau dans l'effondrement et la séquence d'effondrement. Le glacier du Capricorne a progressé dans les années 1970-1980 et a reculé de 1990 à 2006.Les principales discontinuités du flanc étaient déjà présentes en 1948, le nombre de fractures et les déplacements le long des failles majeures ont augmenté dans les années suivantes (voir ici le flanc 1948-2010). Le renflement des talus et les défaillances précurseurs se sont produits au pied de la pente. L'augmentation de la pression de l'eau interstitielle provenant des champs de neige et de l'eau de fonte glaciaire a causé la rupture au pied de la pente. Lors de l'effondrement, nous avons estimé que 6×10^6 m^3 de l'eau résidait au pied de la pente, ce qui a permis la séparation de la phase frontale riche en eau. Le volume total d'effondrement est $53 \pm 3.8 \times 10^6$ m^3. L'effondrement a évolué en quatre sous-parties de 24.6×10^6 m^3, 13.8×10^6 m^3, 9.0×10^6 m^3, et 5.6×10^6 m^3, impliquant des roches de socle et toute la séquence volcanique. Cycles glaciaires, altération hydrothermale et déformation gravitationnelle lente conditionnant la pente à la rupture. La déformation lente des pentes aurait pu être surveillée auparavant et la défaillance prévue des décennies à l'avance. Beaucoup d'autres pentes sont dans le même état que la pente de glissement d'avant 2010, et nous avons identifié plusieurs zones instables, des systèmes de surveillance et d'alerte rapide doivent donc être mis en place, de toute urgence, a fin de réduire les risques consécutifs, y compris les pertes de vie causées par les glissements de terrain du Mount Meager.

Les pentes du Mount Meager, danger et risque

L'analyse historique des photos aériennes, Lidar et InSAR, a permis de calculer la perte de masse des glaciers depuis 1987, et d'identifier et de mesurer les taux de déformation de nombreuses pentes instables au Mount Meager (Chapitre 5). La déglaciation continue est susceptible de déclencher d'autres effondrements importants

pouvant affecter les activités économiques à proximité du volcan et dans les communautés de la vallée de la rivière Lillooet. Le volcan Mount Meager a perdu~1.3 km^3 de glace depuis 1987. Nous avons identifié 27 grands (>5×10^5 m^2) pentes instables. Dix-sept de ces pentes ont été touchées par la récente déglaciation. Quinze des pentes ont des volumes de >10^6 m^3; si elles s'effondraient de manière catastrophique, les infrastructures proches du volcan pourraient être sérieusement affectées. Dix pentes ont des volumes de >10^7 m^3; leur effondrement peut avoir un impact sur les zones peuplées en aval. Les flancs des vallées du ruisseau Job et du ruisseau Devastation ont atteint respectivement -34 ± 10 mm et -36 ± 10 mm sur une période de 24 jours au cours de l'été 2016. Nous considérons que ces pentes sont dans un état critique. Le risque de perte de vie suite à un grand glissement de terrain du Mount Meager a été jugé inacceptable. Des systèmes de surveillance des pentes et d'alerte rapide sont nécessaires de toute urgence pour atténuer les risques. La surveillance InSAR est l'option la plus rapide et la plus rentable du volcan Mount Meager.

Glissements de terrain et éruptions

En cas de défaillance catastrophique du flanc ouest du Plinth Peak, une grande (10^8- 10^9 m^3) avalanche de débris serait générée, impactant les infrastructures et les communautés dans la vallée de Lillooet. Outre l'impact direct du glissement de terrain, la modélisation par éléments finis 2D montre que la décompression résultante sur l'édifice volcanique après l'enlèvement de la masse affecterait le champ de contrainte jusqu'à une profondeur de 6 km et pouvant atteindre des décompressions de 4 MPa. Un tel changement brusque de stress effectif pourrait à la fois déclencher une explosion hydrothermale et affecter le réseau magmatique et à travers une série de processus (propagation de fractures, exsolution de gaz, migration de magma) déclencher une éruption (Chapitre 6). Ces nouvelles connaissances sur la décompression suite à un glissement de terrain au Mount Meager permettent de réévaluer le déclencheur d'éruption 2360 cal yr BP. Un effondrement important provenant de Job Valley avant l'éruption pourrait avoir joué un rôle dans le déclenchement de l'éruption. Bien que les preuves stratigraphiques et la datation au radiocarbone montrent un décalage entre le glissement de terrain et l'éruption, nous interprétons le décalage commet étant lié au temps nécessaire pour que le système magmatique réagisse à la décompression. Le changement de stress consécutif au glissement de terrain a permis aux fractures de se

propager NE de la cicatrice de glissement de terrain et de perturber le système magmatique permettant le mélange de magma et finalement déclenchant l'éruption. (Chapitre 6). D'autres études sont nécessaires pour mieux contraindre le réseau magmatique de Mount Meager, de sorte que de nouveaux modèles numériques puissent être développés et appliqués pour mieux évaluer l'interaction entre la fonte des glaciers, les glissements de terrain et les éruptions au Mount Meager.

Travail futur

Beaucoup de travail futur à Mount Meager est nécessaire. De meilleures contraintes d'âge sur le volcanisme et les glaciations sont nécessaires pour comprendre le système glaciaire, le système volcanique et l'interaction entre les deux. Des connaissances plus approfondies sur l'histoire glaciovolcanique peut aider à comprendre les dangers actuels des glaciers et des glissements de terrain au Mount Meager, ainsi que sur d'autres volcans glaciaires du monde entier. Des cartes de dangers et de risques devraient être produites à Mount Meager; la surveillance des pentes et les systèmes d'alerte précoce et d'alarme doivent être mis en œuvre avec une communication efficace des risques aux responsables locaux, aux communautés et aux parties prenantes.

Les glaciers couverts de débris du Mount Meager

Les glaciers couverts de débris sur le Mount Meager devraient être étudiés plus en détail. Les effets des avalanches de débris et des chutes des roches sur la dynamique des glaciers ainsi que l'influence du substrat rocheux volcanique altéré par l'hydrothermie peuvent être étudiés à l'aide de modèles numériques et de travaux sur le terrain. Les effets thermiques des fumerolles sur le glacier Job sont inconnus et méritent des études. Les glaciers du Mount Meager et les glaciers d'autres volcans peuvent être comparés à des glaciers recouverts de débris provenant de montagnes non volcaniques.

Glaciovolcanisme à Mount Meager?

La cartographie géologique du Mount Meager a été réalisée dans les années 1970 (Read 1978). Les progrès scientifiques d'aujourd'hui sur la compréhension des processus volcaniques et glaciaires pourraient permettre une mise à jour de la carte géologique. Les avancées technologiques telles que Lidar et photographie haute résolution permettent une cartographie de plus haute résolution. La stratigraphie du volcan pourrait être cartographiée plus en détail, en particulier à plus petite échelle (affleurement ou chenal), afin d'identifier davantage d'unités stratigraphiques. Les caractéristiques glaciovolcaniques non cartographiées peuvent être reconnues et des

nouvelles dates pourraient mieux limiter l'âge des glaciations et du volcanisme au Mount Meager.

Mise en œuvre de la surveillance des pentes et communication des dangers et des risques

À l'heure actuelle, la surveillance de la température et des précipitations est utilisée comme système d'avertissement indirecte de glissement de terrain au Mount Meager; cela devrait être accompagné d'observations directes de pentes. Des systèmes de surveillance par satellite et au sol, des systèmes d'alerte précoce et des systèmes d'alarme doivent être mis en place pour réduire les risques sur les lieux des travail situés près du volcan et dans les communautés de la vallée de Lillooet. Une communication des risques efficace, des directives et des protocoles devraient être élaborés et mis en œuvre car la surveillance coûteuse aurait peu d'impact à moins que ses résultats ne soient compris par les personnes à risque. Les applications de médias sociaux et les technologies 3D peuvent aider les locaux à comprendre les dangers et les risques volcaniques.

Modèles de glissement de terrain pour le zonage des dangers

Des simulations numériques sont nécessaires pour déterminer les zones d'impact, et définir le zonage des risques dans la vallée de la rivière Lillooet. Les travaux de Simpson et al. (2006) dans l'identification des zones d'inondation peuvent-être améliorés, également à la lumière de l'événement de 2010. La distance d'impact du glissement de 2010 a été surestimée par le modèle de Simpson et al. (2006). L'analyse des risques de Friele et al. (2008) devrait être mise à jour compte tenu de l'augmentation de la population et des activités économiques près du Mount Meager et des glissements de terrain identifiés dans cette étude.

Le modèle numérique préliminaire du glissement de terrain de 2010 (voir vidéo ici) a été calculé avec le logiciel Volcflow, développé par Kelfoun and Druitt (2005). Des simulations séparées avec différents paramètres de frottement et de cohésion ont été effectuées pour reproduire des phases de rhéologie différentes. Le recalibrage du modèle suer l'événement de 2010 permettrait des scénarios d'impact plus précis pour les pentes instables identifiées.

Déglaciation, glissements de terrain et éruptions

Des études supplémentaires numériques et sur le terrain sont nécessaires pour étudier le lien entre la déglaciation, les glissements de terrain et les éruptions au Mount Meager. Des analyses pétrologiques, géochimiques et géophysiques peuvent aider à comprendre les systèmes hydrothermaux et volcaniques du Mount Meager. Des simulations numériques des variations de contraintes consécutives à des glissements de terrain pourraient contribuer à comprendre la probabilité d'une éruption en cas de grands glissements de terrain.

Les résultats obtenus à Mount Meager apportent un nouvel éclairage sur les effets des glaciations régionales et alpines sur le volcanisme et sur les effets du volcanisme sur les glaciers. Ces nouvelles connaissances peuvent être appliquées à d'autres volcans dans le monde et à d'autres planètes.

Acknowledgements

I would like to acknowledge all the people that supported me though these years of travels and science. First my supervisors. Ben for encouraging me to enrol in the PhD, for being a great mentor, and friend. Brent for his invaluable mentorship and friendship, and for the patience in dealing with the "greasy Italian". They both helped me in developing my scientific interest, encouraging new ideas and making sure I did not get too imaginative, ...and they gave me a roof multiple time (and thank you to Fran and Lorraine to welcoming home). Pierre for the field adventures, professional advices, and friendship. John for slaughtering my manuscripts, the humour, and the friendship. Marco and Gigi that first exposed me to the international academic community and kept encouraging me from the backstage. Glyn for his ongoing optimism and support. Giacomo for the Italian dinners and, together with Geidy and Jean-Pascal, for the successful collaboration with TRE-Altamira. Audray, and Brian for discussion and collaboration. Alex, Kelly, and Melanie for constructive discussions. Bernhard and Farnoush for sharing the Mt Meager passion.

Then all the staff, from both LMV and SFU, that helped me with logistics and bureaucracy. In particular Tarja, Lorena, Matt, Thierry, Audray, Nathalie. And the PhD students. In particular Ale, Silvia and Anne for sharing the office and the fun. Snowy, Carie-Ann, Patrick and Derek to share the dirt and the chaos. Davide for sharing the expat experience. Mohsen for the insightful conversations. The Peruvian connection, friends and colleagues from INGEMMET, and OVI; especially Nelida, Ivonne, Gael, Patricio, Rigoberto, Joseph, Saida, Hugo, Bilbeto, Lionel, Domingo, Marco, Gissel, Luisa.

Lucian, Susanne, Chloe, Aspen, Erik, Brad, Surabhi, Hazel, Sarah, Betka, Omar, Chu, Brian, Annie, Alex, Leif, Dave, Flvien, Jeff(s), Sammy, Sarah, Stefano, Cate, Line, Kai, Melanie, Rachel, Antonina, the SFU climbing wall community (especially Adam and his truck) that helped to endure the Vancouver rain and enjoy the Squamish sun. Taoye, Fares, Magda, Myriam, Auriane, Melody, Audrey, Marie, Ophelie, Floriane, Fanny, Clothilde, Nico, Orya, Romi, Bertrand, Melodie, Baptiste, Tatum, Marie-Anne, Bene, Brahim, Christophe, Swetha, Simon, Diego, Giacomo, Damien, Alexis, Valentin(s), Lois, Juliette, Baptiste, Pierre, Marina, Nathan, Lola, Julie, Vincent, Taya, Yannick(s),

Federica, ChouChou, Camila, Sarah, Coco for sharing the *"Spleen de Clermont"* and the wine with me. Catherine for adopting the Italo-French-Canadian kid and giving him a roof. Cat for the endless support and careful manuscript review.

Finally, I would like to thank my family, and old friends, that have always been cheering for me. Francesco, Ema, Michela, GiuGiu, Giacomo, Betto, Kiki. Special thanks to my grandparent, Carlo, always an inspirational figure and my grandmother, Monet. And everyone that I may have forgotten.

Table of Contents

List of Tables

List of Figures

Chapter 1. Introduction

1.1. Introduction

Mount Meager is a glacier-clad and unstable volcanic massif in British Columbia. Mount Meager has been the site of a recent (2360 cal yr BP) eruption, has had many large landslides originating from its flanks, has an active hydrothermal system, and is presently covered by retreating glaciers. Ongoing deglaciation and high landslide frequency make Mount Meager a perfect case study of landslide processes from a glaciated volcano. The presence of communities and economic activities near the volcano mark the urgency and need for a better understanding of the hazards from Mount Meager.

Studies of Mount Meager have focused either on the volcanological perspective (geochemistry, eruptive styles, etc.) neglecting geotechnical aspects (slope stability, debris flow hazards etc.) or from a geotechnical approach neglecting the volcanological point of view. The glacial history, present day glacial retreat and impacts on the stability of the mountain have also been understudied. The knowledge fragmentation negatively impacts the understanding of the hazard as well as hazard and risk communication to the general public. The different levels of the Canadian government as well as Canadian citizens are generally unaware of the presence of volcanoes and of volcanic hazards in Canada. Political and social unawareness of the hazards manifests in the lack of a consistent volcanic hazard assessment and monitoring that exposes the population to an unacceptable risk. This thesis aims to bring together volcanological, geomorphological and geotechnical approaches to the study of Mount Meager volcano for a better hazard and risk understanding.

1.1.1. Mount Meager and the Garibaldi Volcanic Belt

Mount Meager is a Quaternary, glacier covered, volcanic complex located in Southwestern British Columbia, Canada. It is about 150 km north of the city Vancouver and 65 km from the closest town Pemberton. Mount Meager is part of the Garibaldi Volcanic Belt, which is north of the Cascades volcanic arc. The Garibaldi belt stretches 150 km, includes three major stratovolcanoes, Mount Meager, Mount Cayley, and Mount

Garibaldi, and numerous smaller monogenetic volcanoes (Wilson and Russel 2018). The Garibaldi Volcanic Belt differs from the Cascades in several ways. The Garibaldi Volcanic Belt magmatism is younger (5-15 Ma) than the Cascades (35 Ma), and is related to a hotter subducting plate that resulted in lower eruption rates and narrower arc width (Harry and Green 1999; Mullen et al. 2013; Mullen et al. 2018). With lower eruptive rates, the Garibaldi Volcanic Belt volcanic edifices are relatively small and sit on igneous and metamorphic basement ridge crests (Wilson and Russel 2018) (Figure 1.1). The Cascades volcanoes, on the other hand, created significant landscape morphology, building large stratocones with thousands of metres of relief. The Cordilleran Ice Sheet has affected volcano morphologies in the Garibaldi Volcanic Belt (Wilson et al. 2016; Wilson and Russel 2017, 2018) while the Cascades have only been affected by local ice caps and were not covered by the Cordilleran Ice Sheet (excluding, partially, Mount Baker).

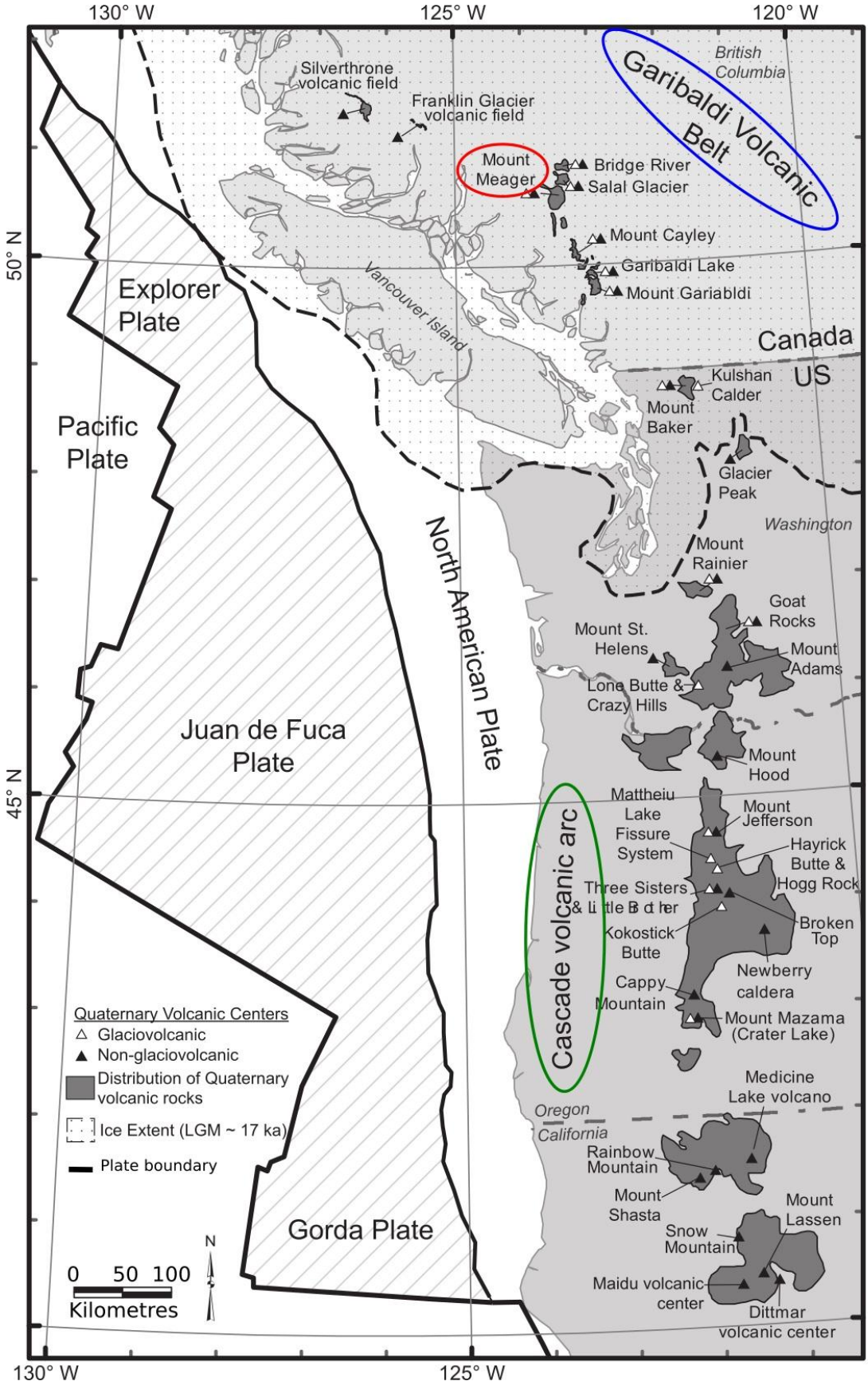
130° W
125° W
120° W
50° N
45° N
40° N
British Columbia
Garibaldi Volcanic Belt
Silverthrone volcanic field
Franklin Glacier volcanic field
Mount Meager
Bridge River
Salal Glacier
Mount Cayley
Garibaldi Lake
Mount Gariabldi
Vancouver Island
Explorer Plate
Pacific Plate
Canada
US
Kulshan Calder
Mount Baker
Glacier Peak
Washington
Mount Rainier
North American Plate
Goat Rocks
Mount St. Helens
Mount Adams
Lone Butte & Crazy Hills
Juan de Fuca Plate
Mount Hood
Mattheiu Lake Fissure System
Mount Jefferson
Hayrick Butte & Hogg Rock
Three Sisters & Little Brother
Broken Top
Kokostick Butte
Newberry caldera
Cappy Mountain
Mount Mazama (Crater Lake)
Cascade volcanic arc
Medicine Lake volcano
Oregon
California
Rainbow Mountain
Mount Shasta
Mount Lassen
Snow Mountain
Maidu volcanic center
Dittmar volcanic center
Gorda Plate
Quaternary Volcanic Centers
Glaciovolcanic
Non-glaciovolcanic
Distribution of Quaternary volcanic rocks
Ice Extent (LGM ~ 17 ka)
Plate boundary
N
0 50 100
Kilometres

Figure 1.1. Map of the Pacific Northwest: Mount Meager, circled in red, the Garibaldi Volcanic Belt, circled in blue, the Cascade Volcanic Arc circled in green, and the Cordilleran Ice Sheet extent in black dashed lines. Note the smaller extension of the Garibaldi Volcanic Belt compared to the Cascade Volcanic Arc, and the boundary of the Cordilleran Ice Sheet, shortly after the Canada-US border. Modified from Wilson and Russel 2018.

1.1.2. Mount Meager landslides and the last eruption

The local relief of Mount Meager is 2200 m, with the peaks about 2700 m asl and the valley bases around 500 m asl. The lower part of the mountain is made of metamorphic and igneous basement and only the upper 600 m are volcanic rocks. The volcanic sequence is comprised of pyroclastic rocks, basaltic-andesitic lava flows and rhyodacite domes (Read 1978, 1990). There is widespread hydrothermal alteration and active hot springs and fumaroles.

Mount Meager last erupted 2360 cal yr BP (Clague et al. 1995; Hickson et al. 1999), and is the epicentre of shallow earthquakes (Friele et al. 2008). A minimum of two hydrothermal events affected the area; an ancient hydrothermal event caused propylitic alteration of the basement rocks and the present system deposited sphalerite, pyrite, clays, carbonates and chlorite in basement and volcanic rocks (NSBG 1985). The recent hydrothermal system manifests as hotsprings and fumaroles (Venugopal et al. 2017). The area has been repeatedly glaciated during the Pleistocene and today Mount Meager hosts alpine glaciers and snow fields. The high relief, hydrothermal alteration, and glacial modification conditions the slopes for failures, leaving the volcanic edifice and the underlying basement rocks in a state of instability.

Mount Meager has been the site of numerous large landslides in the Holocene, along with almost annual smaller events (Figure 1.2). Many studies have focused on mass movements from Mount Meager, documenting catastrophic landslides, slow slope deformation, debris flow and landslide activity following the Little Ice Age glacial retreat (Carter 1932; Mokievsky-Zubok 1977; Jordan 1994; Jakob 1996; Bovis and Evans 1996; Evans 1987; Bovis and Jackob1998; Bovis 1990; Holm et al. 2004; Friele and Clague 2004; Guthrie et al. 2012a, b, Hetherington 2014). The Lillooet River is the main drainage system of the Mount Meager volcanic complex. Studies have focused on the sedimentary record in the Lillooet valley by correlating debris flows and

hyperconcentrated flow deposits with the major landslide events from Mount Meager (Simpson et al. 2006; Friele at al. 2008) and determining flood plain aggradation and delta-front progradation following these sediment pulses (Jordan and Slaymaker 1991; Friele et al. 2005).

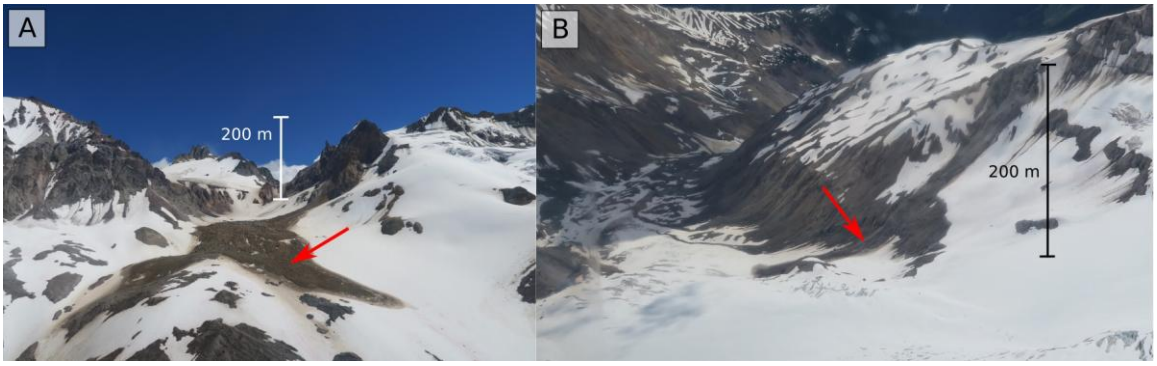

Figure 1.2. Rock avalanches (arrows) at Mount Meager in summer 2018. A) Job Valley. B) Devastation Valley.

The high frequency and magnitude of mass movements at Mount Meager lead Read (1978, 1990) to call it the most landslide prone area in Canada. The major hazard from Mount Meager has been argued to be from landslides rather than direct volcanic activity (eruptions, pyroclastic flow, ash fall or lava flow) (Stewart 2002; Friele et al. 2008). In the case of the 2360 cal yr BP eruption, Hickson et al. (1999) and Andrews et al. (2014) show that secondary eruptive effects, such as river damming and subsequent catastrophic outburst flood, had more widespread impact than the volcanic eruption itself. The 2360 cal yr BP eruption with a Volcanic Explosivity Index (VEI 4), lasted weeks to months and consisted of an initial sub-Plinian explosive phase that transitioned into a Vulcanian phase (Satsiuk et al. 1996; Hickson et al. 1999; Andrews et al. 2014). Welded pyroclastic material blocked the river and formed a lake with a volume of 0.25-1.0 10^9 m^3 that catastrophically drained (Satsiuk et al. 1996; Hickson et al. 1999; Andrews et al. 2014). Deposits from hyperconcentrated flows have been found in drill cores 42-47 km downstream from the volcano and have been interpreted to be the outburst flood deposits (Friele et al. 2008). The eruptive products are underlain and overlain by landslide deposits not directly related to the eruption (Hickson et al. 1999).

1.1.3. Glacier, landslides and volcanoes

An increase in landslide activity can be linked to deglaciation and permafrost degradation (Deline et al. 2015). Glacial erosion removes the support on slopes and glacier cycles repeatedly change the state of stress of slopes, conditioning them for catastrophic collapses (Grämiger et al. 2017). Permafrost thaw, which affects the water circulation and the mechanical behaviour of rock and debris, leads to a decrease in slope stability and an increase in the rock fall frequency and magnitude (Gruber and Haberli 2007; Krautblatter et al. 2013; Dreabling et al. 2017). Numerous studies have documented slope instabilities from deglaciation in high mountains regions (Evans and Clague 1994; Huggel et al. 2008; McColl and Davies 2013; Deline et al. 2015), others have documented landslides from glaciated volcanoes (Vallance and Scott 1997; Holm et al. 2004; Huggel et al. 2007a, b; Ball et al. 2018), but few have studied the effect of ice loss and thermal regime perturbations on the stability of volcanic edifices (Huggel 2009).

Volcanoes add a degree of complexity to the understanding of the effects of ice loss and permafrost degradation on landslide activity. Volcanoes are dynamic environments where deep magmatic and tectonic processes as well as surficial geomorphic process are linked and have rapid effects on the edifice stability. The time-scale of volcano edifice construction can be as short as few days (Pioli et al. 2008); the rapid volcanic and volcanoclastic deposit emplacement contributes to edifice instability. When a volcano grows in a glacial environment the instability is compounded. Lava and ice interaction causes rapid cooling and quenching of volcanic rocks. Water availability from glaciers can increase the fragmentation of erupted material and can enhance hydrothermal circulation and rock alteration (Edwards et al. 2015; Barr et al. 2018b). These phenomena lead to the construction of an even weaker volcanic edifice making glaciated volcanoes especially prone to failure (Vallance and Scott 1997; Huggel et al. 2007a).

Slope failures in both volcanic and non-volcanic glaciated environments generate complex, long runout landslides (Evans and Clague 1994; Deline et al. 2015). Unstable rock and debris slopes catastrophically fail, and commonly transform from rock slides, or rotational landslides into rock or debris avalanches and debris flows (Scott et al. 2002; Geertsema et al. 2006). Kinematic transformations and long landslide runout are related

to the availability of water contributing to the decrease of internal and bed friction angles. In the case of volcanic landslides, the flow transformation and runout is enhanced by the high percentage of fines (Vallance and Scott 1997; Scott et al. 2002; Friele and Clague 2004). The fine particles come from the primary fine grained volcanoclastic material and the subsequent hydrothermal alteration. The combination of water availability and poor geomechanic rock quality make landslides from glaciated volcanoes among the most far-reaching and deadly sub-aerial mass movements (Major and Newhall 1989; van Wyk de Vries and Delcamp 2015).

1.1.4. Hazard and risk at Mount Meager volcano

Volcanoes are sources of multiple hazards, directly from eruptions (lava flow, pyroclasic flows, ash fall, etc.) or indirectly, with mass movements from the volcanic edifices (debris avalanches, lahar, etc.). One of the most deadly volcanic event in the 20th century was a lahar from Nevado del Ruitz volcano in Colombia. The volcanic debris flow, generated form ice and snow melt following an eruption onto a glacier, killed more than 22,000 people (Herd et al. 1986). Volcanic landslide hazard has been recognized at other volcanoes, including the Cascade volcanoes such as Mount Rainier, where extensive hazard and risk studies have been done by the United States Geological Survey (USGS) (Vallance and Scott 1997; Wood and Soulard 2009; Waythomas 2014; Bell et al. 2018). At Mount Meager, despite the numerous hazards studies, only Friele et al. (2008) assessed the risk from large landslides while Stasiuk et al. (2003) presented a synthesis of volcanic hazard in Canada and a quantitative analysis for Mount Cayley volcano. At present, there is the lack of a comprehensive hazard and risk assessment at the Mount Meager volcano.

Along with hazard and risk analysis, effective communication to the local stakeholders is of vital importance. Nevado del Ruiz is a sad example of poor communication between the scientific community and the general public. The hazard was known and so was the risk, but the scientific community was not able to effectively communicate the risk to the local authorities, such that no evacuation occurred (Voight 1990). At Mount Meager both economic activity and resident population are increasing in the proximity of the volcano; the combined lack of a consistent monitoring program and effective risk communication to the local communities could be disastrous.

1.2. Methods

We used field, state-of-art, and innovative remote sensing methods to document slope stability, landslide emplacement dynamics and glacial retreat at Mount Meager volcano. We collected available topography data including digital elevation models (DEM) and satellite imagery, historic aerial photography, oblique helicopter photography, and airborne Lidar. We produced orthophotos and DEMs applying Structure from Motion (SfM) photogrammetry to historic airphotos. We calculated DEMs of Difference (DoD) to evaluate landslide volumes and glacier mass changes. We mapped geomorphic features and rock and sediment types both remotely and in the field. We collected rock and debris samples to characterize the 2010 landslide deposit and emplacement dynamics. We applied satellite InSAR for slope displacement monitoring. Specific methods are presented in each chapter. We discuss here the SfM background as it is a novel technique, and we will briefly give an overview of Lidar and InSAR technologies.

1.2.1. Photogrammetry and Structure from Motion

Historical aerial photography offers the opportunity to document decades of topographic changes, however the full potential of historic airphotos has been hindered by technological limitations. Today's advancement in photogrammetry and computing vision led to the Structure from Motion (SfM) revolution in the geosciences. SfM offers a cost and time-effective alternative to classic photogrammetry, allowing fast and high-resolution three-dimensional topography reproduction for a full exploitation of archival data.

Photogrammetry

Photogrammetry is an early discipline that evolved together with technological advancements in photography, aviation, and computers (Schenk 2005). Photogrammetry has evolved from analogue, to analytical and, in recent years, to digital photogrammetry (Gomarasca 2009; Linder 2009). Ever since the invention of photography, retrieving quantitative information with photographs has been pursued. At the beginning of the 20th century, the stereo plotter was invented and during the First World War, aerial photogrammetry was developed and refined. In the same period, the basic practice for aerial photogrammetry was established as well as the mathematical

theory of the technique. This was the time of “analogue photogrammetry”: analogue methods were used to retrieve precise information from the photographs. In the 1960's, the technique evolved to “analytical photogrammetry” with the invention of the analytical plotter: the restitution process was partly numerical and partly analogue. The evolution of computers and advent of digital photography brings us to the present “digital photogrammetry” era. Analogue cameras have been largely replaced by digital cameras but the workflow still relies on the analogue framework; digital image matching algorithms require manual intervention to satisfy the required precision.

In the aerial photogrammetry survey workflow, nadiral overlapping stereo-airphotos are acquired on strips in parallel trajectories from an aircraft flying at constant altitude (Gomarasca 2009). The airphotos are acquired by a survey-grade metric camera and the area of interest is covered with the smallest number of overlapping images (60% lateral, 20%vertical). The definition of ground control points (GCP) is necessary in order to solve the collinearity equation and retrieve the real world coordinate position of surface features (Wolf and Dewitt 2000), then image matching and semi-automated aerial triangulation algorithms are used to build the three-dimensional geometry and produce an orthophoto and DEM. Commonly, photogrammetric software packages are costly and rely on relatively old image matching methods. These software packages generally apply feature-based image matching algorithms (Haala et al. 2014) that match only selected points at high accuracy but they suffer in areas of poor image texture (Haala and Rothermel 2012). Today, photogrammetry software packages are moving into more modern image matching algorithms and some of them can resolve the three-dimensional geometry of object prior to the introduction of GCP (Fonstad et al. 2013).

Structure from Motion - Multi-view stereo

SfM is commonly seen as an advance in photogrammetry, but there are basic conceptual differences. SfM finds its roots in the field of computer vision where the aim is to get machines to understand scenes through the automatized reconstruction of the three-dimensional geometry of objects (Szeliski 2010); precision and geolocation are not a priority.

SfM origins and modern applications

The origin of SfM dates back to the seventies with the formulation of “the Structure from Motion” theorem. SfM is the computer vision algorithm used to generate three-dimensional point clouds (Structure) in generic object coordinates from photographs taken by a moving sensor (Motion) (Ullman 1979). In the geosciences, the term SfM refers to a composite workflow SfM-multi-view stereo (MVS) algorithm (Carrivick et al. 2016). At first instance, the SfM-MVS algorithm generates a sparse point cloud (SfM method) then creates a dense point cloud by increasing the number of points by the MVS method. In this chapter we will refer to the technique simply as SfM, in the general geoscience connotation.

Modern SfM was developed in the 1990's because of the increased availability of digital imagery. It entered the geosciences community in the past decade, after the studies of Cecchi et al. (2002, 2003) applied to laboratory models and aerial images taken from a hand held camera, and Snavely et al. (2008) that reconstructed cities from photos randomly acquired by tourists. Today, SfM has diffused in all fields of Earth sciences, from the hand-sample scale reconstruction to medium-scale topographic modeling (James and Robson 2012). This technique is commonly applied with pictures taken from a hand-held camera or unmanned aircraft vehicles (UAV) (Carrivick et al. 2016); and few studies have explored the possibility of processing archival airphotos from the past century for diachronic geomorphic studies (Gomez 2014; Gomez et al. 2015).

The SfM products can be of comparable quality with light detection and ranging (Lidar) digital surface models (DSMs) (Westoby et al. 2012; Fonstad et al. 2013). SfM commonly provides a reliable and cheaper alternative to Lidar in DSMs generation and in the past few years the number of studies applying SfM has constantly increased (Carrivick et al. 2016). The SfM drawback was the lack of quality control on the workflow (Westoby et al. 2012; Fonstad et al. 2013; Micheletti et al. 2015) that made scientists consider it as a “black box”. Researchers are now proving the intrinsic quality of SfM generated models and SfM is becoming a fully accepted technology of which both the limitations and advantages are known (James et al. 2017a, b).

SfM workflow

In the SfM workflow, the hardware can be a consumer-grade digital camera with the reconstruction coming from the redundancy of the images taken(Table 1.1). SfM algorithms have been developed to work with off-nadir, convergent photos (Snavely et al. 2008; Furukawa and Ponce 2010). SfM allows the three-dimensional reconstruction of objects and surfaces with sets of overlapping images, without the need of pre-calibrated metric cameras, ground control or any external information (Cecchi et al. 2002, 2003). The collinearity equations are solved using to the redundancy of images (Szeliski 2011), without the need for ground control; hence the three-dimensional model is built a priori in generic x, y, z object coordinates. SfM photo matching is based on multiple scale image matching algorithms (e.g. the scale invariant feature transform, SIFT, Lowe 1999) and global matching methods, where every pixel is matched (Hirschmüller 2008). These algorithms recognize pixel gradients (e.g. shapes) to identify large numbers of common features between images. The ability to recognize shapes allows the matching of photos at different scales, translations, rotations and partially different brightness levels; it also allows the separation of objects from the background (Fonstad et al. 2013). The camera parameters are derived from self-calibration during the bundle adjustment. The SfM derived 3D point data depends only on the scale and quality of the pictures. Ground control is still needed to produce georeferenced models and to export orthophotos and DEMs. The use of precise GCPs can also improve the bundle adjustment (Carrivick et al. 2016). In the case of lack of GCP, it is possible to scale the model by defining the distance between recognizable points.

Table 1.1. Photogrammetry vs SfM.

Technique	Hardware	Survey plan and geometry	Number of pictures	Ground control
Photogrammetry	metric fixed lens camera	nadir parallel photos	minimum necessary overlap	fundamental
SfM	consumer-grade camera	off-nadir photos randomly acquired	overlap redundancy	not necessary

1.2.2. Lidar

Light Detection and Ranging (Lidar) is, at present, the most common survey technique to produce high-resolution topographic data. Lidar uses a laser to measure

the distance (range) between the sensor and the ground surface, directly producing topographic data. The sensor is commonly paired with a GPS and IMU (inertial measurement unit), allowing direct georeferencing. Lidar laser scanning instruments can be mounted on satellites, aircraft (ALS - airborne laser scanner) or ground based (TLS - terrestrial laser scanner). Bathymetric lidar is used to reconstruct submarine topography. Laser ranging techniques to reconstruct topography date back as far as the mid-1960's (Shepherd 1965). However, the technique did not become prevalent until the 1990's, when scanning mechanisms were sufficiently improved, the GPS constellation was completed and high performance IMU developed, allowing the acquisition of directly geo-referenced airborne data (Petri and Toth 2010). The main advantage of Lidar is the possibility of filtering out the vegetation (extracting the ground returns) and generating a bare-earth digital terrain model (DTM). Lidar is the only method today to create DSM and DTM from the same survey (Table 1.2). Lidar is now broadly applied in Earth sciences for DEM generation, surface change detection and geomorphic feature measurements.

Table 1.2. Terminology of digital elevation data.

DSM - Digital Surface Model	Digital surface model is a representation of the earth surface including object above the ground surface (trees, houses, etc.).
DTM - Digital Terrain Model	Digital terrain model is a representation of the bare ground surface, without features above it (trees, houses, etc.). It is the last return of the Lidar pulse (Ferreaz et al. 2009). It is challenging to generate a DTM from a SfM-generated DSM.
DEM - Digital Elevation Model	Digital elevation model is a generic term to indicate topographic data. In the text we refer to SfM-generated DSM with the generic term digital elevation model DEM.

1.2.3. InSAR

Interferometric Synthetic aperture radar (InSAR) is a radar image processing technique. InSAR can be ground, airborne, or satellite-based; we will discuss only the InSAR satellite background and application. Radar satellites send a signal to the ground and measure the reflection of the signal. The measurement is repeated at every passage of the satellite over the area of interest. From the comparison of the different measurements it is possible to retrieve ground displacement information with millimetric precision. The signal phase difference between the repeated measurements is related to a variety of components (topography, atmosphere, etc.) and ground deformation. After

cleaning the signal from the different components it is possible to know the phase difference related to ground motion.

The first InSAR applications occurred in the 1980's (Gabriel et al. 1989). However, it became widely used today with the advancement of SAR processing algorithms in the early 2000's (Persistent Scatter InSAR, Ferretti 2001; Kampes 2006) and the launch of new Sentinel 1 and 2 in 2014 and 2015 acquiring freely available imagery (Torres et al. 2012). InSAR is now an accepted and growing technology both in academia and industry (Ferretti et al. 2015). The capability of InSAR to measure land deformation over large areas with sub-millimetre precision makes this technique useful for many geohazard applications. InSAR allows landslide identification, monitoring and failure forecasting (Chapter 5; Intrieri et al. 2017; Raspini et al. 2018), as well as the detection of uplift and subsidence preceding and following earthquakes (Moro et al. 2017), and volcano deformation (Neri et al. 2009). The first national-wide scale historic and near-real time deformation maps have been produced for Italy (Costantini et al. 2015; Raspini et al. 2018) and the United Kingdom (TRE-Altamira, 2017). InSAR plays an important role in hazard identification and risk mitigation strategy because of its large scale, near-real time survey capabilities.

1.3. Thesis outline

This thesis aims to fill the knowledge gap concerning the interplay of glacier and landslide processes and hazards at Mount Meager volcano. We investigate this gap using remote and field methods. The findings in this thesis may be applicable at other stratovolcanoes in glaciated terrains. In particular, the research questions are:

- What are the characteristics of glaciers on volcanoes and how do present and past glacier activity affect the volcanic edifice stability, slope deformation, collapse dynamics, and landslide rheology and runout?
- How does the 2010 Mount Meager landslide inform us about conditioning and triggering factors, including glacial debutressing, slope deformation, slope failure dynamics, landslide rheology and runout, and deposit characteristics?
- How do we apply the knowledge acquired to other slopes at Mount Meager for effective hazard and risk analysis, including slope monitoring, failure forecasting, warning and alarm systems?

- How can decompression following glacier retreat and landslides affect the hydrothermal and magmatic plumbing systems?

These research questions posed are tackled in the thesis and discussed in the various chapters. The thesis is based on seven chapters. Chapter 1 and 7 are general introduction and conclusions. Chapter 2, 3, 4, 5 and 6 are written in journal-style format and have been published or presented in a peer-reviewed journal, conference proceeding, or conference abstract. Details on authorship and journals are listed in each chapter.

- Chapter 1 presents the general geology and methodology introductions.
- Chapter 2 discuss the application of Structure from Motion photogrammetry to historic aerial photography and documents over half-a-century of glacier and landslide activity at Mount Meager volcano. (To be submitted to *Geomorphology*)
- Chapter 3 describes the 2010 Mount Meager landslide deposit and discusses the emplacement dynamics, rheological evolution and hazard implications. (Published in *Geosphere*).
- Chapter 4 discusses the slope condition and failure mechanisms of 2010 Mount Meager collapse. (Published in *Landslides*).
- Chapter 5 presents an inventory of unstable slopes and discusses hazard and risk at Mount Meager volcano. (Published in the *Geohazards7* conference proceedings).
- Chapter 6 discusses the possible decompression occurring in the volcanic plumbing system after large landslides at Mount Meager. (To be submitted to *Bulletin of Volcanology*).
- Chapter 7 draws the final conclusions of the thesis and discusses future perspectives.

1.3.1. Publication list

Here are listed publications, conference presentations, conference sessions and scientific outreach produced during the PhD work.

Papers

- Roberti G, Ward B, van Wyk De Vries B, Perotti L (2017) Structure from Motion and landslides: The 2010 Mount Meager collapse from slope deformation to debris avalanche deposit mapping. Geotechnical News, p. 20-22.
- Roberti G, Friele P, van Wyk de Vries B, Ward B, Clague JJ, Perotti L, and Giardino M (2017) Rheological Evolution of the Mount Meager 2010 Debris Avalanche, Southwestern British Columbia. Geosphere 13 (2): GES01389.1. doi:10.1130/GES01389.1.
- Roberti G, Ward B, van Wyk de Vries B, Friele P, Perotti L, Clague JJ, and Giardino M (2017) Precursor Slope Distress Leading up to the 2010 Mount Meager Landslide, British Columbia. Landslides 19: 2017, doi:10.1007/s10346-017-0901-.
- Delcamp A, Roberti G, and van Wyk de Vries B (2016) Water in volcanoes: evolution, storage and rapid release during landslides. Bulletin of Volcanology vol.78, p.87, doi:10.1007/s00445-016-1082-8.

Conference papers and presentations

- Roberti G, Ward B, van Wyk de Vries B, Araujo G, Manrique N, and Aguilar R (2018) Estudio geomorfológico y paleoambientale des las avalancha de escombros de Maca y Lari, Valle de Colca. VIII Foro los Volcanes y su Impacto, 26-27 April 2018, Arequipa, Peru.
- Roberti G, Ward B, van Wyk De Vries B, Falorni G, Menounos B, Friele P, Williams-Jones G, Clague JJ, Perotti G, Giardino M, Baldeon G, Freschi S (2018) Landslides and glacier retreat at Mt. Meager volcano: hazard and risk challenges. Geohazard 7 Engineering Resiliency in a Changing Climate, 3- 6 June, 2018, Canmore, Canada.
- Roberti G, Le Corvec N, van Wyk de Vries B, Ward B, Venugopal S, William-Jones G, Clague JJ, Friele P, Falorni G, Baldeon G, Perotti L, Giardino M, and Menounos B (2018) Can glacial retreat-related landslides trigger volcanic eruptions? Insights from Mount Meager, British Columbia. Geophysical Research Abstracts - EGU General Assembly Vol. 20. EGU2018-913, 8-13 April 2018, Vienna, Austria.
- Roberti G, van Wyk de Vries B, Ward B, Le Corvec N, Williams-Jones G, Clague JJ, Falorni G, Menounos B, Friele P, Perotti L, Giardino M, Baldeon G, and

Venugopal S (2018) Hazards posed by large mass movements at Mount Meager volcano, Canada. Geophysical Research Abstracts - EGU General Assembly Vol. 20, EGU2018-912, 8-13 April 2018, Vienna, Austria.

- Roberti G, van Wyk de Vries B, Ward B, Friele P, Clague JJ, Perotti L, Giardino M (2017) From ice melting to multi-phase debris avalanche: the 2010 Mount Meager volcano collapse. Invited talk IAVCEI 2017 - Submission 101, Fostering Integrative Studies of Volcanoes. IAVCEI Scientific Assembly,14-18 August 2017, Portland, Oregon, U.S.A.
- Roberti G, Ward B, van Wyk de Vries B, Perotti L, Giardino M, Friele P, Clague JJ (2017) Application of Structure from Motion to digitized historical airphotos to document geomorphic change over the past century. Geophysical Research Abstracts - EGU General Assembly,Vol.19, EGU2017-4051, 23-28 April 2017, Vienna, Austria.
- Roberti G, Ward B, van Wyk de Vries B, Friele P, Clague JJ, Perotti L, Giardino M (2017) Precursor slope distress leading up to the 2010 Mount Meager landslide, British Columbia., Geophysical Research Abstracts - EGU General Assembly 2017- Vol.6, p.EGU2017-1231.
- Zei C, Giardino M, Perotti L, Roberti G, Ward B, Clague JJ (2017) Historic (1940 to present) changes in Lillooet River planform (BC, Canada). Geophysical Research Abstracts - EGU General Assembly, Vol. 19, EGU2017-14076, 23-28 April 2017, Vienna, Austria.
- Roberti G, van Wyk de Vries B, Ward B, Clague JJ, Friele P, Perotti L, Giardino M (2016) High resolution digital mapping and geomorphological analysis of the 2010 Mount Meager rock-debris avalanche (BC, Canada). Geophysical Research Abstracts - EGU General Assembly, Vol. 18, EGU2016-12328-1,17-22 April 2016, Vienna, Austria.
- Roberti G, Ward B, van Wyk de Vries B, Perotti L, Falorni G, Clague JJ, Giardino M (2015) Mount Meager Volcano, Canada: a Case for Landslides on glaciated volcanoes. AGU Fall Meeting, 14-18 December 2015, San Francisco, California, U.S.A.
- Roberti G, Clague JJ, Friele P, Giardino M, Masera D, Perotti L, and van Wyk de Vries B (2014) High resolution digital mapping and geomorphological analysis of the Mount Meager rock-debris avalanche (BC, Canada). Paper No. 211-10, GSA Annual Meeting, 19-22 October 2014, Vancouver, British Columbia, Canada.

- Masera D, Calhoun N, Clague JJ, Giardino M, Perotti L, Poschinger A, and Roberti G (2014) Geomorphology and geomatics for the study of landforms and deposits related to the Flims and Tamins landslides (Rhein valley, Switzerland). Paper No. 211-11, GSA Annual Meeting, 19-22 October 2014, Vancouver, British Columbia, Canada.

Conference sessions organized

- EGU (European Geoscience Union) General Assembly 2018. GMPV4.8/CL1.34 Arctic, Antarctic and other glaciated terrains volcanism - magmatic, tectonic, geomorphic and climatic implications.
- AGU (American Geophysical Union) Fall Meeting 2018. V038: The Emerging Multidisciplinary Science of Fire and Ice: Understanding the causes, timing and consequences of planetary glaciovolcanism.

Science outreach

- Three Minute Thesis Competition Finals 2018: "Volcanoes in a changing climate".
- EGU (European Geoscience Union) general assembly 2018 Press conference "Hazards in the wake of climate change".
- On the Rocks: your thesis is 3 minutes. "Mr Meager - the Mount Meager project".

Chapter 2. Structure from Motion and historical airphotos to document decades of glacier and landslide activity at Mount Meager volcano [1]

Gioachino Roberti[1,2] , Brent Ward[2], Benjamin van Wyk de Vries[1], Luigi Perotti[3] , Marco Giardino[3] , Pierre Friele[4], and John J. Clague[2]

(1) Université Clermont Auvergne, CNRS, IRD, OPGC, Laboratoire Magmas et Volcans, Aubiere Cedex, France (2) Earth Sciences Department, Simon Fraser University, Burnaby, British Columbia Canada (3) Earth Sciences Department, University of Torino, Torino, Italy (4) Cordilleran Geoscience, Squamish, British Columbia, Canada

2.1. Abstract

Topographic modeling is becoming more accessible due to the development of Structure from Motion (SfM) image matching algorithms in digital photogrammetry. However, little work has been done in using SfM with digitized historical airphotos. Large databases of historical airphotos are available in university, public, and government libraries, commonly as paper copies. The photos can be in poor condition (i.e. deformed by humidity, scratched, or annotated). In addition, the negatives, as well as metadata, may be missing. Processing such photos using classic stereo-photogrammetry is difficult and in many instances impossible. However, SfM can be applied to these photosets to access the valuable archive of geomorphic changes over the last century. We digitized over 500 vertical airphotos of the Mount Meager massif (British Columbia, Canada), acquired between 1947 and 2006 to document glacier and landslide activity. We processed the scans using the commercial SfM software PhotoScan. PhotoScan provided high-quality orthophotos (0.42-1.13 m/pixel) and DSMs (1-5 m/pixel). Changes at Devastation, Mosaic, Job, Affliction, and Bridge River valleys were documented and related to glacier geomorphic parameters. We recorded rock avalanches onto the ice

[1] Part of this chapter has been presented as poster at EGU (European Geoscience Union) 2017 General Assembly: Roberti G, Ward B, van Wyk de Vries B, Perotti L, Giardino M, Friele P, Clague JJ (2017) Application of Structure from Motion to digitized historical airphotos to document geomorphic change over the past century. Geophysical Research Abstracts - EGU General Assembly 2017- Vol.19, p.EGU2017-4051.

and the formation of moraines from the landslide debris. We report fumarolic activity at Job Glacier and discuss the role of volcano ice-interaction in the evolution of Mount Meager. This practical demonstration shows the use of SfM on combinations of archive material.

2.2. Introduction

Surface information and topographic reconstruction over time are fundamental in many landform and natural hazard studies. The classical approach to produce topographic models, and indeed any large scale topographic map, is aerial stereo-photogrammetry. In the past century, airphotos have been extensively acquired leading to the collection of large paper-copy archives. These historic airphotos are a unique resource to document surface changes over the past century (Bjørk et al. 2012; Gomez et al. 2015) but they commonly lie forgotten in university, government, public, and private libraries. In many instances they are deformed by humidity, scratched, or annotated and original negatives and metadata on the camera and the flight mission may be missing. Datasets of aerial photographs can record features that have been modified or have completely disappeared, and they cover remote areas and challenging terrains (high mountains, glaciated terrains) where definition of ground control points is impossible or a very difficult task (Chandler 1999; Lane et al. 2000; Gomez 2014; Gomez et al. 2015; Micheletti et al. 2015). Retrieving topographic information from these datasets with classical digital photogrammetry is difficult or even impossible. Structure from Motion (SfM) is an alternative to photogrammetry and is also able to retrieve surface information from these challenging datasets (Gomez et al. 2015; Bakker and Lane 2016; Roberti et al. 2017 b,c; Mertes et al. 2017; Mölg and Bolch 2017). We digitized over 500 (Table 2.1) historic vertical airphotos with a flatbed A3 format scanner. The commercial SfM software PhotoScan was used to process the digitized photos to produce orthophotos and DEMs. PhotoScan delivered good quality orthophotos (0.42-1.13 m/pixel) and DEMs (1-5 m/pixel) suitable for the geomorphic study of Mount Meager. We processed part of the same dataset as Roberti et al. (2017c, Chapter 4) using 1947, 1951,1962, 1964-65, 1973, 1981, 1990, and 2006 photos. The objectives of this paper are:

- To document over half of a century of glacier fluctuations and landslide activity at Devastation, Mosaic, Job, Affliction and Bridge River valleys in the Mount Meager volcanic complex;

- To describe the different behaviours of the glaciers and landslide events;
- To describe the formation of moraines from landslide debris.

In order to explain the high landslide frequency and the glacier activity at Mount Meager we discuss a conceptual model of the evolution of a volcanic edifice from glacial to interglacial periods. Finally, we outline the advantages of surface reconstruction from archival air photography both in terms of scientific and outreach applications.

2.2.1. Context of glacier and landslide activity at Mount Meager volcano

Mount Meager is a volcanic complex in British Columbia, Canada. It supports numerous alpine glaciers and is known for the high frequency and magnitude of its landslides. Many studies have focused on present and past landslide activity at Mount Meager (Jordan 1994; Jakob 1996; Friele and Clague 2004; Guthrie et al. 2012a, b, Hetherington 2014) but only few studies have investigated the role of recent deglaciation on slope stability (Holm et al. 2004; Roberti et al. 2017c). No studies have focused on the Mount Meager present glacier morphology and activity, nor on the effects of regional glaciation on Mount Meager volcanic activity.

Glacier processes have a major role in shaping the landscape and in conditioning slope stability (Deline et al. 2015). Glaciers erode and oversteepen slopes, condition slope hydrology and the state of stress (McColl et al. 2010; Grämiger et al. 2017). Glaciers also affect volcano shape and eruptive activity, producing a variety of glaciovolcanic morphologies and deposits (Edwards et al. 2015). In turn, volcanoes can affect the present glacier shape and activity (Barr et al. 2018b). Many works have focused on glaciovolcanism in terms of the volcanic edifice morphologies and deposit characteristics (Smellie 2013; Russel et al. 2014; Wilson and Russel 2018), the effect of post-glacial crust decompression on volcanic activity (Rampino et al. 1979; Jellinek et al. 2004; Huybers and Langmuir 2009; Watt et al. 2013), and present volcano-ice related hazards (Major and Newhall 1989; Waythomas 2014; Barr et al. 2018b). Few studies focus on debris-covered glaciers in a volcanic environment (Barr et al. 2018a). There are no studies which focus on the effect of a volcanic bedrock on glacier dynamics, and only few investigate the long term effects of glacial debuttressing on volcanic edifice stability (Capra 2006; Tormey 2010; Capra et al. 2013) .

Here we document the present glacier morphology and activity at Mount Meager volcano, as well as landslide events. Debris-covered glaciers commonly form in landslide and eruptive scars where hillslope erosion rates are high. We hypothesize how the past regional glaciations may have affected the volcanic edifice morphology and stability, influencing today's glacier and landslide processes.

2.3. Methods

In the following section we present the workflow from the digitization of archival paper-copy airphotos, to three-dimensional model generation and geomorphological mapping.

2.3.1. Digitization of historical airphotos and cartographic production

Black and white aerial photographic coverage of Mount Meager exists for 1947, 1948, 1951, 1962, 1964-1965, 1973, 1981, 1990, and color in 2006 (Chapter 4, Roberti et al. 2017c). For this study we processed 1947, 1962, 1964-65, 1973, 1990 and 2006. We could not process 1948 dataset over the whole massif, as the dataset is incomplete. The 1947 dataset covers the entire massif but clouds are present, obstructing geomorphic feature observation. The 1962 dataset has poor overlap in the center of the massif and snow covers most of the slopes.

We used an A3 format flatbed scanner for the digitization of the historical airphotos. The photos were scanned with the direction of the strip (flight) parallel to the charges-coupled device (CCD) array following Linder's (2009) guidelines. The minimum DPI (dot per inch) necessary for the scan have been derived from the scale factor (S) of the photographs (Table 2.2) that it can be calculated as:

$$S = Z/c$$

Where Z is the flight height and c is the focal length. These values are usually recorded on the datastrip of the photographs. In our case, it was commonly impossible to read the values of the flight height on the altimeter on the frames and the focal length was unknown for many flights. Hence, to determine the scale factor of the photographs we used the following procedure:

1. Measure the distance between visible points both on the photographs and on georeferenced basemaps (in this case SPOT satellite images).
2. Obtain values of the real distance and the distance measured on the photos, both expressed in metres.
3. Determine the scale factor by dividing of the real values by the image-values to provide the minimum DPI for the scan.

The list of the images along with their characteristics is in Appendix A, Table A1.

PhotoScan processing

We used Agisoft PhotoScan Professional v1.2.6 SfM software (www.agisoft.com - Agisoft LLC, St. Petersburg, Russia) to process digitized historical airphotos. We have chosen PhotoScan because of its widespread use and proven reliability and precision in geosciences (Remondino et al. 2014; James et al. 2017a) and it contains a complete workflow from image matching to three-dimensional dense reconstruction, georeferencing, orthophoto and DEM generation in a single software package. The PhotoScan matching algorithm is not known as it is protected for commercial reasons, however, PhotoScan uses an image matching process similar to SIFT (scale invariant feature transform) method (Lowe 1999); for the dense reconstruction, it uses pairwise or multi-view stereo approaches (Semyonov 2011). We followed the standard PhotoScan workflow for orthophoto and DEM generation (Figure 2.1). Every step is named after PhotoScan processing; for more information, see PhotoScan User Manual (2017).

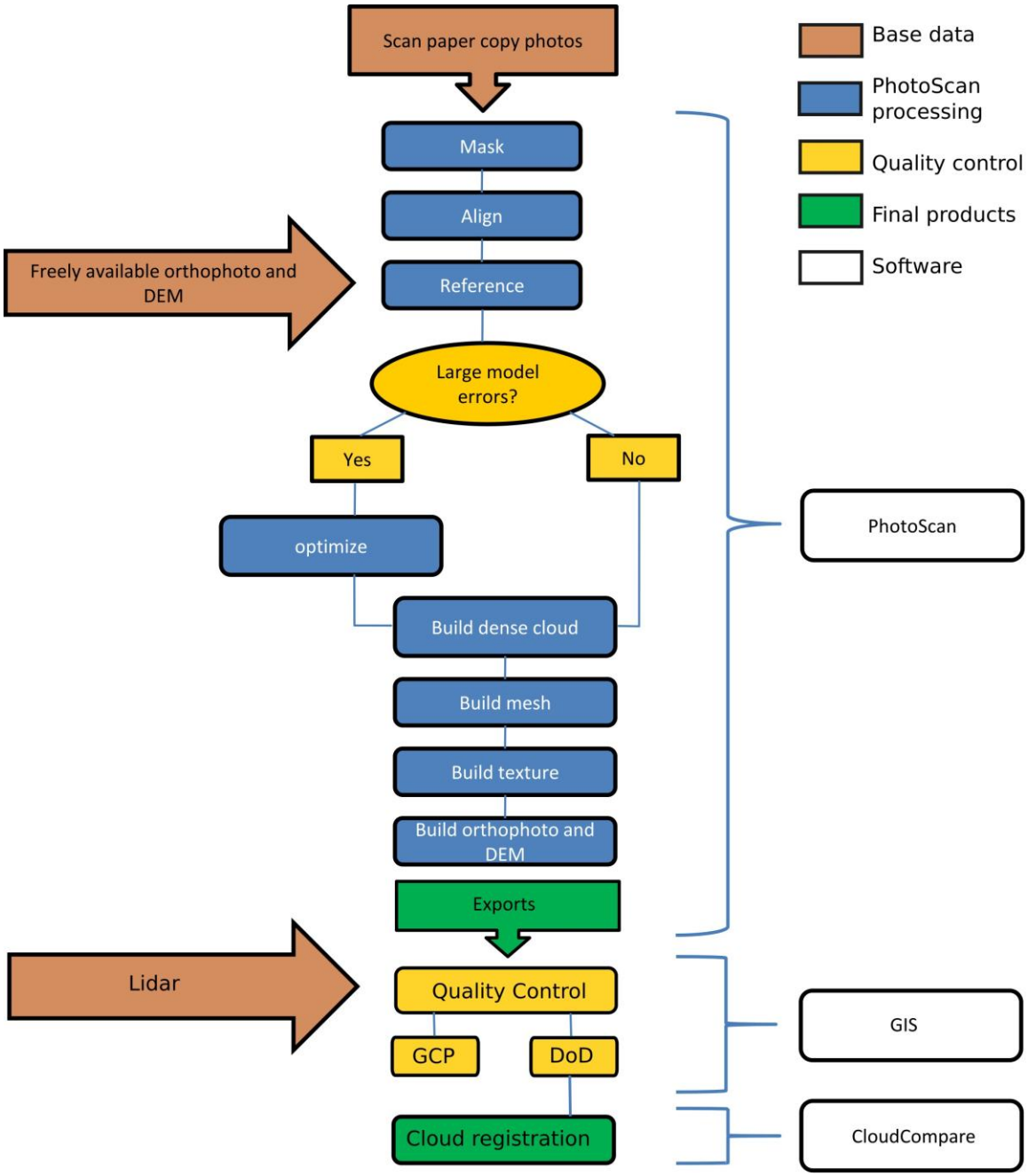

Figure 2.1. SfM workflow from photo digitization to orthophoto, DEM export, and quality control.

1. **Masking photos**. We masked out photo frames and inscriptions to speed up the processing and avoid the presence of artifacts in 3D models, orthophotos and DEMs. Two masking approaches were followed. For the color datasets (2006) we automatically selected the dark pixels of the photo frame and manually excluded annotations. For grayscale datasets (1947, 1951, 1962, 1964-65, 1973, and 1990), we manually masked the photo frames and inscription. The automatic

approach was not suitable for the grayscale datasets as large areas in the images have the same dark tones as the frame.

2. **Align photo**. To generate a point cloud, the software matches features between the photos, defines and filters key points, estimates the camera position and camera parameters (focal length, principal point location, and up to four radial and four tangential distortion coefficients) and reconstructs the scene structure. "High accuracy" setting has been used for photo alignment, and image pair preselection was set to "Generic" (in a first step image pairs are selected by matching photos using lower accuracy setting and then re-matched at higher accuracy).

   The 2006, 1981, 1973, 1962, and 1947 photo datasets were aligned at "high" resolution, 1964 at "medium" resolution and 1990 at "lowest" resolution. The quality of the alignment refers to the size of the photo: at "high" setting the photos are matched at full resolution, while pictures are downscaled of a factor of four at every lower quality setting. We noticed that at "high" setting (full photo resolution) the software was over representing some zones of the photos generating clouds with a heterogeneous distribution of points. In those cases, decreasing of alignment quality led to point clouds with better distributed matches. After the point cloud generation we cleaned the models, deleting incorrectly projected points with manual and automatic selection methods.

   Lower alignment quality generates less detailed models (and coarser final DEMs) but also less artifacts from trees, crevasses and zones of poor texture over ice and snowfields. Downscaling alignment quality means larger matching areas where small shadows and imperfections in the photos are not visible and considered during the matching. Only the larger features will be visible and contribute to the alignment.

   For the1964 and 1990 datasets PhotoScan was not able to align all the pictures in one set. We had to align the different photo strips in separate chunks and later merge the models in one single point cloud matching by manually placed markers, and then proceeded with the next steps of the process.

3. **Referencing**. At this step ground control points (GCP) are identified to georeference the models. During georeferencing, a rigid seven parameter

transformation is applied to translate, scale, and rotate the model to fit the, real world, scene location. Ideally, GCPs should be located in flat, stable areas, far from cliffs, easy to recognize, and of easy access. At Mount Meager, it is very challenging to find points with these characteristics. Snow and glaciers cover the volcano, the valley flanks have very active channels or are forested, and the access to the area is challenging and dangerous.

Instead of field-collected GCP, we defined 21 control points on the standard base maps. Planimetric coordinates were derived from satellite SPOT 10 m imagery and vertical coordinates from the Canada TRIM (Terrain Resource Inventory Map) DEM (18.3 m average accuracy and up to >40m) (NRCan 2013). We selected points in meadows, glacier polished bedrock, little ice age moraines, logging roads and other recognizable features. Not all the points are visible in all the datasets. In the older datasets the logging roads are not present and the higher altitude points can be covered by snow.

4. **Optimization**. The rigid transformation applied during georeferencing cannot correct non-linear error that may be present in the model. Non-linear errors can be related to poor picture overlap, object texture or shape, or lens and scanner deformation. In order to partially correct these types of error, PhotoScan recommends to “optimize” the estimated point cloud, camera position, and camera parameters based on GCP position. However, if the GCPs have low accuracy, they can introduce extra errors. In our case, the GPS planimetric accuracy is larger than 10 m and the vertical accuracy is larger than 40 m, we estimated that the PhotoScan alignment precision was greater than the GCP accuracy and we did not proceed to the optimization of the point clouds. We optimized only the point clouds (1962, 1990) that showed an artificial exaggeration along the Z direction. In those cases, the optimization partially corrected the vertical exaggeration of the models.

5. **Build Dense Point Cloud**. PhotoScan increases the number of points generating a dense point cloud. It calculates the depth map for each photo and produces a large number of points, many of which can be outliers. It is advisable to use a “depth filter” to reduce the number of these points. We used the method “aggressive” recommended for aerial photography. In areas of poor texture

(especially glaciers and snowfields) many incorrect points have been generated; those areas have an artificially rough aspect.

6. **Build Mesh**. PhotoScan interpolates polygons between the points to generate a 3D mesh surface. The setting “Height field” where the interpolation direction is along Z axes is recommended for planar scenes and aerial photography. We used the suggested “high” value for the polygon count.

7. **Build Texture**. A texture of the 3D models is reconstructed here. We used the “orthophoto” mode, where the texture is reconstructed with an orthographic projection. It works well with flat surfaces but not as well with vertical parts. The blending mode was set to “mosaic” as recommended for aerial photography.

8. **Build digital elevation model (DEM).** A rasterized version of the 3D model is generated at this step. Sparse, dense point clouds or mesh can be used as base for the DEM generation. We used the dense point cloud as source of the DEM.

9. **Build orthomosaic**. The orthomosaic is generated on the DEM surface. The blending mode has been left to the default “mosaic” setting.

Artefacts or voids are commonly generated in zones of poor texture (glaciers, snowfields, forested areas, shadows). Clouds can also obscure part of the landscape generating errors in the 3D models. Careful visual model examination is needed to identify and correct such errors. The reconstructed orthophotos and DEMs are suitable for geological qualitative and quantitative observations, despite lens and scanning deformation, poor textures of snow, ice and forest covered areas and poor GCP accuracy. Table 2.1 summarizes the model characteristics for the different photo datasets.

Table 2.1. Airphotos and PhotoScan model characteristics.

Year	Number of pictures	Approximate photo scale	Pixel size (m/pixel)	3D error (pixel)	3D model precision (m)	DEM pixel size (m/pixel)
2006	114	1:13000	0.5	1.2	0.6	2
1990	89	1:13000	0.5	3.0	1.5	2.2
1981	51	1:20000	0.7	1.1	0.8	2.7

1973	116	1:13000	0.5	1.1	0.6	1.9
1964	29	1:25000	1.3	1.4	1.8	5
1962	108	1:15000	0.5	1.4	0.7	1.8
1951	11	1:60000	2.2	1	2.2	4.3
1947	50	1:20000	1.1	1.4	1.5	4.3

2.3.2. Cartographic product validation and GIS mapping

The cartographic suitability of the PhotoScan generated orthophoto and DEMs was tested by comparison with a Lidar DEM acquired in 2015-2016. We followed two different approaches to assess the SfM products (Figure 2.1). First, we compared X, Y, and Z coordinates of 22 control points between the PhotoScan models and the Lidar reference. Secondly, we did raster to raster differencing between the datasets and the Lidar to evaluate the DEM quality. Then, to reduce systematic errors (tilting, doming etc.), we 1) re-aligned a subset of the photos and 2) co-registered DEM subsets in CloudCompare (CloudCompare 2018). Photo re-alignment and DEM co-registration improved the DEMs, allowing more precise DEM comparison and volume calculations.

Check Points

Following the ASPRS (2014) guidelines, we applied the root mean square error (RMSE) approach to evaluate the SfM-derived cartographic products. The RMSE of x, y, z coordinates of at least 20 control points (CP) taken from the PhotoScan exports and a reference at higher accuracy is calculated. $RMSE_x$, $RMSE_y$, $RMSE_z$, and $RMSE_r$ are defined as follows:

$$\mathrm{RMSE_x} = \sqrt{\frac{1}{n}\sum_{i=1}^{n}\left(x_{i(\mathrm{map})} - x_{i(\mathrm{reference})}\right)^2}$$

$$\mathrm{RMSE_y} = \sqrt{\frac{1}{n}\sum_{i=1}^{n}\left(y_{i(\mathrm{map})} - y_{i(\mathrm{reference})}\right)^2}$$

$$\mathrm{RMSE_z} = \sqrt{\frac{1}{n}\sum_{i=1}^{n}\left(z_{i(\mathrm{map})} - z_{i(\mathrm{reference})}\right)^2}$$

$$\mathrm{RMSE_r} = \sqrt{\mathrm{RMSE_x^2} + \mathrm{RMSE_y^2}}$$

Statistically, 68 % and 95 % errors are within 1 standard deviation (σ) and 2σ , respectively, of the mean (ASPRS 2014). The horizontal accuracy at 95% (HA 95%) and vertical accuracy at 95% (VA 95%) confidence level is defined by the following empirical equations:

$$\mathrm{HA}\,95 = 1.7308 \times \mathrm{RMSE_r}$$

$$\mathrm{VA}\,95 = 1{,}9600 \times \mathrm{RMSE_z}$$

HA 95 and VA 95 approximate the maximum error on either side of the mean of 95% of the planimetric and altimetric values. This method tends to overestimate the error as the mean error increases. We defined 22 check points on the Lidar and the photo datasets and calculated $RMSE_x$, $RMSE_y$, $RMSE_z$, $RMSE_r$, HA 95, and VA 95 (Table 2.2).

Table 2.2. $RMSE_x$, $RMSE_y$, $RMSE_z$, $RMSE_r$, HA 95, and VA 95 for the different photo datasets.

Year	RMSEx	RMSEy	RMSEr	RMSEz	HA 95 (m)	VA 95 (m)
2006	10	9	13	25	23	49
1990	6	9	11	8	19	15
1981	11	12	16	40	28	78
1973	29	41	50	25	86	49
1964	23	28	36	30	62	59
1962	15	8	17	90	30	176
1951	13	22	25	14	25	28
1947	20	28	35	17	61	34

DEM of difference

In order to better assess the error on the Z value of the SfM derived DEMs, we calculated the DEM of difference (DoD) between each dataset and the Lidar DEM. The SfM derived DEMs have systematic errors (Figure 2.2). The models are tilted (1964, 1981, 2006, Figure 2.2), showed doming effect (1962, Figure 2.2) or had steps between the different flight stripes (2006, Figure 2.2). In order to reduce these errors we re-aligned subsets of photos and increased the number of control points in the PhotoScan

processing. A smaller number of images requires less computational power, produces smaller, more manageable point clouds where wrongly projected points are easier to identify and remove. Also more control points can be easily placed; thus improving the overall 3D model generation and georeferencing process (see Chapter 4). Then we co-registered point cloud subsets in CloudCompare (CloudCompare 2018). The registration in CloudCompare eliminated the systematic tilting and corrected some of the doming effects. We registered pairs of point clouds, choosing each time the higher resolution cloud as reference. This approach reduced the cloud registration errors to 1-10 m. Figure 2.3 and 2.4 are two examples of DEM analysis for the pre-2010 collapse slope (shown in Figure 2.3) and Devastation Valley (Figure 2.4). In the pre-2010 collapse slope, it is possible to observe the glacier mass loss, a precursory failure from the toe of the slope, and an increase in displacement along the major fault that conditioned the failure (see Figure 4.4 and Chapter 4 for more details about the 2010 failure).

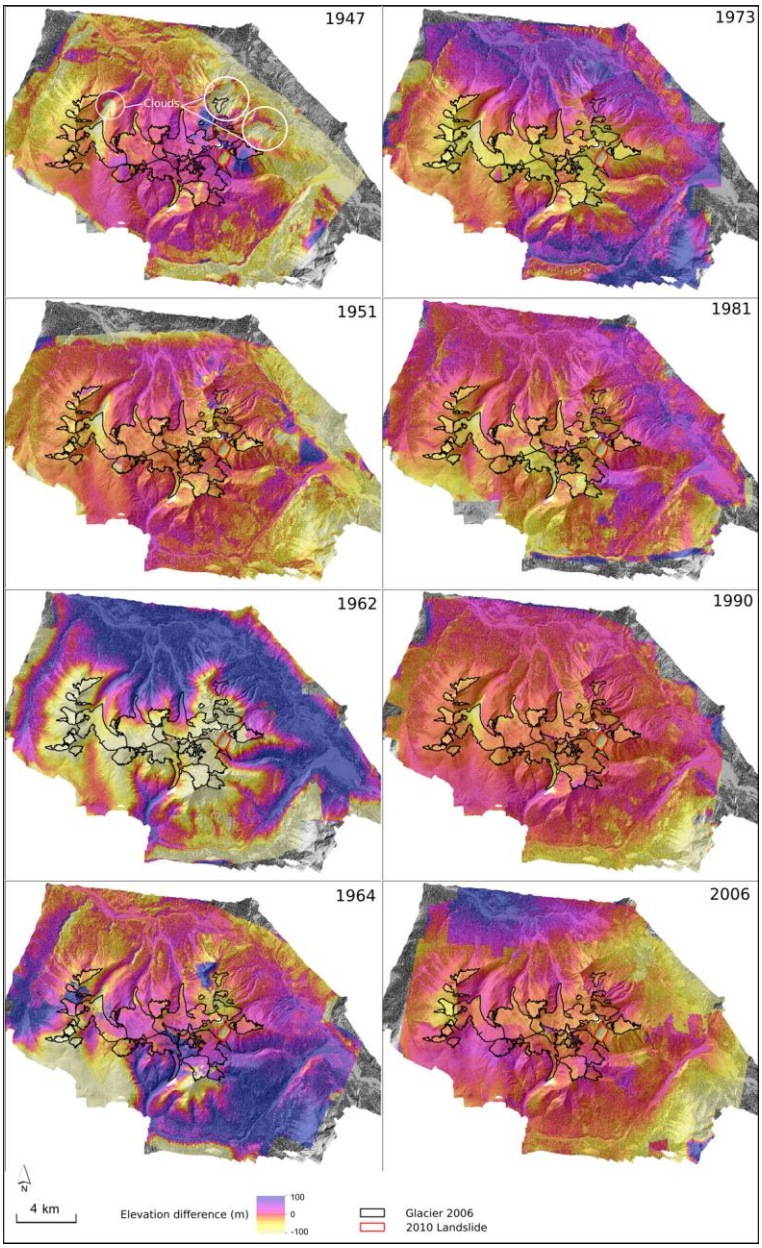

Figure 2.2. **DEMs of difference between the photo datasets and the Lidar reference. Black outlines are the glaciers in 2006. Red outline is the 2010 landslide scar. In the 1947 dataset, artifacts are generated by clouds. Despite systematic errors (doming, photo strip misalignment, tilting) that are present in all the datasets, the glacier mass loss is visible in some datasets without further processing.**

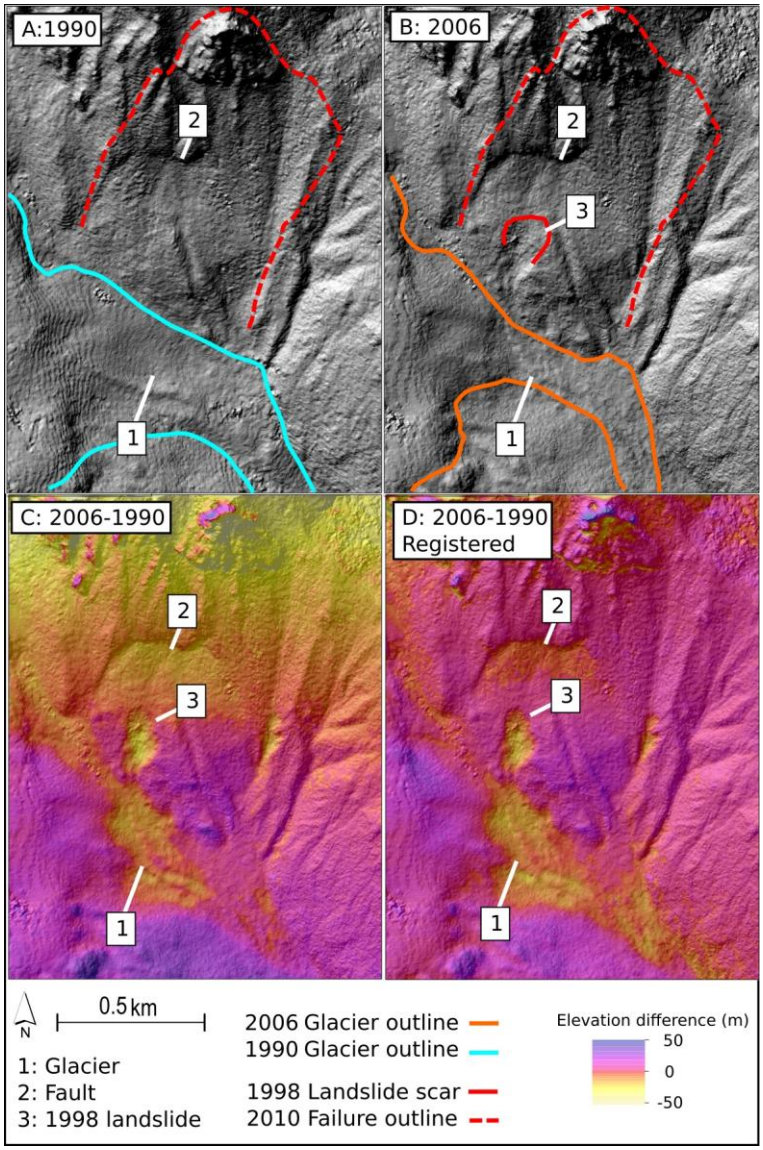

Figure 2.3. **Comparison of 1990 and 2006 datasets for the pre-2010 failure slope. A)Shaded relief model of the 1990 DEM. The glacier outline, the 2010 failure, and a major fault associated with the 2010 failure are indicated. B) Shaded relief model of the 2006 DEM. The glacier outline, 2010 failure, 1998 landslide scar, and major fault are indicated C) 2006-1990 DoD, note the systematic yellow to purple transition from the top to the bottom of the figure, indicating tilting between the two DEMs. The glacier, 1998 landslide scar and fault are indicated. D) 2006-1990 DoD after CloudCompare registration. The systematic tilting is corrected and the elevation difference in stable areas is 2 m. Glacier mass loss, 1998 scar and displacement along the fault are visible in the DoD. See Chapter 4 for the description of the 2010 slope deformation prior to the collapse.**

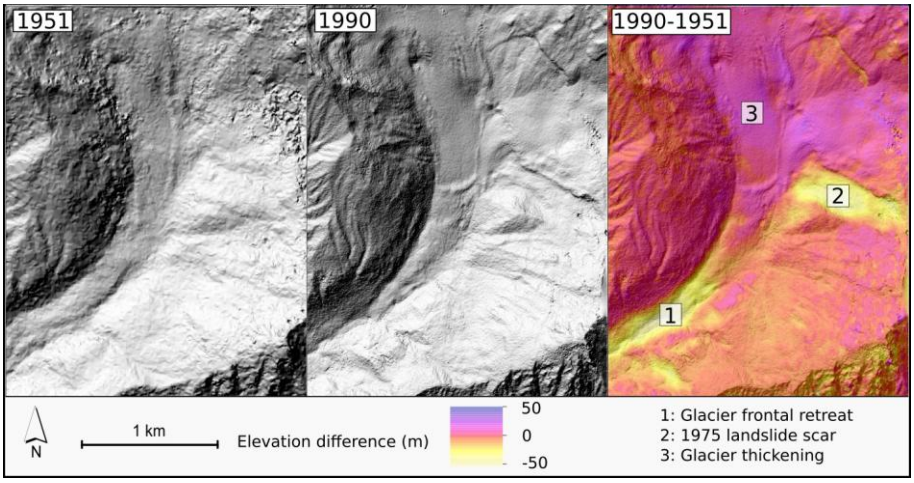

Figure 2.4. Comparison of 1951 and 1990 datasets for Devastation Valley. A) Shaded relief model of the 1951 DEM. B) Shaded relief model of the 1990 DEM. C) DoD after CloudCompare registration. Glacier frontal retreat (1), the 1975 landslide scar (2) and glacier thickening (3) are visible. The elevation difference between 1951 and 1990 DEMs in stable areas is 10.6 m. Note the artificially rough surface in the 1951 DEM.

Mapping

The descriptions of the geomorphological evolution of the glacier basins (Figure 2.5) are subdivided into Devastation (Figure 2.6), Mosaic (Figure 2.7), Job (Figure 2.8), Affliction (Figure 2.9), and Bridge River (Figure 2.10). We considered the glacier length from the highest elevation point to the glacier front. We measured the glacier basin area including steep slopes surrounding the glacier that produce snow avalanches and rock falls onto the glacier, which contribute to both glacier ice mass and debris cover. We distinguished active and stagnant ice near the terminus of the glacier based on the presence or absence of crevasses as indicator of ice flow, plus hummocky topography indicating stagnant ice. Glacier outlines, moraines, landslides deposits, scars, and fractures are mapped at 1:20,000. Considering the high georeferencing error (19-89 horizontal and 15-179 vertical), the measurements of the glacier front and moraine positions in the different datasets are relative to each year and not compared directly; we compared by defining stable reference lines in each dataset from which we referred the measurements. In the Devastation Valley the reference line is passing by the 1947 landslide apex (Figure 2.6 H), in Mosaic (Figure 2.7 H), Job (Figure 2.8 J) and Bridge River (Figure 2.10 I) glaciers the reference is a line passing by a gully in their respective Little Ice Age moraines, and in Affliction Valley it is line intersecting a tension fracture near the Little Ice Age maximum (Figure 2.9 J). These absolute lengths are not affected

by the georeferencing error of each dataset, but only by the polygon digitization error (which depends on the mapping scale and operator precision) and by the model precision (pixel error); this allows relatively precise measurements even in poorly georeferenced maps. The graphic error at 1:20,000 is 4 m, and it is larger than the bundle adjustment error (pixel error) of all datasets (0.6-2.2 m), allowing no further error consideration when mapping at this scale. The values of retreat rate are calculated by dividing the difference between the absolute front position distance from the reference line by the year difference between the considered datasets. This gives an average retreat rate for the time between photos and does not take into account any glacier fluctuations.

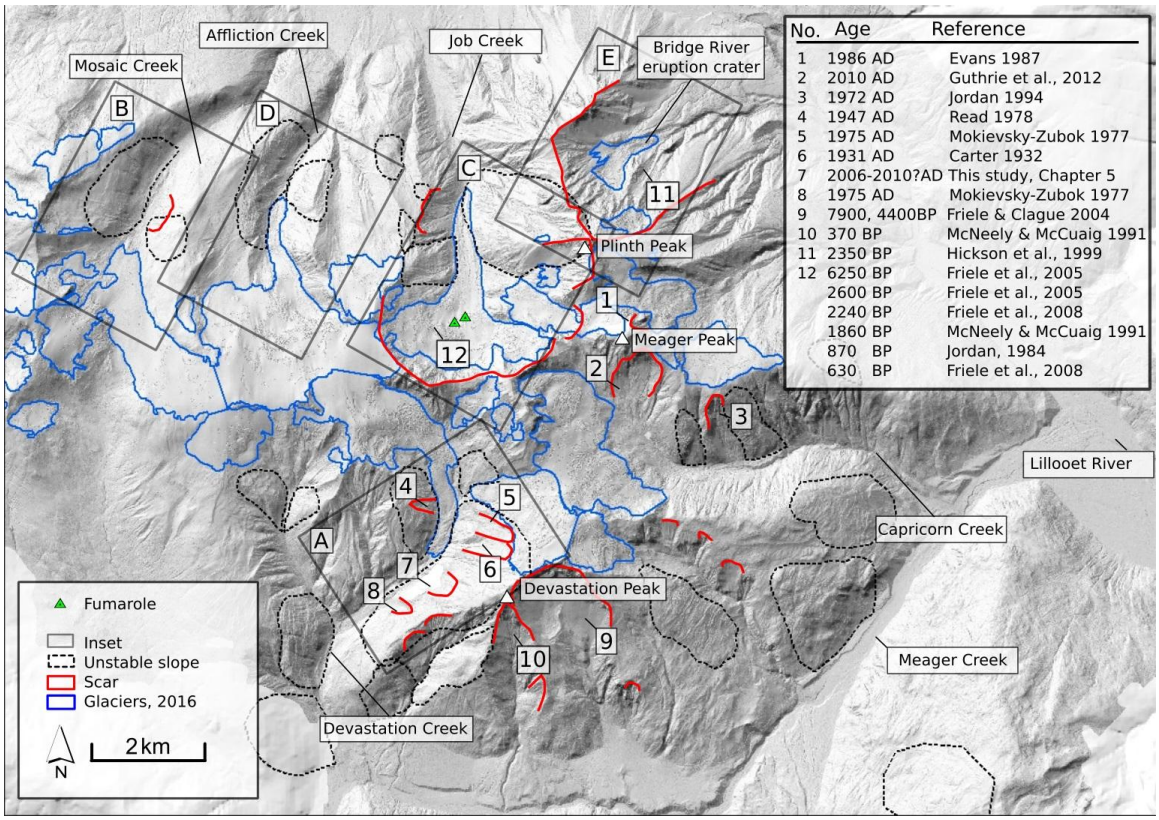

Figure 2.5. Overview of the Mount Meager volcanic complex showing the 2016 glacier extent, landslide scars with reference number, unstable areas, and figure locations. Inset A) Figure 2.6. B) Figure 2.7. C) Figure 2.8. D) Figure 2.9. E) Figure 2.10.

2.4. 1947-2016 geomorphic changes at Mount Meager volcano

2.4.1. Devastation

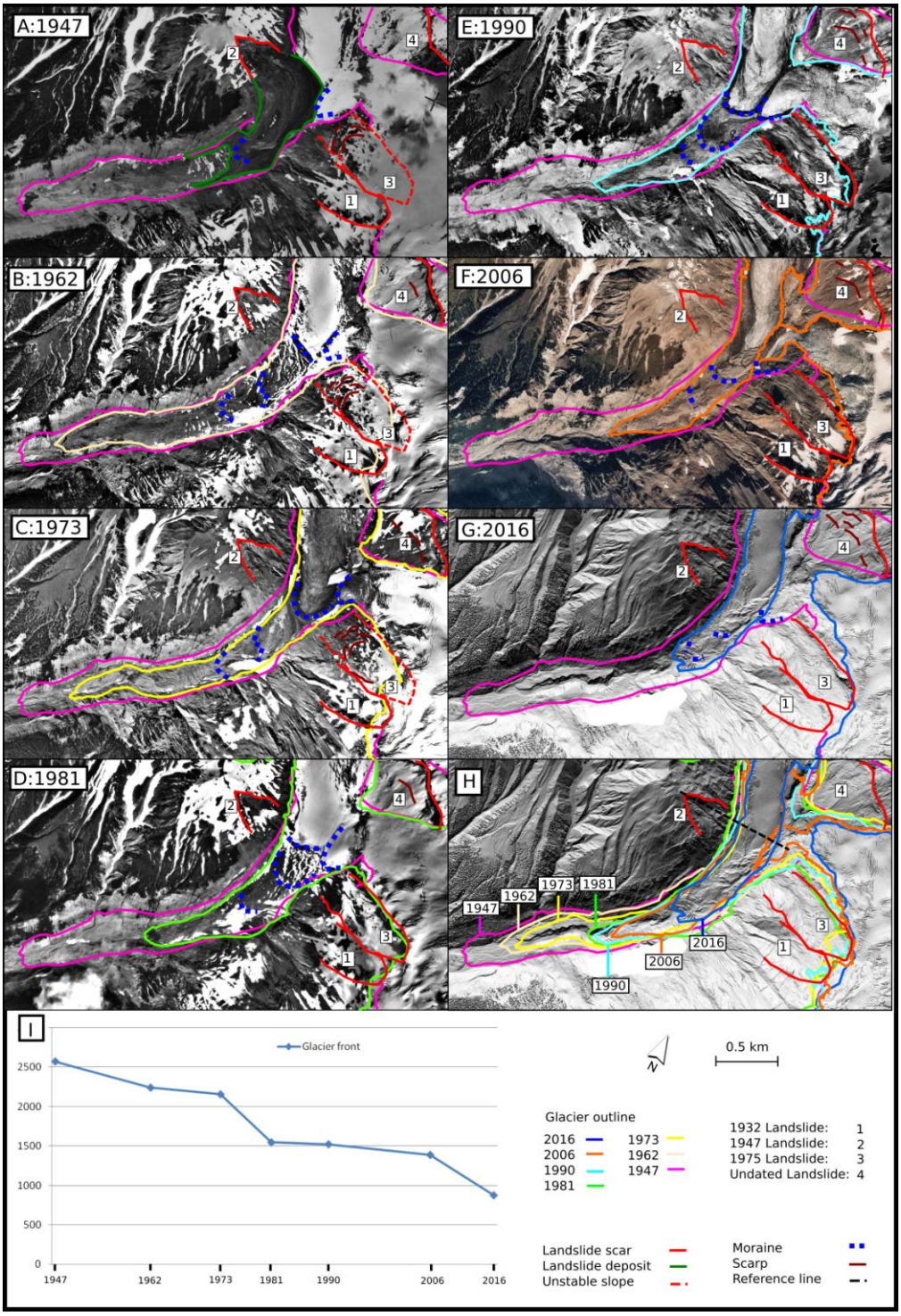

Figure 2.6. Devastation Valley from 1947 to 2016. Glacier outlines, moraines, landslide deposits, scars, and scarps are indicated. A) 1947: glacier at its maximum extent, note the 1947 landslide deposit. B) 1962: glacier has carried the 1947 landslide deposit to form an arched moraine back from the terminus of the glacier. C) 1973: while the debris-covered front has receded the landslide debris/moraine has advanced further. D) 1981: glacier front has receded and a new moraine formed from the 1975 landslide debris. Note the 1975 landslide scar. E) 1990: glacier front has receded, note the arched moraine from the 1975 landslide debris. F) 2006: glacier has receded. G) 2016 (Lidar data): glacier has receded further. H) 2016 (Lidar data) with glacier outlines. I) Change in the glacier front position over the photo period. Years in x-axis and metres from the reference line in the y-axis. Note the decrease of recession during 1962-1973 and 1981-2006 periods.

Devastation Glacier presently extends 3.7 km from 2200 to 1400 m asl. It originates from the same ice cap as the Mosaic and Affliction glaciers and flows to the SE. The basin area is 3 km^2 with headwalls up to 0.7 km high (Table 2.3). Landslides in 1947 and 1975 deposited debris on the glacier, which was subsequently deformed into moraines.

The 1947 photo dataset shows the fresh landslide deposit on the glacier and the maximum glacier extent (Figure 2.6 A). The 1947 landslide scar has a triangular shape 0.26 km high and 0.27 km wide at the base. The landslide spread 1.8 km (L) onto the glacier with a vertical drop of 0.5 km (H) giving a *Fahrböschung* (travel angle) of 15°. The landslide debris was funnelled by lateral moraines and split into two lobes shortly after overtopping a debris ridge on the glacier. Darker and lighter debris streaks are visible on the landslide surface. Debris ridges and crevasses extend 1.2 km from the 1947 landslide deposit indicating active ice. The total debris-covered ice downstream from the 1947 landslide is 1.7 km. The terminal 0.5 km of the glacier has a subdued hummocky topography indicating stagnant ice.

The stagnant ice snout retreated between 1947 and 1973 at a rate of ~16 m yr^{-1}, retreat increases between 1973-1981 (~76 m yr^{-1}), and decreases to ~6 m yr^{-1} between 1981 to 2006 to increase again between 2006 to 2016 (~51 m yr^{-1}) (Figure 2.6 I). The active ice terminus retreated at ~14 m yr^{-1} between 1947 and 1973, at ~88 m yr^{-1} between 1973 and 1981 but advances at ~13 m yr^{-1} between 1981-1990 and then retreated between 1990 and 2016 at ~10 m yr^{-1} (Figure 2.6 A-I). The total frontal retreat from 1947 to 2016 is 1.7 km.

By 1962 the glacier had carried the 1947 landslide debris to form two moraines. The upstream landslide debris limit formed an arched moraine ridge, while towards the terminus of the landslide deposit, a s-shaped moraine is formed (Figure 2.6 B). Both 1947 landslide debris ridges moved downstream at ~11 m yr^{-1} between 1962 and 1981. In 1981 the moraines have been covered by the 1975 landslide debris but are still recognizable. Movement of the moraines increased to ~28 m yr^{-1} between 1981 and 1990. It decreased to ~6 m yr^{-1} in the 1990-2016 period. In the 2006 image the lower moraine is not recognizable anymore and the upper moraine is eroded.

In the 1947, 1962 and 1973 datasets the 1975 pre-failure slope is partly obscured by clouds and snow; however, counter scarps are visible in the lower part of the slope (Figure 2.6 A, B, C). The 1981 dataset shows the 1975 collapse scar and landslide debris on the glacier. The collapse scar is 0.3 km wide and 1 km high (Figure 2.6 D) and the deposit extends for 6.7 km (L) to the Devastation-Meager Creeks confluence with a vertical drop of about 1.2 km (H) giving a *Fahrböschung* (travel angle) of 10° (see Mokievsky-Zubok 1977 for further details). In 1981 the 1975 landslide debris has been deformed into an arched moraine. The 1975 moraine advanced at ~20 m yr^{-1} between 1981 and 1990, ~9 m yr^{-1} between 1990 and 2006 and ~5 m yr^{-1} between 2006 and 2016. By 2006 the ice is not transporting the 1975 moraine, which has breached (Figure 2.6 F). The area between the active ice and the 1975 moraine is now occupied by a dissected flat surface.

2.4.2. Mosaic

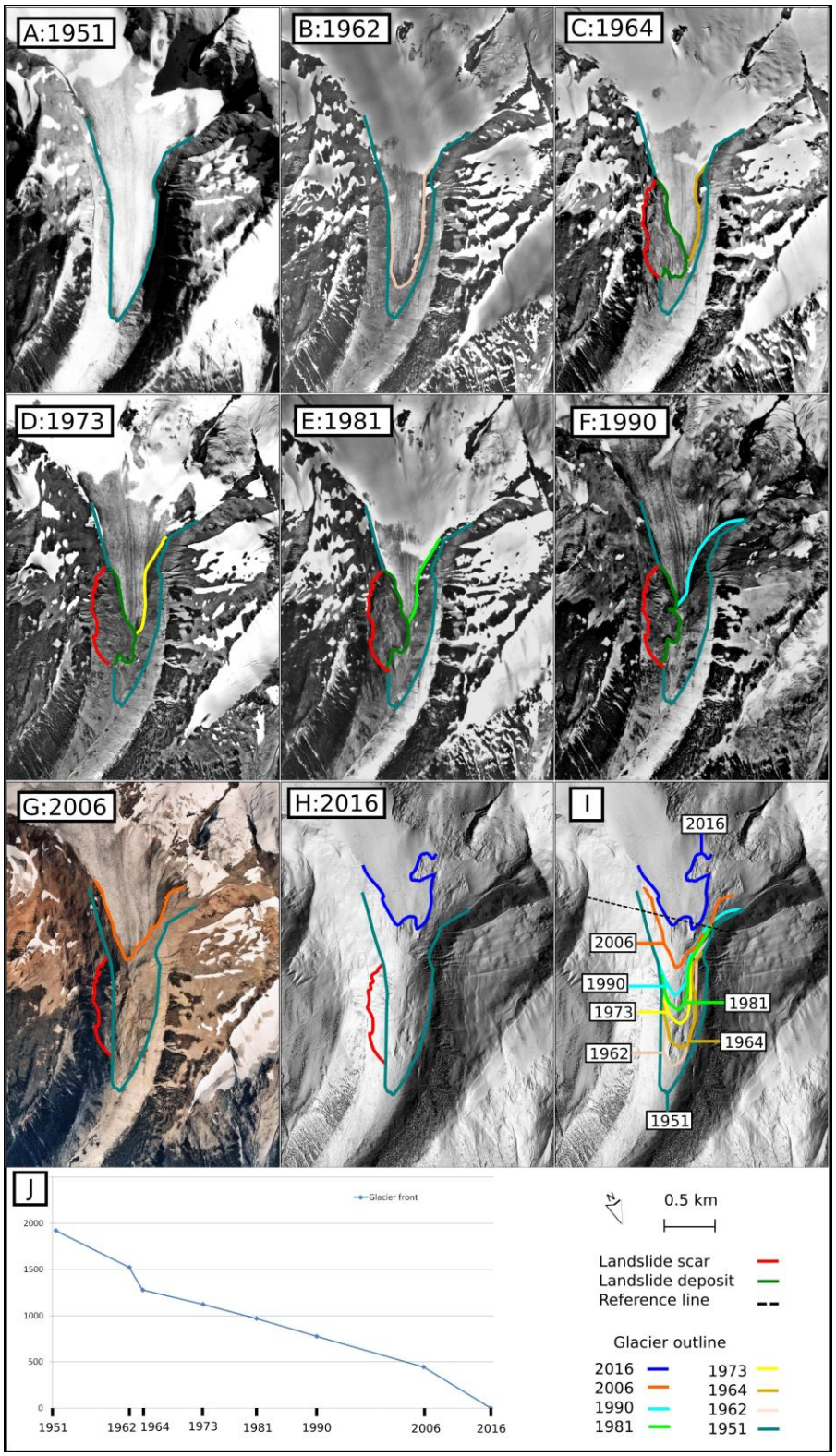
A:1951
B:1962
C:1964
D:1973
E:1981
F:1990
G:2006
H:2016
I
2016
2006
1990
1973
1962
1981
1964
1951
J
Glacier front
2000
1500
1000
500
0
1951
1962
1964
1973
1981
1990
2006
2016
0.5 km
Landslide scar
Landslide deposit
Reference line
Glacier outline
2016
2006
1990
1981
1973
1964
1962
1951

Figure 2.7. Mosaic valley from 1951 to 2016 period. Glacier outlines, landslide deposits, scars, and scarps are indicated. The glacier has been retreating since 1951. A) 1951. B) 1962. C). 1964: note the lateral moraine collapse on the glacier. D) 1973. E) 1981.F) 1990. G) 2006: note that the landslide deposit has been eroded away. H) 2016 Lidar data. I) 2016 Lidar data and glacier outlines. J) Change in the glacier front position over the photo period. Years in x-axis and metres from the reference line in the y-axis.

Mosaic glacier extends from 2200 m asl to 1600 m asl and presently extends for 3 km length. The north facing basin is 2.5 km^2. There are not significant cliffs to accumulate debris on this glacier. In 1947 photoset Mosaic glacier is obscured by clouds. In 1951 the glacier is at its maximum extent and retreated 1.5 km by 2016 (Figure 2.7, A-H). Glacier frontal retreat decreased from ~49 m yr^{-1} during the 1951-1964 period, to ~20 m yr^{-1} during the 1964 to 2006 and then increased to ~45 m yr^{-1} between 2006 and 2016 (Figure 2.7, H). Between 1962 and 1964 the western lateral moraine collapsed on the glacier, partially covering it (Figure 2.7, C.). By 2006 the deposit has been eroded away (Figure 2.7, G.).

2.4.3. Job

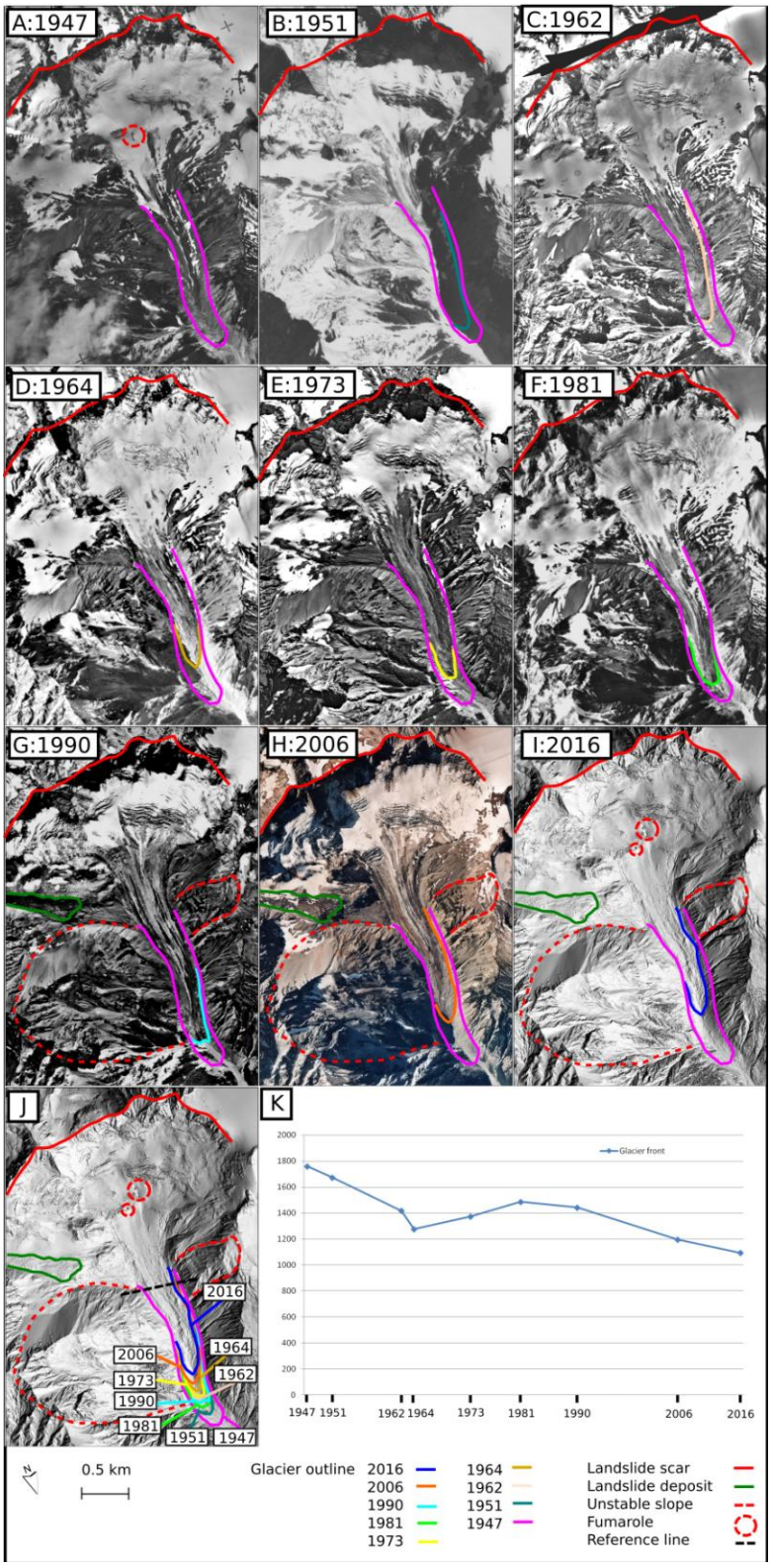
A:1947
B:1951
C:1962
D:1964
E:1973
F:1981
G:1990
H:2006
I:2016
J
K
2016
2006
1964
1973
1962
1990
1981
1951
1947
Glacier front
2000
1800
1600
1400
1200
1000
800
600
400
200
0
1947 1951
1962 1964
1973
1981
1990
2006
2016
N
0.5 km
Glacier outline
2016
2006
1990
1981
1973
1964
1962
1951
1947
Landslide scar
Landslide deposit
Unstable slope
Fumarole
Reference line

Figure 2.8. Job valley from 1947 to 2016. Glacier front, unstable slopes landslide scars, landslide deposits and fumaroles are indicated.The glacier retreated in the 1947-1964 period, advanced between 1964 and 1981 and retreated between 1981 and 2016. A) 1947: note the dark spot on the glacier marking the fumarole position. B) 1951. C) 1962. D) 1964. E) 1973. F) 1981. G) 1990: note debris on glacier. H) 2006. I) 2016 Lidar J) 2016: Lidar and glacier outlines. K) Summary of changes of glacier front position over the photo period. Years in x-axis and metres from the reference line in the y-axis.

Job Valley has been the source of many large landslides (Figure 2.5) which generated the large (2.8 km^2) north facing amphitheatre now occupied by the glacier (Simpson et al., 2006). Job Glacier is presently 2.8 km long and descends from 2000 m asl to the glacier front at 1200 m asl. It is surrounded by headwalls up to 0.5 km high. In 1947 the glacier was at its maximum relative extent and a streak of dark material is visible where the fumarolic ice caves appeared in 2016 (Figure 2.8, A)**.** The glacier snout is covered by debris. The glacier retreated between 1947 and 1964 (~28 m yr^{-1}), advanced between 1964 and 1981 (~12 m yr^{-1}), and retreated from 1981 to 2016 (~11 m yr^{-1}). The total frontal retreat from1947 to 2016 is 0.7 km (Figure 8, A-K). In the 1990 photo a debris streak 1 km long and up to 0.2 km wide is visible on the west part of the glacier, indicating a landslide. In 2016, fumarolic ice caves are visible in the glacier.

2.4.4. Affliction

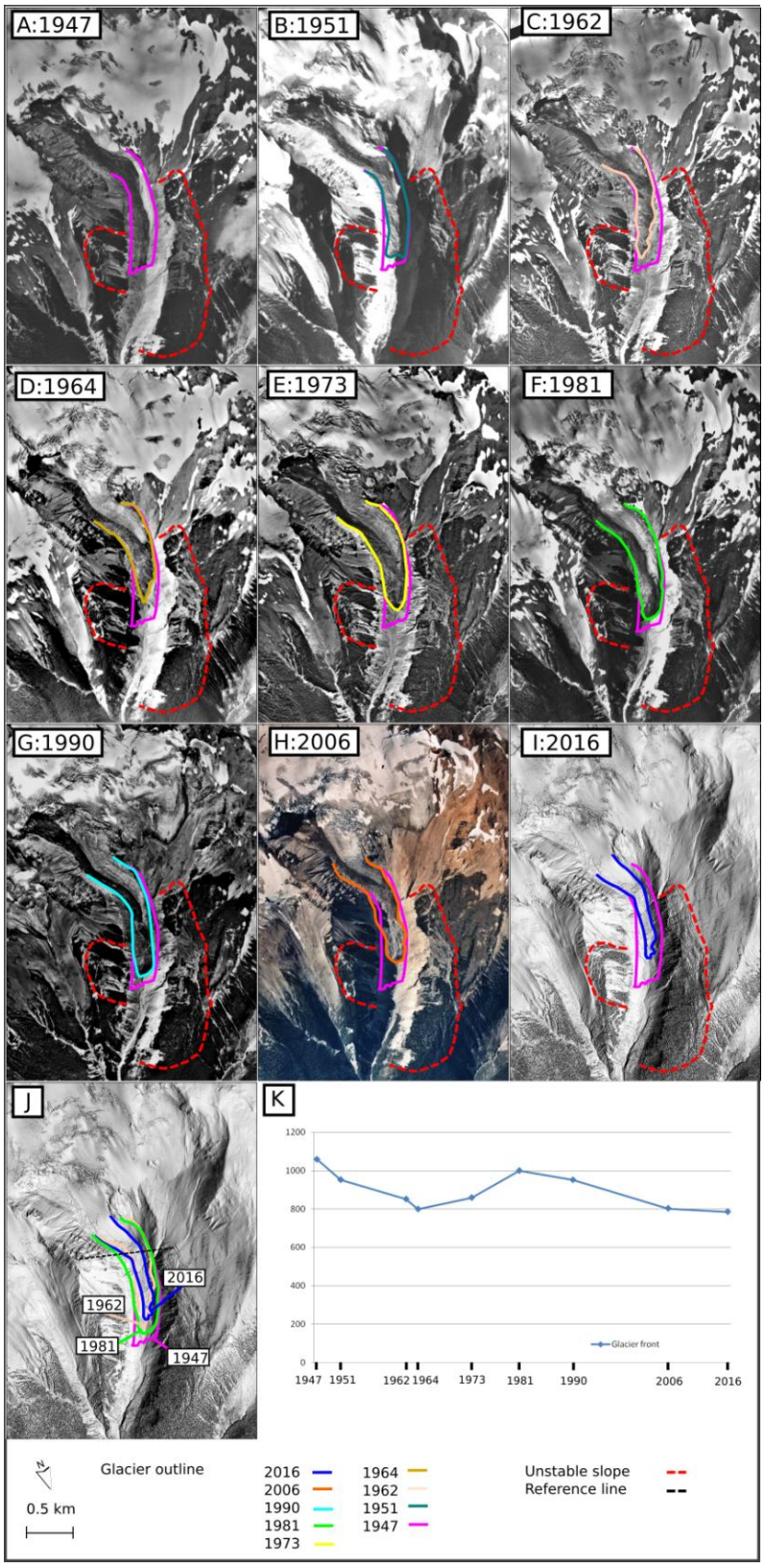

Figure 2.9. Affliction valley, 1947-2016. Glacier front and unstable slopes are shown. Note constant debris cover on the west side of the glacier. The glacier retreated in the 1947-1964 period, advanced between 1964 and 1981, and retreated between 1981 and 2016. A) 1947. B) 1951. C) 1962. D) 1964. E) 1973. F) 1981. G) 1990. H) 2006. I) 2016 Lidar. J) 2016 Lidar and glacier outlines summary. K) Changes in the glacier front position over the photo period. Years in x-axis and metres from the reference line in the y-axis.

Affliction Glacier extends for 3.2 km from 2200 m asl to the glacier front at 1500 m asl. The glacier basin is north facing and is 3.6 km^2. There is a 0.3 km high cliff producing debris that covers the west part of the glacier. Debris-free and debris-covered glacier zones follow the same activity trend. The Affliction Glacier was at the maximum relative extent in the 1947 photo-dataset. The glacier retreated between 1947 and 1964 (~15 m yr^{-1}), advanced between 1964 and 1981 (~11 m yr^{-1}) and retreated from 1981 to 2016 (~6 m yr^{-1}). The total glacier retreat is 0.3 km from 1947 to 2016 (Figure 2.9, A-K). Both valley sides show counter scarps and fractures.

2.4.5. Bridge River

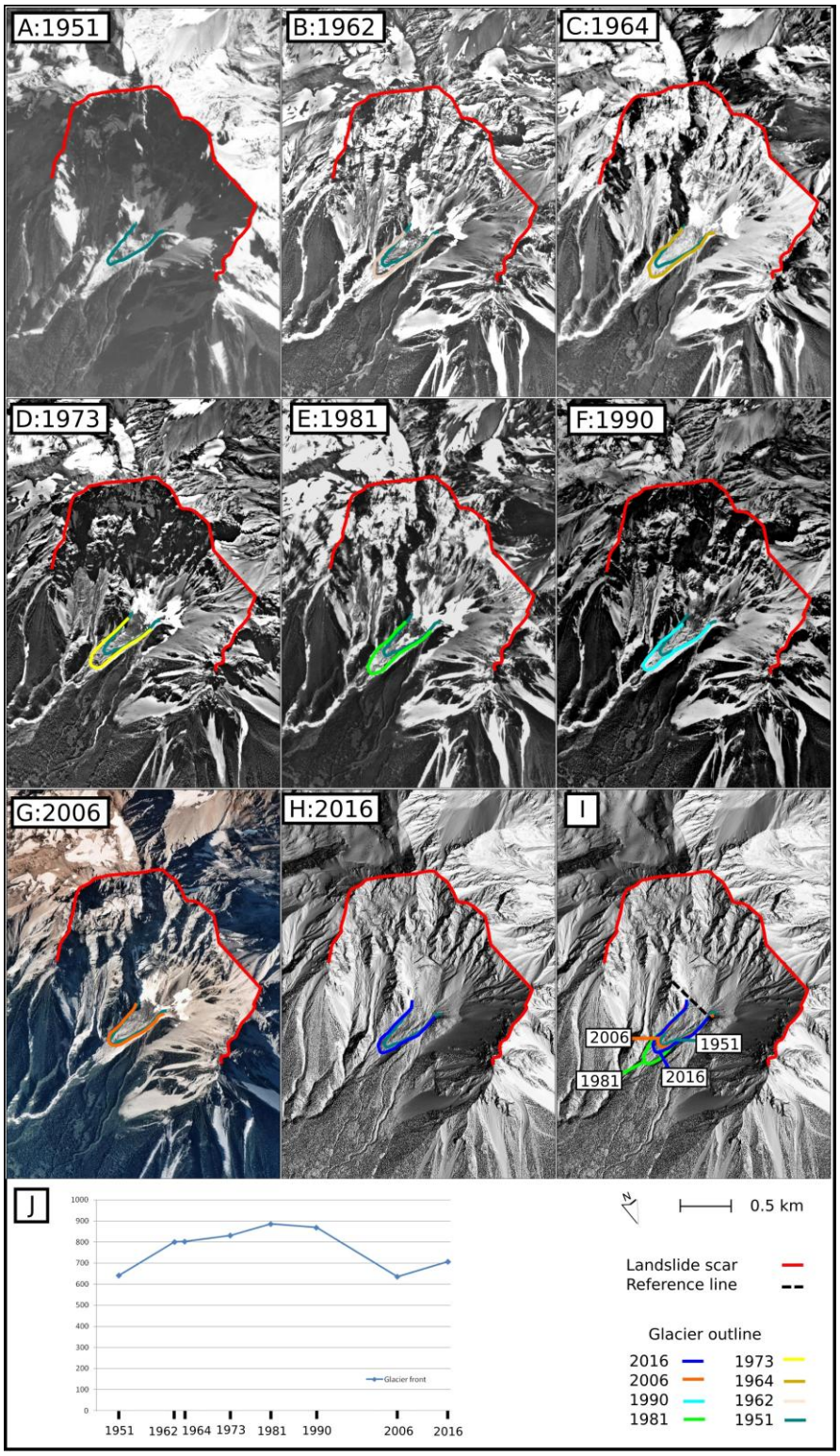

Figure 2.10. Bridge River Glacier, 1951-2016. Glacier outlines and eruptioncrater/landslide scar are indicated. The glacier advanced between 1951 and 1990, retreated between 1990-2006, and readvanced in the 2006-2016 period. A) 1951. B) 1962. C) 1964. D) 1973. E) 1981. F) 1990. G) 2006. H) 2016 Lidar. I) Lidar 2016 with glacier outlines. J) Changes in the glacier front position over the period of the photographic record. Years in x-axis and metres from the reference line in the y-axis.

The Bridge River Glacier is located in the eruption-triggered landslide scar and crater of the 2360 cal yr BP eruption. It is 1.1 km long and extending from 1700 to 1200 m asl. It sits in a 1.5 km^2 northeast facing amphitheatre, surrounded by up to 1 km high headwalls (Table 2.3). In 1947 clouds obscure the area. The glacier advanced in the 1951-1990 period (~8 m yr^{-1}), receded between 1990 and 2006 (~15 m yr^{-1}) and readvanced between 2006 and 2016 (~+4 m yr^{-1}) (Figure 2.10, A-H). The total glacial advance since 1951 is + 0.07 km.

Table 2.3. Glacier parameters. N=North; NE = Northeast; SE = Southeast. a = referred to the 1947 dataset. b = referred to the 1951 dataset.

Glacier	Accumulation zone elevation (m. asl)	Glacier front elevation in 2016 (m. asl)	Glacier front elevation in 1947/51 (m. asl)	Glacier length (km)	Headwall height (km)	Basin area (km^2)	Relative front position in 2016 (km)	Aspect
Devastation	2200	1400	1150[a]	3.7	0.7	3	-1.7	SE
Mosaic	2200	1600	1500[b]	3	0	2.5	-1.5	N
Job	2000	1200	1100[a]	2.8	0.5	4	- 0.7	N
Affliction	2200	1500	1350[a]	3.2	0.3	3.6	- 0.3	N
Bridge River	1700	1200	1250[b]	1.1	1	1.5	+ 0.07	NE

2.5. Discussion

Glacier activity over the 1947-2016 period varies between glaciers. Devastation and Mosaic glaciers retreated for the whole study period. Job and Mosaic glaciers retreated overall but they had a short readvance in the 1970-1980's. Bridge River Glacier advanced overall but it retreated between 1990 and 2006. Mosaic, Job, and Affliction had an increase in retreat rate between 1962 and 1964. Devastation Glacier retreated 1.7 km, Mosaic Glacier retreated 1.5 km, Job Glacier retreated 0.7 km, Affliction Glacier retreated 0.3 km, and Bridge River Glacier advanced 0.07 km.

Devastation

At Devastation Glacier, we observe the maximum retreat (1.7 km) of the Mount Meager glaciers. Stagnant ice retreat rate increased from 1973 to 1981 and from 2006 and 2016. The active ice retreated a with similar trend, except that the active ice had a readvance from 1981-1990 period. The active ice readvance and the debris-covered glacier retreat slowdown in 1980-1990's both could be related to the 1975 landslide or to the regional climatic trend. Short readvance in the 1970-1980's are observed at Job and Affliction, at Capricorn glaciers (Chapter 4), and in other glaciers in British Columbia (Koch et al. 2009). At Devastation, the climate-driven readvance could have been delayed by local conditions (it is the only basin with a southeast aspect) or it is related to the landslides. If it is related to the 1975 landslide there is a lag between the landslide occurrence and the glacier response.

Devastation glacier is an example of how rock and debris avalanches can form moraines. Rock avalanche sourced moraines have been inferred by deposit facies (Shulmeister et al. 2009), but only a few cases document fresh rock avalanche deposit on glacier and track the deposit modifications by the ice (Hewitt 2009; Shugar and Clague 2011; Shugar et al. 2012). At Devastation we can trace the movement of the 1947 and 1975 landslide debris and the formation of arched moraines. Although the 1975 landslide covers the 1947 moraine, it is still possible to trace the motion. The moraine advance increased in the 1981-1990 photo period, as for the active ice. The glacier transported the 1975 landslide deposit moraine until the 1990 dataset. By 2006, the debris-free ice is not in contact with the moraine that has now breached. The area between the moraine and the clean ice is occupied by a flat-ish dissected surface. We interpret this morphology as a remnant of a proglacial lake, formed when the ice retreated from the moraine. The breach in the moraine could indicate a sudden lake drainage that may have resulted in a glacial lake outburst flood. No trace of this is recorded in the photos.

The debris cover of Devastation glacier is predominantly from rock or debris avalanches falling onto the ablation zone, rather than rock falls occurring in the accumulation zone and exhumed in the ablation zone (Anderson et al. 2016). Prior to the 1947 landslide, the glacier was already debris-covered for at least 1.7 km. The 1947 landslide had a relatively short runout: it stopped against transverse debris ridges on the

glacier. These ridges and debris cover prior to the 1947 landslide are likely part of the 1932 landslide deposit and possibly other landslides from the basin (4 in Figure 2.6, for example). Slope deformation has been documented by InSAR techniques and more large landslides are expected from this basin (See Chapter 5). These may further change the glacier's morphology and flow.

Mosaic

Mosaic Glacier retreated 1.5 km during the study period. The retreating trend does not contain any readvance in the 1970-1980's. It showed a retreat acceleration between 1962 and 1964. This rapid glacier retreat may have caused the lateral moraine collapse, as observed at other glaciers (Blair 1994). The landslide debris-covered part of the glacier snout but did not affect the glacier retreat trend. The lack of debris cover may contribute to its retreat pattern, which is different from the nearby Job and Affliction glaciers.

Job

The Job Glacier retreated 0.7 km since 1947. Between 1962 and 1964 there is an increased retreat but the in the 1970-1980's the glacier had a short-lived readvance. The increase in retreat between 1962 and 1964 is also observed at Mosaic and Affliction glaciers. This increase may be related to the fact that in a 2-year time span the data does not average as for other longer time intervals. The readvance in the 1970-1980's is recorded by Affliction, Capricorn (Chapter 4) and other glaciers in British Columbia (Koch et al. 2009).

The Job basin is an amphitheatre formed by the collapse of several large landslides (Figure 2.5, Friele et al. 2008). In the 1947 and 2016 datasets fumarole manifestations can be seen. The 1947 dark debris streak could have been the deposit of a small hydrothermal eruption which was covered by the glacier in the following years. The presence of diffuse volcanic gasses in the area have been known since the 1970's (Peter Read, personal communication) and have been studied during the geothermal exploration in the area (NSBG 1980; 1981), but the vent location was not determined. The presence of fumaroles in the center of a landslide collapse scar could be indicative of a relation between hydrothermal activity and the large landslides from Job basin. Other slopes in the basin have shown signs of instability and displacement has been

measured by means of InSAR techniques (See Chapter 5). The relation between past and ongoing deformation and hydrothermal activity needs to be addressed in detail.

Affliction

The Affliction Glacier retreated 0.3 km since 1947. It shows a similar trend to Job Glacier. The retreat accelerated between 1962 and 1964, then it readvanced in the 1970-1980's. The debris-covered streak on the west is generated by continuous erosion of a rock cliff. Slope deformation on the valley flank has been documented by Bovis (1990), and present displacement measured by InSAR (Chapter 5).

Bridge River

The Bridge River Glacier is the only advancing glacier (+0.07 km) in the Mount Meager volcanic complex; it is the smallest and lowest elevation glacier (Table 2.3). The geomorphology of the Bridge River basin affects the glacier dynamics. The Bridge River Glacier is located in the 2360 cal yr BP eruption amphitheatre, surrounded by headwalls 1 km high. We argue that the high headwalls are responsible for this contrasting trend of the glacier. The amphitheatre would be able to shade the glacier minimizing ablation; funnel snow avalanches onto the glacier increasing accumulation; and sourcing rock falls and rock avalanches, provide insulating debris cover. Increase in rock fall caused by warming of rock walls in the permafrost region (Gruber and Haeberli 2007) can contribute to the increase in the debris cover. Terrestrial laser scanner and photogrammetry surveys could determine the actual rock fall frequency and magnitude from the headwalls of the glacier. This glacier is fortunately in line of sight of mining and hydropower installations, so survey projects are easier than in other glacier areas. Other parameters, such as winter precipitation, and air temperature, need to be considered for a complete assessment of Bridge River and the other glaciers behaviors.

2.5.2. Landslides and debris-covered glaciers on a volcano

In order to explain the present glacier and landslide activity at Mount Meager, we discuss a conceptual framework of the evolution of a volcanic edifice interacting with glaciers. We first consider an active volcano during a glacial period when a thick (~1 km) regional ice sheet occupies the landscape. We then consider the same volcano, transitioning to an interglacial period during which alpine glaciers are sustained. During

glacial periods, ice processes would prevail over volcanic processes. The shape of the volcano, the eruptive style, and the mass movements would be strongly affected by the presence of ice. The volcanic edifice would be formed following eruption rate and ice melting relation laws and the eruptive products would increase in explosivity and fragmentation due to the availability of water (Edwards et al. 2015). The available water could also enhance hydrothermal alteration. The shape of the volcanic edifice is conditioned by the interaction with ice and will form flat-topped tuyas rather than the classical cone of a stratovolcano (Russell et al. 2014). The edifice may not be able to collapse and form debris avalanches, but meltwater could accumulate and rapidly drain as catastrophic *jökulhlaups*. During interglacial periods, when only small alpine glaciers may be present, volcanic processes would prevail. Glaciers in this stage do not control the volcanic edifice shape and eruptive style but, rather the volcano would condition the glaciers' activity (Barr et al. 2018). The presence of erodible and altered rocks would favour the formation of debris-covered glaciers, which are also conditioned by the volcano morphology as they form in craters and landslide scars. The volcanic edifice is highly unstable because it was formed under a thick ice sheet, and now unsupported, can collapse and form debris avalanches.

At Mount Meager there are no documented signs of volcanic activity during glacial periods (Wilson and Russel 2018). But, the age of the volcano (~2 Ma, Read 1978), the fact that southern British Columbia has been covered multiple times by an extensive Quaternary ice sheets (Clague and Ward 2011), that even today there are glaciers on the volcano, and that Read (1978) documented two, and Stasiuk et al. (1996), and Hickson et al. (1999), one till within the Mount Meager stratigraphic sequence, suggest past volcano-ice interaction. Even in case of absence of direct volcanic activity during glacial periods, glaciations have covered and eroded the volcanic rocks conditioning the volcano's morphology. In this study we did not investigate the possibility of volcanic activity of Mount Meager during glacial periods but we argue that the present high landslide frequency and the glaciers' morphologies are, in part, from the inherited edifice instability derived from volcano-ice interaction. Past volcanic edifice building, conditioned by regional ice sheets, lead to unstable slopes and today's debris-covered glaciers, that are forming in landslide and eruption scars. Further studies are needed to better constrain the glaciovolcanic history of Mount Meager to confirm this hypothesis.

2.5.3. The value of historic photography.

We documented more than half-a-century of glacier activity and landslides at Mount Meager volcano using SfM photogrammetry to process historic airphotos. This is a new approach and provides many opportunities. The method has been hindered by the difficulty of assessing the quality of the SfM-derived product when using historic airphotos in poor conditions, representing areas that have changed, and lacking of good ground control points. Here we proposed a practical method that does not require high quality ground control and where measurements can be done in a relative coordinate system.

The advantages of processing historic airphotos with SfM photogrammetry include a fast, user-friendly workflow; the retrieval of information from photos that are otherwise not processable; large areas visualized at high resolution in 3D; and multiple years of coverage. From a scientific point of view, this technique allows the documentation of geomorphic changes such as glacier retreat, slow moving landslides, debris flows, fluvial processes, land use (logging, subdivision development), etc. during the period of airphoto coverage. The increase in information can shed new light on the effects of recent climate change and the human impact on geomorphic processes. The increase in availability of 3D data also has commercial, scientific outreach, and educational applications. Easy visualization allows users to better understand the natural processes. Three-dimensional topographic models can be easily managed in 3D visualization and analysis software or in virtual and augmented reality environments (Onsel et al. 2018) and can be used to generate 3D time-lapse of surface changes (see here the Mosaic glacier from 1951 to 2016).

2.6. Conclusions

We processed historic airphotos with Structure from Motion photogrammetry to document more than half-a-century of glacier and landslide activity at Mount Meager volcano. We focused on Devastation, Mosaic, Job, Affliction and Bridge River glaciers. We draw the following conclusions:

- SfM is a valid alternative to classic photogrammetry for topographic reconstruction from historical airphotos. We propose a workflow that does not

require high precision ground control and the measurements can be done in relative coordinate systems.

- The glaciers at Mount Meager have different behaviours. Devastation Glacier retreated the most, 1.7 km in 70 years, and has been affected by two (1947 and 1975) rock avalanches. The glacier deformed the landslide debris to form moraines. Mosaic glacier retreated 1.5 km, does not have a debris cover, and has been the site of a moraine collapse. Job and Affliction glaciers had a short-lived readvance in the 1970-1980's and have a total retreat of 0.7 and 0.3 km, respectively. Job Glacier is located in a large collapse scar and fumarolic activity has likely been present since 1947. Bridge River Glacier is located in the 2360 cal yr BP eruption crater and it is the only advancing glacier (+0.07 km). Major rock falls, rock avalanches, and landslides are observed from the slopes of each glacier basin.
- We document moraines that formed from large amounts of debris deposited onto Devastation glacier from landslides. This can cause misinterpretation of the paleoclimate record if these moraines are preserved and though to be climatically related.
- We propose a conceptual model to explain the high landslide frequency and the glacial activity at Mount Meager. Past glaciations and hydrothermal activity condition present volcanic edifice stability and glacier morphology. Rocks are fractured and altered by interaction with past ice sheets and today's glaciers are debris-covered and sit in collapse scars formed because of the inherited instability of the mountain.
- Three-dimensional historic photographic reconstruction finds many scientific and outreach applications. It gives access to otherwise unused datasets and allows documentation of recent geomorphic changes. Visualization of three-dimensional models helps non-scientific users to better understand natural processes.

2.7. Acknowledgments

Discussions with Leif Anderson helped us to formulate some of the debris-covered glaciers ideas and the evolution of a volcanic edifice from glacial to interglacial periods. We thank Peter Read for sharing is knowledge of the Mount Meager volcano. Discussion with Davide Donati helped to imporve the SfM-CloudCompare workflow

Financial support for the 2015 Lidar data acquisition was provided by NSERC through Discovery Grants to Clague and Menounos and the Canada Foundation for Innovation (Menounos). Natural Resources Canada (NRCan), through Melanie Kelman, provided funds for the 2016 Lidar dataset. Financial support for Roberti's PhD salary was partially provided by the "End of an Arc: The Remarkable Life and Death of a Volcanic Arc" project, a French-Canadian partnership and partially by Graduate and Teaching assistant fellowships, and by Chair funds to Ward.

Chapter 3. Rheological evolution of the Mount Meager 2010 debris avalanche, southwestern British Columbia [2]

Gioachino Roberti[1,3], Pierre Friele[2], Benjamin van Wyk de Vries[1], Brent Ward[3], John J. Clague[3], Luigi Perotti[4], and Marco Giardino[4]

(1) Université Clermont Auvergne, CNRS, IRD, OPGC, Laboratoire Magmas et Volcans, Aubiere Cedex, France (2) Cordilleran Geoscience, Squamish, British Columbia, Canada (3) Earth Sciences Department, Simon Fraser University, Burnaby, British Columbia Canada (4) Earth Sciences Department, University of Torino, Torino, Italy

3.1. Abstract

On 6 August 2010, a large (~50 Mm^3) debris avalanche occurred on the flank of Mount Meager in the southern Coast Mountains of British Columbia, Canada. We studied the deposits to infer the morphodynamics of the landslide from initiation to emplacement. Structure from motion (SfM) photogrammetry, based on oblique photos taken with a standard SLR camera during a low helicopter traverse, was used to create high-resolution orthophotos and base maps. Interpretation of the images and maps allowed us to recognize two main rheological phases in the debris avalanche. Just below the source area, in the valley of Capricorn Creek, the landslide separated into two phases, one water-rich and more mobile, and the other water-poor and less mobile. The water-rich phase spread quickly, achieved high superelevation on the valley sides, and left distal scattered deposits. The main water-poor phase moved more slowly, did not superelevate, and formed a thick continuous deposit (up to ~30 m) on the valley floor. The water-poor flow deposit has structural features such as hummocks, brittle-ductile faults, and shear zones. Our study, based on a freshly emplaced deposit, advances understanding of large mass movements by showing that a single landslide can develop multiple rheology phases with different behaviors. Rheological evolution and separation

[2] This paper has been published in 2017 in *Geosphere*: Roberti G, Friele P, van Wyk de Vries B, Ward B, Clague JJ, Perotti L, Giardino M (2017) Rheological evolution of the Mount Meager 2010 debris avalanche, southwestern British Columbia. Geosphere 13(2):1–22. https://doi.org/10.1130/GES01389.1

of phases should always be taken into account to provide better risk assessment scenarios.

3.2. Introduction

Landslides are one of the major hazards in mountainous regions. When volcanoes are present in the mountains, the hazard is compounded, as volcanic rocks are weak and hydrothermal alteration further weakens both the volcano and the country rock. Thus, potentially unstable volcanic edifices pose a significant hazard to people living in their vicinity. They are prone to large collapses, which can generate fast-moving debris avalanches that may travel far from their source (Siebert 2002; van Wyk de Vries and Davies 2015). Some collapses occur during eruptions, but many happen during quiescent periods and are not directly related to eruptive activity (Friele et al. 2008; Shea and van Wyk de Vries 2010). Causative factors include rapid uplift and erosion as well as weak materials that form the flanks of the volcanoes and commonly slowly deform under the influence of gravity (van Wyk de Vries and Francis 1997; Reid and Brien 2006; van Wyk de Vries and Davies 2015).

Volcanic and non-volcanic debris avalanches are complex mass movements in which multiple rheologies can coexist (Iverson et al. 2015; Coe et al. 2016), affecting overall behavior and runout. An understanding of these processes is vital for appropriate modeling, hazard and risk evaluation, and possible mitigation strategies (Kelfoun 2011; Jakob et al. 2013; Iverson et al. 2015).

The deposits and surface morphology of many prehistoric volcanic debris avalanches have been studied to infer transport and emplacement processes (Vallance and Scott 1997; Takarada et al. 1999; Capra and Macias 2000; Bernard et al. 2008; Roverato et al. 2014). Studies of these events, however, are limited, as surface features commonly have been degraded or totally lost. Very few studies document in detail fresh deposits emplaced soon after the events (Plafker and Ericksen 1978; Glicken 1996). And even in most of these cases, there is a lack of eyewitness accounts and video documentation.

A landslide in August 2010 at Mount Meager in the southern Coast Mountains of British Columbia (Canada) provided us with a unique opportunity to examine the deposit

of a volcanic debris avalanche before it was significantly eroded, and thus to improve understanding of debris avalanche rheology and emplacement mechanisms.

Guthrie et al. (2012a, b) provided a first description of the event, including seismic signal analysis, a general geomorphic description, and numerical modeling. Roche et al. (2011) studied the effects of the landslide on the Lillooet River discharge. Allstadt (2013) analyzed the seismic data from the event to infer velocity and emplacement dynamics. Moretti et al. (2015) produced a numerical simulation of the event. At present, there has been no detailed study of the geomorphology and rheology of the 2010 Mount Meager landslide, a gap that we fill in this work.

The objective of this study is to refine understanding of the emplacement kinematics and dynamics and the rheology of the Mount Meager debris avalanche in order to advance knowledge of such events. We achieved this objective by constructing a high-resolution orthophoto and digital elevation model (DEM) using Structure from Motion (SfM) and through detailed geomorphologic mapping (at 1:1000 scale) and grain-size analysis. This new technology can be applied to other debris avalanches around the world to offer valuable new insights into the morphodynamics of large landslides.

3.2.1. Setting

Mount Meager (2680 m above sea level [asl]) is a Pliocene to Holocene volcanic complex 200 km north-northwest of Vancouver, British Columbia (Figure 3.1). It lies within the Lillooet River watershed, 65 km upstream of the town of Pemberton.

The Mount Meager massif is a group of coalescent stratovolcanoes that formed during four episodes of volcanism: one minor Pliocene episode and three major Quaternary episodes. Read (1977; 1979; 1990) subdivided the eruptive products into nine volcanic assemblages. The most recent eruption was an explosive event that occurred 2360 cal yr BP (Clague et al. 1995; Hickson et al. 1999). Rocks involved in the 2010 landslide were mainly intrusive porphyritic rhyodacite, flows, and breccia units of the Plinth and Capricorn assemblages—the youngest assemblages in the massif (Read 1990).

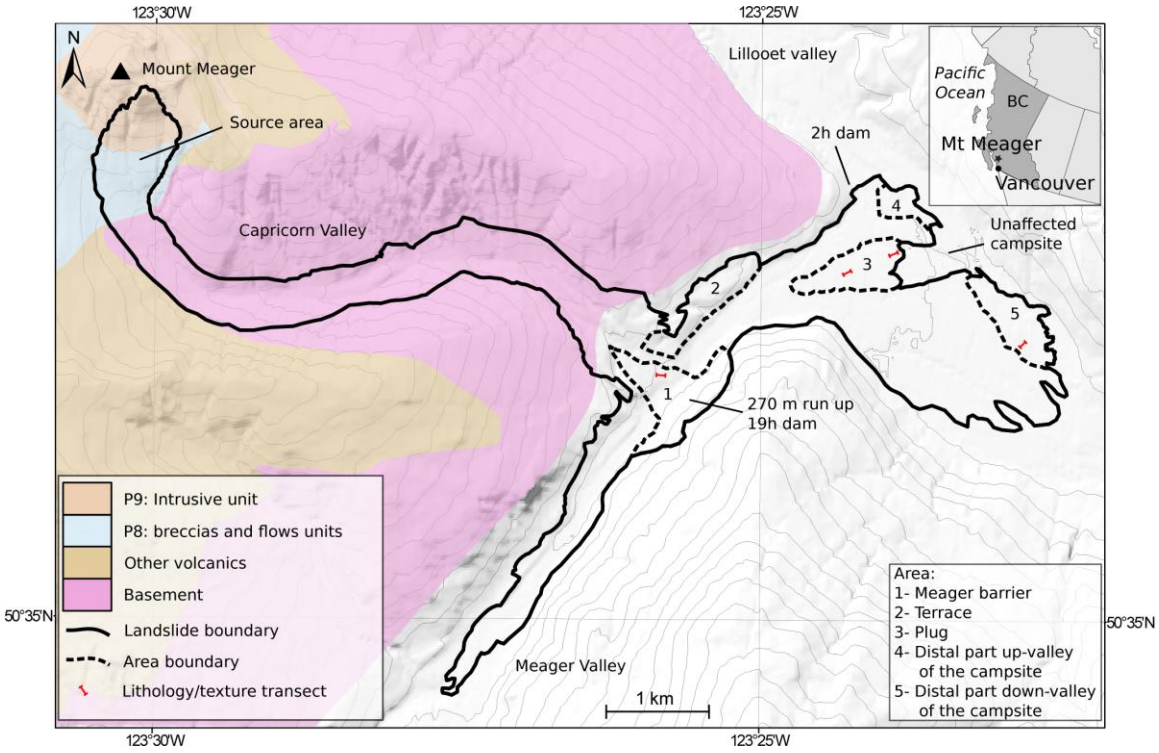

Figure 3.1. Mount Meager area (British Columbia) (geology after Read 1979), showing margins of the Mount Meager 2010 landslide, the locations and durations of the landslide dams, and the five deposit areas discussed in the paper. The locations of the lithology transects are shown by red lines. Inset map shows the location of the study area in western Canada (BC—British Columbia).

3.2.2. Landslides on Mount Meager

Volcanism, associated hydrothermal alteration, and erosion have weakened the rocks that form the Mount Meager massif, as they have at most stratovolcanoes around the world (Finn et al. 2001; Siebert 2002; Pola et al. 2014).The considerable topographic relief of the massif (up to 2000 m) and its steep slopes, combined with recent thinning and retreat of alpine glaciers (Holm et al. 2004), have left much of the massif in a state of instability (Read 1990; Friele et al. 2005; Friele and Clague 2009).

Evidence of active slope processes affecting the massif include sackungen, debris flows, and debris and rock avalanches (Mokievsky-Zubok 1977; Jordan 1994; Bovis and Evans 1996; Jakob 1996; Friele and Clague 2004). In particular, Capricorn Creek, a tributary of Meager Creek, was the source of debris flows and debris avalanches larger than 100,000 m^3 in 1931, 1933–1934, 1944–1945, 1972, 1998, 2009, and 2010 (Carter 1932; Jakob 1996; Bovis and Jakob 2000; Guthrie et al. 2012a). Using

dendrochronology, Jakob (1996) extended the historical record of landslides in the Meager Creek watershed to 330 years ago. He identified 13 large debris flows and/or hyperconcentrated flows, an average of one event every 25 years. These landslides entered Meager Creek and caused significant channel aggradation and instability downstream. Some of them also blocked Meager Creek, forming landslide-dammed lakes (Mokievsky-Zubok 1977; Bovis and Jakob 2000; Guthrie et al. 2012a, 2012b). Very large collapses of the flank of the massif have generated at least three Holocene debris flows that traveled downstream to presently populated areas in Lillooet River valley (Friele and Clague 2004; Friele et al. 2005; Simpson et al. 2006).

3.2.3. The 2010 event

On 6 August 2010, the south flank and secondary peak (2554 m asl) of Mount Meager collapsed, producing a long-runout debris avalanche (Guthrie et al. 2012a, 2012b) (Figure 3.1). The collapse evolved as several subfailures (Allstadt 2013; Moretti et al. 2015). The debris accelerated to speeds of 60–90 m/s as it traveled 7 km down Capricorn Creek to Meager Creek (Allstadt 2013). At the Capricorn Creek–Meager Creek confluence, the front of the debris sheet ran 270 m up the opposing valley wall and split into two lobes, one of which ran ~3.4 km upstream and the other 4.7 km downstream to Lillooet River where it spread out over the valley floor before coming to rest 2 km below the Meager Creek– Lillooet River confluence. Field evidence showed that some deposition occurred along the entire travel path, but most of the debris was deposited at the mouth of Capricorn Creek and in Lillooet River valley (Guthrie et al., 2012a,b).

Guthrie et al. (2012a, b) concluded that the 2010 landslide involved the failure of $48.5 \times 10^6 m^3$ of rock. It thus was similar in size to the 1965 Hope slide in southwest British Columbia (Mathews and McTaggart 1969; Bruce and Cruden 1977) and almost twice the size of the famous 1904 Frank slide in southwest Alberta (Cruden and Krahn 1973; Cruden and Martin 2007). The vertical elevation drop from the source area to the distal limit of the debris (H) is 2185 m, and the total path length (L) is 12.7 km. These values yield a *Fahrböschung* (travel angle, arctan H/L) of 9.8°. The average velocity of the landslide was 45 m/s (Allstadt 2013). The landslide produced the equivalent of a M 2.6 local earthquake, with long-period seismic waves that were recorded by seismometers as far away as southern California and northern Alaska.

A mass of debris up to 30 m thick blocked Meager Creek at the mouth of Capricorn Creek, and a 10–15-m-thick debris barrier formed across Lillooet River. A stream gauge on Lillooet River 65 km downstream of Meager Creek recorded an initial rapid drop in discharge, followed ~2 hr later by a rise in discharge after Lillooet River breached its dam. About 19 hr later, discharge spiked following overtopping and breaching of the Meager Creek barrier (Roche et al. 2011; Guthrie et al. 2012a, b). Because this flood wave was built on a low base flow, it did not exceed the bankfull discharge of Lillooet River in Pemberton and caused no property damage.

The outburst floods resulting from the two dam breaches modified much of the original surface of the landslide deposit. However, an extensive area retained its original structure and morphology a year after the event, allowing us to conduct this study.

We use the term “debris avalanche” to describe the 2010 landslide because most of the deposit shows features typical of a volcanic debris avalanche (Glicken 1991; Ui et al. 2000; Shea and van Wyk de Vries 2008; Paguican et al. 2014; van Wyk de Vries and Delcamp 2015). However, the landslide started as a rockslide before rapidly transforming into a channelized debris avalanche. It left a broad range of deposits, which we describe in detail below. They include hummocky faulted debris avalanche deposits, smoother ridges and striated debris flow–like deposits, and deposits from turbid water that scoured bark from trees and embedded stones in trunks.

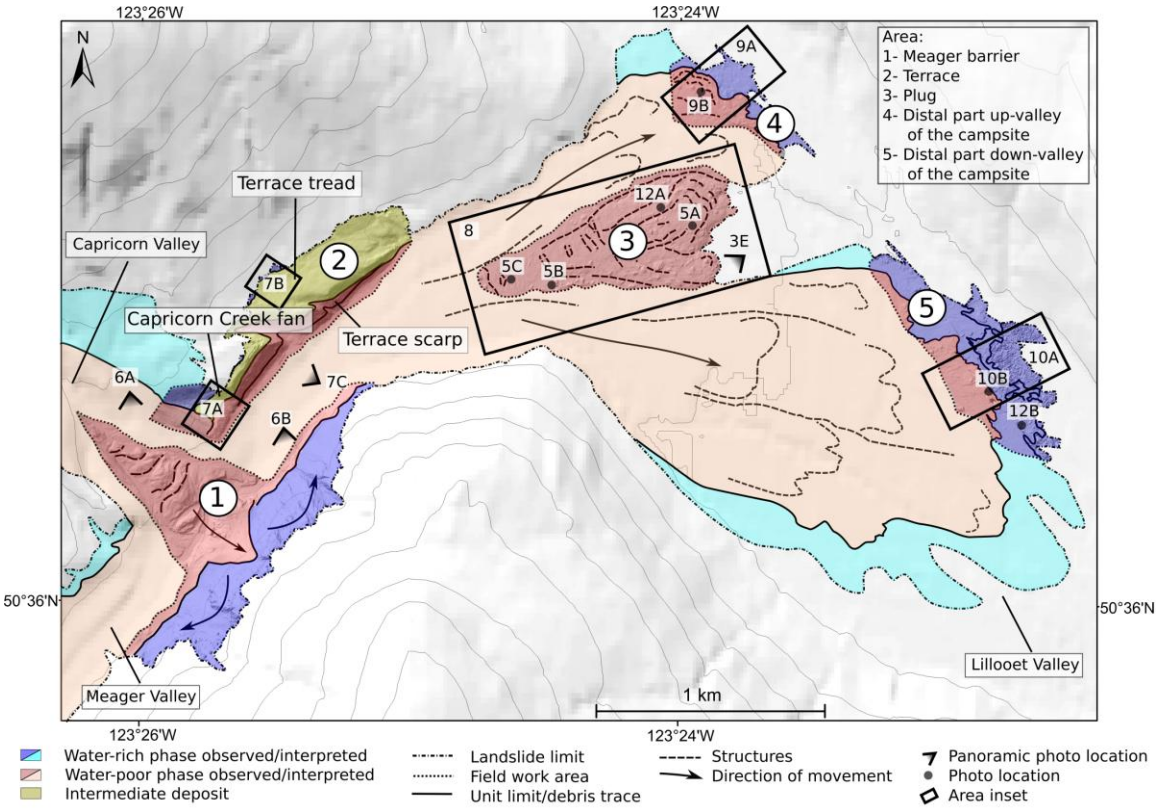

Figure 3.2. Map of Mount Meager landslide deposits and structures. Also indicated are locations of photographs shown in other figures. Numbers in circles identify the five deposit areas.

3.3. Methods

3.3.1. Photography and Structure from Motion

To produce a base map for geomorphic mapping, we took oblique digital photos one year after the landslide with a single lens reflex (SLR) camera during low-level helicopter flights over the accumulation zone. The photos were processed using the SfM and multiview stereo (MVS) algorithms (Snavely et al. 2008; James and Robson 2012; Westoby et al. 2012; Fonstad et al. 2013; Micheletti et al. 2015) to produce three-dimensional topographic models from which we extracted a high-resolution orthophoto (0.08 m/pixel ground resolution) and a DEM (0.34 m/pixel ground resolution). Centimetre-size clasts are resolvable on the imagery.

Uncertainties and limitations of SfM mostly stem from the automated work-flow, in which sources of errors are difficult to individualize and control (James and Robson 2012; Fonstad et al. 2013; Remondino et al. 2014; Micheletti et al. 2015). Nevertheless,

the SfM-derived DEMs are comparable in quality to most Lidar DEMs (James and Robson 2012; Westoby et al. 2012; Fonstad et al. 2013; Remondino et al. 2014; Micheletti et al. 2015; Smith et al. 2015).

We also used oblique digital photos taken from a helicopter the morning after the landslide, before the flood from the Meager Creek dam breach. Although these photos could not be used for SfM analysis, they were useful for evaluating geometries and facies relations that were subsequently destroyed by the flood.

3.3.2. Field mapping

We produced a geomorphic map of the landslide deposits at a scale of 1:1000 from field observations made between August and October 2012 and from the orthophoto and the DEM. We identified and classified geomorphic features, facies, and related facies associations within those parts of the deposit that had not been modified by erosion. For the purpose of discussion, we subdivide the debris avalanche deposit below the mouth of Capricorn Creek into five areas that we refer to as Meager barrier, terrace, plug, distal up, and distal down (Figures 1 and 2).

3.3.3. Grain size and lithologic analysis

We chose four sample sites distributed along the length of the deposit from the Meager barrier to the distal margin for grain-size and lithological analyses (Figure 3.1). At each site, we placed a 100 m tape parallel to the flow direction. Clast lithologies were recorded at 1 m intervals along the tape and visually classified as basement rock (B), gray porphyritic felsic rhyodacite (GPF), red porphyritic felsic rhyodacite (RPF), and other volcanic rocks (OV). “Other volcanic rocks” include gray, red, and white aphanitic rocks, gray and cream colored porphyritic rocks, and pumice. One-kilogram bulk samples were collected for grain-size analysis at stations 20, 40, 60, 80, and 100 m along the tape. For each of these samples, 100 of the largest clasts >4 mm retained from sieving were also lithologically classified. Ten other bulk samples were collected from selected stations on the deposit, two from mixed debris and four each from pulverized blocks and altered blocks.

The samples were split into >1 mm and <1 mm fractions. The 1–4 mm fraction was dry sieved while the <1 mm fraction was submitted to ALS Global Laboratory (Burnaby, British Columbia) for hydrometer analysis following ASTM protocol D422. We then integrated the sieve and hydrometer data to produce grain-size distributions truncated at 4 mm.

3.4. Results

We first describe facies, structures, and hummocks, and then describe and interpret each of the five areas that constitute the debris avalanche deposit.

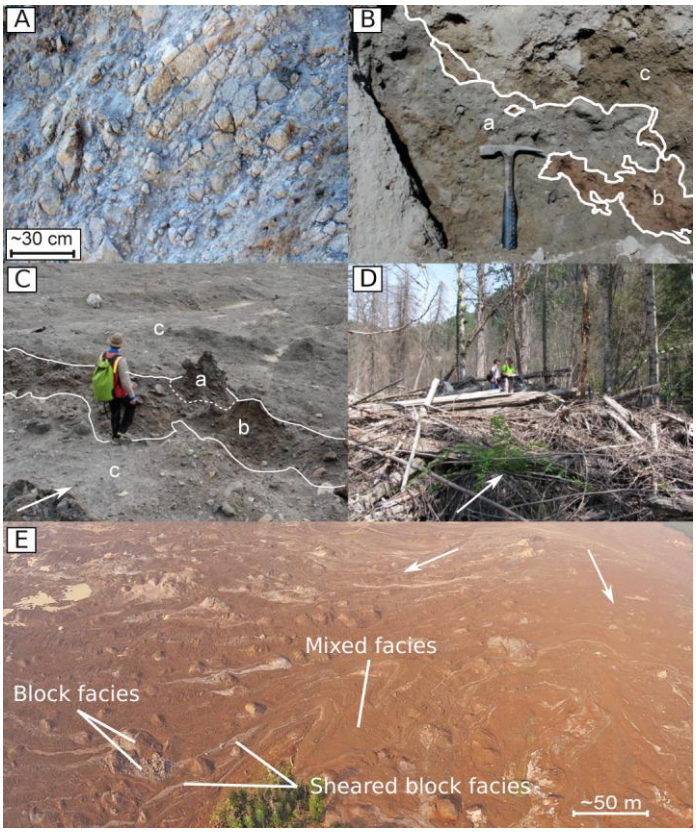

Figure 3.3. Photographs of typical Mount Meager landslide deposit facies. White arrows indicate flow direction. (A) Block facies. (B) Contacts between mixed facies (a), sheared block facies of gray rhyodacite (b), and sheared block facies of red rhyodacite (c). Hammer is ~30 cm. (C) A coherent but highly brecciated block (a) disaggregated by shear to form sheared block facies (b). The surrounding material is mixed facies (c). (D) Woody debris facies. (E) Aerial photograph of the debris avalanche deposit in Lillooet River valley taken the morning after the event, before the dam on Meager Creek breached (photo courtesy of D.B. Steers).

3.4.1. Facies

The **block facies** comprises highly brecciated but intact masses of red or gray rhyodacite, altered cream colored rhyodacite, and altered and unaltered basement rock derived from the source area. Blocks are tens to hundreds of cubic meters in volume and form hummocks one to several meters high. They commonly have a “jigsaw puzzle” fabric (Figure 3.3A) and a silt-to-clay loam matrix. The fine fraction (<2 mm) of zones of hydrothermally altered blocks contains 19%–29% clay, whereas the fine faction of unaltered blocks contains 2%–5% clay (Figure 3.4).

The **sheared block facies** is localized in shear zones within the block facies and occurs as discrete zones or streaks of coherent lithology in the deposit. It is a product of fragmentation and disaggregation of blocks by shear during the final stage of debris emplacement (Appendix B, Figure B1 and B2). The form of the block facies has been destroyed, but the lithology of the source block has been retained. Streaks of sheared block facies define the direction of movement of the debris avalanche (Figures 3.3C–3.3E)

The **mixed facies** is a fully mixed debris consisting of brown matrix-supported diamicton (Figures 3.3B, 3.3C, and 3.3E). It comprises particles ranging from clay to medium-size boulders. The matrix (<2 mm) is a sandy loam, with a clay content of 3%–8% (Figure 3.4). The gravel fraction consists of 19%–29% basement rock, 49%–64% gray porphyritic rhyodacite, 4%–10% red porphyritic rhyodacite, and 9%–12% other volcanic rocks. This facies also contains abraded wood fragments, and its surface supports rare kettle holes left from the melt of blocks of glacier ice derived from Capricorn Glacier in the source area.

The **woody debris facies** comprises partially abraded tree stumps, stems, and branches derived from the forest destroyed by the debris avalanche and pushed to the margins of the deposit (Figure 3.3D).

The **entrained facies** consists of fluvial channel or overbank sediments and colluvium incorporated into the landslide by scour and thrusting. This facies is distinguished from others by its well-sorted texture and rounded and sub-rounded clasts. The entrained facies is a minor constituent of the landslide deposit (Appendix B, Figure B3).

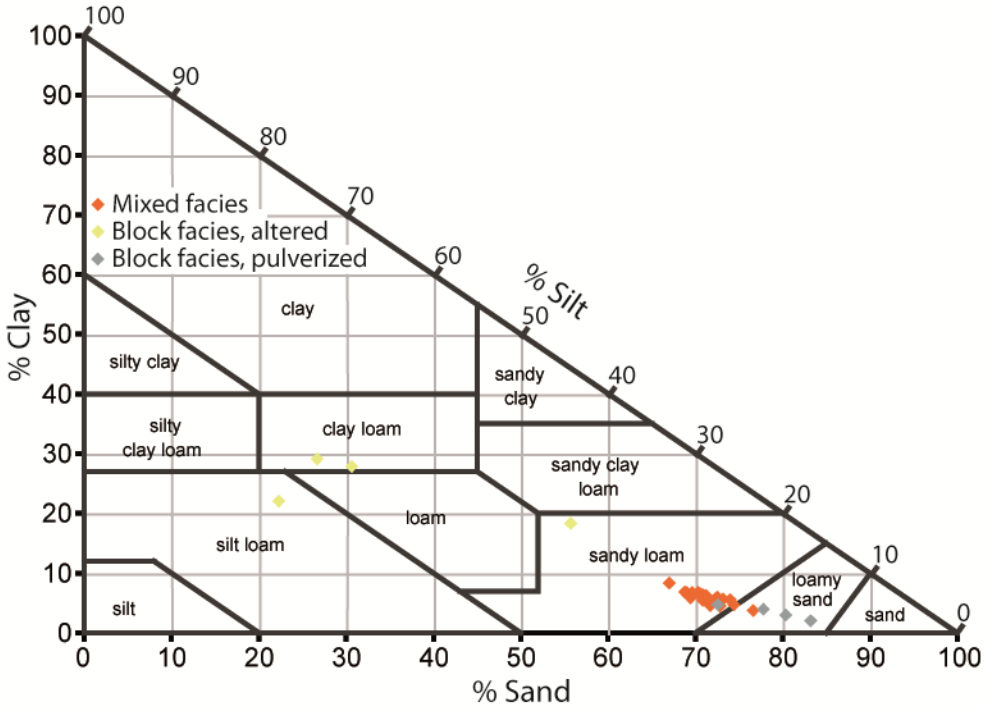

Figure 3.4. Sand-silt-clay ratios of samples of the Mount Meager debris avalanche matrix. Fields indicate the 12 classes of soil textural classification (Soil Survey Division Staff 1993).

3.4.2. Structures

The principal structures are linear forms associated with thrust, normal, and strike-slip faults. They include scarps, ridges, and linear depressions and, in some cases, mark lithological and facies boundaries (Figure 3.5).

Compressional ridges are perpendicular to flow. They are rounded and commonly sinuous along their length (Figure 3.5A). At eroded edges of the deposit, compressional ridges are underlain by diffuse shear zones or thrust faults marked by displaced lithologies.

Strike-slip faults are meter- to multi-meter-wide linear depressions with low relief, oriented parallel to the flow direction (Figure 3.5B). They are commonly associated with splay faults, grabens, and compressional ridges.

Normal faults are marked by scarps with straight slopes (Figure 3.5C). In some cases, they occur in pairs and form grabens (Figure 3.5D). Normal faults strike

perpendicular to the flow. Where seen in cross-section, normal faults are either single sharp faults or broad shear zones (Figure 3.5D).

3.4.3. Hummocks

Hummocks are 1–8 m in height, 1–40 m in length, and 1–30 m in width; volumes range from 1 m^3 to ~2 × 10^3 m^3. Shapes are round or ellipsoidal. Hummocks are composed of block facies (either gray or red porphyritic rhyodacite), entrained facies, or a mix of block, mixed, and sheared block facies.

Mixed hummocks typically have a core of block facies and sheared block facies and a carapace of mixed facies (Appendix B, Figure B4). The boundary between the core and carapace is sharp to gradational; in some cases flame structures intrude the core.

The entrained facies hummocks are composed of either fluvial sand and gravel or sand (Appendix B, Figure B5). This hummock type is rare and found only at the distal margin of the debris avalanche. The entrained facies hummocks are smaller than the block and mixed hummocks, with a volume of ~1–3 m^3.

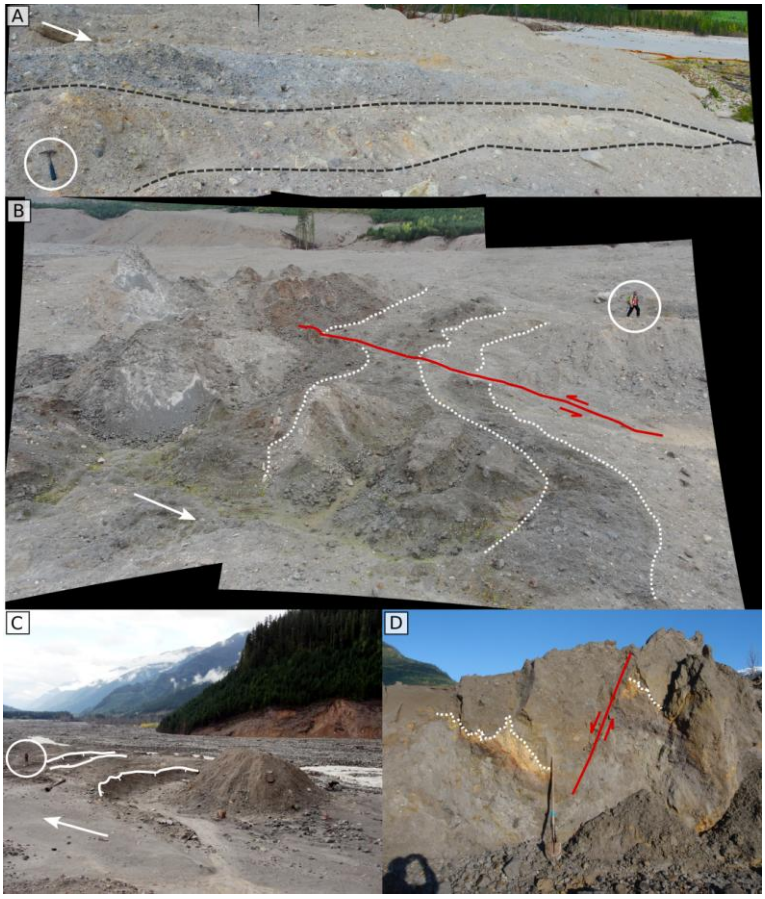

Figure 3.5. **Photographs of typical structures in the Mount Meager landslide debris. White arrows indicate flow direction. (A) Compressional ridges (hammer ~30 cm). The black lines show thrusts separating compressional ridges of gray rhyodacite and cream-colored, altered sheared block facies. (B) Panoramic view of a shear zone (circled person for scale). The red line marks a strike-slip fault; the white dotted lines highlight lithological markers that show the displacement along the fault. A graben is visible in the foreground. (C) View down Lillooet River valley showing extensional features in the plug; normal fault scarps are indicated by white lines. The graben in front of the circled standing person is perpendicular to the flow direction. Note the runup on the valley side. (D) Normal fault trace exposed in section. White dotted lines here indicate lithological markers. The shovel is 1.5 m in length.**

3.4.4. Area descriptions

Area 1: Meager barrier

The southeastern valley wall of Meager Creek, opposite the mouth of Capricorn Creek (area 1 in Figures 3.1 and 3.2), was stripped of all trees up to 270 m above the valley floor by the landslide. Only a patchy veneer of landslide debris remains on this slope. At the foot of the slope, and extending across Meager Creek valley to the mouth

of Capricorn Creek valley, is thick debris forming the barrier that dammed Meager Creek for 19 hr. The Meager barrier deposit is 700 m long, 50–500 m wide (increasing in width from the apex to the southeastern side of the valley), and ~30 m thick, thinning toward Capricorn Creek.

The barrier supports irregular ridges that are perpendicular to the flow direction (Figure 3.6A). Seven major compressional ridges are present on the northwestern side of the barrier. In contrast, the southernmost 200 m of the barrier surface, nearest the southeastern valley wall, is an irregular hummocky deposit.

The compressional ridges are southeast verging and identified by a basal thrust. The difference in height between each depression and the tops of adjacent ridges is as much as 12 m. The ridges increase in length from 50 to 300 m in a northwest-southeast direction; the longest ridges span the full width of the deposit. Streaks of sheared block facies trend parallel to the ridges (Appendix B, Figure B6). Only a few blocks, in the form of low broad hummocks, rise above the surface of the Meager barrier. Larger blocks (up to 900 m^3) locally underlie the ridges (Appendix B, Figure B7). We observed only a few altered blocks in this area.

The 200-m-long distal portion of the Meager barrier, below the opposing wall of Meager Creek, was eroded during the dam breach, but pre-breach helicopter photos (Figure 3.6A) show a northwest-verging thrust associated with a ridge, indicative of compression and contraction. Many hummocks of gray rhyodacite are present near the valley side in this area.

Three lineaments are evident on the southeastern valley wall above the barrier (Figure 3.6B). The highest lineament is a debris line that extends up to 270 m above the valley floor and marks the limit of the debris avalanche on the slope. The debris boundary separates the area stripped of trees from undisturbed forest. An intermediate lineament marks the limit of the debris barrier on the slope. The lowermost lineament is ~20 m above the valley floor and is consistently parallel to it.

Area 1 Interpretation

The front of the debris avalanche swept across Meager Creek and ran up the southeastern wall of the valley, completely removing the forest and scouring the forest

floor. The maximum limit reached by the debris is marked by the conspicuous trimline high on the valley wall. In the barrier deposit, the major compressional ridges formed at the foot of the slope as the forward movement of the debris avalanche in this area was impeded and the debris was compressed. The debris stopped first at its front while the back was still moving. We interpret the Meager barrier deposit to be related to seismometer “signal H” of Guthrie et al. (2012a) and the “aftershock” of Allstadt (2013), representing a final summit collapse of the secondary Mount Meager peak ~2 min after the main event. The hummocks of gray rhyodacite at the foot of the opposing slope are likely a product of runup and collapse of this late-stage emplacement.

We interpret the three lineaments on the southeastern valley wall to have formed during different phases of the debris avalanche. The high lineament was produced by the energetic and mobile front of the water-rich phase of the debris avalanche. The intermediate line is slightly younger and associated with barrier emplacement (Figure 3.6B). The lowest line marks the trace of the valley-confined flowing mass—the water-poor phase—that reached Lillooet River valley.

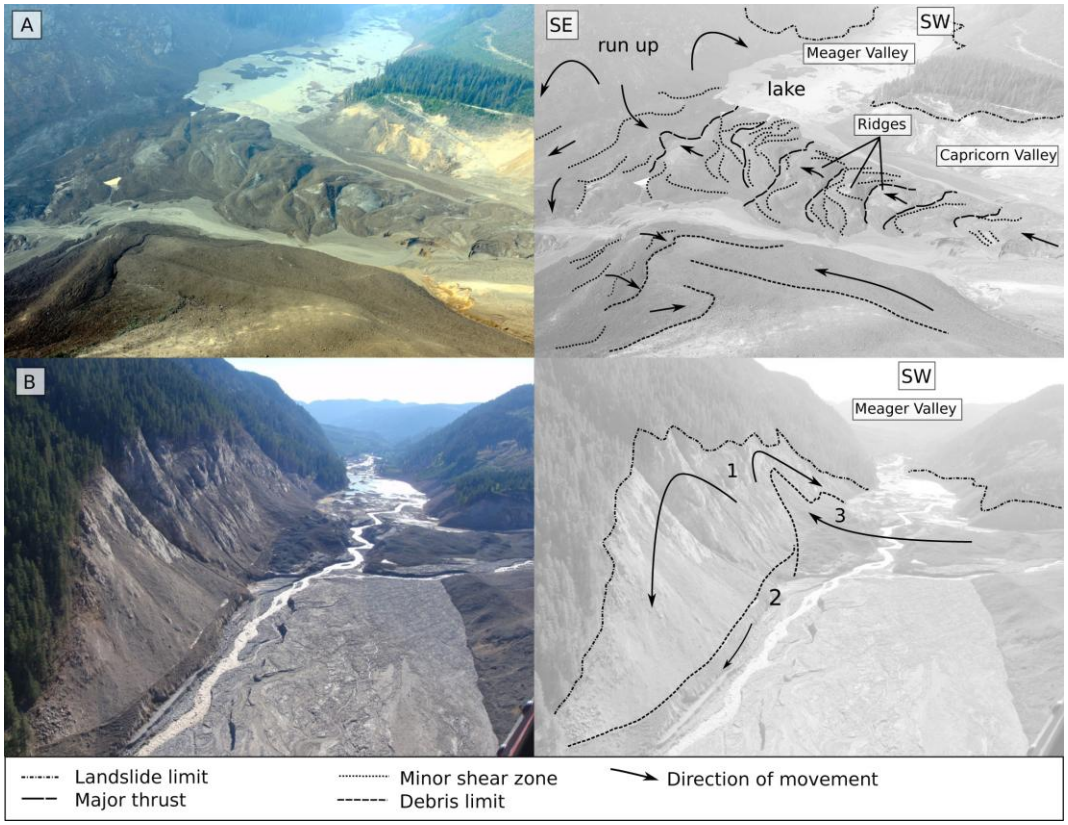

Figure 3.6. **(A) Sketch of the Meager barrier (area 1) based on a photograph taken before the dam breach, showing compression. (B) Sketch of the barrier area after the dam breach. The limit of the debris avalanche and lower debris lines on the valley side are marked: 1— high lineament caused by runup of the first pulse; 2— debris line left by the bulk of the mass flowing toward Lillooet River valley; 3— debris line left by runup and collapse of Meager barrier debris. Arrows indicate the direction of movement. Photos courtesy of D.B. Steers.**

Area 2: Terrace

The terrace (area 2 in Figures. 3.1 and 3.2) is located on the northwestern side of Meager Creek. It lies ~60–100 m above the valley floor and is underlain by glacial sediments. Remnants of two Holocene fans overlie the terrace at the mouth of Capricorn Creek. Both of the fans, and the terrace itself, were incised by Capricorn Creek sometime during the Holocene. The modern pre-2010 Capricorn Creek fan is inset into the terrace. Part of the frontal wave of the debris avalanche ran up onto the terrace northeast of Capricorn Creek after being deflected off of the valley wall in area 1. It removed second-growth forest on the terrace and left a veneer of debris. We recognize three subareas of area 2: (1) the Capricorn Creek fan, (2) the terrace tread, and (3) the terrace scarp.

The Capricorn Creek fan subarea is characterized by two fan levels, both of which are inset into the terrace. The lower fan surface is 20 m above the floor of Capricorn Creek and extends ~250 m up Capricorn Creek and 160 m down Meager Creek. The higher fan surface is 60 m above the floor of Capricorn Creek and extends 200 m down Meager Creek. Two units, a and b, of landslide debris are present within the Capricorn Creek fan (Figure 3.7A). Unit a occurs in what Guthrie et al. (2012a) termed "the spray zone", a discontinuous veneer of silt, sand, and gravel within an area of stripped and damaged trees at the limit of the debris avalanche. Unit b, which borders unit a, is a blanket of mixed facies material with a surface characterized by up to 1-m-high compressional ridges and longitudinal and transverse ridges. Unit b has three lobes; the first, b1, is a major northwest-southeast–trending debris ridge parallel to the terrace scarp on the northeastern side of Capricorn Creek. It is 220 m long, 25 m wide, and 2 m high. The second lobe, b2, is associated with an east-west–oriented fold that is 70 m wide and 100 m long. This lobe contains an east-west ridge that is 10 m wide, 80 m long, and 0.5 m high. A third debris lobe, b3, overlaps lobes b1 and b2 and is parallel to and near the edge of the terrace.

The second subarea of area 2—the terrace tread—extends ~600 m along Meager Creek valley. It is up to 200 m wide and 60–80 m above the valley floor. The tread is dissected by five gullies that are older than the landslide (Figure 3.2). Two units of landslide debris (a and b), similar to those present in the Capricorn Creek fan, are present here (Figure 3.7B). Unit a, located between the undamaged forest and unit b, comprises a thin layer of discontinuous debris within a zone of stripped and damaged vegetation up to 30 m wide. Downed tree stems at the margin of the deposit indicate the direction of flow, which is slightly transverse to the trend of the limit of the landslide. Lobes of debris entered the forest obliquely to the main flow direction. Unit b sharply borders unit a along a front 0.5–1 m high and comprises scattered block facies hummocks within a blanket of mixed facies up to 1.5 m thick. Compressional ridges 10–20 m long, 1–8 m wide, and up to 0.5 m high are parallel to the valley side. The hummocks are up to 12 m in diameter and 2.5 m high. Some of the hummocks have extensional grabens and partially collapsed sides. The boundary between units a and b at the downstream end of the terrace coincides with a concentration of altered blocks and sheared block facies streaks.

A thin veneer of mixed facies debris covers the third subarea of area 2—the terrace scarp. Two lineaments are present on the scarp and are parallel to its margin (Figure 7C). The higher lineament, which is about one-third of the vertical distance below the top of the terrace, slopes downvalley and merges with the valley floor at the end of the terrace. It is continuous with lobe b3 in the Capricorn fan area and extends up the largest upstream gully dissecting the terrace. The lower lineament is ~5 m above the valley floor. The two lineaments merge at the downvalley end of the scarp.

Area 2: Interpretation.

The many units and debris lines present in this area indicate that the terrace records different landslide pulses. In the terrace fan, unit a and lobe b1 are traces of the flow coming down Capricorn Creek before reaching the Meager Creek valley side. Unit a is the deposit of the frontal highly mobile flow (water-rich phase), while b1 is of the less-mobile debris-rich flow (water-poor phase). Lobes b2 and b3 are the deposits of different pulses of the flow after the impact on the southeastern wall of Meager Creek valley. Then the debris avalanche overrode the terrace tread and scarp. On the terrace tread, unit a is the expression of the frontal water-rich phase, and unit b is the deposit of an intermediate-water-content phase. Unit b on the terrace tread was water-rich enough to run over the terrace but could still support structures and hummocks. It is continuous with b2 on the terrace fan. The debris lines on the terrace scarp correlate with pulses of the water-poor phase. The upper debris line is continuous with lobe b3 and marks the maximum thickness of the water-poor material responsible for the plug deposit (see below); the lower line records the tail of the flow, or a surge related to the final "aftershock" collapse at the headwall of the landslide.

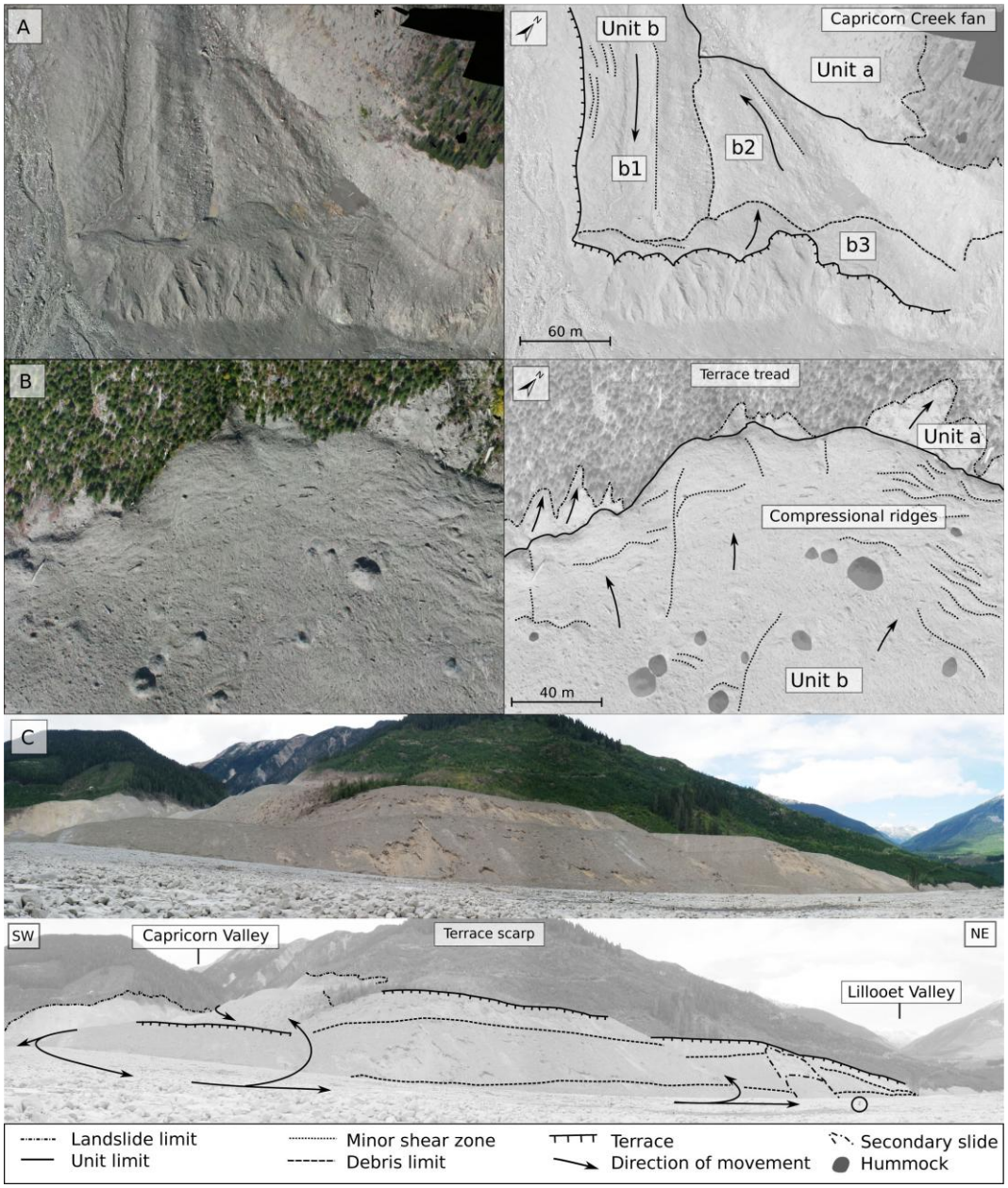

Figure 3.7. **(A) Orthophoto of the Capricorn Creek fan (part of area 2 of the Mount Meager landslide), showing unit a and unit b (the latter a product of three lobes: b1, b2, and b3). (B) Orthophoto of the central portion of the terrace tread showing unit a (water-rich flow deposit) and unit b (intermediate-water-content phase). The latter supports hummocks and deformation structures. Ridges indicate compressional motion against the valley side. (C) Panoramic view of the terrace scarp, debris trimlines, and post-depositional sloughing (person in the circle at lower right for scale). Image courtesy of C.-A. Lau.**

Area 3: Plug

The plug is in the center of the Meager Creek fan in Lillooet River valley

(area 3 in Figures 3.1 and 3.2). It has a triangular shape and is ~1200 m long and 100–500 m wide. Debris of the 2010 landslide in this area is up to 15 m thick. Lateral lobe wings and late-stage slurries were present along the external margins of the lobes but were removed by the dam-breach flood.

The plug is composed of block, sheared block, and mixed facies, with lithologic zoning resulting from the disaggregation of blocks into long tails, streaks, and discrete zones of sheared block facies. Hummocks are common and are 1–8 m high, 1–30 m wide, and 1–40 m long; they have volumes of 1–2 × 10^3 m^3. Low areas between hummocks exhibit deformation structures including shear zones, ridges, grabens, and lobes.

The west end of the plug, where Meager Creek enters Lillooet River valley, is characterized by collapsed hummocks, thrust and strike-slip faults, and well-developed grabens. Compressional features are cut by shear structures that are, in turn, cut by extensional structures (Figure 3.8).

Farther east, toward the center of the plug area, the deposit is characterized by flow-parallel strike-slip faults. The faults are dextral and oriented southwest-northeast on the north side of the plug, and sinistral and oriented west-east on the south side. Grabens transverse to the flow direction have northwest-southeast orientations (Figure 3.8). Strike-slip faults occur in areas of ridges, depressions, and sheared hummocks and mark the boundaries between the central part and the lateral parts of the debris avalanche that continued to flow to the east.

Two distal debris lobes extend from the main mass of debris and terminate on the Lillooet River floodplain with sharp fronts 7–10 m high, forming the east edge (front) of the plug. The point where the two lobes separate is 620 m from the west end of the plug. The more northerly lobe is 500 m long and up to 330 m wide. The southerly lobe is 450 m long and up to 150 m wide. The northern lobe is characterized by en echelon sigmoidal ridges, bounded by shear zones that accommodated the deformation at the point of bifurcation. The distal front of the lobe is marked by compressional ridges oriented northwest-southeast and northeast-southwest that terminate against and partially overtop hummocks. The north margin of the lobe is characterized by a system of dextral strike-slip faults spaced 30–50 m apart and oriented southwest-northeast.

They displace hummocks and form pull-apart basins and push-up landforms. The strike-slip faults separate steps and drop down to the north-northwest

In the southern lobe, the flow direction changes from southeast to east, then to the northeast. Strike-slip faults on the north side of this lobe are sinistral; those on the south side are dextral (Figure 3.8). The area between the two lobes has an irregular surface morphology, which we attribute to compression and thrusting by the debris flowing around it; some dead trees are still standing in this area.

In photos taken the morning after the landslide (Figure 3.3E) and before the breach of the Meager barrier, fluid slurries are visible at the margins of the plug. Muddy afterflow continued from Capricorn Creek valley for days after the event as loose debris was eroded and flushed downstream by the creek.

Area 3: Interpretation.

The hummocks are rigid portions of the landslide mass that commonly slowed and came to rest sooner than the surrounding material. This is evidenced by flow structures and spreading and extension of some hummocks in the flow direction. As the hummocks were carried, rotated, and tilted by the flowing mass, they were also deformed, fractured, and disaggregated. Mixed material wraps around individual hummocks.

Discrete faults, shear zones, pull-apart basins, and push-up structures are evidence of the dynamic interactions between different parts of the flowing mass. Cross-cutting relations between faults indicate multiple generations of deformation structures. Differential movement of the debris led to localized compressional, extensional, and transtensional stresses. Extensional structures are dominant at the west end of the plug, where they cut thrust and strike-slip faults. Strike-slip structures are dominant in the central part of the plug, cutting and displacing thrusts. Later normal faults are also present in this area, providing evidence for a change from a compressional to an extensional regime. The plug front to the east is dominated by thrust faults, reflecting the compressional regime in the area. There is no evidence of a highly mobile water-rich phase extending beyond the steep leading east edge. This may be related to different trajectories of the frontal wet-phase and the subsequent dry-phase flows. The water-rich

phase had higher mobility and caromed more as it traveled down Meager Creek. The water-poor phase had lower mobility and stayed more valley confined.

Geometrical patterns and kinematic indicators allow a possible reconstruction of the deformation history of the debris in the plug area (Appendix B, Figure B8). Primarily, compression dominated as debris, flowing in a single direction, rapidly decelerated at the flow front. Then, the debris started to flow in several different directions while decelerating at different rates. Lateral margins of the plug continued to move and deposit debris downstream in areas 4 and 5. Strike-slip faults formed to accommodate the deformation. Finally, the debris mass stopped and there was a general spreading and relaxation, with normal faults forming over the entire surface. The later slurries indicate that after the emplacement of the plug material, water remobilized part of the debris.

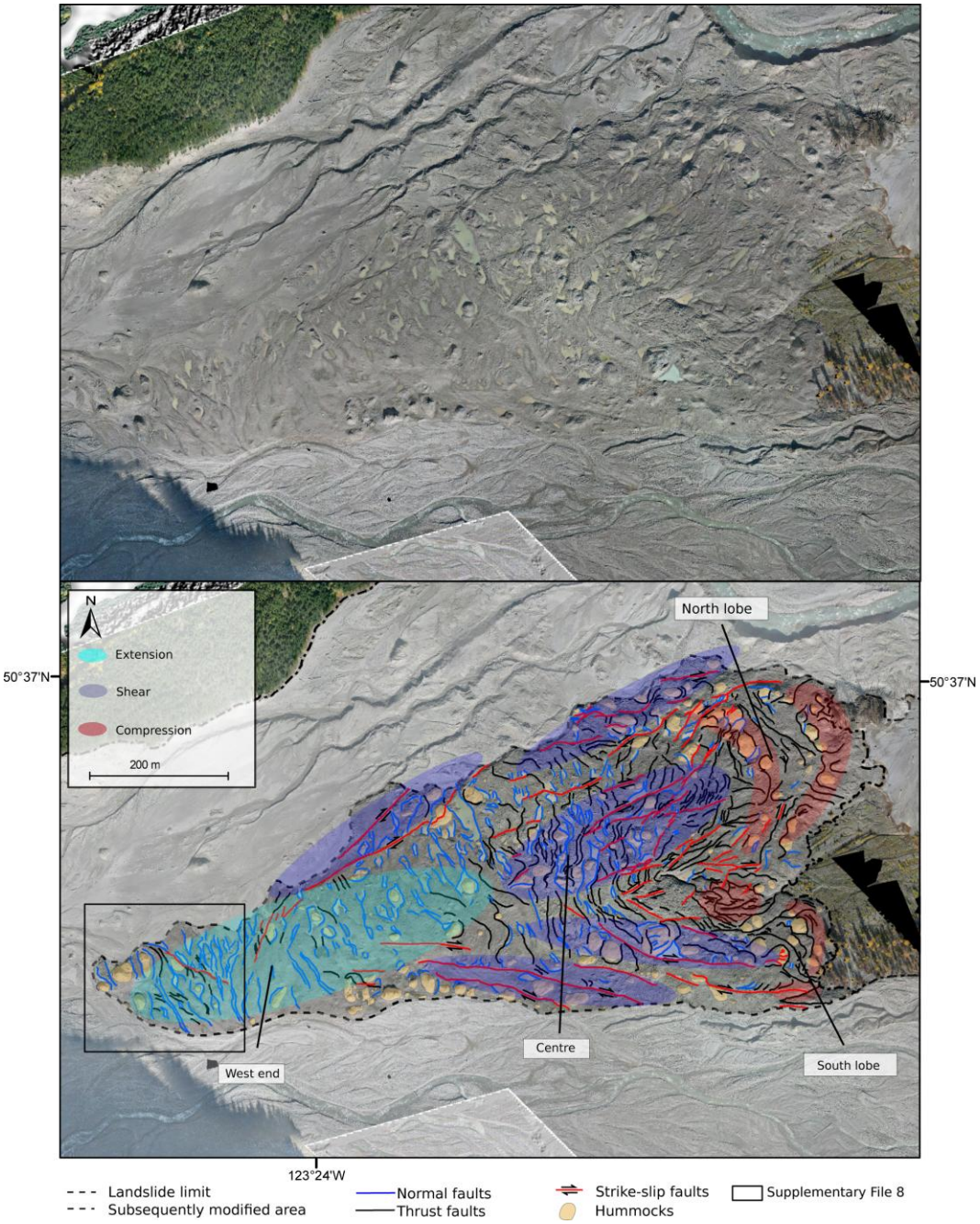

Figure 3.8. Orthophoto of the plug area, Mount Meager landslide (area 3). Structures indicate different stress regimes: extension (light blue) at the west corner of the plug; shear (purple) in the central part and at the sides; and compression (red) at the front and between the two lobes. Box indicates location of Appendix B, Figure B8, which shows structures and deformation sequence.

Area 4: Distal zone upvalley of the campsite ('distal up')

Area 4 encompasses the marginal zone of the landslide between Lillooet River and the unaffected forest to the east, and is northwest of the British Columbia Forest

Service campsite (Figure 3.1). The distal up area is 470 m wide and 450 m long (area 4 in Figures 3.1 and 3.2). The maximum thickness of the debris is 4 m. Piles of trees up to 3 m high form the eastern edge of the landslide. Lillooet River sediments were entrained by the landslide in this area. The most distinctive feature in area 4 is a 2.5–4-m-high scarp, which marks the underlying, pre-landslide east bank of Lillooet River.

Two units of landslide debris are present in the distal up area (Figures. 3.9A and 3.9B). Unit a is <1 m thick and consists mainly of mixed and woody debris facies, but includes hummocks of both block and entrained facies that were bulldozed to the margin of the deposit (Figure 3.9A). Tree stems are oriented orthogonal to the flow direction and are in contact with standing, abraded, and tilted trees. At the river edge, entrained fluvial sediment was bulldozed into compressional ridges and hummocks.

Unit b is thicker and comprises debris similar to the deposits that form the plug, with meter-high hummocks and compressional ridges (Figure 3.9A). In the northwestern part of area 4, unit b can be further subdivided into two different subunits. One has compressional ridges up to 3 m high and 20 m long and is in contact with the buried bank of Lillooet River. The other, which laps onto the first, has subdued ridges and lobes and some faults. Unit a flowed onto the terrace on which the Forest Service campsite is located, whereas unit b was stopped by it (Figure 3.9B).

Moving downstream (southeast) in area 4, a fan-shaped lobe of thick debris covers the terrace and terminates in a 3–4-m-high front that is in contact with standing trees. Some trees were pushed forward and tilted back into the debris field by this lobe.

Farther downstream, at the southeastern end of area 4, Lillooet River has eroded the terrace to form a new bank. The contact between the river sediments and the landslide debris is exposed in the riverbank, and here the debris is 0.5–2 m thick.

Area 4: Interpretation.

The deposit in area 4 reflects interactions with preexisting topography and different flow rheologies. The riverbank divided the flow in two: the water-rich phase (unit a) ran up over the bank, whereas the water-poor debris (unit b) was largely redirected and channeled by the bank. At the downstream end of area 4, unit b is in contact with, and laps onto, unit a.

The debris avalanche displaced Lillooet River water in area 4. Thus the fluid front is well developed here, extending as much as 180 m beyond the dense deposit. Eyewitnesses described a rush of muddy water along the logging road behind the campsite associated with this phase of the landslide (Guthrie et al. 2012a).

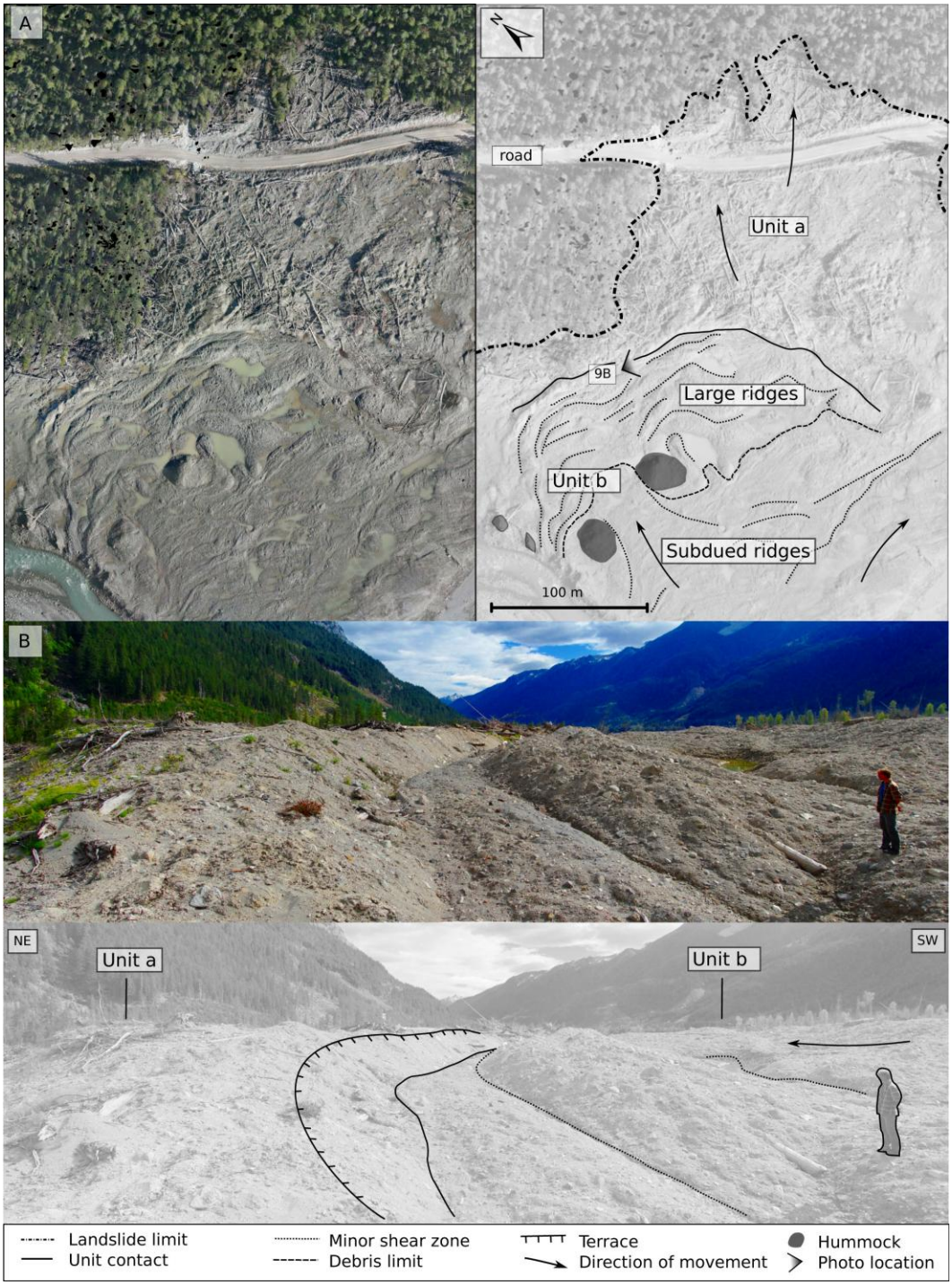

Figure 3.9. **(A) Orthophoto of the distal part of the Mount Meager landslide deposit upstream of the unaffected Forest Service campsite (area 4), showing units a and b. Location of B is shown. (B) Partially buried terrace scarp showing the boundary between units a and b.**

Area 5: Distal zone downvalley of the campsite ('distal down')

Area 5 is the most distal part of the landslide, located southeast (downstream) of the Forest Service campsite and extending from Lillooet River to the undisturbed forest on the east. The distal down area is ~1000 m wide and 350 m long (area 5 in Figures 3.1 and 3.2). The deposit thickness decreases from ~5–7 m to zero in the direction of flow.

We recognize two main depositional units (a and b) in area 5 (Figures 3.10A and 3.10B). Unit a is the transition from a zone of dead drowned trees into woody debris, and then into a zone of sparse debris and small hummocks. In unit a, the number of standing trees decreases inward toward unit b. Some trees are tilted and their stems abraded to heights of 6 m, with pebbles and cobbles embedded in the wood. The zone of dead drowned trees with no debris (Figure 3.10A) is 500 m wide and up to 200 m long with respect to the northeastern flow direction. An accumulation of woody debris, which lies west of the zone of dead trees, is up to 6 m thick and has a width of 8–100 m. Still farther west is an area of discontinuous debris with small (1–9 m^3) hummocks of block and entrained facies and sparse tree stems (Figure 3.10B). The debris in this area occurs in several lobes, the largest of which is 20–180 m wide.

Unit b is a deposit of hummocky debris up to 7 m thick. It extends as much as 150 m outward (northeast) from Lillooet River (Figure 3.10A). The hummocks are mainly block facies and have volumes of 100–120 m^3 (Figure 3.10B). Areas between hummocks have a slightly ridged morphology, but the structure is not well expressed. This unit laps onto unit a; locally the two are separated by a scarp ~2 m high.

Area 5: Interpretation.

The deposits in area 5 record a succession of events. A flood of water-rich material arrived first. It inundated the forest at the distal margin of the debris avalanche and left a frontal log jam and, just behind it, a zone of small hummocks (unit a). Water-poor debris arrived next, depositing unit b against the water-rich deposits. As was the case in area 4 upstream of the campsite, the front of the debris avalanche incorporated or displaced water from Lillooet River, sending unit a as much as 350 m beyond the limit of the denser material.

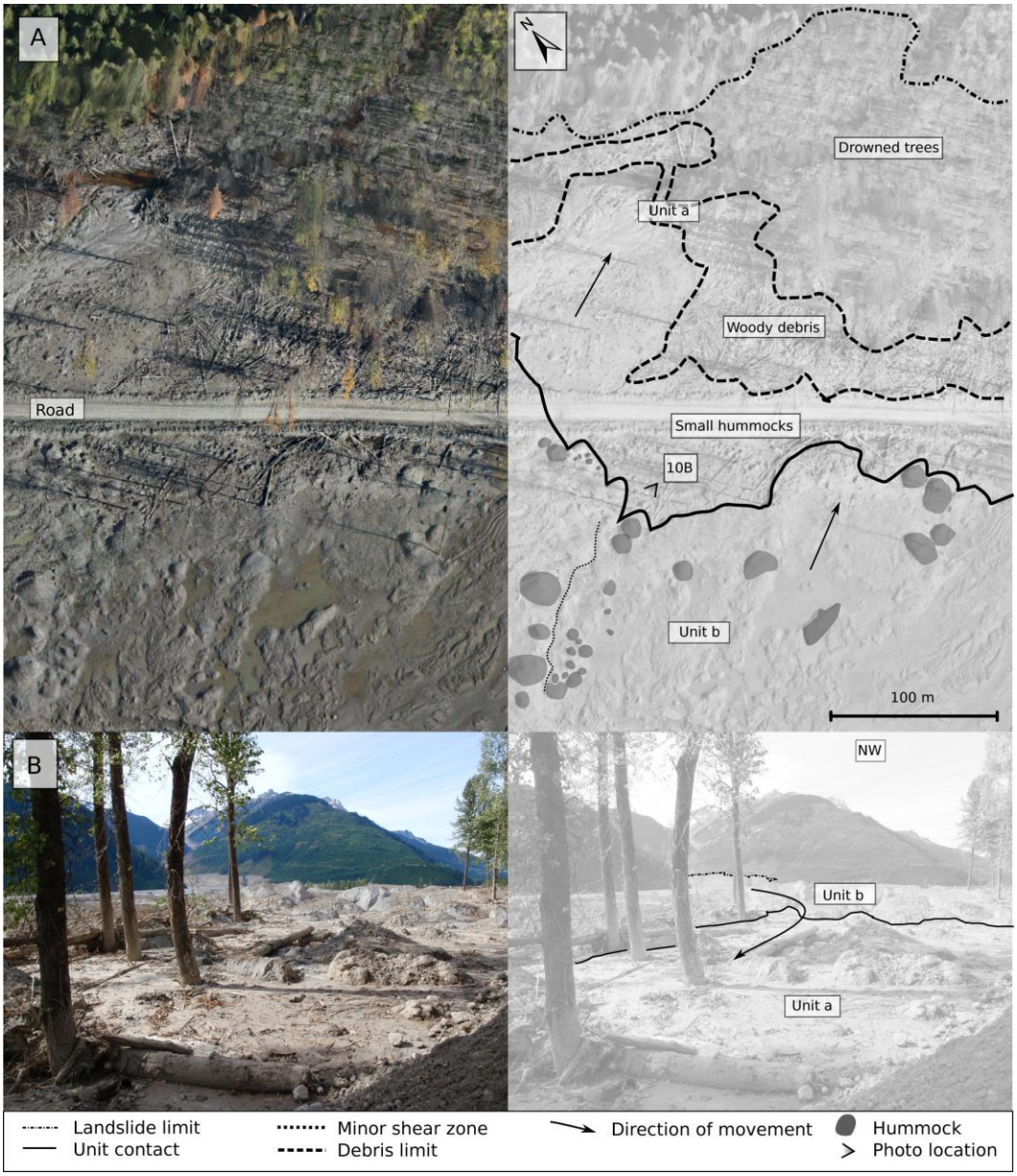

Figure 3.10. (A) Orthophoto of the distal part of the Mount Meager landslide deposit downstream of the unaffected Forest Service campsite (area 5) showing units, hummocks, shear zones, and the direction of movement. Location of B is shown. (B) Contact between thick hummocky debris (unit b) and the discontinuous debris veneer with small hummocks (unit a).

3.5. Discussion

Detailed study of the facies and surface morphology of the 2010 Mount Meager debris avalanche allows us to infer emplacement mechanisms, the relative timing of phases, and flow rheology. The structure and form of the deposit differ along the

landslide path, providing information on transport and depositional processes and the evolution of the debris avalanche. Our interpretation of the flow dynamics and flow separation is presented below, along with their hazard implications.

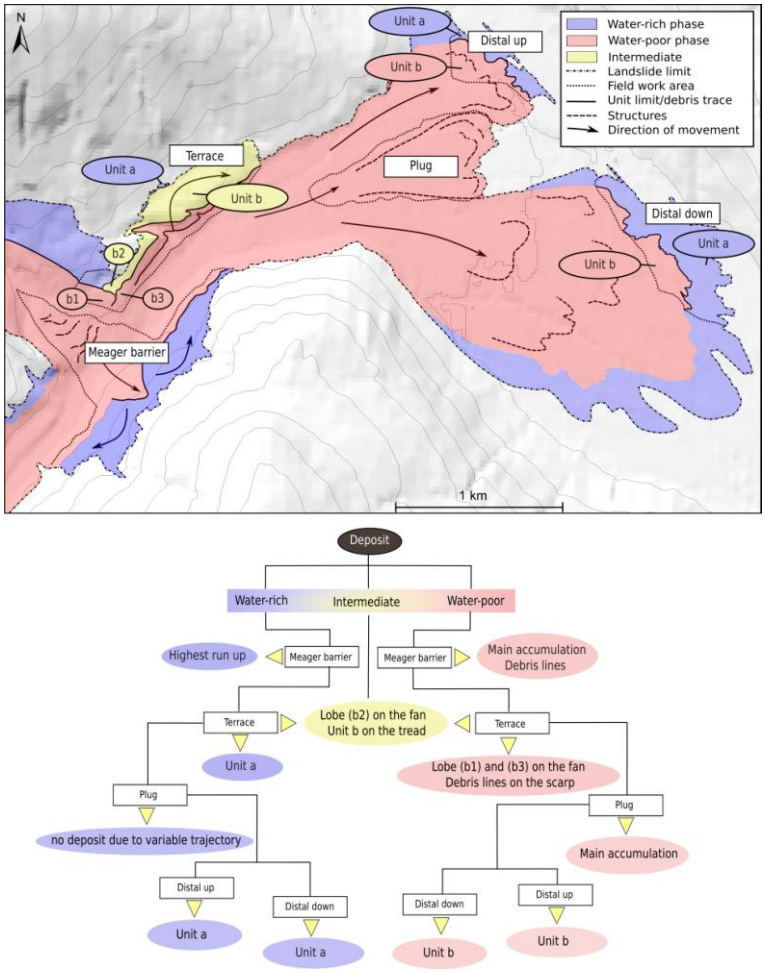

Figure 3.11. Top: Summary sketch map showing the distribution of water-rich and water-poor deposits of the Mount Meager landslide. Bottom: Flow chart summarizing the correlation between rheology phases, areas, and deposits. The water-rich phase produced the high debris line at the Meager barrier and deposited unit a in the terrace, distal up, and distal down areas. There are no traces of the water-rich phase in the plug area. The water-poor phase produced the lower debris line at the Meager barrier and left the thick body of debris in that area. It left the debris lines on the terrace scarp and unit b (lobes b1 and b3) on the terrace fan and in the distal up and distal down areas. The plug was also deposited by the water-poor phase. Unit b on the terrace tread and lobe b2 on the terrace fan are interpreted as deposited by an intermediate-water-content phase.

3.5.1. Lithology and grain size

The lithology of the landslide debris provides insight into its depositional processes. The distribution of altered material is particularly instructive. Altered materials are associated with block facies and sheared block facies streaks. Altered block and sheared block facies are more common at the downstream end of the plug than at the upstream end. Mud balls and altered sheared block facies streaks were also noted along the downstream margin of the terrace area. Conversely, the Meager barrier has less debris of the altered block and sheared block facies; it is primarily composed of very large gray porphyritic rhyodacite blocks within mixed material. We infer that this lithological zoning reflects the structure of the original rock mass in the source area: hydrothermally altered rock at the base of the source scarp and fresh rock typical of the volcanic plug higher up on the scarp.

The mixed material is dominantly silty clayey sand with clay percentages ranging from 5% to 8%. Altered sheared block facies samples may have up to 30% clay, whereas the fresh unaltered sheared block facies is 2%–5% clay (Figure 3.4). The average clay content by facies is 6.1% mixed, 24.6% altered block, and 3.6% pulverized block. A mixing ratio of 12% altered to 88% pulverized is required to get 6.1% clay in the mixed facies. This simple analysis suggests that ~12% of the failed rock mass was hydrothermally altered. Furthermore, within the mixed material there is no apparent trend in the mean clay content from upstream to downstream, suggesting that the material became well mixed as it traversed Capricorn Creek.

Figure 3.12. Rheology end-member deposits, Mount Meager landslide. (A) Thick debris, hummocks, and faults of the water-poor phase in area 3. The red line marks strike-slip faults; the white dotted lines delineate block and sheared block facies. (B) Woody debris and dead trees of the water-rich phase downstream of the unaffected Forest Service campsite. White arrow indicates the direction of movement.

3.5.2. Rheology phases

There is evidence of multiple pulses of flow of diminishing magnitude over time, but the deposits can be generally classified into two main rheology types: water-poor and water-rich (Figure 3.11). These two rheology types are, in reality, end members in what was a continuum. The water-poor end member produced thick debris avalanche–like deposits, with abundant large hummocks. Kinematic structures reveal sequential movement related to pulses in the emplacement process (Figure 3.12A). The water-rich end member is responsible for a flood-like deposit with sparse tree stems amid standing trees with meter-high splash lines and trunk erosion, and has no significant lithic debris (Figure 3.12B). This end member, however, transitions into woody debris, which in turn

transitions into an area with hummocks morphologically similar to those of the debris flow and hyperconcentrated flow deposits. Structural discontinuities, including faults, shear zones, and compressional ridges, delineate zones with distinct internal morphological characteristics that are related to one of the two end members. However, the boundaries between these deposits are not sharp everywhere, suggesting gradual phase transitions (areas 4 and 5). Distinct debris lines indicate multiple pulses (areas 1 and 2) with different rheologies.

The water-rich phase is evident along the margins of the debris avalanche deposit, except at the front of the plug area. Water-rich flow deposits are overlain by, but extend beyond, the deposits of the water-poor phase. In the plug area (area 3), the debris terminates with a sharp front and there is no evidence of a leading water-rich phase, suggesting that the two phases followed different trajectories as they entered the Meager Creek–Lillooet River confluence area.

The two phases had different velocities and different paths that were controlled by the complex topography over which the debris avalanche traveled. The sinuous longitudinal form of Capricorn Creek valley (Figure 3.1) resulted in centripetal and centrifugal forces that generated a marked separation of debris. The water-rich phase accelerated, achieving higher velocities and thus reaching farther up the valley sides, while the less-mobile water-poor core moved along the valley bottom. These differences in trajectory led to different deposits along Meager Creek and in Lillooet River valley.

Our evidence suggests that the water-rich phase preceded the water-poor phase, in contrast with the conclusion of Guthrie et al. (2012b) that a first, drier front came to rest in the plug area ~10 km from the source area and “the flow crossed the Lillooet River on both sides and over this plug” (p. 670). A water-rich phase followed by a water-poor phase is not unusual in debris flows and debris avalanches (cf. Oso landslide, Washington, USA; Iverson et al. 2015).

However, the water-rich slurries at the west end and margins of the plug suggest that some water-rich flows followed the emplacement of the plug. Copious water may have flowed from the source scar and remobilized part of the newly deposited material after the plug came to rest. It is thus difficult to distinguish a fluid tail contemporaneous

with the debris avalanche from secondary debris mobilization by water flowing down Capricorn Creek.

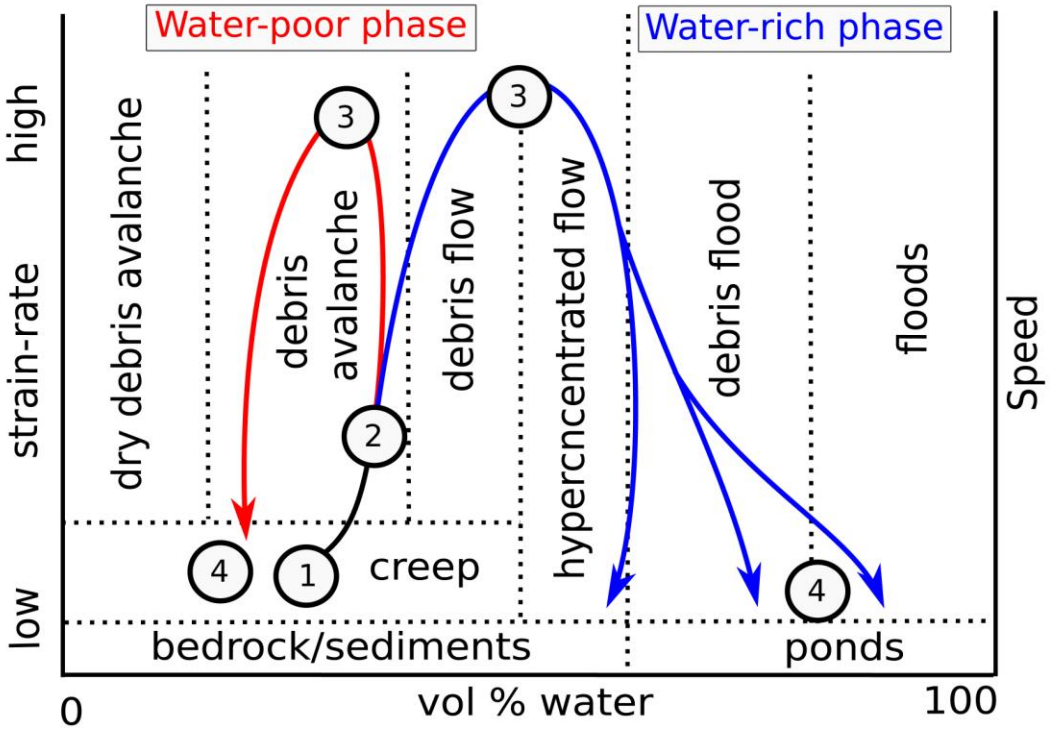

Figure 3.13. Conceptual diagram showing stages in the evolution of the Mount Meager debris avalanche. (1) The south flank of Mount Meager fails. (2) The rock mass breaks up, spreads, and liquefies as it begins to accelerate down Capricorn Creek valley. Water escapes from beneath the debris avalanche, forming the advance water-rich phase (blue line); the bulk of the mass, in comparison, is relatively dry (red line). Although the two phases interact, they follow different paths and leave separate deposits. (3) Both phases achieve very high velocities before impacting the south valley wall of Meager Creek. They decelerate as they spread up and down Meager Creek and into Lillooet River valley. (4) Final deceleration and cessation of flow.

3.5.3. Summary of the event

Figure 13 summarizes our view of the 2010 Mount Meager debris avalanche in terms of rheology and velocity from its beginning to its end. The x-axis in the figure is the proportion of water and sediment in the flow, from debris avalanche to clear-water flood; the y-axis indicates both the strain rate and velocity. The different fields are based primarily on morphology. We postulate four stages in this history:

- Stage 1. The south flank of Mount Meager failed following infiltration of water generated by snowmelt and permafrost thaw into hydrothermally altered rock and colluvium on the lower part of the slope. In the first several seconds, the collapsed material behaved as a single mass and the motion was relatively slow, with an average speed of 4 m/s (Allstadt 2013) (Figure 3.14A).
- Stage 2. The failed mass accelerated rapidly, disaggregated, and spread as it started to flow down the valley of Capricorn Creek. High water pressure caused liquefaction and forced the water upward and outward, creating a mobile, water-rich frontal flow (Figure 3.14B).
- Stage 3. The water-rich flow accelerated and superelevated at the bends in Capricorn Creek valley, causing the high runups documented by Guthrie et al. (2012a, b). It entered Meager Creek valley slightly in advance of the slower water-poor flow. Both ran up the opposing valley wall and turned back toward the opposite side of the valley. The water-rich phase split in two lobes (Figure 3.14C). One lobe overrode the terrace (area 2) and then flowed back toward Meager Creek to affect area 5 downvalley of the Forest Service campsite. A second lobe was deflected by the terrace and followed a straight trajectory to area 4 upvalley of the campsite. Both lobes decelerated, leaving thin debris, small hummocks, and standing water, indicative of further flow separation. The most distal deposit of the water-rich phase in areas 4 and 5 shows evidence of extreme water content as the flow displaced and incorporated water from Lillooet River.
- Stage 4. After impacting the southeast wall of Meager Creek valley, the water-poor phase deposited thick debris in the Meager Creek–Lillooet River confluence area (Figure 3.14D). During final emplacement, it separated into three lobes: a central, less mobile one (area 3) and two lateral wings that flowed farther, crossing Lillooet River and leaving the water-poor deposits in areas 4 and 5. As the water-poor phase decelerated and came to rest, it developed ductile-brittle deformation structures. It did not travel as far as the water-rich phase.

Although the water-rich and water-poor phases had different trajectories due to their differences in volumes and velocities, they did not behave totally independently. The presence of intermediate deposits suggests that they interacted. Furthermore, their separation in time was minor, perhaps only seconds.

The scenario outlined above is consistent with an analysis of seismic records of the landslide by Allstadt (2013). She concluded that “there is even a hint of what could be interpreted as two separate surges visible in the vertical component of the force-time function. The vertical component of the force ... has a shorter duration than the eastward component and is followed by a second smaller upward pulse” (p. 15). The multiple debris lines on the valley sides, however, suggest more than two surge waves; some may not have been large enough to generate clear seismic signals.

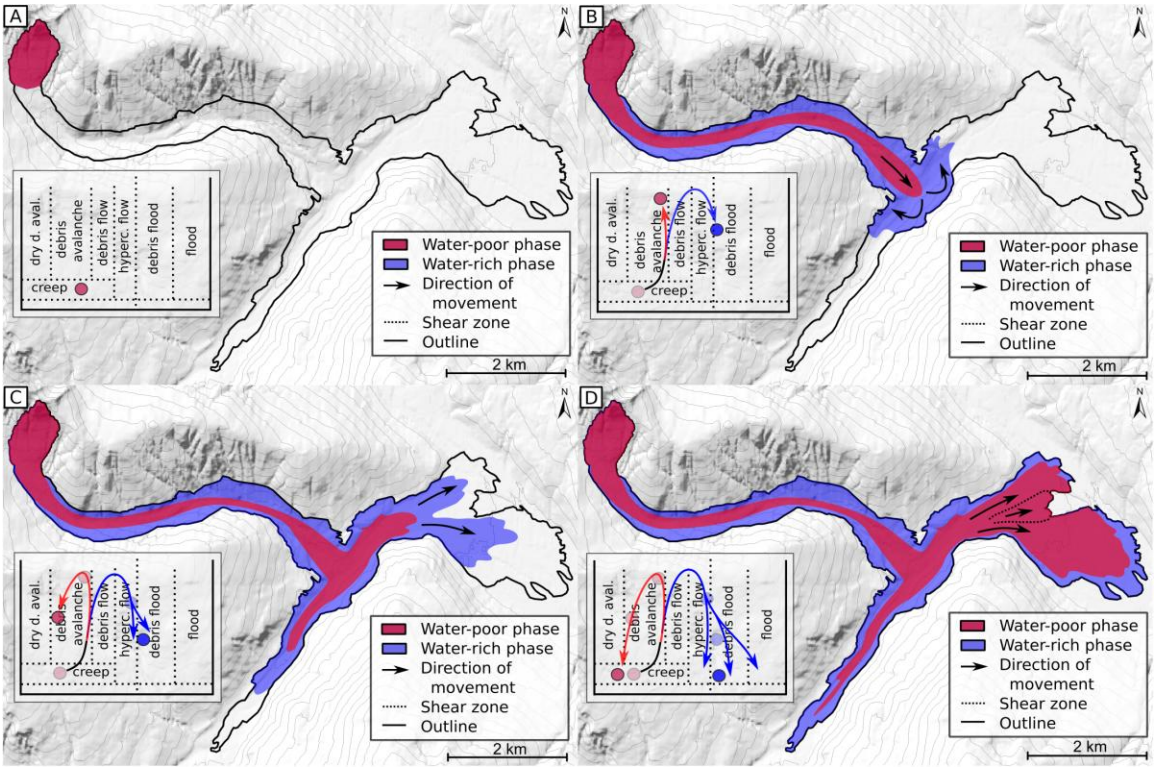

Figure 3.14. Schematic diagram showing the evolution of the Mount Meager debris avalanche with inferred rheological behavior. (A) At initiation, the collapsed material behaves as a single phase. (B) The water-rich phase forms as the debris avalanche moves down the valley of Capricorn Creek. Upon reaching Meager Creek, it runs 270 m up the south valley wall. (C) It then flows both up and down Meager Creek valley. (D) The water-rich phase travels farther than the water-poor phase. The latter leaves a thicker deposit, which displays deformation structures that develop during final emplacement. d. aval.—debris avalanche; hyperc.—hyperconcentrated.

3.5.4. Hazard implications

Transformation of a dry debris avalanche into a saturated debris flow has been inferred for many events (Palmer and Neall 1989; Vallance and Scott 1997; Capra and

Macias 2000; Scott et al. 2002; Tost et al. 2014). In the case of the Mount Meager event, the transformation was partial, and multiple rheologies coexisted, with different mobilities, velocities, and trajectories. Our observations show that debris avalanches can be multiphase events with debris avalanche, debris flow, hyperconcentrated flow, debris flood, and flood-like components or phases (Figure 3.13). This complexity may be more common than presently thought and may apply to other debris avalanche events. Here, different rheologies were clearly expressed in the deposit textures because the high sinuosity of the valley caused extreme separation of water-rich and water-poor phases. Also, the photo documentation immediately after the event allowed us to differentiate ephemeral water-rich deposits and flow traces that are not preserved in older events.

Numerical modeling of debris avalanches takes into account only dry granular material (Pudasaini and Hutter 2003; Zahibo et al. 2010), and the models typically are single phase (Takahashi 2007; Pudasaini 2011). Only simplified, two-phase models traditionally are used for debris flows (Iverson 1997; Pudasaini et al. 2005; Jakob et al. 2013). Recently, Pudasaini (2012) and Pudasaini and Krautblatter (2014) have proposed a more complete two-phase model for debris flows and debris avalanches that simulates the separation of a fluid front, drier core, and fluid tail.

The complexity of the 2010 Mount Meager debris avalanche highlights the difficulties of modeling such events and assessing the risk they pose to downvalley populations and infrastructure. The separation of water-poor and water-rich phases in complex topography has to be simulated to reproduce the different deposit types and the runout of each phase.

3.6. Summary and conclusions

Field evidence and detailed geomorphic mapping of the 2010 Mount Meager landslide allowed us to document the development of multiple rheology phases with different mobilities and trajectories. As the collapsed mass disaggregated and started to flow along Capricorn Creek, it separated into a faster water-rich phase and a slower water-poor phase. The water-rich phase caromed down Capricorn Creek, ran high up the southeastern wall of Meager Creek valley, and overtopped a terrace on the opposite side of the valley, while the water-poor phase was more confined to the valley floor. The shapes of Capricorn and Meager Creek valleys contributed to the phase separation and

deposit emplacement. The water-rich phase left the most distal deposit, but its deposit is not observed everywhere at the distal margin because the flow separated and was deflected by the topography. The less-mobile, water-poor phase left a continuous deposit.

Lithological zones in the deposit preserve the original distribution of rock in the source area, with hydrothermally altered rock derived from the base of the scar reaching the distal limit of the debris avalanche and gray rhyodacite rock higher on the flank of Mount Meager dominating more proximal deposits. Grain-size analysis and rough mixing estimates suggest that ~12% of the failed rock mass was hydrothermally altered.

Finally, this event raises new challenges for multi-rheology phase modeling of debris avalanches and hazard mapping. There were no fatalities in this particular event, but lack of understanding of the complex behaviour of such landslides could result in inaccurate hazard assessment, placing populations at risk from catastrophic rock slope failures.

3.7. Acknowledgments

We thank Engielle Paguican-Fabbro for taking the helicopter photos used for the SfM processing. Diego Masera, Mirko Francioni, Nancy Calhoun, and Hazel Wong assisted with field work. Discussions with Patrick Englehardt, Carie-Ann Lau, Snowy Haiblen, Libby Griffin, and Tatum Herrero helped us formulate some of our ideas, and we thank Fran van Wyk de Vries and Cat Lit for manuscript improvement. We thank Tim Davies and Lucia Capra for the paper review. Financial support for the research was provided by geoNatHaz (EU-Canada Co-operation Project in Higher Education, Training and Youth) and the Region Auvergne, France.

Chapter 4. Precursory slope distress prior to the 2010 Mount Meager landslide, British Columbia [3]

Gioachino Roberti[1,2] , Brent Ward[2] , Benjamin van Wyk de Vries[1] , Pierre Friele[3] , Luigi Perotti[4] , John J. Clague[2] , and Marco Giardino[4]

(1) Université Clermont Auvergne, CNRS, IRD, OPGC, Laboratoire Magmas et Volcans, Aubiere Cedex, France (2) Earth Sciences Department, Simon Fraser University, Burnaby, British Columbia Canada (3) Cordilleran Geoscience, Squamish, British Columbia, Canada (4) Earth Sciences Department, University of Torino, Torino, Italy

4.1. Abstract

In 2010, the south flank of Mount Meager failed catastrophically, generating the largest ($53 \pm 3.8 \times 10^6$ m^3) landslide in Canadian history. We document the slow deformation of the edifice prior to failure using archival historic aerial photographs spanning the period 1948-2006. All photos were processed using Structure from Motion (SfM) photogrammetry. We used the SfM products to produce pre-and post-failure geomorphic maps that document changes in the volcanic edifice and Capricorn Glacier at its base. The photographic dataset shows that the Capricorn Glacier readvanced from a retracted position in the 1980's then rapidly retreated in the lead-up to the 2010 failure. The dataset also documents 60 years of progressive development of faults, toe bulging, and precursory failures in 1998 and 2009. The 2010 collapse was conditioned by glacial retreat and triggered by hot summer weather that caused ice and snow to melt. Meltwater increased porewater pressures in colluvium and fractured rocks at the base of the slope, causing those materials to mobilize, which in turn triggered several secondary failures structurally controlled by lithology and faults. The landslide retrogressed from the base of the slope to near the peak of Mount Meager involving basement rock and the overlying volcanic sequence. Elsewhere on the flanks of Mount Meager, large fractures have developed in recently deglaciated areas, conditioning these slopes for future collapse. Potential failures in these areas have larger volumes than the 2010 landslide.

[3] This paper has been published in 2017 in *Landslides*: Roberti G, Ward B, van Wyk de Vries B, Friele P, Perotti L, Clague JJ, Giardino M (2017) Precursory slope distress prior to the 2010 Mount Meager landslide, British Columbia. Landslides 15(4):637–647

Anticipated atmospheric warming over the next several decades will cause further loss of snow and glacier ice, likely producing additional slope instability. Satellite- and ground-based monitoring of these slopes can provide advanced warning of future landslides to help reduce risk in populated regions downstream.

4.2. Introduction

Large landslides and debris flows are common on the slopes of active and inactive volcanoes, and especially those that presently support glaciers or that have been incised by glaciers and streams in the past. Although many researchers have examined the relationship between deglaciation and volcanic eruptions (Rampino et al. 1979; Jellinek et al. 2004; Huybers and Langmuir 2009; Watt et al. 2013) and between eruptions and large-scale collapses of volcanic edifices (Voight et al. 1981, 2002; Siebert 1984; Glicken 1996), investigations of deglaciation as a mass wasting trigger in volcanic environments are few; notable exceptions include Holm et al. (2004), Capra (2006), and Capra et al. (2013). And only recently have researchers begun to document landslides from presently ice-clad volcanoes (e.g. Huggel et al. 2007, 2008).

Glaciers can destabilize volcanoes in many ways. They abrade and fracture already weak, highly fractured flows and pyroclastic deposits, and remove support from the base of oversteepened slopes, changing stress regime and further decreasing their stability (Huggel 2009; McColl et al. 2010; Grämiger et al. 2017). Water from melting ice easily enters these fractured rocks, increasing pore water pressure, which in turn causes instability (Terlien 1998). In active volcanoes, heated fluids also hydrothermally alter and further weaken host rocks (Reid et al. 2001; Finn et al. 2001; Pola et al. 2012, 2014; Wyering et al. 2014). Saturated, weakened, and altered rocks may deform by creep processes (Cecchi et al. 2004; Pola et al. 2014; Heap et al. 2015; Heap and Wadsworth 2016), inducing gravitational distress that can culminate in collapse (van Wyk de Vries and Francis 1997; Cecchi et al. 2004). Large amounts of water may be stored in the porous and permeable rocks of the volcanic edifice (Delcamp et al. 2016; Detienne 2016), and in the event of a deep-seated collapse of a volcanic flank, can transform a simple rockslide into a mobile debris avalanche or debris flow (Roverato et al. 2011; Capra et al. 2013; Delcamp et al. 2016; Roberti et al. 2017).

The Mount Meager massif (Figure 4.1) is a good example of a volcanic complex that is susceptible to failure conditioned by the aforementioned processes. It has been deeply dissected by glaciers and subject to glacier retreat, leaving steep slopes in volcanic and basement rocks that have been subject to hydrothermal alteration. A rich archive of historical aerial photographs (1948, 1964-1965, 1973, 1981, 1990 and 2006) is available to document more than one-half century of topographic changes caused by gravitational deformation.

On 6 August 2010, the south flank of Mount Meager failed, generating a large debris avalanche that travelled down the valleys of Capricorn and Meager creeks and into the Lillooet River valley nearly 13 km from the source (Figure 4.1) (Guthrie et al. 2012; Allstadt 2013; Moretti et al. 2015). Roberti et al. (2017) describe the deposit of this landslide and interpret its kinematics and dynamics. Here we complement previous studies with an assessment of the source area of the landslide in the lead-up to the catastrophic failure of 2010. Using high resolution DEMs generated from aerial photographs, we track both deformation of the slope and the activity of Capricorn Glacier at its toe over a 62-year period. Mapping of lithologic units and structures exposed in the rock slope allowed us to document slow progressive deformation. We refine the previous volume estimate of the failed rock mass (Guthrie et al. 2012) and estimate its water content. Merging our observations of precursory slope distress with the seismic record of the collapse (Allstadt 2013), we infer a retrogressive failure sequence. Finally, we discuss the effects of hydrothermal alteration, continuing deglaciation, and groundwater storage on the stability of the larger Mount Meager volcanic massif, as well as the factors that condition and could trigger failures in the future.

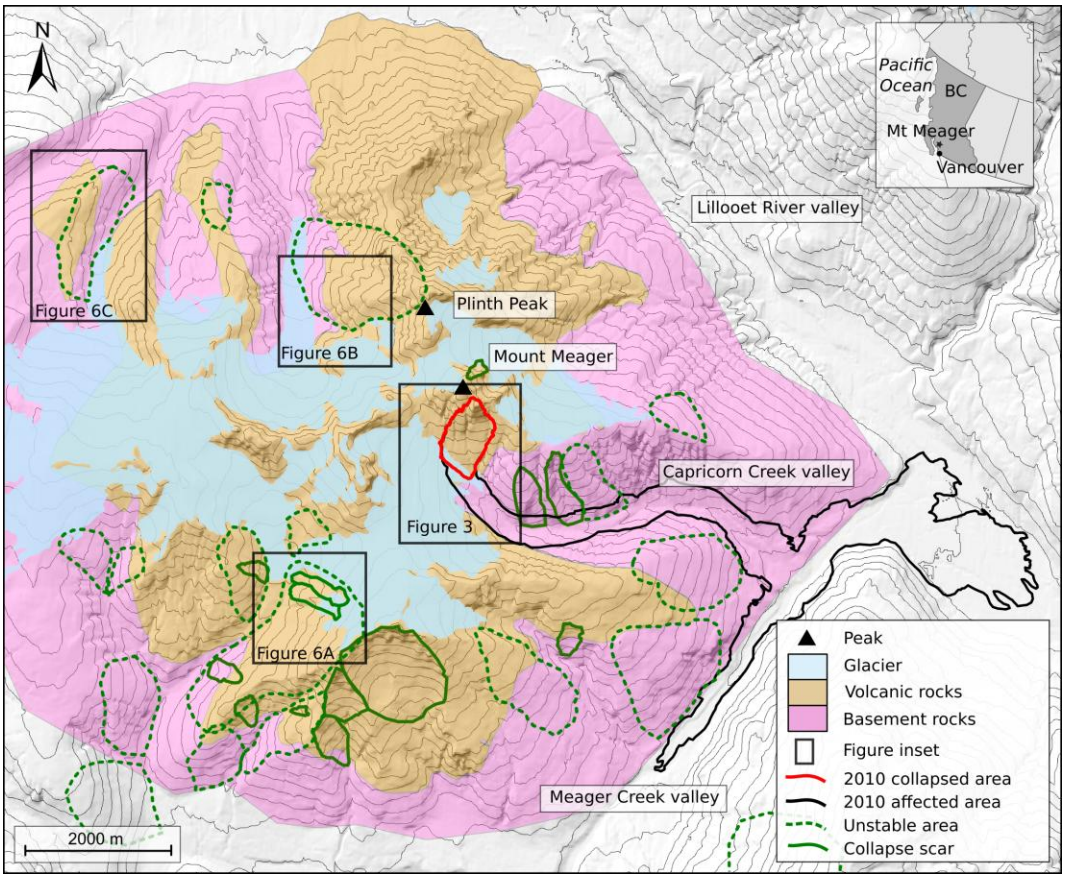

Figure .4.1. Location map and geology of Mount Meager volcanic complex (geology after Read 1978). Also shown is the headscarp and deposit of the 2010 landslide, as well as other gravitational instabilities in the area. Inset map shows the location of Mount Meager.

4.2.1. Context of the Mount Meager failure

The Mount Meager massif is a partially glacier-covered volcanic complex located in the southern Coast Mountains of southwest British Columbia, 60 km northwest of the town of Pemberton (Figure 4.1). It is a coalescent group of volcanic centers of Pliocene to Holocene age that have been built on top of Mesozoic granitic and metamorphic basement rocks (Read 1978, 1990). The last eruption, from near Plinth Peak, happened about 2400 years ago and produced a small flow, ignimbrite, and a plume of ash that reached as far east as the Alberta Rocky Mountains (Clague et al. 1995; Hickson et al. 1999). The massif comprises a suite of eruptive products, including pyroclastic rocks, basalt flows, and rhyodacite domes (Read 1978, 1990). Parts of the volcanic pile have been hydrothermally altered, and active fumaroles and hotsprings are present on the flanks of the massif. The area was repeatedly glaciated by ice caps and the Cordilleran

Ice Sheet during the Pleistocene (Clague and Ward 2011) and presently supports numerous small glaciers. The volcanic and basement rocks have been deeply dissected by glacial and fluvial erosion and by mass movements, leaving steep slopes and a current local relief of up to 2200 m.

The Mount Meager massif has been the site of numerous prehistoric and historic landslides (Friele et al. 2008). The most recent large landslide, which happened on 6 August 2010, involved over 50 x 10^6 m^3 of highly fractured and altered volcanic and basement rocks on the south flank of Mount Meager. The path height of 2185 m and the maximum path length of 12.7 km yield a *Fahrböschung* (travel angle) of 9.8°. The landslide generated an equivalent magnitude 2.6 earthquake, and long-period seismic waves were recorded at stations as far away as southern California and northern Alaska. Examination of the seismograph records suggested that the peak velocity of the landslide was 90 m/s and the collapse occurred retrogressively. Based on the seismic data, Allstadt (2013) concluded that the primary failure occurred in two stages separated by about 20 seconds, followed 40 seconds later by a smaller collapse, and finally, about two minutes later, by a fourth and final failure.

The failed area was partly covered by glaciers at the peak of the Little Ice Age (ca. AD 1570–1900; Grove 1988; Matthews and Briffa 2005). Much of this ice was lost due climate warming in the 20th and early 21st centuries (Bovis and Jakob 2000; Holm et al. 2004), and today the flanks of Mount Meager are largely ice-free. The 2010 and other large landslides on the Mount Meager massif stem, in part, from glacier erosion and retreat and attendant stress changes of its unstable slopes (McColl et al. 2010; Grämiger et al. 2017) and, in part, from the low strength of the fractured and hydrothermally altered volcanic rocks that underlie the massif (Evans and Clague1994; Holm et al. 2004). Recent thaw of alpine permafrost also may have contributed to instability through the loss of ice cohesion and the liberation of water in near-surface rocks and sediments (Geertsema et al. 2006; Allen et al. 2009).

Elevated pore water pressures may have triggered the 2010 landslide because it occurred at the end of a lengthy, late summer heatwave that exacerbated glacier melt and permafrost thaw. The link between rapid snow and ice melt during hot weather has been noted in the case of other large landslides at Mount Meager (Mokievsky-Zubok 1977; Bovis and Jakob 2000; Holm et al.2004) and in other alpine areas (Chleborad

1997; Gruber et al. 2004; Gruber and Haeberli 2007; Harris et al. 2009; Keiler et al. 2010). Based on this relation, road-building and forestry operations in the Meager Creek watershed had been suspended before the landslide occurred.

4.3. Methods

4.3.1. Structure from Motion (SfM)

Topographic modeling is becoming more accessible and more widely used due to recent advances in digital photogrammetry (James and Robson 2012; Remondino et al. 2014; Micheletti et al. 2015; Smith et al. 2015; Kolzenburg et al. 2016). For this study, we processed digitized historic aerial photographs and digital oblique photos with the Structure from Motion (SfM) and multi-view-stereo (MVS) algorithms (Snavely et al. 2008; James and Robson 2012; Westoby et al. 2012; Fonstad et al. 2013; Micheletti et al. 2015) to produce 3D topographic models from which orthophotos and DEMs (Digital Elevation Models) were subsequently created.

A large set of historical British Columbia government vertical aerial photographs is available for the Mount Meager massif. The area was photographed in 1947, 1948, 1962, 1964-1965, 1973, 1981, 1990, and 2006. The photographs are available only as paper copies produced from the original negatives, and many of them are in poor condition (i.e. deformed by humidity, scratched, or ink-annotated). In addition, metadata on the camera and flight mission are not, in all cases, available. It would be difficult, if not impossible, to process these photos using classic stereo-photogrammetric techniques. Fortunately, we were able to construct high-quality orthophotos and digital surface models (DSMs) using Structure from Motion software.

We processed and analyzed photographs from 1948, 1964-1965, 1973, 1981, 1990, and 2006 to chronicle the evolution of the massif. The 1947 and 1962 photos were not processed because the area of interest was covered by clouds in 1947 and by snow in 1962. We took oblique digital photographs with a single-lens reflex (SLR) camera during a low-level helicopter flight 23 days after the failure. Comparison of the DEMs produced from 2006 and 2010 photos allowed us to refine the estimate of the volume of the failed rock mass and to compare the source area before and after the landslide. We made field observations of the 2010 landslide source area in 2016 to ground-truth the

geology as mapped by Read (1978, 1990) and to map structures in the scar left by the landslide.

4.3.2. Quality assessment

The SfM-MVS workflow generates 3D models in arbitrary object coordinates. The precision of the model depends on image quality and the 3D reconstruction algorithm. The cartographic accuracy of the final orthophoto and DEM depends on the accuracy of the geographic coordinate source used in the georeferencing process. We scanned all photos at 800 DPI, following Linder's (2009) guidelines. The pixel size of digitized airphotos depends on the scanning resolution and on the approximate scale factor of the photograph (Appendix C, Table C1). The resulting 3D models have reconstruction errors of 0.9-1.8 pixels and precision of 0.4-1.5 m (Table 4.1).

When georeferencing scanned images, it is preferable to use coordinates from a source with high accuracy (ASPRS 2014); a common approach is to perform a differential GPS field survey. For this study, it was not feasible to perform such a survey due the inaccessibility of much of the source area and danger of rock falls. Instead, we used georeferenced points on British Columbia Government standard base maps. Planimetric coordinates were derived from SPOT 10-m resolution imagery, and elevations were extracted from the Canada TRIM (Terrain Resource Inventory Map) DEM (18.3 m average accuracy) (NRCan 2013). We calculated the overall positioning accuracy based on FGDC (1998) and ASPRS (2014) recommendations. The resulting horizontal accuracy with 95% confidence (HA 95) is 15-42 m and the vertical accuracy with 95% confidence (VA 95) is 17-63 m (Table 4.1).

Table 4.1. Precision and accuracy of the different datasets.

Year	Pixel size (m/pixel)	Reprojection error (pixel)	Precision (m)	HA 95 (m)	VA 95 (m)
2006	0.42	1.15	0.48	32.01	17.17
1990	0.51	0.91	0.46	29.68	23.46
1981	0.65	0.36	0.23	35.5	16.09
1973	0.43	1.8	0.77	15.15	22.96
1964	1.13	1.37	1.55	36.52	63.92
1948	0.93	1.14	1.06	42.82	23.00

4.3.3. Glacier area errors

We mapped the snout of Capricorn Glacier, which lies at the base of the failed slope, on each georeferenced orthophoto. Uncertainties in the mapped extent of the glacier are related to inherent errors in the base map, errors introduced by manually tracing the margins of the glacier, and to problems in discriminating ice, snow, and snow-covered ice. To account for these errors, we buffered the perimeter of the glacier based on the cartographic precision of the orthophoto. The uncertainty includes both base map errors and errors related to ice-margin tracing. The final precision for the glacier area estimates was calculated as the root of the squared sum of buffer areas (Diolaiuti et al. 2012; D'Agata et al. 2013). Changes in the area of the glacier over time are shown in Figure 4.2.

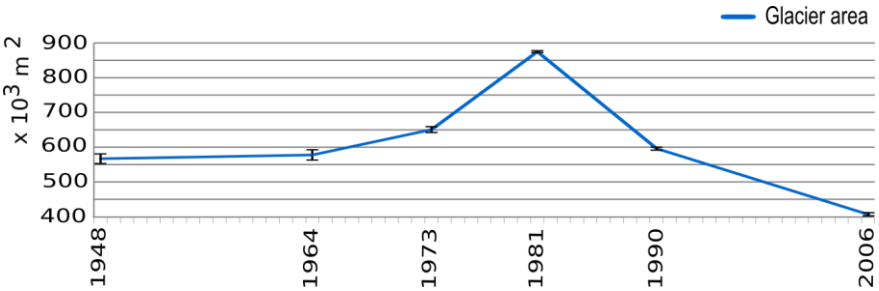

Figure 4.2. Change in extent of Capricorn Glacier over the period of the photographic record. Note the readvance of the glacier that culminated around 1981, followed by rapid retreat to the present. Black lines delineate error bars.

4.3.4. Volumetric errors

We compared topography derived from British Columbia airphotos acquired in 2006 with that derived from the post-landslide 2010 oblique helicopter photos at a pixel-by-pixel level to estimate the volume of the failed rock mass. To minimize errors in this exercise, we co-registered the two surfaces by matching recognizable points in the 3D models. To assess this error, we compared the two surfaces in areas where no significant change would be expected and assumed the same error would be present where the mass failed (Gardelle et al. 2013). The standard deviation (σ) in the elevation difference is ±6 m. The resulting uncertainty in the volume estimate is expressed as volumetric variation (σ_{vs}) and is defined by the mean of the formula $\sigma_{vs} = \sigma A$, where the area (A) of the failed rock mass is 6.4 $x10^5$ m^2. The volumetric error calculated in this

manner is ±3.8 x 10^6 m^3. We estimated the volume of the 2010 landslide by differencing the 2006 and 2010 DEMs. A small failure from the source area in 2009 had a volume of about 2-3 x 10^5 m^3 (Cordilleran Geoscience 2009); we did not subtract this volume from our estimate as it is only a fraction of the calculated error.

Guthrie et al. (2012) obtained an estimate of the volume of the 2010 Mount Meager landslide of 48.5 x 10^6 m^3 by differencing a pre-event 25-m-resolution TRIM DEM developed from 1987 stereo-photos and a post-event 5-m-resolution DEM derived from GeoEye stereo imagery obtained in August and September 2010. They did not clearly state the potential error in the estimate, but it is likely ±15%, or ± 7.27 x 10^6 m^3 (Moretti et al. 2015) given that the pre-event DEM had a resolution of 25 m (Guthrie et al. 2012). Other uncertainties in the volume estimate stem from the fact that landslides in 1998 and 2009 affected the source scarp between the 1987 photo date and the 2010 landslide.

4.4. Results

4.4.1. Glacier change

Glaciers in the southern Coast Mountains began to retreat significantly from their Little Ice Age maximum positions shortly after the start of the 20th century (Koch et al. 2009). There was a short-lived readvance of most glaciers in British Columbia around the middle of the century. Between 1948 and 1973, Capricorn Glacier advanced at an average rate of 3 x 10^3 m^2 yr^{-1}. The average rate of advance increased to 28 x 10^3 m^2 yr^{-1} between 1973 and 1981. Soon thereafter, the glacier again began to retreat. It retreated at an average rate of at 31 x 10^3 m^2 yr^{-1} between 1981 and 1990, and 12 x 10^3 m^2 yr^{-1} between 1990 and 2006. By 2006, the glacier had retreated past the base of the slope that would fail in 2010, and only a patch of debris-covered ice remained.

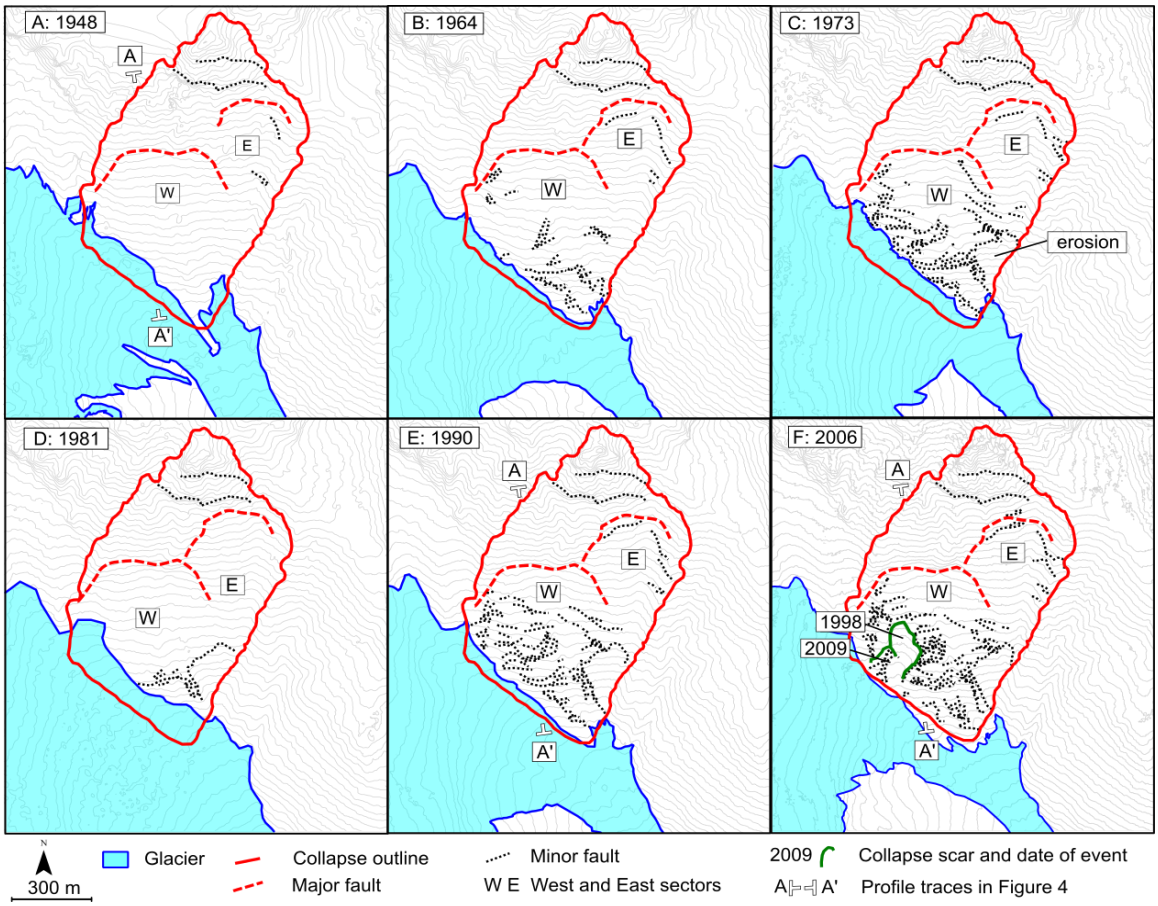

Figure 4.3. Maps of the head-scarp area of the 2010 landslide from 1948 to 2006. Locations of the margin of Capricorn Glacier through time, the outline of the 2010 headscarp, and faults are shown. A) 1948: Major faults are already present. B) 1964-1965. Diffuse deformation at the toe of the slope. C) 1973: A large portion of the slope toe (~1.5 x10^6 m^3) has been removed by erosion, and major and minor faults have expanded. D) 1981: Snow covers most of the area. Capricorn Glacier is at its maximum 20th century extent. E) 1990: Diffuse deformation and some bulging at the toe of the slope. F) 2006: Diffuse deformation, bulging, the scar of the 1998 landslide, and the source area of the 2009 event.

4.4.2. Pre-event flank conditions, 1948-2006

Prior to the 2010 landslide, the south face of Mount Meager extended from 1700 m asl at its base in upper Capricorn Creek to 2550 m asl at the summit peak. We subdivide this face into two areas (Figure 4.3). The upper portion, leading to the peak, was nearly vertical with rock cliffs and pinnacles; the lower portion, formed in fractured

rock and covered in part by colluvium, had a convex glacially undercut profile (red line in Figure 4.4). These two parts of the face were separated by normal faults (Figure 4.3). Faults further subdivided the lower portion of the face into west (W) and east (E) sectors. The W sector was bordered by a fault striking W-E and dipping south; it intersected the slope at about 2050 m asl. The E sector was bordered by a fault striking NW-SE and dipping southwest; it intersected the slope at about 2200 m asl The base of the unstable area was located at about 1700 m asl at the Little Ice Age trimline of Capricorn Glacier. Between 1948 and 2006, displacements increased along normal faults and the density of faults increased (Figure 4.3) as the toe progressively bulged (Figure 4.4). This progressive deformation led to the landslides in 1998 and 2009 (Figure 4.3F).

The sequence of changes in the slope that would fail catastrophically in 2010 is as follows:

- 1948. Faults that delineate the W and E sectors are present. The W sector is well defined, but it is not internally dissected by minor faults. The bounding fault in the E sector is present but does not appear connected to its counterpart in the W sector. Snow covers the toe of the slope, obscuring detail in that area (Figure 4.3A).
- 1964-1965. Minor faults have developed in the W sector. The west side of the toe shows widely spaced faults (Figure 4.3B), and the east side is dissected by three deep gullies.
- 1973. The west sector of the toe has bulged, and a large volume of colluvium and fractured and altered rocks (~1.5 x 10^6 m^3) on the east side of the toe has been removed by erosion (Figure 4.3C).
- 1981. The area is mostly covered by snow, obscuring morphological and structural detail (Figure 4.3D). Minor faults probably continued to propagate, and rock continued to degrade.
- 1990. Fractures in the W sector are wider, and the toe has further deformed and eroded (Figure 4.3E).
- 2006. Four years before the catastrophic collapse, the fault delineating the W sector has accumulated 10-40 m of displacement, decreasing eastward. The bounding fault of the E sector has up to 15 m of displacement. The toe area

includes the headscarp of the 1998 landslide (Bovis and Jakob 2000) and is marked by horst and graben structures (Figures 4.3F and 4.5A).

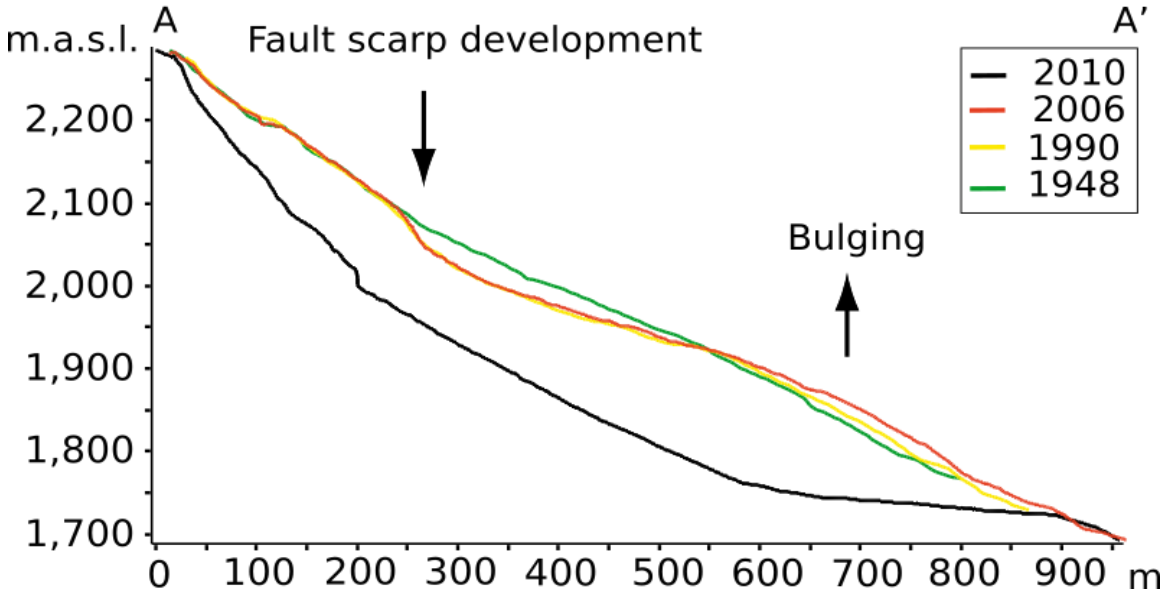

Figure 4.4. Topographic cross-sections of the flank of Mount Meager in 1948, 1990, 2006, and 2010. Note major faulting, sagging, and bulging of the toe of the slope in the lead-up to the 2010 landslide. Arrows show relative directions of motion.

4.4.3. 2010 collapse

The 2010 failure involved the entire edifice sequence from the basement to the ridge crest. The estimated volume of the collapse is 53 ± 3.8 x 10^6 m^3. We estimated sector volumes by parsing the slope using mapped faults: 24.6 x 10^6 m^3 for the W sector, 13.8 x 10^6 m^3 for the E sector, 9.0 x 10^6 m^3 for the portion above the W sector, and 5.6 x 10^6 m^3 for the rock peak.

The detachment surface is a step-shaped amphitheatre with a steep upper section (60-90°) that is 200 m high on the east and a less steep (5-40°) lower portion. The lower basal sliding surface is located within igneous basement rocks judging from the position of adjacent basement outcrops outside the scar (Figure 4.5B). Rocks involved in the failure are, from top to bottom, an intrusive rhyodacite plug, block and ash layers, volcanic breccia, and quartzdiorite basement (Figure 4.5B). The volcanic rocks are part of the Capricorn (0.09 Ma) and Plinth (0.1±0.02 Ma) assemblages of Read (1978, 1990). The rhyodacitic plug forms the peak of the mountain; the other units are

present on the lower portion of the scar and are now partly covered by talus (Figure 4.5B).

1. Intrusive rhyodacite plug (unit P9i of Read 1978). This unit is pervasively fractured, with meter-scale steep columns and horizontal fractures. Parts of the unit display ochre-colored hydrothermal alteration.

2. Block and ash layers. Read (1978) mapped this unit as rhyodacitic lava flows (unit P9f). However, no lava flows are evident in the scar and the surrounding area. Rather, block and ash layers form a carapace surrounding the intrusive plug. The layers have thicknesses of several meters and dip 30-40°.

3. Volcanic breccias (unit P8x of Read 1978). These basal breccias are fractured and hydrothermally altered.

4. Quartzdiorite (unit Mqd of Read 1978) unconformably underlies the volcanic sequence. The contact was covered by debris soon after the 2010 landslide, but it can be seen at the margins of the scar (Figure 4.5B). Lithological analysis of the landslide deposit by Roberti et al. (2017) showed that it contains ~20-30% basement rock, some hydrothermally altered.

The lower part of the source slope has been intensively hydrothermally altered. Moving upward in the sequence, the block and ash layers are relatively fresh and the rhyodacite plug is only locally altered.

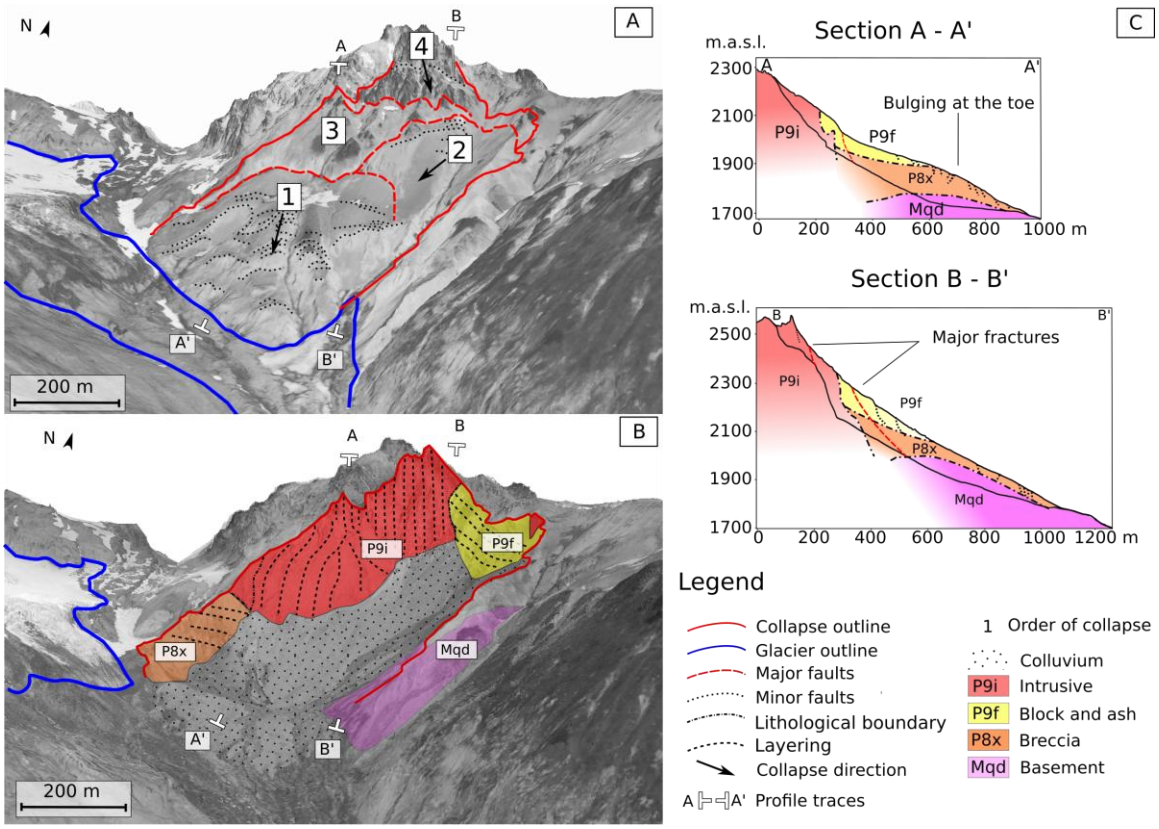

Figure 4.5. **A) Flank of Mount Meager four years before the collapse in 2010 (modified from Delcamp et al. 2016), showing the head scarp of the landslide, failure domains, directions of collapse, faults, and the terminus of Capricorn Glacier. 1) First failure: direction of movement 191°; volume 24.6 x10^6 m^3. 2) Second failure: direction of movement 217°; two pulses about 20 seconds apart; volume 13.8 x10^6 m^3. 3) Third failure: direction of movement mainly vertical; 40 seconds after the two main failures; volume 9.0 x10^6 m^3. 4) Fourth failure: direction of movement mainly vertical towards the SE; two minutes after the third failure; volume 5.6 x10^6 m^3. Movement directions and timing from Allstadt (2013). B) Headscarp of 2010 landslide after the collapse (modified from Delcamp et al. 2016), showing bedrock units described in the paper. C) Pre-and post-failure cross-sections of the source area. m.asl = metres above sea level.**

4.4.4. Meteorological trigger

Landslides at Mount Meager in 1975 and 1998 occurred during hot weather in late July and early August, respectively (Figure 4.6; Mokievsky-Zubok 1977; Bovis and Jakob 2000). Given this history, summer temperatures and precipitation are now monitored to control operational shutdowns at work sites around the volcano (Cordilleran Geoscience 2012). In September 2009, a landslide destroyed the road crossing at

Capricorn Creek (Cordilleran Geoscience 2009). In 2010, work undertaken to repair the crossing was shut down due to a sustained heatwave in late July and early August. The six-day running mean of daily maximum temperatures recorded by an automated station near the mouth of Capricorn Creek exceeded 28°C from July 18 until August 5, just prior to the catastrophic failure. Maximum temperatures peaked between July 24 and 31, when the six-day running mean exceeded 32°C (Figure 4.6).

4.4.5. Water in the source rocks

Immediately after the 2010 collapse, abundant water was observed issuing from the scarp and accumulating in a pond at its west edge. Seepage continued in the days following the landslide (Delcamp et al. 2016). The largest visible spring was on the west side of the headscarp at about 1800 m asl, near the source of the failures in 1998 and 2009. A small glacier and permanent snow field about 500 m above and to the northwest of this spring may have fed water into the slope. Seepage was also observed on the east side of the scar at about 2100 m asl, fed by the glacier sitting on the other side of the ridge crest. At the same elevation, just outside of the scar, springs in the block and ash flow deposits marked the local water table. Above this level, the upper portion of the slope is highly fractured and likely well drained.

Based on the locations of the seepage zones in the scarp, we estimate that at least 40% of the rock mass that failed (21×10^6 m^3) contained abundant water. Altered and fractured volcanic rocks can store up to 30% water by volume (Delcamp et al. 2016), leading us to estimate at maximum 6×10^6 m^3 of water was released from the rock mass upon failure.

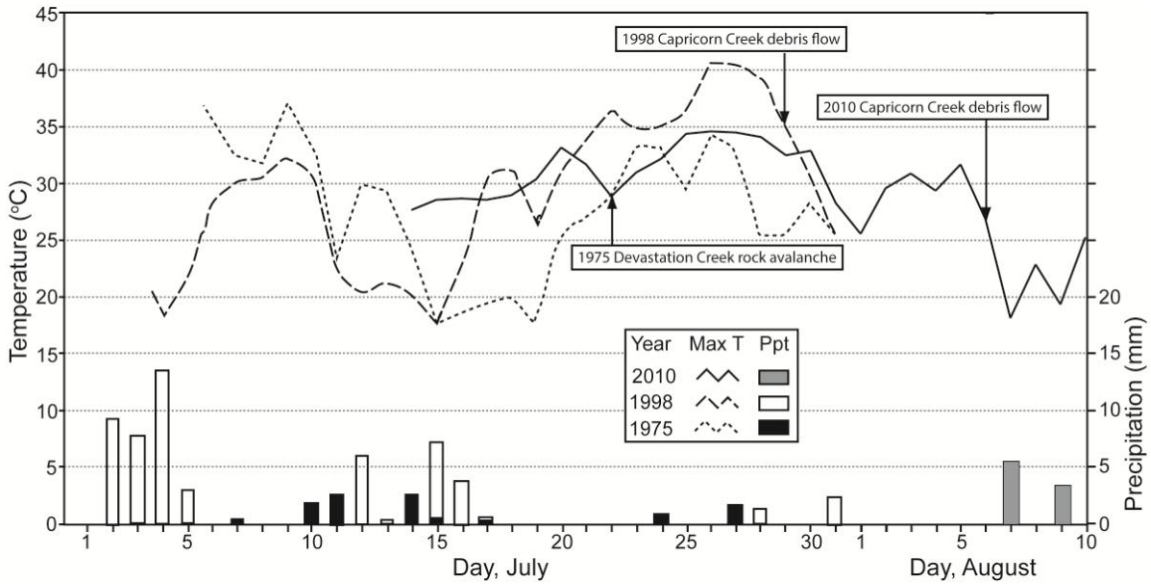

Figure 4.6. Daily maximum temperature and daily total precipitation at Pemberton over the period 1 July –10 August 1975, 1998, and 2010 in relation to landslides (modified from Bovis and Jakob 2000). The 1975, 1998, and 2010 landslides happened after sustained summer heatwaves. No significant precipitation is recorded during the three periods. Max T maximum daily temperature, Ppt precipitation.

4.5. Discussion

4.5.1. Glacier activity

The activity of Capricorn Glacier between 1948 and 2006 is consistent with that of other glaciers in the southern Coast Mountains (Koch et al. 2009). In spite of brief advances between the 1950's and 1970's, most small glaciers in this region have lost about half of their mass since the end of the Little Ice Age (Bovis and Jakob 2000; Holm et al. 2004; Koch et al. 2009). Capricorn Glacier loaded and then unloaded the south flank of Mount Meager. It eroded rock from the toe of the slope, while water from glacier and snow melt penetrated the volcanic rocks of the massif.

4.5.2. Progressive failure

Major faults that controlled the 2010 failure were already present in 1948. In the following years, displacements on these faults increased and an array of minor faults appeared, accompanied by bulging and precursory collapses at the toe of the slope (Figure 4.4). The bulging toe was eroded by meltwater, further destabilizing the slope

above. Bulging of the toe increased rock damage and likely fractured rock bridges along the future failure plane, reducing the overall factor of safety.

The detachment surface and the failure sequence were structurally controlled. The basal sliding surface projects to the thalweg of the glacially eroded Capricorn Creek valley. The base of this detachment includes volcanic breccia and basement rock. Rocks in the lower portion of the sequence are altered and saturated. The formation of a pond at the toe of the failed rock mass immediately after the event (Delcamp et al. 2016) indicates that rocks along the basal sliding surface had low permeability. It seems likely that at least part of this surface followed a boundary between altered, fractured basement rocks and less permeable, less fractured basement rocks.

The failure sequence consisted of four phases. The initial failure involved the fault-bounded W and E sectors of the lower part of the slope (Figure 4.5A). Failure of the W and E rock masses generated the two initial pulses recorded by seismographs. Allstadt (2013) extracted the directions taken by the failing rock masses from the seismic records. The direction of the first pulse was 191°; we interpret this to record failure of the W sector, which was controlled by a W-E-striking, S-dipping fault. The direction of the second pulse, which immediately followed the first, was 217°; we interpret this to record the failure of the E sector, controlled by the NW-SE-striking fault system. Volumes calculated from the geometry of the faults indicate failures of 24.6×10^6 m^3 in the W sector and 13.8×10^6 m^3 in the E sector (Figure 4.5). This result differs from estimates derived from numerical modeling (Moretti et al. 2015), which yielded 14×10^6 m^3 and 27.5×10^6 m^3, respectively, for the first and second stages of the landslide. We believe our estimates are valid as they are based on observed structures, rather than calibration from a numerical model.

The two primary failures left the upper part of the edifice unsupported, leading to a third failure above the W sector, which we estimate to have had a volume of 9.0×10^6 m^3. Two minutes later, the fourth and final phase involved collapse of the unsupported secondary peak, with a primarily vertical fall toward the SE (Allstadt 2013). A change in slope divides the secondary peak into two rock masses with individual volumes of about 2.8×10^6 m^3 (Figure 4.5A). Separate, although nearly contemporaneous, failure of these rock masses supports Allstadt's (2013) inference that this last phase consisted of two sub-failures. Our estimate of the total volume of the fourth event (5.6×10^6 m^3), however,

differs substantially from Allstadt's estimate (0.3 x 10^6 m^3), based on the magnitude of the generated force derived from seismic data.

Lithological zoning in the source area is replicated to some extent in the landslide deposit, i.e. the deposit exhibits remnant stratification (Voight et al. 1981; van Wyk de Vries et al. 2001; Valderrama et al. 2016). Highly altered rocks are found at the base of the scarp, consistent with the abundance of these rocks in the distal debris. In contrast, the peak consists of an intrusive volcanic unit, which dominates the debris at the mouth of Capricorn Creek (Roberti et al. 2017).

4.5.3. Causes and failure mechanism

Granitic and metamorphic rocks underlie Capricorn Creek valley and some of the adjacent lower slopes. Volcanic rocks unconformably overlie these basement rocks and are covered in many places by snow and ice. The condition of the basement is not known at all sites, but judging from exposures at the head of Capricorn Creek, these rocks are likely to be fractured and altered for some distance below the volcanic contact. The presence of weak rocks at the base of the volcano can have a strong destabilizing effect (van Wyk de Vries et al.2001; Cecchi et al. 2004; Detienne 2016), and large volumes (>5 x 10^6 m^3) of rock can undergo gravitation damage and displacement (Kilburn and Petley 2003).

Inflow of meltwater during the warm summer of 2010 likely elevated pore water pressures beneath the steep south slope of Mount Meager. The reduction in effective stress, coupled with the progressive removal of support at the toe by erosion and fracturing induced by slow deformation, brought the slope to catastrophic failure (two loud cracks heard by the witnesses; Guthrie et al. 2012). The weight of the overlying stratigraphic sequence pushed out the basal breccia and basement units, leading to collapse of the slope above. The first force generated by the collapse had a mainly horizontal orientation and a slow initial acceleration of 0.39 m/s^2 (Allstadt 2013). The large amount of water expelled from the moving rock mass (up to 6 x 10^6 m^3) generated a debris avalanche with a water-rich front and water-poor core (Roberti et al. 2017).

The slow initial acceleration, large volume of the failure, and presence of hydrothermally generated clays and fluids fit the slow, self-cracking model proposed by

Kilburn and Petley (2003). Large catastrophic collapses are generally preceded by a period of accelerating deformation due to internal fracturing that is enhanced by the presence of fluids (Kilburn and Petley 2003). Hence, in the case of the 2010 Mount Meager failure, there was no singular distinct triggering event, but rather a combination of destabilizing factors, including the long summer heatwave that contributed, over time, to the collapse. The increase in the number and size of faults, and the precursory failures at the toe of the slope in the years prior to the landslide suggest that slow acceleration could have been detected using monitoring methods such as photogrammetry, LIDAR, InSAR, in-situ strain meters, or GPS. If so, it might have been possible to predict the approaching failure by extrapolating the linear inverse-deformation rate trend (Kilburn and Petley 2003; Rose and Hungr 2007; Carlà et al. 2017; Loew et al. 2017).

Alpine glaciers around the world are receding due to climate warming (Liggins et al. 2013). In many mountain ranges, most glaciers will disappear by the end of this century (DeBeer and Sharp 2007; Schieffer et al. 2007; Clarke et al. 2015). Glacier retreat will further destabilize steep slopes (Evans and Clague 1994; Huggel et al. 2013) and provide an additional source of water for elevating pore pressures within unstable rock masses, both of which can cause marginally stable slopes to collapse.

Evidence of deep-seated gravitational deformation is widespread on flanks of the Mount Meager massif (Bovis 1990; Read 1990; Jordan 1994; Van der Kooij and Lambert 2002; Roberti et al. 2015). Examples are shown in Figure 4.7, and include the eastern flank of Devastation Creek valley (Figure 4.7A), the western flank of Plinth Peak (Figure 4.7B), and the western flank of Affliction Creek valley (Figure 4.7C). Many of these slowly deforming slopes have retreating glaciers at their toes. The 1931 and 1975 Devastation landslides (ca. 3×10^6 m^3, Carter 1932; and ca. 26×10^6 m^3, Mokievsky-Zubok 1977; Figure 4.7A) are examples, and may represent similar precursors of a larger flank collapse like the 2010 failure. The estimated areas of instability are 3.6×10^6 m^2 at Devastation Creek, 2.7×10^6 m^2 at Plinth Peak, and 1.3×10^6 m^2 at Affliction Creek. Assuming an average depth of failure of 100 m for these gravitational slope instabilities (Kilburn and Petley 2003), volumes of potential future failures are in the range of 3.6×10^6 m^3, 2.7×10^6 m^3, and 1.3×10^6 m^3 for Devastation Creek, Plinth Peak, and Affliction Creek, respectively. Volcanic landslides of this size could travel tens of kilometers downstream and potentially impact settled areas in Pemberton Meadows

(Friele and Clague 2004; Simpson et al. 2006). The continuing deformation of these large sagging rock masses can be monitored and used to forecast their possible catastrophic failure. Given that the risk of injury and death downstream has been deemed unacceptable (Friele et al. 2008), it would seem prudent to implement slope displacement monitoring at Mount Meager.

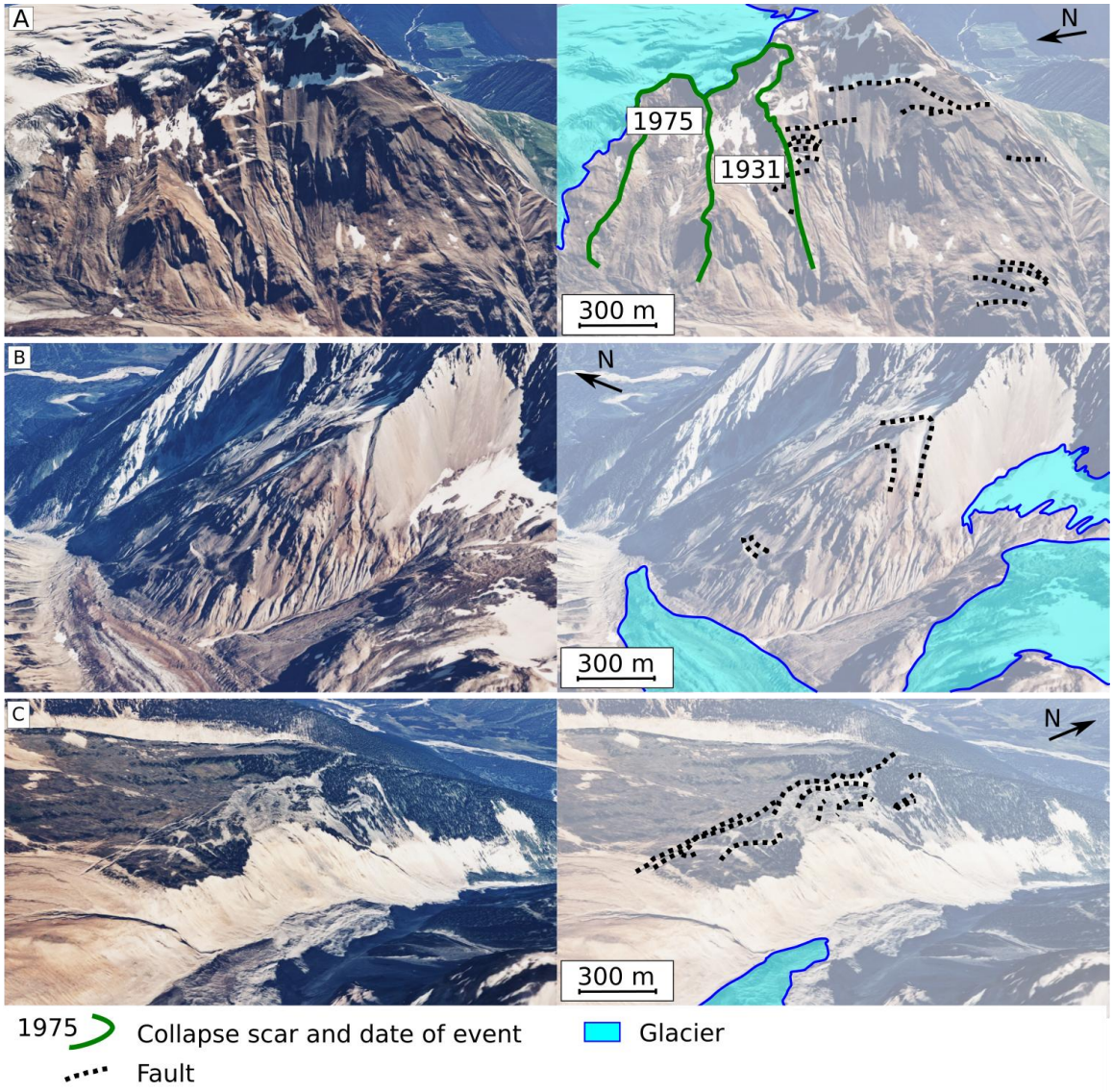

Figure 4.7. Continuing instability on the Mount Meager massif. A) East flank of Devastation Creek valley. B) West flank of Plinth Peak. C) West flank of Affliction Creek valley.

4.6. Conclusions

The south flank of Mount Meager experienced deep-seated gravitational deformation for decades prior to its final catastrophic collapse in August 2010. We have documented pre-event progressive deformation of the slope using historical vertical airphotos to provide insight into the causes of the collapse. In particular, we draw the following conclusions:

1. After substantial retreat in the early 20th century, Capricorn Glacier advanced between 1964 and 1981 and then rapidly retreated from 1990 to 2006.

2. Major gravitationally generated faults were already present in 1948. They continued to develop, and other cracks formed at the toe of the slope, manifested by sagging and bulging, until the time of the landslide.

3. Lithologies involved in the collapse are, from bottom to top, hydrothermally altered basement rocks and volcanic breccias, block and ash deposits, and rhyodacitic intrusive rocks.

4. The 2010 collapse involved the entire volcanic edifice from the basement to the top of a secondary peak. The collapse started with failure of the basement and basal breccia units. The remaining unsupported block and ash deposits failed next, followed by the intrusive rocks at the peak.

5. The rock mass that failed in 2010 was partially saturated with about 6 x 10^6 m^3 of water. Immediately after collapse, this water was available to transform the landslide into a highly mobile debris avalanche with multiple rheologies.

6. The volume of 2010 failure is 53 ± 3.8 x 10^6 m^3. This volume is a refinement of a previous estimate and confirms that the event is the largest historic landslide in Canada.

7. Volcanic rocks at Mount Meager had been weakened by hydrothermal alteration and by fracturing caused by deep-seated gravitational deformation. The flank was also weakened by glacial cycles and left unsupported by glacier retreat and toe erosion. The increase in pore water pressures resulting from ice and snow melt during the warm summer of 2010 triggered the landslide.

8. Other very large (>100 x 10^6 m^3), slowly deforming instabilities are present on the Mount Meager massif. The same destabilizing factors at play in the lead-up to the 2010 landslide are likely to accelerate ongoing deformation and cause more large landslides.

Using the event sequence documented here, and with dedicated monitoring, deformation can be tracked and catastrophic failures forecast. Volcanic landslides of this volume can impact populated areas downvalley, resulting in an unacceptable level of risk. We recommend implementation of slope displacement monitoring at Mount Meager.

4.7. Acknowledgments

We thank Rick Guthrie and an anonymous journal reviewer for their helpful comments on a draft of the paper. Financial support for the research was provided by NSERC Discovery Grants to Clague and Ward, and by the "End of an Arc: The Remarkable Life and Death of a Volcanic Arc" project, a French-Canadian partnership. Discussion with Andreas Kaab and Matt Lato helped us to formulate some of our SfM ideas.

Chapter 5. Landslides and glacier retreat at Mount Meager volcano: hazard and risk challenges [4]

Gioachino Roberti[1,2], Brent Ward[2], Benjamin van Wyk de Vries B.[1], Giacomo Falorni[3], Brian Menounos[4], Pierre Friele[5], Glyn Williams-Jones [2], John J. Clague[2], Luigi Perotti [6], Marco Giardino [6], Geidy Baldeon[3], Stefano Freschi[6]

(1) Université Clermont Auvergne, CNRS, IRD, OPGC, Laboratoire Magmas et Volcans, Aubiere Cedex, France (2) Earth Sciences Department, Simon Fraser University, Burnaby, British Columbia, Canada. (3) TRE-ALTAMIRA Inc., Vancouver, British Columbia, Canada (4) Geography Program and Natural Resources and Environmental Studies Institute, University of Northern British Columbia, Prince George, British Columbia, Canada (5) Cordilleran Geoscience, Squamish, British Columbia, Canada (6) Earth Sciences Department, GeoSitLab - GIS and Geomatics Laboratory, University of Torino, Torino, Italy

5.1. Abstract

Mount Meager is a glacier-clad volcanic complex in southwest British Columbia. In the summer of 2010, melting snow and ice caused by warm weather triggered the collapse of 53 Mm^3 of rock and debris from Mount Meager's south flank, generating the largest historic landslide in Canada. In 2016 fumaroles formed ice caves in one of its glaciers, raising concern about the potential for eruptive activity. Following these events, we carried out a geomorphic study of the volcano. Employing satellite-based differencing methods, we measured movements on previously identified unstable slopes and documented the recent retreat of glaciers on the volcanic complex. It is likely that glaciers will continue to thin and recede, and that slopes will continue to deform, possibly leading to catastrophic collapses similar to the 2010 event. Previous work concluded that the level of risk posed by large landslides at Mount Meager is unacceptable. In spite of this conclusion, little has been done to manage the risk by local or provincial

[4] This paper has been published in 2018 in the *Geohazard 7 conference proceedings*: Roberti G, Ward B, van Wyk de Vries B, Falorni G, Menounos B, Friele P, Williams-Jones G, Clague JJ, Perotti G, Giardino M, Baldeon, G, and Freschi S (2018) Landslides and glacier retreat at Mount Meager volcano: hazard and risk challenges. *Geohazard 7 Engineering Resiliency in a Changing Climate* June 3 - 6, 2018, Canmore, Canada

governments over the past decade. With new hydropower infrastructure near the volcano and continued population growth in the Lillooet River valley downstream, it is clear that the landslide risk is increasing.

5.2. Introduction

Mount Meager is a volcanic complex in southwest British Columbia, Canada, about 150 km north of Vancouver and 65 km northwest of the town of Pemberton. The volcanic complex formed over the past two million years (Read 1979) and last erupted about 2360 years ago (Clague et al. 1995; Hickson et al. 1999). Today, it hosts an active hydrothermal system and fumarole field (Venugopal et al. 2017) and it is a site of shallow earthquakes (Friele et al. 2008). It was periodically covered by glaciers during the Pleistocene Epoch (Clague and Ward 2011), and presently supports alpine glaciers (Holm et al. 2004; Koch et al. 2009). The volcano has a long record of landslides (Friele et al. 2008), stemming from extensive hydrothermal alteration of the volcanic rocks, glacial erosion, and recent glacier retreat (Holm et al. 2004; Roberti et al. 2017c). The most recent large landslide, in 2010, is the largest in Canadian history (Roberti et al. 2017c). Glacier retreat has also exposed hydrothermal vents at Mount Meager, affecting water circulation, temperature, and chemistry. In 2016, fumaroles formed ice caves in Job Glacier on the north side of Mount Meager. The basin of Job Creek is also one of the most unstable catchments on the massif and the source of some of its largest (10^8-$10^9 m^3$) prehistoric landslides (Friele et al. 2008).

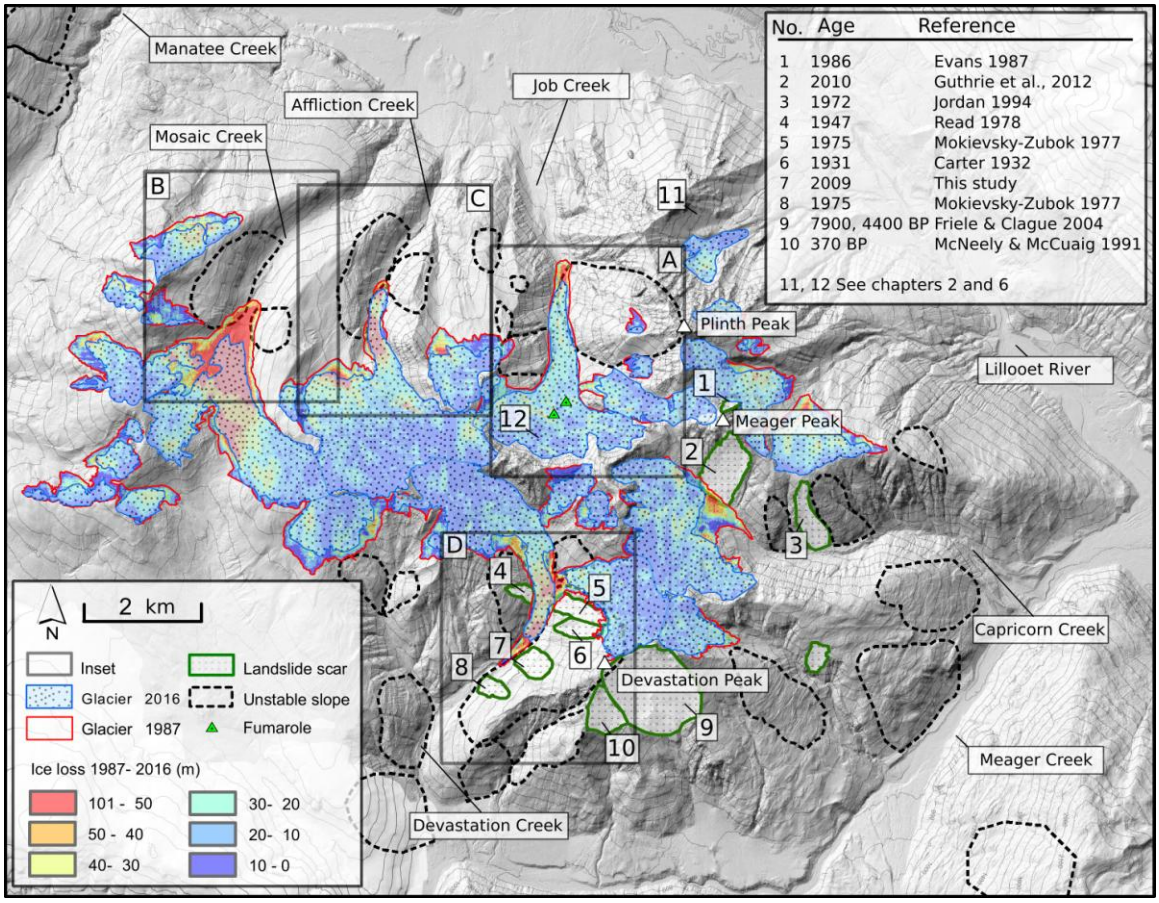

Figure 5.1. Overview of the Mount Meager volcanic complex, showing glaciers, ice loss, fumaroles, past landslides, unstable slopes. A) Figure 5.2. B) Figure 5.3. C) Figure 5.4. D) Figure 5.5.

Many studies have focused on the stability of Mount Meager (Jordan 1994; Jakob 1996; Friele and Clague 2004; Holm et al. 2004; Friele et al. 2005; Simpson et al. 2006). Friele et al. (2008) quantified the debris flow risk to residents and infrastructure in the Lillooet river valley, 32-75 km downstream from the volcano. In light of international standards (Leroi et al. 2005), they deemed the risk to be unacceptable, but little mitigation by local authorities (e.g., education, land zoning) has been done. Meanwhile, two hydropower plants have been built at the foot of the volcano, and a new access road for forestry operations in Meager Creek valley, just south of Mount Meager, is being constructed. There are active mining operations on the east flank of the volcano, and the population in the Lillooet River valley is rapidly growing (Statistics Canada 2017).

Although previous researchers have recognized the importance of glacier retreat on slope stability at Mount Meager, we are far from a complete understanding of the effects of deglaciation on the volcanic system, notably in terms of stability, hydrothermal

circulation and relations between the two. Here we present a geomorphic study of the Mount Meager Volcanic Complex, with a focus on major slope instabilities and recent glacier retreat. We discuss volcanic and landslide hazards in relation to a previous risk analyses (Friele et al. 2008). Finally, we suggest a monitoring framework for the volcanic massif.

5.3. Methods

We used remote sensing methods and site-specific field work to map and describe landslide and glacial activity at Mount Meager. We applied Structure from Motion (SfM) photogrammetric methods to British Columbia Provincial Government vertical aerial photographs to produce orthophotos of the volcano. Lidar (Light detection and ranging) data were acquired in 2015 and 2016, from which we produced an up-to-date digital elevation model (DEM). Interferometric Synthetic Aperture Radar (InSAR) analysis was carried out to identify unstable slopes and constrain deformation rates. Comparison of the 2015-2016 Lidar-derived DEM and a DEM resulting from the 1987 British Columbia Terrain Resource Inventory Map (TRIM) allowed us to document nearly three decades of glacier retreat on the volcanic massif.

5.3.1. Structure from Motion (SfM)

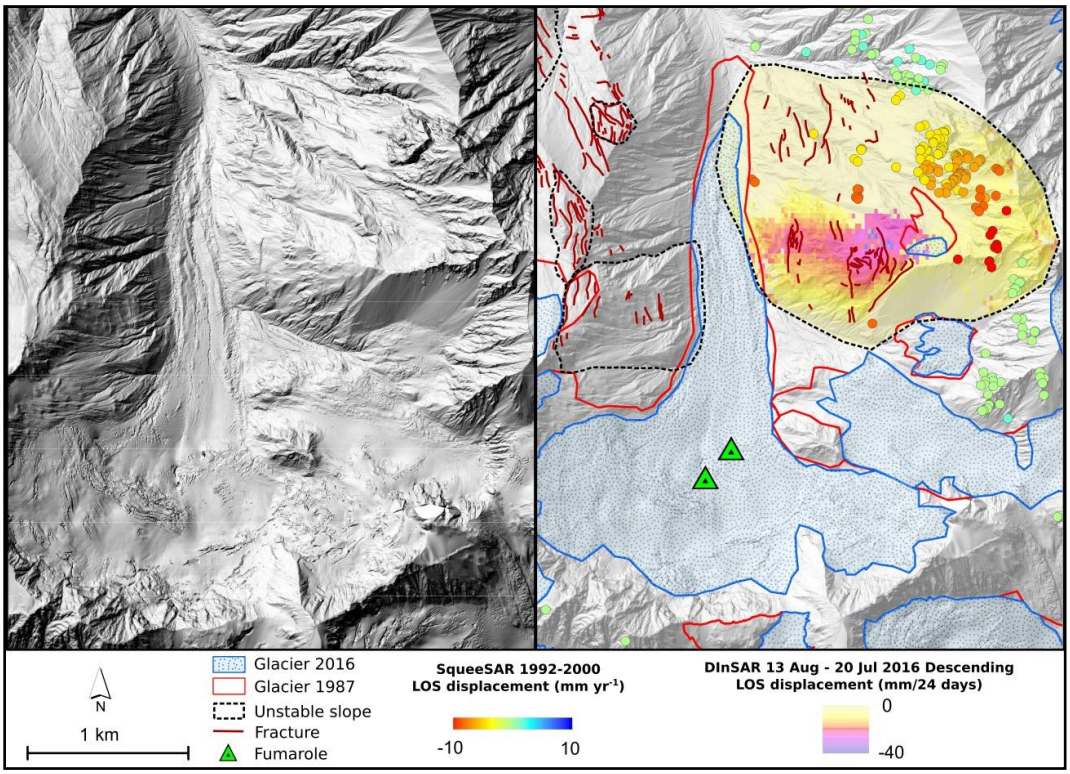

Figure 5.2. Job Creek valley (Inset A, Figure 5.1), showing past and present glacier outlines, unstable slopes, fractures, and fumaroles. SqueeSAR displacement data, and DInSAR deformation map are also shown. The volume estimate of the unstable slopes is 10^8-10^9 m^3.

SfM is a photogrammetry technique based on computing vision algorithms (Carrivick et al. 2016). The use of SfM has rapidly increased in the last few years, rivaling Lidar as a tool for acquiring high-resolution topography (Westoby et al. 2012; Fonstad et al. 2013). SfM is generally applied to photographs taken with a hand-held camera or from an Unmanned Aircraft Vehicle (UAV) (James and Robson 2012). In comparison, few studies have explored the application of Structure from Motion (SfM) to digitized historical vertical aerial photographs (Gomez et al. 2015; Bakker and Lane 2016; Roberti et al. 2017b). In this study we processed 114 British Columbia Government vertical aerial photographs acquired in the summer of 2006 (see Roberti et al. 2017c for details on data processing). Part of this dataset was used by Roberti et al. (2017c) to constrain slope deformation prior the 2010 Mount Meager landslide and constrain the volume of the landslide.

5.3.2. Lidar

Aerial Lidar technology enables acquisition of high-resolution topographic data over large areas. Vegetation can be automatically removed to produce 'bare-earth' DEMs suitable for geomorphic analysis. Lidar covering the Mount Meager Volcanic Complex was acquired during summer 2015 and 2016 with a Riegl VQ-580 scanner equipped with an Applanix POS AV910 inertial measurement unit/GNSS receiver for geolocation and orientation of the scanner relative to the surveyed terrain. The Southern sector of the volcano was surveyed in 2015 whereas the Northern half of the volcano was surveyed in 2016. Point cloud density averaged 2.57 points m^{-2}, and we generated 1 m terrain models from these data. Slope, aspect and shaded relief maps were then generated from the DEM.

5.3.3. Interferometric Synthetic Aperture Radar

Satellite-based InSAR methods allow measurement of displacement with millimetric precision over large areas (Ferretti et al. 2015). The first radar satellites were launched in the 1990's and the number of available satellite systems continues to increase. In this study, we used freely available radar satellite images from the European Space Agency (ESA) ERS 1-2 and Sentinel-1 constellations. The ERS 1-2 dataset consists of 33 images spanning the period June 3rd 1992 to September 23rd 2000 with a nominal 35-day revisit frequency. The imagery was acquired from satellite track 471, along a descending orbit with a 24.9° look angle and 5.6 cm wavelength. Acquisitions from the Sentinel-1 satellites started in late 2014 and are currently continuing with a 12-day revisit frequency. Three separate datasets are being acquired from both ascending and descending orbits.

We processed the ERS dataset with the SqueeSAR algorithm (Ferretti et al. 2011), which identifies point targets (Permanent Scatterers, PS) and distributed scatterers (DS), to produce a point cloud with high precision measurements of displacement. The analysis produced 3,182 measurement points (MP) over the 313 km^2 of Mount Meager area, leading to a point density of 10 MP km^{-2}.

The Sentinel imagery is being used to generate differential interferograms (DInSAR) and produce displacement maps over the Mount Meager massif. DInSAR

identifies changes in signal phase between pairs of SAR images and, coupled with a high-resolution DEM, allows the measurement of ground displacement that occurs in the period between the two image acquisition dates with ± 10 mm precision. As InSAR is hindered by the presence of vegetation and snow cover the best results are obtained by comparing images acquired during the summer or early fall. This approach provides the best results in terms of spatial coverage but does not allow detection of deformation over long periods of time nor does it provide the deformation history that can be obtained with the SqueeSAR approach.

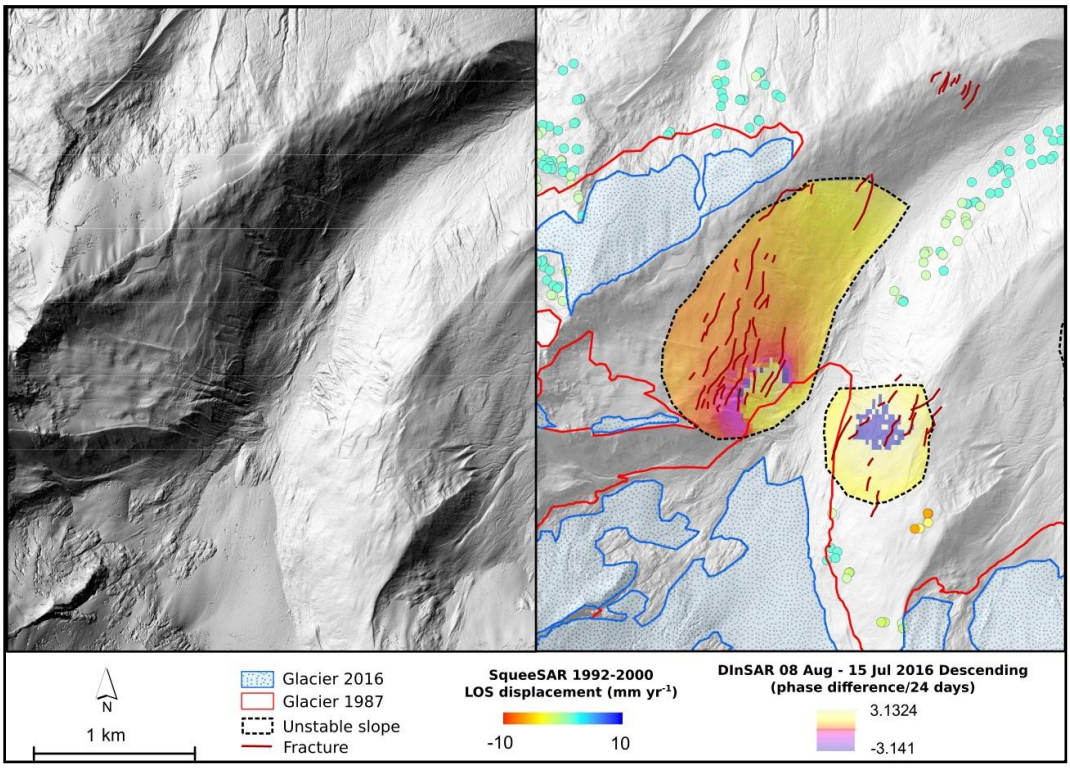

Figure 5.3. Mosaic Creek valley (Inset B, Figure 5.1), showing past and present glacier outlines, unstable slopes and fractures. SqueeSAR displacement data, and DInSAR phase difference are also shown. The volume estimate for the unstable west and east flanks is 10^8-10^9 m^3.

5.3.4. Landslide mapping

We identified unstable slopes and mapped scarps, trenches, and fractures on the 2006 orthophoto and the 2015-2016 Lidar DEM. InSAR analysis constrained the motion on some of the unstable slopes and allowed us to identify other instabilities with less evident geomorphic expression. We have estimated the volumes of these instabilities

from their geometry, lithology, and an assumed minimum depth of failure of 100 m (Kilburn and Petley 2003).

5.3.5. Glacier changes 1987-2016

We generated a DEM-of-difference (DoD) by comparing the 1987 Trim and the 2015-2016 Lidar DEMs. DoD analysis allowed us to detect slope movements and measure glacier extent and mass balance. To assess possible DoD errors, we looked at elevation differences in stable areas where the change should be zero. The difference in these areas yielded a σ_{DoD} of 10.7 m. To assess possible errors in volumes we applied the formula $\sigma_{Vol} = \sigma_{DoD} d^2(n)^{0.5}$(Lane et al. 2003), where *d* is the size of the raster cell and *n* the number of cells. The area of ice cover is represented by 331,537 pixels (*n*) of 18.3-m size (*d*). The resulting volumetric uncertainty, σ_{Vol} , is 0.002 km^3. This would be considered a minimum error because of issues related to digitization and inaccuracy in the TRIM data.

5.4. Results

5.4.1. 1987-2016 DEM comparison

Comparison of the 1987 and 2015-2016 DEMs indicated a total ice loss of 1.3 ± 0.002 km^3. Present ice cover on the massif is about 28 x 10^6 m^2. Most of the ice loss is in glacier ablation zones and is manifested by significant retreat of glacier termini (Figure 5.1). Individual glacier termini have retreated, on average,15 m yr^{-1}; some small glaciers and snowfields disappeared between 1987 and 2016 (Figure 5.1). Job Glacier downwasted up to 50 m just downflow from an ice fall, near the firn line, where in 2016 fumaroles formed ice caves. Its present area is 2.7 ×10^6 m^2.

Comparison of the two DEMs revealed a previously unidentified landslide area. The DoD shows loss of mass in the east fork of Devastation Creek valley (7 in Figure 5.1) and accumulation of material on the valley floor. To better constrain the date of this slope failure, we analyzed available airphotos and optical satellite imagery, and found that the landslide occurred between July 27 th and August 27th 2009 (Image courtesy of Planet). The area of the failure is 0.2×10^6 m^2, and its volume is estimated to be in the range 10^6 - 10^7 m^3.

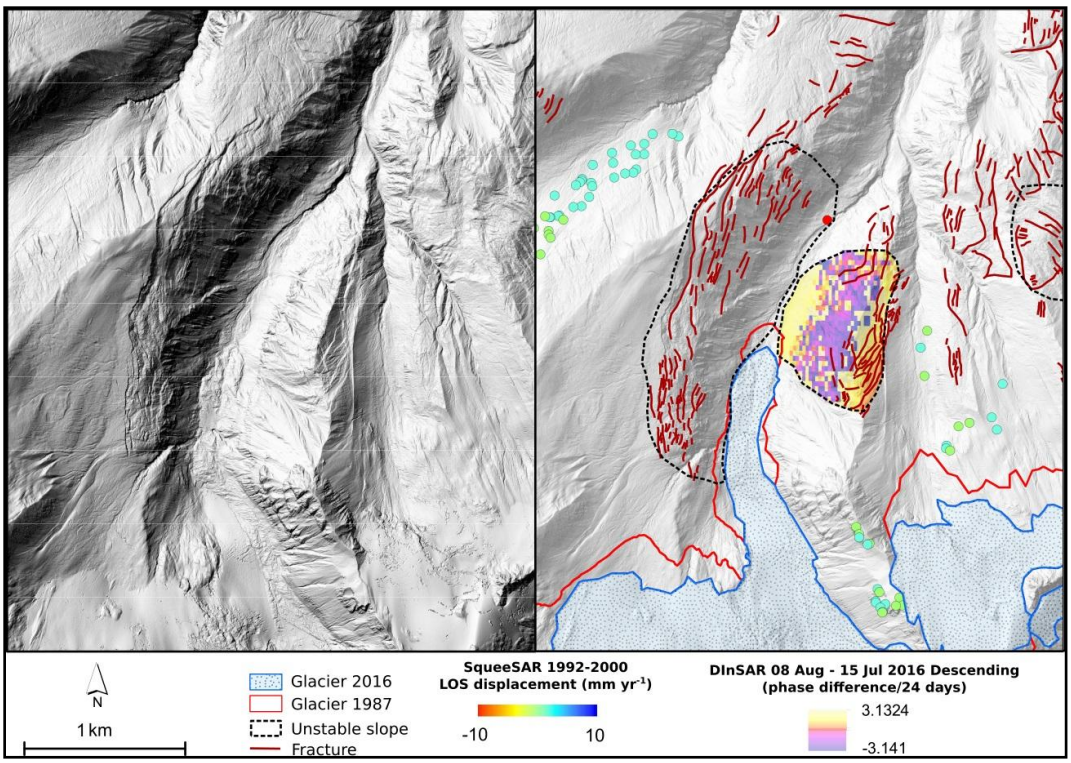

Figure 5.4. Affliction Creek valley (Inset C, Figure 5.1), showing past and present glacier outlines, unstable slopes, fractures, SqueeSAR displacement data, and DInSAR phase difference. The volume estimate is of 10^8-10^9 m^3 and 10^7-10^8 m^3 for the west and east flank.

5.4.2. Landslide inventory and InSAR deformation data

Most slopes on the Mount Meager Volcanic Complex show signs of instability. We identified 27 large (>5×10^5 m^2) potential landslide sites (Table 5.1), characterized by cracks, counter scarps, bulging profiles, and small collapses. Cracks generally are parallel to valley axes and exist from the base of the slopes to ridge crests. Of these 27 sites, nine have been deglaciated recently; the toes of the slopes were covered by glacier ice in 1987, but were largely ice-free in 2016. Eight sites are >1700 m asl, where permafrost may be present. Ten sites are at lower elevation in vegetated terrain. We estimate that 12 sites could generate 10^8-10^9 m^3 landslides, seven could generate 10^7-10^8 m^3 landslides, six 10^6-10^7 m^3 landslides, and two 10^5-10^6 m^3 landslides (Table 5.1).

SqueeSAR analysis of the 1992-2000 ERS data, shows motion at four sites (Table 5.1). The displacement is along the satellite line of sight (LOS) and negative values indicate motion away from the satellite along the 24.9° look angle. LOS displacements of up to -17 mm yr^{-1} were found on the east flank of Job Creek (Inset A in

Figure 5.1, Figure 5.2). Displacements on the north side of Meager Creek valley are up to -12 mm yr^{-1}, and the southeast side of the valley up to -8 mm yr^{-1}. Displacements on the east side of Mosaic Creek are up to - 7 mm yr^{-1} (Inset B in Figure 5.1, Figure 5.3).

The Sentinel-1 DInSAR data shows motion at eight sites (Table 1). Displacement occurs for some sites throughout the summer (July-September), while others only move at the beginning of the summer season (July-August). Specifically, the west and east flanks of Mosaic Creek (Inset B in Figure 5.1, Figure 5.3) show movement fringes in the July and August DInSAR results, but not in the August-September period. The east flank of Affliction Creek (Inset C in Figure 5.1, Figure 5.4), the east flank of Job Creek (Inset A in Figure 5.1, Figure 5.2), and the east flank of Devastation Creek (Inset D in Figure 5.1, Figure 5.5), move throughout the summer (July-September). The east flank of Devastation Creek valley is the largest unstable slope we identified (3.6×10^6 m^2); the second largest unstable slope is the east flank of Job Creek (2.7×10^6 m^2) (Table 5.1). We converted the deformation at Job and Devastation creeks from phase information to line-of-sight displacement. Displacements at Job Creek are up to -34±10 mm and at Devastation are up to -36±10 mm over a 24-day period in July-August 2016. Collapse of either of these slopes could generate a 10^8-10^9 m^3 landslide.

Table 5.1. Inventory of unstable slopes on the Mount Meager volcano.

Basin	Area (m^2)	Volume (m^3)	Deglaciated since 1987?	Motion	
				SSAR	DSAR
Devastation	3.6×10^6	10^8-10^9	Yes	-	✓
Job	2.7×10^6	10^8-10^9	Yes	✓	✓
SE Meager	2.2×10^6	10^8-10^9	No*	✓	-
Meager	2.1×10^6	10^8-10^9	No	-	-
Meager	1.6×10^6	10^8-10^9	No	-	-
Devastation	1.5×10^6	10^8-10^9	No	-	-
Meager	1.5×10^6	10^8-10^9	No	-	-
Mosaic	1.4×10^6	10^8-10^9	Yes	-	✓
Affliction	1.3×10^6	10^8-10^9	Yes	-	-
Manatee	1.3×10^6	10^8-10^9	No	-	-
Devastation	1.1×10^6	10^8-10^9	No	-	-
Manatee	1.0×10^6	10^8-10^9	No	-	-
Devastation	0.8×10^6	10^7-10^8	Yes	-	✓
N Meager	0.8×10^6	10^7-10^8	No *	✓	-
Capricorn	0.7×10^6	10^7-10^8	No	-	-
Meager	0.6×10^6	10^7-10^8	No	-	-
Job	0.6×10^6	10^7-10^8	Yes	-	-
Affliction	0.5×10^6	10^7-10^8	Yes	-	✓
Devastation	0.5×10^6	10^7-10^8	No *	-	-
Mosaic	0.4×10^6	10^6-10^7	Yes	✓	✓
Lillooet	0.4×10^6	10^6-10^7	No*	-	-
Capricorn	0.3×10^6	10^6-10^7	No	-	-
Devastation	0.3×10^6	10^6-10^7	Yes	-	✓
Job	0.3×10^6	10^6-10^7	No*	-	-
Devastation	0.3×10^6	10^6-10^7	No*	-	✓
Job	0.1×10^6	10^5-10^6	No*	-	-
Job	5×10^5	10^5-10^6	No *	-	-

Notes: Volume estimates are based on geometry, lithology. and a minimum depth of failure of 100 m. SSAR = SqueeSAR. DSAR = DInSAR. SE= southeast. N = north. *Above vegetation limit, possible permafrost.

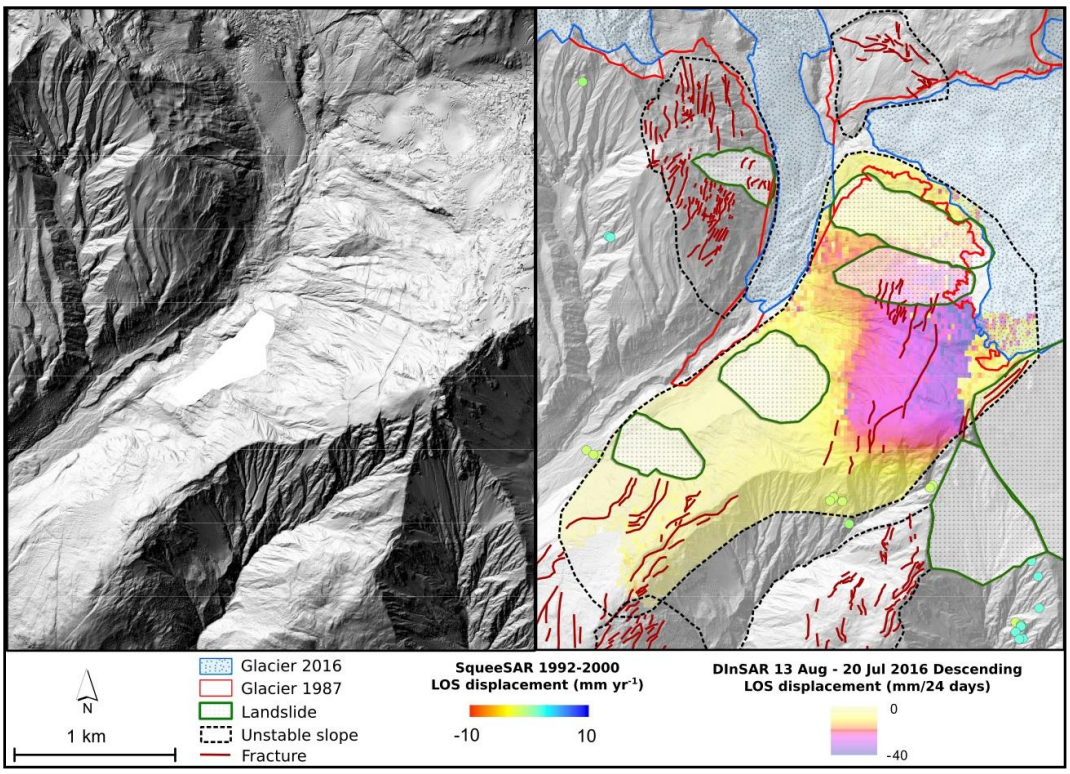

Figure 5.5. Inset D in Figure 5.1. The Devastation Creek valley showing past and present glacier outlines, unstable slopes, fractures, SqueeSAR displacement data, and DInSAR deformation map. The volume estimate is of 10^8-10^9 m^3. LOS = line of sight.

5.5. Discussion

5.5.1. Glacial retreat at Mount Meager volcano

The Mount Meager volcano has lost ~1.3 km^3 of ice since 1987. The scale of deglaciation is comparable to that elsewhere in the Coast Mountains and in other high mountains around the world. If climate continues to warm, as is likely, most glaciers at Mount Meager will have disappeared by the end of this century (Bolch et al. 2010; Clarke et al. 2015).

5.5.2. Volcano-ice interaction hazards

In 2016 fumaroles were observed emitting gases from Job Glacier. The fumaroles have probably been active beneath the glacier for a long time, but only recently has the ice thinned enough that the hot gases could reach the surface of the glacier. The hazard posed directly by the gases is localized to the ice caves and

immediate surroundings. The possibility of an eruption from the volcano is unknown, but ice melt can cause landslides and decompression from both ice loss and landslides might destabilize hydrothermal and magmatic systems and trigger an eruption (*cf* Waythomas 2012). Even a small eruption would rapidly melt a large amount of Job Glacier ice, generating a long runout debris flow. A tragic example of such an event is the 1985 eruption of Nevado del Ruiz in Colombia. A small eruption beneath the summit ice-cap caused a debris flow that killed more than 22,000 people over 60 km from the volcano (Herd et al. 1986). At present no volcanic or volcano-ice interaction hazard assessments have been made for Mount Meager.

5.5.3. Landslide hazards

Of the 27 slopes with signs of instability that we identified, nine slopes have been recently deglaciated and eight are at elevations where permafrost degradation is likely to be happening. Glacier retreat and permafrost thaw could destabilize these slopes. Meltwater from snow and ice can infiltrate slopes and increase porewater pressures, conditioning them for catastrophic collapse, as happened at Mount Meager in 2010. Hetherington (2014) conducted edifice-scale slope stability analysis using numerical modeling and showed that that even small changes in water supply could trigger deep-seated failure. The calculated factor of safety (FOS) showed that many sites are at incipient failure.

Collapses of these slopes can generate highly mobile, far-reaching debris flows. Five of the unstable slopes we identified could generate a 10^8-10^9 m^3 debris flow that might reach populated areas in the Lillooet River valley (four past documented events: 2600, 4400, 6250, 7900 BP) Another five slopes could generate landslides with volumes of 10^7-10^8 m^3 that might extend some distance down Lillooet valley (three past documented events: 2170 BP, 1975, 2010). Five more could generate a 10^6-10^7 m^3 flow that could reach downstream of the Meager-Lillooet confluence (1860, 870, 370 BP; 1931, 1998), and two sites have volumes of 10^5-10^7 m^3 and would likely be confined in the proximal valleys of Meager Creek and upper Lillooet River. See Simpson et al. (2006) for the inundation zones extents and Friele et al. (2008) for a compilation of past events. Ten slopes are forested and have not been directly affected by recent deglaciation; we consider these slopes less likely to generate catastrophic collapses. Seven of them have volumes in the 10^8-10^9 m^3 range, two in the 10^7-10^8 m^3 range, and

one in the 10^6-10^7 m^3 range. Three of the vegetated slopes (southeast Meager and east Manatee valley sides) are not underlain by volcanic rocks.

5.5.4. InSAR deformation data

ERS SqueeSAR data provided valuable historic information spanning an 8-year period while the Sentinel-1 DinSAR data provided short-term data during the summers of 2015 and 2016. The ERS analysis showed motion on four slopes, with rates up -17 mm yr^{-1} at Job Creek. Analysis of Sentinel-1 data showed motion on eight slopes, including deformation of about 35 mm over a 24-day period on the east flanks of Job and Devastation creeks (Figure 5.2 and 5.5). The Job and Devastation Creek slopes are of particular concern as they have been recently deglaciated and have large open fractures indicative of precursory collapse. Our catalogue of deforming slopes is likely incomplete; more slopes might be deforming and be in critical condition but are not visible due to adverse satellite look angles, the presence of vegetation or snow cover.

5.5.5. Risk from landslides and volcanic activity at Mount Meager

Friele et al. (2008) deemed the risk of loss of life from a large landslide from Mt, Meager to be unacceptable. This conclusion was based on an analysis of the frequency and size of past landslides and their runout and combined with a consideration of acceptable risk criteria for landslides in other jurisdictions. In view of the history of landslides on the massif, including the 2010 landslide, future collapses are certain. This inevitability must be considered in view of the recent increase in infrastructure near Mount Meager and the increase in population and related infrastructure in the Pemberton area. Today, two hydropower plants, a new access road, and mining operations are in the range of 10^6-10^7 m^3 debris flows. Homes, roads, and bridges are in the range of 10^9 m^3 debris flows. The only active risk mitigation strategy is restriction of public and industrial users from upper Lillooet River valley during high and extreme weather conditions (Cordilleran Geoscience 2012). There is a water-level gauge on the Lillooet River 35 km downstream from the volcano, which might alert residents to sudden changes in the discharge of the river, such as a drop in flow caused by formation of a landslide dam. However, this gauge is remote from the proximal zone of a potential catastrophic slope failure, resulting in a warning delay of several hours. Furthermore, different mechanisms that might cause a rapid increase in river level (e.g. normal flood

or a surge) cannot be easily resolved. Therefore, there is no early warning system or defensive structures that might reduce the risk to the population downstream of Mount Meager.

5.5.6. Slope monitoring and early warning system

Although non-eruptive volcanic landslides are difficult to predict, Roberti et al (2017c) showed that the 2010 Mount Meager landslide should not have been unexpected. Signs of deformation were evident on the pre-failure slope, and slope monitoring might have allowed the landslide to have been forecast (Intrieri et al. 2017). In this study, we have identified additional unstable slopes and have measured displacement rates with InSAR techniques. To reduce the risk of injury and loss of life from landslides at Mount Meager, we recommend the establishment of slope deformation monitoring and an early warning system. Both can be achieved using satellite InSAR. InSAR allows precise displacement monitoring over large areas in near-real time, making the technique suitable for an early warning system (Ferretti et al. 2015; Intrieri et al. 2017). The availability of free Sentinel imagery with near worldwide coverage has the potential to significantly boost this type of application. The main limitations in the use of InSAR are slope geometry and the loss of coherence in areas covered by snow and forest. Most of the slopes of concern at Mount Meager, such as the east flank of Job Creek valley and the east flank of Devastation Creek valley, have favourable orientations for displacement detection (E-W). Despite the area being covered by snow for most of the year, deformation can be detected during the summer season, when movements are expected to be greatest and when the human presence near Mount Meager is more common. Other remote and ground-based methods can be integrated into an InSAR monitoring system. Optical satellite imagery and aerial Lidar data can provide information on deformation rates in areas of unsuitable InSAR geometry. Photogrammetry, Lidar, and ground-based GPS can be employed to monitor slopes considered to be most hazardous. Automated photogrammetric stations are inexpensive and can be integrated with periodical (weekly/monthly) terrestrial Lidar surveys. Direct GPS slope instrumentation is an established technique, but in this case involves a high risk of instrument loss. Sensors could also be installed in the major valleys (Devastation, Job, Capricorn, Mosaic, and Affliction) and in Lillooet River valley

to provide warnings of collapses. Numerical modelling can be applied to better constrain the possible runouts and to develop hazard maps.

5.6. Conclusions

DEMs, Lidar, SfM, InSAR analysis, and field work allowed us to document glacier retreat and slope instability on the Mount Meager volcanic complex. We draw the following conclusions:

1. Mount Meager volcano has lost ~1.3 km^3 since 1987. Present-day glacier cover is 28×10^6 m^2

2. In 2016 fumaroles were observed in Job Glacier. Although the hazard from volcanic gases is localized, an eruption under the glacier would melt a large volume of ice and generate far-reaching debris flows. Further studies are needed to better constrain the possibility of a volcanic eruption at Mount Meager.

3. We have documented 27 large (>5×10^5 m^2), potentially unstable sites, 17 of which have become ice-free recently. Fifteen of the slopes have volumes >10^6 m^3; if they were to fail catastrophically, infrastructure near the volcano might be affected. Ten have volumes >10^7 m^3; their failure might impact populated areas downstream.

4. InSAR is an invaluable resource to study slope instabilities. The 1992-2000 ERS SqueeSAR analysis identified ground motion at four sites. The east flank of the valley of Job Creek moved at -17 mm yr^{-1} over the 8-year period. 2015 and 2016 Sentinel-1 DInSAR data highlighted motion at eight sites. Among these, the east slopes of Job Creek and Devastation Creek valleys moved up to -34±10 mm - 36±10 mm, respectively, over a 24-day period during the summer of 2016. We consider these slopes to be in a critical condition for failure.

5. The risk of loss of life was deemed unacceptable in 2008. Today, in a first-order estimate, the risk has increased.

6. An InSAR-based slope monitoring and early warning system should be implemented at Mount Meager volcano to mitigate the high level of risk.

5.7. Acknowledgments

Financial support for the 2015 Lidar data acquisition was provided by NSERC through Discovery Grants to Clague and Menounos and the Canada Foundation for Innovation (Menounos). Natural Resources Canada (NRCan), through Melanie Kelman, provided funds for the 2016 Lidar dataset. Fieldwork was supported by Chairs grants to Ward. The InSAR analyses were provided by TRE-Altamira. We thank Planet for the imagery access to document the 2009 Devastation landslide.

Chapter 6. Could glacial retreat-related landslides trigger volcanic eruptions? Insights from Mount Meager, British Columbia [5]

Gioachino Roberti[1,2], Brent Ward[1], Benjamin van Wyk de Vries[2], Nicolas Le Corvec[2], , Swetha Venugopal[1,2], Glyn Williams-Jones[1], John J. Clague[1], Pierre Friele[3], Giacomo Falorni[4], Geidy Baldeon[4], Luigi Perotti[5], Marco Giardino[5], and Brian Menounos[6]

(1) Earth Sciences Department, Simon Fraser University, Burnaby, British Columbia, Canada (2) Université Clermont Auvergne, CNRS, IRD, OPGC, Laboratoire Magmas et Volcans, Aubiere Cedex, France (3) Cordilleran Geoscience, Squamish, British Columbia, Canada (4) TRE-ALTAMIRA Inc., Vancouver, British Columbia, Canada (5) Earth Sciences Department, GeoSitLab - GIS and Geomatics Laboratory - University of Torino, Torino, Italy (6) Geography Program and Natural Resources and Environmental Studies Institute - University of Northern British Columbia, Prince George, British Columbia, Canada

6.1. Abstract

Volcanoes deform under their own weight, as they are built of weak rocks, and glaciers further weaken them by loading, unloading, and eroding them. These processes reduce the stability of volcanic slopes, increasing the likelihood of a catastrophic failure. Unloading of volcanic edifices during glacier retreat, erosion, and catastrophic mass movements could affect the magmatic plumbing system and potentially cause an eruption. Mount Meager, an ice-clad volcanic complex in British Columbia, Canada, is known for its large landslides and a major eruption about 2360 cal yr BP. In 2010 a major collapse associated with glacier retreat occurred on the south flank of Mount Meager, and in 2016, fumaroles formed ice caves in one of its glaciers. This glacier is bordered by a large unstable slope presently moving about 3.5 cm/month. If this slope

[5] Part of this chapter has been presented at EGU (European Geoscience Union) 2018 General Assembly: Roberti G, Ward B, van Wyk de Vries B, Le Corvec N, Venugopal S, Williams-Jones G, Clague JJ, Friele P, Falorni G, Baldeon G, Perotti L, Giardino M, and Menounos B. Can glacial retreat-related landslides trigger volcanic eruptions? Insights from Mount Meager, British Columbia. Geophysical Research Abstracts - EGU General Assembly 2018-Vol. 20, EGU2018-913-1, 2018.

fails, a long runout debris avalanche would reach the floor of Lillooet River valley, with possible destructive effects on infrastructure. The unloading of the volcanic edifice from an abrupt failure would also have unknown consequences on the magmatic plumbing system. Based on numerical model simulations carried out to constrain the stress change, the failure would affect the stress field to depths of up to 6 km, with changes in effective stress of up to 4 MPa. From geochemical, geophysical, and petrological data, we infer the presence of a magmatic chamber at 3-10 km depth. The change in effective stress following the landslide has the potential to destabilize the magmatic chamber and trigger an eruption. With this model, we infer that a major collapse could have had a role in the 2360 cal yr BP eruption. We document a previously observed, but not described in detail collapse in the Job Valley that could have triggered the 2360 cal yr BP eruption. Changes in glacier cover can influence magmatic processes through a chain of events involving deep erosion, over steepening, unloading, mass movements, and depressurization.

6.2. Introduction

Mount Meager is a glaciated volcanic complex in British Columbia, its activity spans ~2 Ma (Read 1978), with the most recent eruption in 2360 cal yr BP (Hickson et al. 1999). Today, Mount Meager hosts an active hydrothermal system and is the site of shallow earthquakes (Venugopal et al. 2017; Friele et al. 2008). It is known for its pre-historic and historic large landslides (Friele et al. 2008), of which, the 2010 debris avalanche is the largest in Canadian history. Following the 2010 landslide, recent studies (particularly this thesis) have focused on the stability of Mount Meager and the link with recent deglaciation. A refined attention on this link allowed the identification of many large unstable slopes (Chapter 5). One of these, the west flank of Plinth Peak, is of particular concern. It has deformation exceeding 3 cm over 24 days during Summer 2016 (obtained from InSAR interferometry, see Chapter 5); it is near an amphitheatre collapse scar, now hosting a retreating glacier and a fumarole field.

The link between landslides and volcanic activity has been studied at many volcanoes (e. g. Siebert 2002; Waythomas 2012; Delcamp et al. 2018). Edifice collapse can be triggered by magmatic intrusion and in turn the change in the stress field after a collapse can cause dyke intrusions, vent migrations and subsequent eruptions (Pinel and Jaupart 2005; Manconi et al. 2009; Delcamp et al. 2012; Maccaferri et al. 2017). In

this study, we present a numerical model to investigate the effects on the stress field prior to and after the eventual collapse of the west flank of Plinth Peak. We discuss how this stress change could affect the hydrothermal and volcanic plumbing systems leading to an eruption. We also document another large edifice collapse from Job Valley, which occurred sometime before the 2360 cal yr BP eruption. The collapse originated from the amphitheatre collapse scar near Plinth Peak, now occupied by Job Glacier and the fumarole field. Discussion on decompression mechanisms after the eventual collapse of Plinth Peak and the documentation of the collapse from Job Valley, allow the examination of the eventual role of an edifice collapse in the 2360 cal yr BP eruption. The collapse could have decompressed the volcanic plumbing system and through a series of processes (fracture propagation, magma migration, gas exsolution, etc.) could have contributed to the eruption. This work shows how landslide processes from glaciated volcanoes could have an important role to play in eruptive dynamics and provides an argument in support of detailed monitoring of the changes in glacier cover on volcanoes worldwide.

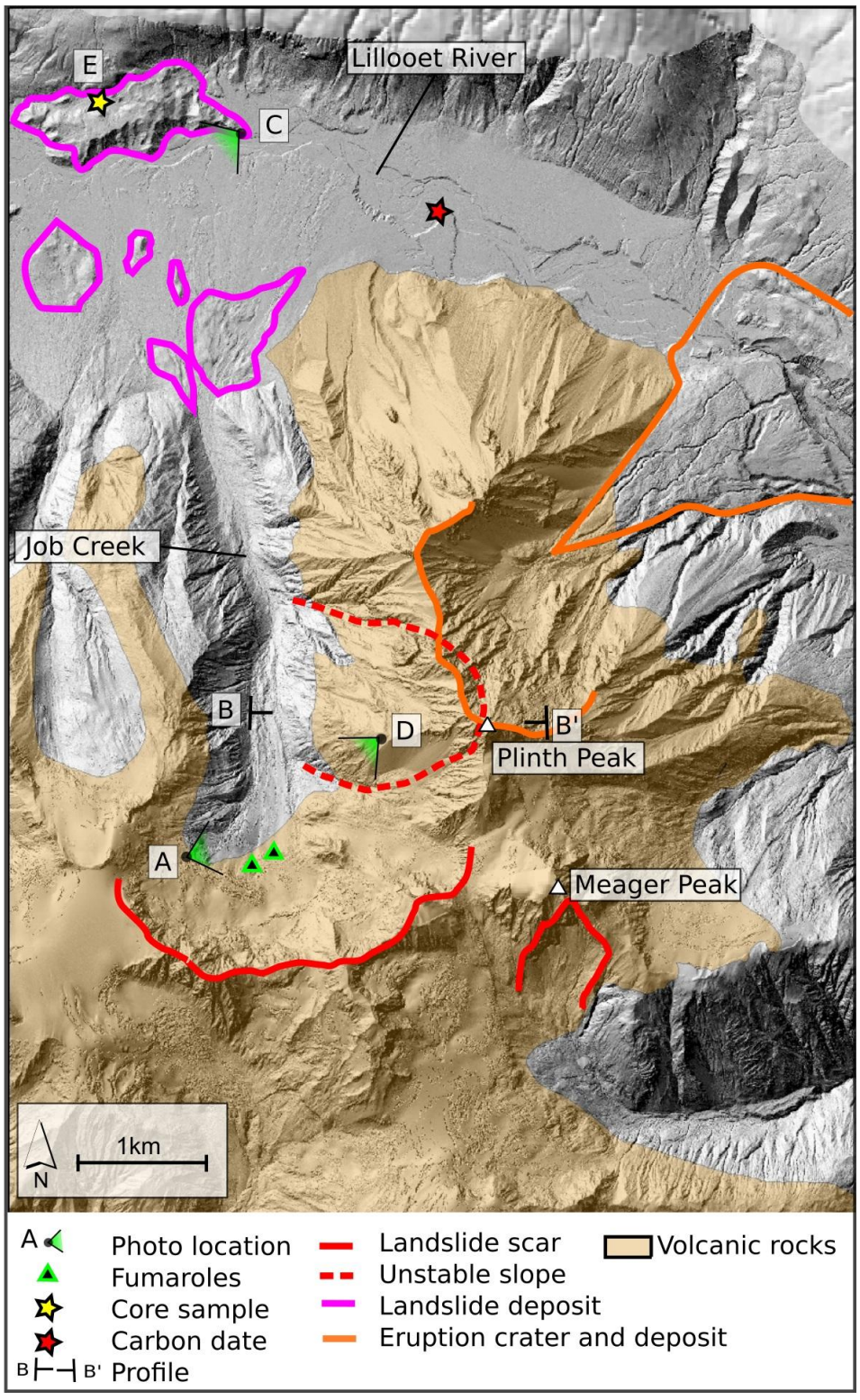
E
C
Lillooet River
Job Creek
B
D
B'
Plinth Peak
A
Meager Peak
N
1km
A
Photo location
Fumaroles
Core sample
Carbon date
B
B'
Profile
Landslide scar
Unstable slope
Landslide deposit
Eruption crater and deposit
Volcanic rocks

Figure 6.1. Job Valley, Plinth Peak, and the 2360 cal yr BP eruption crater. Scars, unstable slopes, landslides, eruption deposits, photos, fumaroles, sample, and profile locations are indicated. A) Figure 6.2. B) Figure 6.3. C) Figure 6.4. D) Figure 6.5. E) Figure 6.6. Basemap is a hillshaded rendering of the LiDAR data from 2015-16.

6.3. Methods

We describe the geology and structure of the west flank of Plinth Peak and Job Valley from historical aerial imagery, Lidar data, literature analysis and field work. Field work at Plinth, Job Glacier and landslide deposit at the mouth of Job Valley was conducted in October 2017. We collected a core sample on the landslide deposit to constrain the temporal relation between the 2360 cal yr BP eruption and the precursor landslide.

We used a 2D finite element model (FEM) with COMSOL Multiphysics® to explore the effect of the collapse of Plinth Peak on the state of stress within the Mount Meager volcanic edifice. Through COMSOL, we describe the lithostatic stress before and after the removal of the landslide material. We divided the 2D elastic domain in two areas: a simplified volcanic and country rock model. We used Plinth's 2360 cal yr BP eruption dacite to model the volcanic edifice and the Fall Creek Stock monzogranite for the country rock (Campbell et al. 2013; Russel personal communication 2018). Plinth's dacite has a Young's modulus (Ec) of 12 GPa, a density (ρc) of 2500 kg/m^3, and a Poisson's ratio (μ) of 0.30. The monzogranite has Young's modulus (Ec) of 21 GPa a density (ρc) of 2800 kg/m^3, and a Poisson's ratio (μ) of 0.29 (Table 6.1).

Table 6.1. Density, Young's modulus and Poisson's ration used to model the volcanic edifice and the country rocks. Data from a) Russel, personal communication (2018) and b) Wohletz and Heiken (1992).

Rock Type	Density (kg/m^3)	Young's modulus (GPa)	Poisson's ratio
Plinth Dacite	2570-2620[a]	7.61-12.75[a]	0.27-0.32[a]
Fall Creek Stock monzogranite	2610[a]-2810[b]	21.52[b]	0.29[b]

6.4. Results

6.4.1. The west flank of Plinth Peak.

The west flank of Plinth Peak forms a prominent knob in Job Valley, about 2 km from the Job Glacier headwall. The west flank of Plinth Peak has an extent of 2.7 $\times 10^6$ m^2 and it rises 1000 m from Job Glacier to the ridge crest (Figure 6.2). We divide the description into the lower and upper slopes. The lower slope extends 6 $\times 10^5$ m^2 and 600 m from Job Glacier to a major N-S striking and 45° west dipping fault. Vertical displacement along the fault is up to 40 m as seen in the fault scarp. From Read (1978), the lower 150 m of the slope are basement rock, above this is 400 m of yellow-red altered andesitic flow and breccia from Pylon assemblage (p3x and p3f) and the upper 50 m is grey rhyodacite flows from Plinth assemblage (p9f). The Little Ice Age trimline is 200 m above present day glacier position and the glacier has thinned up to 50 m and frontally retreated about 400 m since 1981 (Figure 6.2; Chapter 2 and 5). Two systems (E-W and NW-SE) of counter scarps characterize the slope. DInSAR analysis with Sentinel-1 satellite show displacement in this part of the slope of -34±10 mm over a 24-day period from July to August 2016 (Chapter 5). The displacement is -30 ±10 mm over a 12-day period in July 2017.

The upper slope extends 400 m above the lower slope (Figure 6.2), with vertical cliffs between buttresses in which the horizontally layered rhyodacitic lava flows of Plinth assemblage (p9f) can be seen. SqueeSAR analysis of the 1992-2000 ERS data indicate LOS (line of sight) displacements up to -17 mm yr^{-1}. Analysis of the 2015-2018 Sentinel-1 data indicate LOS displacements of up to -10 mm yr^{-1}.

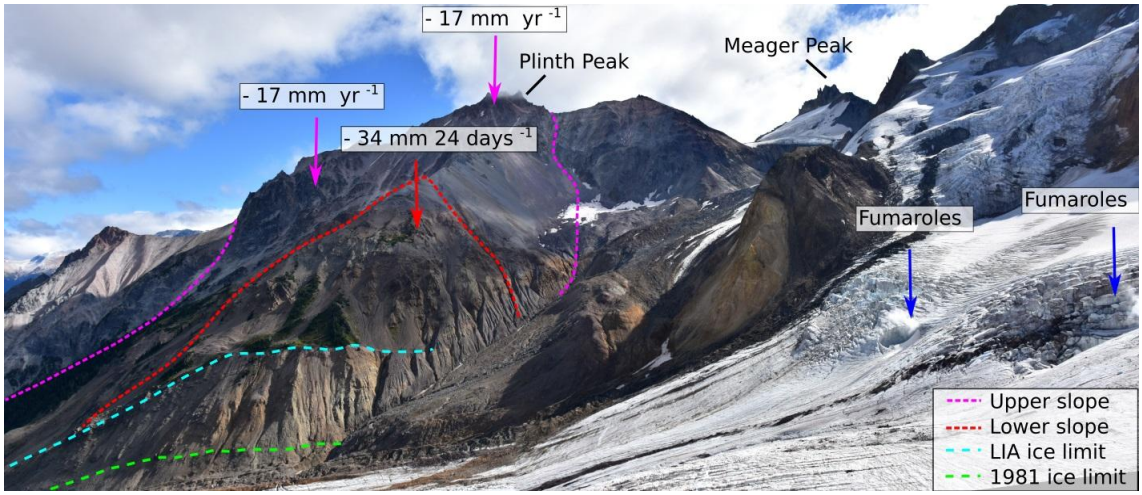

Figure 6.2. The west flank of Plinth Peak. Little Ice Age (LIA) and 1981 glacier limits, lower and upper zone of deformation are outlined. Note fumaroles ice caves in the foreground.

We obtained the geometry of the failure by superimposing E-W profiles of the west flank of Plinth (B-B' in Figure 6.1) and of Job Valley 500 m to the south, assuming that the failure would remove the bulge of the west flank of Plinth Peak to reach the profile of Job Valley (Figure 6.3). The 2D stress field modelling in COMSOL shows that the removal of the west flank of Plinth Peak would affect the effective stress to a depth 6 km for up to 4 MPa (Figure 6.3). Most of the decompression would occur at toe of the slope, about 1 km downstream of the fumaroles.

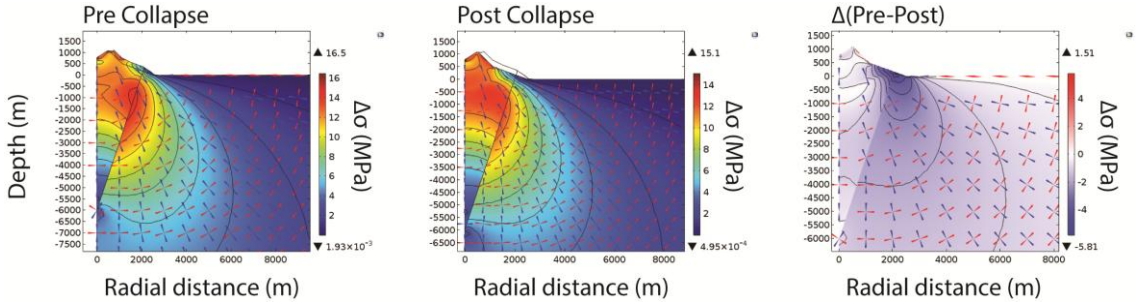

Figure 6.3 Stress field before and after the collapse. The oblique line separates volcanc to the left and basement rocks to the right. The change in effective stress after the collapse would be up to 4 MPa and would reach a depth of 6 km.

6.4.2. The Job landslide

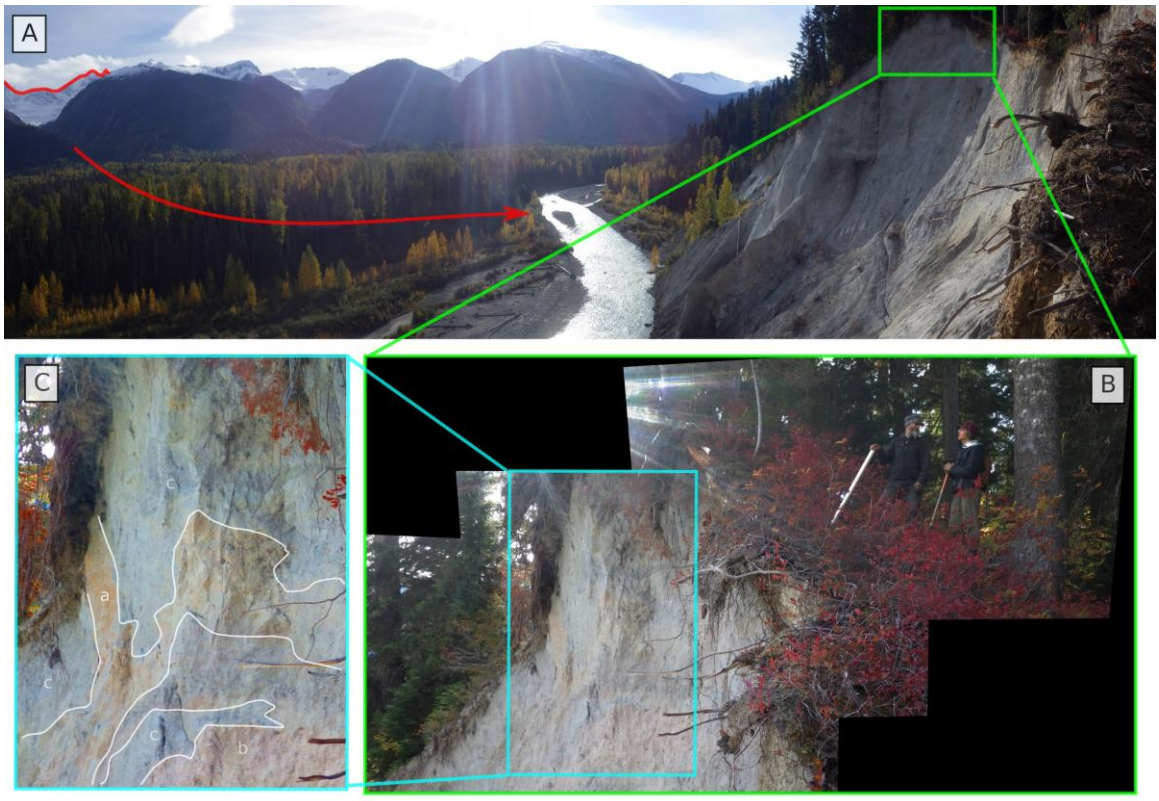

Figure 6.4. A) Panoramic view of debris avalanche outcrop on the Lillooet River. Red line indicates the source and red arrow indicates the avalanche path. B) Outcrop Detail. C) Detail on the lithologies: a, flame of yellow debris, b red debris, and c gray debris.

There is a 2 km long, and >100 m thick, hummocky landslide deposit located at the Job Creek-Lillooet River confluence (Figure 6.1). The deposit is a matrix supported, massive polylithological diamicton. Flames of red-yellow altered material are present (Figure 6.4). The matrix is a silty-gravelly-sand. Clasts are commonly centimetre-sized, with rare metre size blocks. The lack of large blocks may indicate high degree of fragmentation during transport. Considering the deposit thickness and extent, and the yellow and red altered lithology of the deposit, we correlate the depositional event to the formation of the large amphitheatre shaped collapse scar at Job Valley (Figure 6.5). The Job Valley is the only scar of size comparable to the deposit extent and has widespread hydrothermal alteration, consistent with the deposit material.

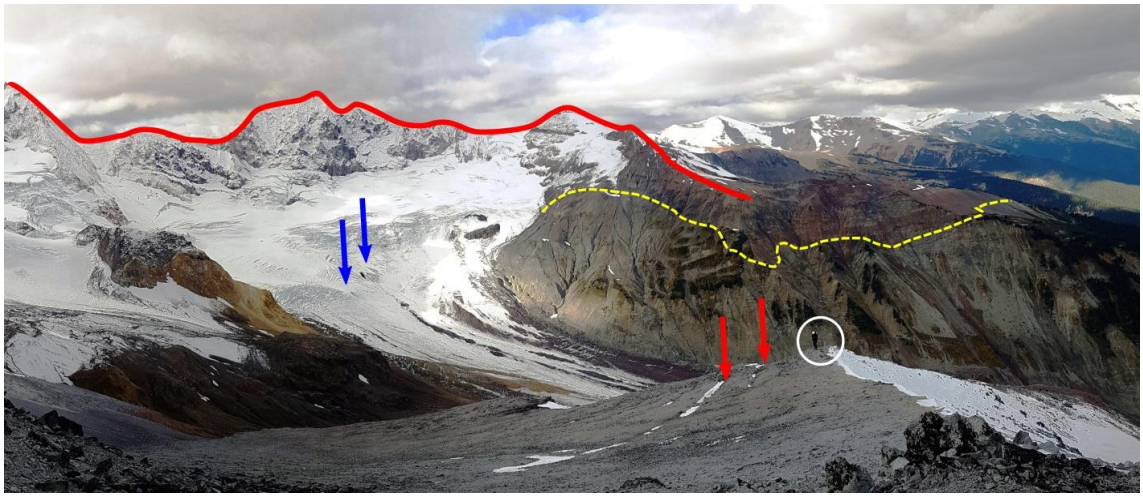

Figure 6.5 **Panorama of the amphitheatre shaped collapse scar from the west flank of Plinth. The red line shows the collapse scar, the yellow dashed line the approximate location of the contact of the volcanic and the basement rocks (after Read 1978). The blue arrows indicate the fumaroles and ice caves. The red arrows show fractures on the west flank of Plinth. Person in circle as scale. Note the yellow altered rocksleft of the fumaroles. Image courtesy of H. Wong.**

We collected a 1.5 m core sample in an inter-hummock area of the landslide deposit; the stratigraphy is shown in Figure 6.6. The base (0 to 5 cm) are massive matrix supported diamicton, 30-40% in clast content. Clasts (1 cm) are subangular to subrounded of volcanic lithologies while the matrix is gravelly-silty-sand. The diamicton transition to 23 cm of stratified sand and gravel. Layers are 1 to 4 cm thick and normally graded. A 0.5-1 cm humic stain overlies the top of the sand. Fourteen centimetres of stratified pumice lie over the humic stain, the contact is sharp. The bottom 1.5 cm of the pumice is well sorted very fine rounded-clast gravel, the following 3 cm are fine to coarse sand that transition to 5 cm fine rounded-clast gravel. The gravel transition to 5 cm of sand and silty sand. Brown to black stains are present in the finer part, suggesting reworking. The rounding of the pumiceous material clasts indicates reworking by water. An inclined sharp contact separated the pumiceous material to the top 108 cm of peat. A sample of the humic stain was examined for material suitable for radiocarbon dating, but no suitable material was found.

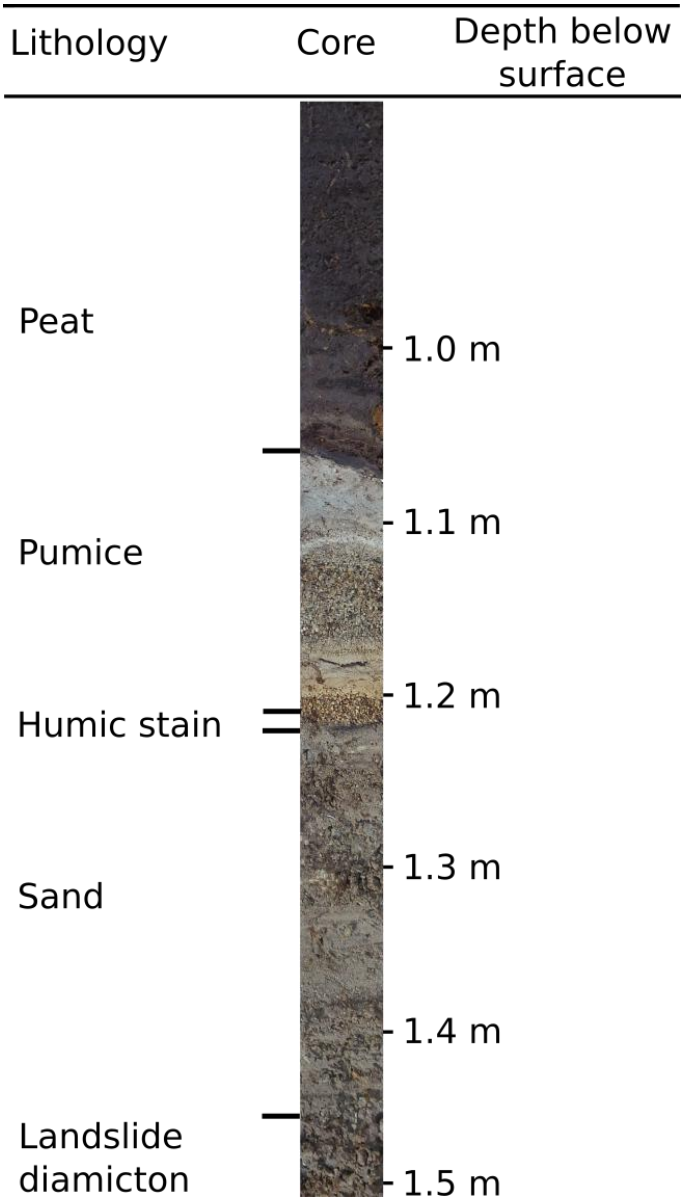

Figure 6.6. Core sample from the landslide deposit near the Job Creek and Lillooet River intersection. Note the 2360 cal yr BP eruption pumice separated from the landslide diamicton by sand and humic stains.

6.5. Discussion

6.5.1. The Plinth collapse

Considering displacement rates, geometry, geological setting and factor of safety (FOS) calculated by Hetherington (2014), the west flank of Plinth Peak is at incipient failure. The fumaroles ice caves at Job Glacier may accelerate glacier melting affecting the stability of the slope. The base of the slope, affected by glacial cycles, underwent

recent deglaciation and showed high deformation rates, is likely to fail first. The collapse would likely trigger retrogressive failures culminating in a large failure involving the whole slope, similar to the evolution of the 2010 collapse (Chapter 4). The failing rock mass would fracture and liquefy transforming from a rockslide into a debris flow. The estimated volume of the debris flow is 10^8-10^9 m^3 (Class 9 debris flow, Jackob 2005). The hydropower infrastructures near the Keyhole falls would be impacted (within the reach of 10^7 m^3 debris flow) as well as populated areas in Pemberton Meadows and Pemberton (in the case of a 10^9 m^3 debris flow). See Simpson et al. (2006) and Hetherington (2014), for inundation zones of debris flows from Mount Meager.

Decompression following the collapse of Plinth Peak will affect the stress field to a 6 km depth. This sudden decompression can directly affect the near surface hydrothermal system at Job Glacier. The decompression could also affect the deeper magmatic plumbing system. The geothermal gradient is 80-100 °C/km with recorded temperatures in geothermal explorative drill holes of up to 270 °C (Ghomshei et al. 2013). Shallow earthquakes at 1- 6.7 km depth (Friele et al. 2008) are recorded below Mount Meager. The high geothermal gradient and seismic activity could indicate the presence of magma at shallow depths (3-10 km). The stress perturbation of the system can trigger a series of processes (fracturing and magma propagation, gas exsolution, magma differentiation and mixing) and can lead to an eruption. Olivine melt inclusion analysis of basalts form the Mosaic assemblage (p10f, Read 1978;) indicate magmatic source at 22 km (1057–1142 ˚C and 0.4 - 6.8 kbars, Venugopal et al. in press) for the basalts. The decompression following the landslide would not affect these deeper, mafic, reservoirs, unless there was a telescoping of events down the system. The localised decompression would be unlikely to induce partial melting in the mantle.

6.5.2. The Job landslide and the 2360 cal yr BP eruption.

Twelve vertical holes, 10-40 m deep, were drilled 32-65 km downstream of Mount Meager in the Lillooet River valley to determine its sedimentary structure (Friele et al. 2005). The drill holes sedimentary record document three volcanic debris and two hyperconcentrated flows. As landslides at Mount Meager commonly have rock or debris avalanche and debris flow phases (Friele and Clague 2004, Roberti et al. 2017a), these distal deposits are relatable to landslide deposits near the volcano. Radiocarbon ages on

wood fragments in flow and landslide deposits, and in overlying and underling layers, allowed dating and correlation of these events (Friele et al. 2008).

Friele et al. (2008) briefly described the landslide deposit at the mouth of Job Valley discussed in the paper and tentatively correlates it to a 6250±30 ^{14}C yr BP (7076–7302 cal yr BP) debris flow found in drill core 32 km downstream from Mount Meager. However, the stratigraphy of the landslide deposit at the mouth of Job Valley analyzed here contains pumice and landslide diamicton, separated only by 23 cm of sand and one cm of organic matter. The sample is from an inter-hummock area where rain events could accumulate tens of centimetres of sand and organic matter in a few months or years. Alternatively, these sandy layers could have been deposited days after the landslide emplacement by post-landslide mud flows, as observed on the 2010 landslide (Delcamp et al. 2016). The close spatial relation between the Job landslide diamicton and pumice suggests a shorter time span between the emplacement of the two deposits, thus we do not think the Job landslide is source of the 6250±30 ^{14}C yr BP distal deposit.

Friele et al. (2005), Simpson et al. (2006) and Friele et al. (2008) documented a volcanic debris flow deposit found in drill cores at 32-50 km downstream from Mount Meager dated 2540–2970 cal yr BP. This event inundated the entire 2 km width of the Lillooet River valley to a depth > 4 m. It is a poorly sorted, massive, clay-rich (>3-5 % of matrix) diamiction, and is overlain by a pumice deposit. Between the pumice and diamicton is a charcoal layer. Diamicton is 10-30% of rounded and subrounded clast content, and clast are of volcanic lithologies. Chlorite, illite, and smectite minerals in the matrix are indicative of moderate temperature hydrothermal alteration at the source (Simpson et al. 2006). The pumice is resedimented layer of reverse graded gravel-sized pumiceous clasts rounded at the base and angular at the top. Desloges and Gilbert (1994) documented an acoustic reflector in the Lillooet lake dated 2495±670 ^{14}C years and interpreted to be a debris flow deposit. A debris flow deposit is also documented 3 km downstream of the Job landslide deposit (Friele et al. 2008) and dated 2650±60 ^{14}C yr BP (2591-2897 cal yr BP). We think that these debris flow deposits represent the debris flow phase of the Job Valley landslide documented in this paper. The total volume of the landslide is estimated at ~10^9 m^3. This is the only known event to have reached Lillooet lake, about 70 km from Mount Meager. This event may have left a trace also in the oral history of the local Lil'wat First Nation community. An oral story of a "great flood" was passed down through generations: *"[...] they got back there, their place was bare*

because the water was so rough it took all the ground off the valley down towards the mouth of the Lillooet River [...]. So Pemberton Meadows became liveable. All those swamps were filled and the people came down there instead of staying at their place" (Kennedy and Bouchard 2010).

The landslide was not immediately followed by the eruption; the two events are separated by several months to centuries, as indicated by the stratigraphy at Job Valley, in drill cores, and by the carbon ages obtained from the drill samples (Friele et al. 2005; Simpson et al. 2006; and Friele et al. (2008). The triggering of the 2360 cal yr BP eruption was inferred to be from magma mixing (Stasiuk et al. 1996). This very large (~10^9 m^3) landslide, however, would have most likely perturbed the stress field by allowing fracture propagation and fluid migration. The decompression following the landslide could have allowed the ascent of deeper, less differentiated magma which mixed with a shallow, more differentiated magma chamber that ultimately triggered the eruption. The time lag between landslide and eruption could be related to the time that the magmatic system took to react to the decompression. The location of the vent, NE of Job amphitheatre collapse scar, could have also been conditioned by the large collapse. Field and numerical studies document how vents can migrate following an edifice collapse (Maccaferri et al. 2017). Our model of the change in stress field after the failure of the west flank of Plinth show maximum decompression to the west of the landslide. Delcamp et al. (2012) showed field evidence of how dykes intrude around collapse scars and Maccaferri et al. (2017), with a numerical approach, showed lateral vent migration after a collapse. Zurek et al. (2015) also argued a whole rift migration following large landslides. The stress field perturbation after the Job Valley collapse could have conditioned the location of the vent and triggered a sequence of events that lead to the eruption.

The cause of the landslide of Job Valley is unknown. Both Simpson et al. (2006) and Friele et al. (2008) discuss the possibility of minor eruptive activity as the triggering mechanism. An undated lava dome and flows are located near the Job amphitheatre scar rim; these are the most fresh-looking volcanic features at Mount Meager but they have not yet been studied in detail. The presence of fumaroles and extensive hydrothermal alteration of the rocks in the Job Valley (Figure 6.2 and 6.4) may indicate that hydrothermal system pressurization could have had a role in the collapse (van Wyk de Vries and Francis 1997; Reid 2004). Considering the broader tectonic context of

Mount Meager, regional stresses have a role in the morphology and volcanic activity as observed at other volcanic centres (Mathieu et al. 2011). N-S striking fractures are found in the basement near the 2360 cal yr BP vent (Ghomshei et al. 2013). The orientation of Job Valley is N-S and the volcanic activity at Mount Meager has migrated from the south to the north in the last 2 Ma (Read 1978). These N-S structures may have controlled past volcanic and landslide activities and could have a role in future edifice collapses and eruptions.

Further field and numerical studies are needed to better constrain the magmatic plumbing system, the link between deglaciation, edifice stability and eruptions, and the effects of the regional tectonic stresses on the edifice morphology of Mount Meager. Slope, seismic, and gas monitoring are needed to better constrain landslide and eruption hazards. Early warning systems and risk zonations are needed in order to mitigate the risk of life loss from large landslides at Mount Meager volcano.

6.6. Conclusions

In this study, we describe the large unstable slope of Plinth Peak near the retreating Job Glacier, the potential stress field perturbation if the whole slope fails, and the potential consequences on the magmatic plumbing system. We also describe a large landslide deposit that originated from Job Valley and discuss the probability that the landslide had a role in triggering the 2360 cal yr BP eruption.

At Plinth Peak, the high deformation rates and rapid glacial retreat are factors that favour an abrupt slope failure as shown by the 2010 debris avalanche (Chapters 3-5). We applied a 2D finite element model to assess the state of stress after an eventual catastrophic slope failure. Change in effective stress would reach a 6 km depth with up to 4 MPa decompression. Such changes in confining pressure could trigger a hydrothermal explosion from the shallow hydrothermal system expressed at Job Glacier. Fracture propagation, magma migration, and gas exsolution following decompression could also lead to a magmatic eruption. Such a landslide and eruption would impact infrastructures and communities near the volcano.

The model of the stress change and new field description of a large rock avalanche originated from Job Valley suggest that the past landslide may have had a

role on the 2360 cal yr BP eruption dynamics. The large (~10^9 m^3) collapse that created Job Valley preceded the eruption by, at most, a few centuries. It left the amphitheatre collapse scar now occupied by Job Glacier and the fumaroles. The decompression on the magmatic system could have allowed new magma to rise and mix, leading to the 2360 cal yr BP eruption sometime after this large landslide occurred. The post landslide stress field re-organization could have caused vent migration and eruption to one side (NE) of the scar. The trigger for the collapse is still unknown but may be related to the hydrothermal activity and continued fluvio-glacial erosion.

Understanding present day glacier-landslide-volcanic system interaction is vital. The whole system, where fumaroles melt ice, that affects slope stability, that in turn decompresses the magmatic system, is a powerful potential sequence of events which should be investigated in more detail. The collapse of the west flank of Plinth would have a devastating effect on the volcanic edifice and in the valley downstream; and with a subsequent accompanying eruption, the impact would be much greater. Hazard and risk studies that consider these process chains are needed at Mount Meager volcano. Regular monitoring of this system should be implemented to mitigate the risk to local communities from landslides and eruptions.

6.7. Acknowledgments

Alex Wilson and Kelly Russell provided the data for Mount Meager rock properties used in the model. We thank Hazel Wong, Brad Woods, Erik Young, and Kai Friele for the help in the field. Financial support for the 2015 Lidar data acquisition was provided by NSERC through Discovery Grants to Clague and Menounos and the Canada Foundation for Innovation (Menounos). Natural Resources Canada (NRCan), through Melanie Kelman, provided funds for the 2016 Lidar dataset. Fieldwork was supported by Chair grants to Ward. The InSAR analyses were provided by TRE-Altamira. Financial support for Roberti's PhD salary was partially provided by the "End of an Arc: The Remarkable Life and Death of a Volcanic Arc" project, a French-Canadian partnership.

Chapter 7. Summary and conclusions

7.1. Synthesis

Mount Meager is a glaciated volcanic complex in British Columbia, Canada and it is known for numerous landslides and an eruption 2360 cal yr BP. The link between glaciers, landslides, and volcanic activity has been poorly constrained, moreover so has the resulting hazard and risk to local communities. This thesis brings together Quaternary geology, volcanological, geotechnical, and natural hazards approaches to better understand the interplay of processes at Mount Meager volcano for better hazard and risk assessments.

7.1.1. The value of historic photography and half a century of geomorphic changes at Mount Meager Volcano

Chapter 1 is a literature review, and we explored the problematic of a volcano in a changing cryosphere. Volcanoes are multi-faceted systems to which glaciers add to an already existing high degree of complexity. The hazards from glaciated volcanoes are among the deadliest on the planet. Climate change is causing glacier retreat, contributing to conditioning slopes for failure. Failures from volcanic edifices can transform into long-runout debris avalanches with devastating effects downstream.

Chapter 2 documents archival data research on the rich airphoto datasets over Mount Meager. The innovative approach of processing these airphotos with Structure from Motion (SfM) photogrammetry allowed fast 3D topographic reconstruction over the whole Mount Meager area from 1947 to 2006. The possibility of analyzing over 50 years of geomorphic changes at Mount Meager has permitted the identification of glacier and landslide activity. Each of the glaciers has different advancing and retreating trends, morphologies and debris cover. Slopes have deformed and collapsed generating long-runout landslides. In order to explain the high landslide frequency at Mount Meager we presented a conceptual model of the evolution of a volcanic edifice together with multiple regional glaciations. Volcanic activity during the ice ages builds weaker edifices that are prone to collapses during interglacial periods. Glaciers first condition the shape of the volcano during glacial periods, but, in interglacial periods, the glaciers are conditioned by

the volcanic activity. Besides the scientific value of historic photography, the contribution of multitemporal 3D data visualization to outreach services is invaluable. Examples from this work are some 3D time-lapse images that can be easily understood by and are interesting to the non-scientific public (see here Mosaic Glacier and here the south flank of Mount Meager prior to the 2010 collapse).

7.1.2. The 2010 Mount Meager landslide deposit

On 6 August 2010 the south flank of Mount Meager failed generating the largest landslide in Canadian history. In Chapter 3 we describe the landslide deposit, emplacement dynamics and rheological evolution. As the south flank of Mount Meager failed, the mass fractured and liquefied separating into a frontal, faster, water-rich flow and a slower, water-poor core. The two phases followed different trajectories leaving different deposits. The water-poor phase left a distal scattered deposit and caused the high runups observed on the valley sides. The water-poor phase stayed valley-confined, leaving a thick hummocky deposit. Crude lithological zoning in the deposit respects the original source flank structure with hydrothermally altered material from the base of the slope found in distal deposit. The clay content in the deposit indicates that at least 12% of the slope was hydrothermally altered. The different rheologies and trajectories had different impacts on the valleys sides (see here the runout model of the 2010 landslide water-rich phase) and this shows the importance of considering multiple rheologies and flow transformation when modelling debris avalanches and producing hazard maps.

7.1.3. The slope prior to the 2010 Mount Meager landslide

To understand the dynamics of the 2010 landslide emplacement we moved our attention to the condition of the slope prior to the failure (Chapter 4). Using historic air photography, we documented slope deformation and glacier activity from 1948 to 2006. With field work, we improved constraints on the geology and structures of the collapse scar. We recalculated the collapse volume, we discussed volume and the role of water in the collapse and the collapse sequence. Capricorn glacier, located below the failure scar, advanced in the 1970's-1980's, and retreated from 1990 to 2006. The major discontinuities in the flank were already present in 1948, and the number of fractures and displacements along major faults increased in the following years (see here the flank 1948-2010 time-lapse). Slope bulging and precursory failures occurred at the toe of

the slope. Increase in pore water pressures from snowfields and glacial meltwater are the most likely cause of the failure at the toe of the slope. We estimated that 6×10^6 m^3 of water was residing at the toe of the slope, which allowed the separation of the frontal water-rich phase. The total failure volume was $53 \pm 3.8 \times 10^6$ m^3. The collapse evolved in four subfailures of 24.6×10^6 m^3, 13.8×10^6 m^3, 9.0×10^6 m^3 , and 5.6×10^6 m^3 respectively, involving some basement rocks and the entire volcanic sequence. Glacial cycles, hydrothermal alteration, and slow gravitational deformation conditioned the slope for failure. The slow slope deformation reported in this study could have been monitored previously and the failure forecasted decades in advance. Many other slopes are in the same condition as the pre-2010 landslide slope, and we have identified several failures-to-be, thus monitoring and early warning systems should be implemented, with urgency, to reduce consequential risks, including loss of life from Mount Meager landslides.

7.1.4. The slopes of Mount Meager, hazard and risk

Historic airphoto analysis, Lidar, and InSAR allowed the calculation of glacier ice mass loss since 1987, and identification and measurement of deformation rates of many unstable slopes at Mount Meager (Chapter 5). The continuing deglaciation is likely to trigger other large collapses that can affect economic activities near the volcano and in communities in the Lillooet River valley. Mount Meager volcano has lost ~1.3 km^3 of ice since 1987. We identified 27 large ($>5\times10^5$ m^2) unstable slopes. Seventeen of these slopes have been affected by recent deglaciation. Fifteen of the slopes have volumes of $>10^6$ m^3; if they were to fail catastrophically, infrastructures near the volcano may seriously be affected. Ten slopes have volumes of $>10^7$ m^3; their failure may impact populated areas downstream. The Job Creek and Devastation Creek valley flanks moved up to -34±10 mm and -36±10 mm, respectively, over a 24-day period during the summer of 2016. We consider these slopes to be in a critical condition for failure. The risk of life loss following a large landslide from Mount Meager has been deemed unacceptable. Slope monitoring and early warning systems are urgently needed to mitigate the risk. InSAR monitoring is the most rapid and cost effective option at Mount Meager volcano.

7.1.5. Landslides and eruptions

In the case of catastrophic failure of the west flank of Plinth Peak, a large (10^8-10^9 m^3) long-runout debris avalanche would be generated, impacting infrastructures and communities in the Lillooet Valley. Besides the direct impact of the landslide, 2D finite element modelling show that the resulting decompression on the volcanic edifice after the mass removal would affect the stress field to a depth of 6 km and up to 4 MPa. Such an abrupt change in effective stress could both trigger an hydrothermal explosion and affect the magmatic plumbing system and through a series of processes (fracture propagation, gas exsolution, magma migration) trigger an eruption (Chapter 6). These new insights on decompression following a landslide at Mount Meager allows the re-evaluation of the 2360 cal yr BP eruption trigger. A large collapse originated from Job Valley prior to the eruption may have had a role in triggering the eruption. Although stratigraphic evidence and radiocarbon dating show a lag between the landslide and the eruption, we interpret the lag to be related to the amount of time the magmatic plumbing system took to react to the decompression. The stress change following the landslide allowed fractures to propagate to the NE of the landslide scar and perturbed the magma system that allowed magma mixing that ultimately triggered the eruption (Chapter 6). Further studies are needed to better constrain the Mount Meager magmatic plumbing system such that new numerical models can be developed and applied to better assess the interaction between glacier retreat, landslides, and eruptions at Mount Meager.

7.2. Future work

Much future work at Mount Meager is needed. Better age constraints on volcanism and glaciations are needed to understand the glacial system, volcanic system and the glaciovolcanic interaction. Deeper knowledge on the glaciovolcanic history can help understand the present day glacier and landslide hazards at Mount Meager, as well as in other glaciated volcanoes worldwide. Hazard and risk maps should be produced at Mount Meager; slope monitoring and early warning and alarm systems should be implemented along with effective risk communication to local officials, communities, and stakeholders.

7.2.1. Mount Meager debris-covered glaciers

The debris-covered glaciers on Mount Meager should be studied more in detail. The effects of rock avalanches and rock falls on the glacier dynamics as well as the influence of hydrothermally altered volcanic bedrock on the glacier dynamics can be investigated with numerical modelling and field work. The thermal effects of the fumaroles on Job Glacier is unknown and merits investigation. Mount Meager glaciers and glaciers from other volcanoes could be compared to debris-covered glaciers form non-volcanic mountains.

7.2.2. Glaciovolcanism at Mount Meager?

Geological mapping at Mount Meager was carried out in the 1970's (Read 1978). Today's scientific advancement in understanding of volcanic and glacial processes would allow the geological map to be updated. Technological advances such Lidar and high resolution photography allow higher resolution mapping. Volcano stratigraphy could be mapped in further detail, particularly at a smaller scale (outcrop or channel) so that more stratigraphic units could be identified. Unmapped glaciovolcanic features may be recognized and new dates could better constrain the timing of glaciations and volcanism at Mount Meager.

7.2.3. Slope monitoring implementation, and hazard and risk communication

At present, indirect temperature and precipitation monitoring are used as landslide warning systems at Mount Meager; this should be accompanied by direct slope observations. Satellite and ground based monitoring, early warning, and alarm systems should be implemented to reduce risk at work sites near the volcano and in the communities in the Lillooet Valley. Effective risk communication, guidelines, and protocols, should be developed and implemented, because the expensive monitoring would have little impact unless its results were understood by those at risk. Social media applications and 3D technologies can help to make locals understand volcanic hazards and risks.

7.2.4. Landslide runout models for hazard zonation

Runout numerical simulations are needed to better constrain hazard impact zones and define risk zonation in the Lillooet River valley. The work done by Simpson et al. (2006) in identifying inundation zones can be improved, also in light of the 2010 event. The runout of the 2010 landslide was over-estimated by the Simpson et al. (2006) model. The risk analysis by Friele et al. (2008) should be updated considering the increase in population and economic activities near Mount Meager and in light of the potential landslides identified in this study.

A preliminary numerical model of the 2010 landslide runout (see video here) has been calculated with the software Volcflow, developed by Kelfoun and Druitt (2005). Separate simulations with different friction and cohesion parameters have been carried out to reproduce the runout of the different rheology phases. Model recalibration of the 2010 event would allow more precise runout scenarios of the identified unstable slopes.

7.2.5. Deglaciation, landslides and eruptions

Further field and numerical studies are needed to investigate the link between deglaciation, landslides, and eruptions at Mount Meager. Petrological, geochemical, and geophysical analysis can help in understanding the Mount Meager hydrothermal and volcanic plumbing systems. Numerical simulations of stress changes following landslides could help to constrain the probability of an eruption in case of large landslides.

The findings at Mount Meager can shed new light on the effects of regional and alpine glaciations on volcanism, and on the effects of volcanism on glaciers. The new knowledge could be applied at other volcanoes worldwide, and on other planets.

References

Allen SK, Gruber S, and Ownes IF (2009) Exploring steep permafrost bedrock and its relationship with recent slope failures in the Southern Alps of New Zealand. Permafrost and Periglacial Processes, v. 20, p. 345–356.

Allstadt K (2013) Extracting source characteristics and dynamics of the August 2010 Mount Meager landslide from broadband seismograms. Journal of Geophysical Research: Earth Surface, v. 118, p. 1472–1490, doi:10.1002/jgrf.20110.

Anderson LS, and Anderson RS (2016) Modeling Debris-Covered Glaciers: Response to Steady Debris Deposition. Cryosphere, v. 10(3), p. 1105–1124, doi:10.5194/tc-10-1105-2016.

Andrews GDM, Russell JK, and Stewart ML (2014) The History and Dynamics of a Welded Pyroclastic Dam and Its Failure. Bulletin of Volcanology, v. 76(4), p. 1–16, doi:10.1007/s00445-014-0811-0.

ASPRS (American Society of Photogrammetry and Remote Sensing) (2014) ASPRS positional accuracy standards for digital geospatial data. Photogrammetric Engineering & Remote Sensing, v. 81(3), p.26.

Ball JL, Taron J, Reid ME, Hurwitz S, Finn C, and Bedrosian P (2018) Combining Multiphase Groundwater Flow and Slope Stability Models to Assess Stratovolcano Flank Collapse in the Cascade Range. Journal of Geophysical Research: Solid Earth, v. 123(4), p 2787-2805, doi:10.1002/2017JB015156.

Bakker M, and Lane SN (2016) Archival Photogrammetric analysis of river-floodplain systems sing Structure from Motion (SfM) methods. Earth Surface Processes and Landforms, v. 42, p. 1274–1286, doi:10.1002/esp.4085.

Barrl ID, Dokukin MD , Kougkoulos I, Livingstone SJ, Lovell H, Małecki J, and Muraviev AY (2018a) Using ArcticDEM to Analyse the Dimensions and Dynamics of Debris-Covered Glaciers. Geosciences, v. 8(6), 216, doi:10.3390/geosciences8060216.

Barr ID, Lynch CM, Mullan D, De Siena L, and Spagnolo M (2018b) Volcanic Impacts on Modern Glaciers: A Global Synthesis. Earth-Science Reviews 182 (April). Elsevier, v. 182, p. 186-203, doi:10.1016/j.earscirev.2018.04.008.

Bernard B, van Wyk de Vries B, Barba D, Leyrit H, Robin C, Alcaraz S, and Samaniego P (2008) The Chimborazo sector collapse and debris avalanche: Deposit characteristics as evidence of emplacement mechanisms. Journal of Volcanology and Geothermal Research, v.176, p.36–43, doi:10.1016/j.jvolgeores .2008.03.012.

Bjørk AA, Kjær KH, Korsgaard NJ, Khan SA, Kjeldsen KK, Andresen CS, Box JE, Larsen NK, and Funder S (2012) An aerial view of 80 years of climate-related glacier fluctuations in southeast Greenland. Nature Geoscience, v. 5(6), p. 427–432, doi:10.1038/ngeo1481.

Blair RW (1994) Moraine and valley wall collapse due to rapid deglaciation in Mount Cook National Park, New Zealand. Mountain Research and Development, v. 14, p. 347-358.

Bolch T, Menounos B, and Wheate R (2010) Landsat-Based Inventory of Glaciers in Western Canada, 1985 – 2005. Remote Sensing of Environment, v. 114 (1), p. 127–137, doi:10.1016/j.rse.2009.08.015.

Bovis M (1990) Rock-slope deformation at Affliction Creek, southern Coast Mountains, British Columbia. Canadian Journal of Earth Sciences, v. 27, p. 243–254.

Bovis M, and Evans SG (1996) Extensive deformations of rock slopes in southern Coast Mountains, southwest British Columbia, Canada. Engineering Geology, v. 44, p. 163–182, doi:10.1016/S0013-7952(96)00068-3.

Bovis M, and Jakob M (2000) The July 29, 1998, debris flow and landslide dam at Capricorn Creek, Mount Meager Volcanic Complex, southern Coast Mountains, British Columbia. Canadian Journal of Earth Sciences, v. 37, p. 1321–1334, doi:10.1139/e00-042.

Bruce I, and Cruden D.M (1977) The dynamics of the Hope slide. Bulletin of the International Association of Engineering Geology, v. 16, p. 94–98, doi:10.1007/BF02591458.

Campbell ME,. Russell JK, and Porritt LA (2013) Thermomechanical Milling of Accessory Lithics in Volcanic Conduits. Earth and Planetary Science Letters, v. 377–378, p 276–286. doi:10.1016/j.epsl.2013.07.008.

Capra L (2006) Abrupt climatic changes as triggering mechanisms of massive volcanic collapses. Journal of Volcanology and Geothermal Research, v. 155, p.329–333, doi:10.1016/j.jvolgeores.2006.04.009.

Capra L, Bernal JP, Carrasco-Núñez G, and Roverato M (2013) Climatic fluctuations as a significant contributing factor for volcanic collapses. Evidence from Mexico during the Late Pleistocene. Global and Planetary Change, v. 100, p. 194–203, doi:10.1016/j.gloplacha.2012.10.017.

Capra L, and Macias JL (2000) Pleistocene cohesive debris flows at Nevado de Toluca Volcano, central Mexico. Journal of Volcanology and Geothermal Research, v. 102, p. 149–167, doi:10.1016/S0377-0273(00)00186-4.

Carlà T, Intrieri E, Di Traglia F, Nolesini T, Gigli G, and Casagli N (2017) Guidelines on the use of inverse velocity method as a tool for setting alarm thresholds and forecasting landslides and structure collapses. Landslides, v. 14(2), p. 517–534, doi:10.1007/s10346-016-0731-5.

Carrivick JL, Smith MW, and Quincey DJ (2016) Structure from Motion in Geosciences, John Wiley & Sons, Pondicherry, India, 210p.

Carter NM (1932) Exploration in the Lillooet River watershed. Canadian Alpine Journal, v. 21, p. 8–18.

Cecchi E, Lavest JM, and van Wyk de Vries B (2002) Videogrammetric reconstruction applied to volcanology perspectives for a new measurement technique in volcanology. Image Analysis and Stereology (IAS), v 21(1), p. 31-36.

Cecchi E, van Wyk de Vries B, Lavest JM, Harris A, and Davies M (2003) N-view reconstruction: a new method for morphological modelling and deformation measurement in volcanology. Journal of Volcanology and Geothermal Research, v. 123, p. 181-201.

Cecchi E, van Wyk de Vries B, and Lavest JM (2004) Flank spreading and collapse of weak-cored volcanoes. Bulletin of Volcanology, v. 67, p. 72–91, doi:10.1007/s00445-004-0369-3.

Chleborad AF (1997) Temperature, Snowmelt, and the Onset of Spring Season Landslides in the Central Rocky Mountains. U.S. Geological Survey Open-File Report 97-27, 35 p.

Clague JJ, Evans SG, Rampton VN, and Woodsworth GJ (1995) Improved age estimates for the White River and Bridge River tephras, western Canada. Canadian Journal of Earth Sciences, v. 32, p. 1172–1179, doi:10.1139/e95-096

Clague JJ, and Ward B (2011) Pleistocene glaciation of British Columbia. In Ehlers L, Gibbard PL, Hughes PD (eds.), Quaternary Glaciations-Extent and Chronology a Closer Look. Developments in Quaternary Science 15, Elsevier, Amsterdam, Netherlands, p. 563–573, doi:10.1016/B978-0-444-53447-7.00044-1

CloudCompare (version 2.8.1) [GPL software]. (2018). Retrieved from http://www.cloudcompare.org/.

Clarke GKC, Jarosch AH, Anslow FS, Radich V, and Menounos B (2015) Projected deglaciation of western Canada in the in the 21st century century. Nature Geoscience, v. 8, p. 372–377, doi:10.1038/NGEO2407.

Chandler J (1999) Effective application of automated digital photogrammetry for geomorphological research. Earth Surface Processes and Landforms, v. 24(1), p. 51–63.

Coe JA, Baum RL, Allstadt KE, Kochevar BF Jr, Schmitt RG, Morgan ML, White JL, Stratton BT, Hayashi TA, and Kean JK (2016) Rock-avalanche dynamics revealed by large-scale field mapping and seismic signals at a highly mobile avalanche in the West Salt Creek valley, western Colorado. Geosphere, v. 12, p. 607–631, doi:10.1130 /GES01265.1.

Cordilleran Geoscience (2009) Capricorn Creek Debris Flow Hazard & Risk Management Review. Report to Metro Vancouver Squamish District, Ministry of Forests, Lands and Natural Resource Operations, 24p.

Cordilleran Geoscience (2012) Volcanic Landslide Risk Management, Lillooet River Valley, BC: Start of North and South FSRs to Meager Confluence, Meager Creek and Upper Lillooet River. Report to Squamish District, Ministry of Forests, Lands and Natural Resource Operations, 27p.

Costantini M, Minati F, Ciminelli MG, Ferretti A, and Costabile S (2015) Nationwide Ground Deformation Monitoring by Persistent Scatterer Interferometry. IEEE Geoscience and Remote Sensing Society, the International Geoscience and Remote Sensing Symposium 2015 (IGARSS 2015), 25–31 July 2015, Milano, Italy.

Cruden DM, and Krahn J (1973) A re-examination of the geology of the Frank Slide. Canadian Geotechnical Journal, v. 10, p. 581–591, doi:10.1139/t73-054.

Cruden DM, and Martin, DK (2007) Before Frank slide. Canadian Geotechnical Journal, v. 44, p. 765–780, doi:10.1139/t07-030.

D'Agata C, Bocchiola D, Maragno D, Smiraglia C, and Diolaiuti GA (2013) Glacier shrinkage driven by climate change during half a century (1954-2007) in the Ortles-Cevedale group (Stelvio National Park, Lombardy, Italian Alps). Theoretical and Applied Climatology, v. 116, p. 169–190, doi:10.1007/s00704-013-0938-5.

DeBeer CM, and Sharp MJ (2007) Recent changes in glacier area and volume within the southern Canadian Cordillera. Annals of Glaciology, v. 46, p. 215–221.

Delcamp A, Poppe S, Detienne M, and Paguican EMR (2018) Destroying a Volcanic Edifice—Interactions Between Edifice Instabilities and the Volcanic Plumbing System. In Burchardt S (eds.), Volcanic and Igneous Plumbing Systems, Understanding Magma Transport, Storage, and Evolution in the Earth's Crust, Elsevier, Amsterdam, p. 231-257, doi:10.1016/B978-0-12-809749-6.00009-1.

Delcamp A, Roberti G, and van Wyk de Vries B (2016) Water in volcanoes: Evolution, storage and rapid release during landslides. Bulletin of Volcanology, v. 78(12), p. 12, doi:10.1007/s00445-016-1082-8.

Delcamp A, Troll VR, van Wyk de Vries B, Carracedo JC, Petronis MS, Pérez-Torrado FJ, and Deegan FM (2012) Dykes and structures of the NE rift of Tenerife, Canary Islands: a record of stabilisation and destabilisation of ocean island rift zones. Bulletin of Volcanology, v. 74(5), p. 963–980, doi:10.1007/s00445-012-0577-1.

Deline P, Gruber S, Delaloye R, Fischer L, Geertsema M, Giardino M, Hasler A, Kirkbride M, Krautblatter M, Magnin F, McColl S, Ravanel L, and Schoeneich P (2015). Ice Loss and Slope Stability in High-Mountain Regions. In Haeberli W, Whiteman C, and Shroder JF (eds.), Snow and ice-related hazards, risks and disasters, Hazards and disasters series, Elsevier, Amsterdam, p. 521-561, doi:10.1016/B978-0-12-394849-6.00015-9.

Desloges JR, Gilbert R (1994) Sediment source and hydroclimatic inferences from glacial lake sediments: the postglacial sedimentary record of Lillooet Lake, British Columbia. Journal of Hydrology, v. 159, p. 375–393..

Detienne M (2016) Volcanic Flank and Sector Collapses; Unravelling the Role of Hydrothermal Alteration Using Combined Mineralogical, Experimental, and Numerical Modelling Studies. PhD thesis, Université catholique de Louvain, Louvain-la-Neuve, 401 p.

Diolaiuti G, Bocchiola D, D'Agata C, and Smiraglia C (2012) Evidence of climate change impact upon glaciers' recession within the Italian Alps: The case of Lombardy glaciers. Theoretical and Applied Climatology, v. 109, p. 429–445, doi:10.1007/s00704-012-0589-y

Draebing D, Krautblatter M, and Hoffmann T (2017) Thermo-Cryogenic Controls of Fracture Kinematics in Permafrost Rockwalls, Geophysical Research Letters, v. 44 (8), p. 3535–3544, doi:10.1002/2016GL072050.

Edwards BR, Russell JK, and Gudmundsson MT (2015) Glaciovolcanism. In Sigurdsson H, Houghton B, Rymer H, Stix J, and McNutt S (eds.) The Encyclopedia of Volcanoes (Second edition), London, Academic Press, p. 377–393.

Evans SG, and Clague JJ (1994) Recent climatic change and catastrophic geomorphic processes in mountain environments. Geomorphology, v. 10, p. 107–128.

Evans SG (1987) A rock avalanche from the peak of Mount Meager, British Columbia. Current Research, Part A, Geological Survey of Canada Paper 87-1 A, p. 929- 934.

Ferreaz A, Bretar F, Jacquemoud S, and Gonçalves GR (2009) The Role of Lidar Systems in Fuel Mapping. Report 13, p 42.

Ferretti A, Fumagalli A, Novali F, Prati C, Rocca F, and Rucci A (2011) A new algorithm for processing interferometric data- stacks: SqueeSAR. IEEE Transactions on Geosciences and Remote Sensing, v. 49, p. 3460–3470.

Ferretti A, Davide C, Fumagalli A, Novali F, and Rucci A (2015) InSAR data for monitoring land aubsidence: Time to think big. Proceedings of the International Association of Hydrological Sciences, v. 92(1), p. 1–4, doi:10.5194/piahs-372-331-2015.

FGDC (Federal Geographic Data Committee) (1998) Geospatial Positioning Accuracy Standards. Part 3: National Standard for Spatial Data Accuracy. Subcommittee for Base Cartographic Data. U.S. Geological Survey, Reston, VA, 28 p.

Finn CA, Sisson TW, and Deszcz-Pan M (2001) Aerogeophysical measurements of collapse-prone hydrothermally altered zones at Mount Rainier volcano. Nature, v. 409, p. 600–603, doi:10.1038 /35054533.

Fonstad MA, Dietrich JT, Courville BC, Jensen JL, and Carbonneau PE (2013) Topographic Structure from Motion: A new development in photogrammetric measurements. Earth Surface Processes and Landforms, v. 38, p. 421–430, doi:10.1002/esp.3366.

Friele P, and Clague JJ (2004) Large Holocene landslides from Pylon Peak, southwestern British Columbia. Canadian Journal of Earth Sciences, v. 41, p. 165–182.

Friele P, and Clague JJ (2009) Paraglacial geomorphology of Quaternary volcanic landscapes in the southern Coast Mountains, British Columbia. In Knight J, and Harrison S (eds.), Periglacial and Paraglacial Processes and Environments: Geological Society London Special Publication 320, p. 219–233, doi:10.1144/SP320.14.

Friele P, Clague JJ, Simpson K. and Stasiuk M (2005) Impact of a Quaternary volcano on Holocene sedimentation in Lillooet River valley, British Columbia: Sedimentary Geology, v. 176, p. 305–322, doi:10.1016/j.sedgeo.2005.01.011.

Friele P, Jakob, M, and Clague JJ (2008) Hazard and risk from large landslides from Mount Meager volcano, British Columbia, Canada. Georisk: Assessment and Management of Risk for Engineered Systems and Geohazards, v. 2, p. 48–64, doi:10.1080/17499510801958711.

Furukawa Y, and Ponce J (2010) Accurate, dense and robust multiview stereopsis. IEEE Transactions on Pattern Analysis and Machine Intelligence, v. 32(8), p.1362–1376.

Gabriel AK, Goldstein RM, and Zebke HA (1989) Mapping small elevation changes over large areas: differential radar interferometry. Journal of Geophysical Research, v. 94, p. 9183–9191.

Gardelle J, Berthier E, Arnaud Y, and Kääb A (2013) Region-wide glacier mass balances over the Pamir-Karakoram-Himalaya during 1999–2011. The Cryosphere, v. 7, p. 1263–1286, doi:10.5194/tc-7-1263-2013.

Geertsema M, Clague JJ, Schwab JW, and Evans SG (2006) An overview of recent large catastrophic landslides in northern British Columbia, Canada. Engineering Geology, v. 83, p. 120–143.

Ghomshei M, Sadlier-Brown T, and Hassani F (2013) Current Status of the Pebble Creek (North Meager) Geothermal Project, Southwestern British Columbia, 23rd World Mining Congress, Montreal, 11-15 August, Paper 858, p 10.

Glicken HX (1991) Sedimentary architecture for large volcanic debris avalanches. In Smith GA, and Fisher RV (eds.), Sedimentation in Volcanic Settings: Society of Economic Paleontologists and Mineralogists Special Publication 45, p. 99–106, doi: 10.2110/pec.91.45.0099.

Glicken HX (1996) Rockslide-debris Avalanche of May 18, 1980, Mount St. Helens Volcano, Washington. U.S. Geological Survey Open-File Report 96-677, 90 p., 5 plates, http://pubs.usgs.gov /of /1996 /0677/.

Gomarasca M (2009) Basics of Geomatics. Springer, Netherlands, 689 p., doi:10.1007/978-1-4020-9014-1.

Gomez C (2014) Digital Photogrammetry and GIS-Based Analysis of the Bio-Geomorphological Evolution of Sakurajima Volcano, Diachronic Analysis from 1947 to 2006. Journal of Volcanology and Geothermal Research, v.280, p. 1–13, doi:10.1016/j.jvolgeores.2014.04.015.

Gomez C, Hayakawa Y, and Obanawa H (2015) A study of Japanese landscapes using Structure from Motion derived DSMs and DEMs based on historical aerial photographs: New opportunities for vegetation monitoring and diachronic geomorphology. Geomorphology, v. 242, p. 11–20, doi:10.1016/j.geomorph.2015.02.021.

Grämiger LM, Moore JR, Gischig VS, Ivy-Ochs S, and Loew S (2017) Beyond debuttressing: Mechanics of paraglacial rock slope damage during repeat glacial cycles. Journal of Geophysical Research: Earth Surface, v. 122(4), p. 1004–1036, doi:10.1002/2016JF003967.

Geertsema M, Clague JJ, Schwab JW, Evans SG (2006) An overview of recent large landslides in northern British Columbia, Canada. Engineering Geology, v. 83, p. 120-143.

Grove JM (1988) The Little Ice Age. Methuen, London and New York, 498 p.

Gruber S, and Haeberli W (2007) Permafrost in steep bedrock slopes and its temperatures-related destabilization following climate change. Journal of Geophysical Research: Earth Surface, v. 112, p. 1–10, doi:10.1029/2006JF000547.

Gruber S, Hoelzle M, and Haeberli W (2004) Permafrost thaw and destabilization of Alpine rock walls in the hot summer of 2003. Geophysical Research Letters, v. 31, p. 1–4, doi:10.1029/2004GL020051.

Guthrie RH, Friele P, Allstadt K, Roberts N, Evans SG, Delaney KB, Roche D, Clague JJ, and Jakob M (2012a) The 6 August 2010 Mount Meager rock slide-debris flow, Coast Mountains, British Columbia: Characteristics, dynamics, and implications for hazard and risk assessment. Natural Hazards and Earth System Science, v. 12, p. 1–10, doi:10.5194/nhess-12-1-2012.

Guthrie RH, Friele P, Allstadt K, Roberts N, Evans SG, Delaney KB, Roche D, Clague JJ, Jakob M, and Cronmiller D (2012b) The August 06, 2010 Mount Meager rock slide- debris flow, Coast Mountains, British Columbia. In Eberhardt E, et al. (eds.), Landslides and Engineered Slopes: Protecting Society through Improved Understanding: London, Taylor & Francis Group, v. 48, p. 665–674.

Haala N (2014). Dense image matching final report, Euro SDR Publication Series, Official Publication N 64, p. 115–145.

Haala N, and Rothermel M (2012) Dense Multi-Stereo Matching for High Quality Digital Elevation Models. Photogrammetrie, Fernerkundung, Geoinformation (PFG), v. 4, p. 331–343.

Harris C, Arenson LU, Christiansen HH, Etzelmüller B, Frauenfelder R, Gruber S, Haeberli W, Hauck C, Hölzle M, Humlum O, Isaksen K, Kääb A, Kern-Lütschg MA, Lehning M (2009) Permafrost and climate in Europe: Monitoring and modelling thermal, geomorphological and geotechnical responses. Earth-Science Reviews, v. 92, p. 117–171, doi:10.1016/j.earscirev.2008.12.002.

Harry DL, and Green NL (1999) Slab dehydration and basalt petrogenesis in subduction systems involving very young oceanic lithosphere. Chemical Geology v. 160, p. 309–333.

Heap MJ, Wadsworth FB (2016) Closing an open system: Pore pressure changes in permeable edifice rock at high strain rates. Journal of Volcanology and Geothermal Research, v. 315, p. 40–50, doi:10.1016/j.jvolgeores.2016.02.011.

Heap MJ, Farquharson JI, Baud P, Lavallée Y, Reuschlé T (2015) Fracture and compaction of andesite in a volcanic edifice. Bulletin of Volcanology, v. 77(6), p 1-19 p., doi:10.1007/s00445-015-0938-7.

Herd DG, and Comite de Estudios Vulcanologicos (1986) The 1985 Ruiz volcano disaster. EOS, Transactions of the American Geophysical Union, v. 67, p. 457–460.

Hetherington RM (2014) Slope stability analysis of Mount Meager, south-western British Columbia, Canada. M.Sc. thesis, Michigan Technological University, Houghton, Michigan, 68 p.

Hewitt K (2009) Rock avalanches that travel onto glaciers and related developments, Karakoram Himalaya, Inner Asia. Geomorphology v.103(1), p. 66–79, doi:10.1016/j.geomorph.2007.10.017.

Hickson CJ, Russell JK, and Stasiuk MV (1999) Volcanology of the 2360 BP eruption of Mount Meager Volcanic Complex, British Columbia, Canada: Implications for hazards from eruptions in topographically complex terrain. Bulletin of Volcanology, v. 60, p. 489–507, doi:10.1007/s004450050247.

Hirschmüller H (2008) Stereo Processing by Semi-Global Matching and Mutual Information, IEEE Transactions on Pattern Analysis and Machine Intelligence, v. 30 (2), p. 328-341.

Holm K, Bovis M, Jakob M (2004) The landslide response of alpine basins to post-Little Ice Age glacial thinning and retreat in southwestern British Columbia. Geomorphology, v. 57, p. 201–216. doi:10.1016/S0169-555X(03)00103-X.

Huggel C (2009) Recent extreme slope failures in glacial environments: Effects of thermal perturbation. Quaternary Science Reviews, v. 28, p. 1119–1130, doi:10.1016/j.quascirev.2008.06.007.

Huggel C, Caplan-Auerbach J, Waythomas CF, Wessels RL (2007a) Monitoring and modeling ice-rock avalanches from ice-capped volcanoes: A case study of frequent large avalanches on Iliamna Volcano, Alaska. Journal of Volcanology and Geothermal Research, v.168, p. 114–136, doi:10.1016/j.jvolgeores.2007.08.009.

Huggel C, Ceballos J L, Pulgarín B, Ramírez J, and Thouret J-C (2007b) Review and Reassessment of Hazards Owing to Volcano-Glacier Interactions in Colombia. Annals of Glaciology, v. 45, p.128–136. doi:10.3189/172756407782282408.

Huggel C, Caplan-Auerbach J, and Wessels R (2008) Recent extreme avalanches: Triggered by climate change? EOS, transactions, American Geophysical Union, v. 89(47), p. 469–470, doi:10.1029/2008EO470001.

Huggel C, Salzamann N, and Allen S (2013) High-mountains slope failures and recent and future warm extreme events. In McGuire B, Maslin M (eds.), Climate Forcing of Geological Hazards. Wiley-Blackwell, Oxford, UK.

Huybers P, and Langmuir C (2009) Feedback between deglaciation, volcanism, and atmospheric CO2. Earth and Planetary Science Letters, v. 286, p. 479–491, doi:10.1016/j.epsl.2009.07.014.

Intrieri E, Raspini F, Fumagalli A, Lu P, Del Conte S, Farina P, Allievi J, Ferretti A, and Casagli N (2017) The Maoxian landslide as seen from space: Detecting precursors of failure with Sentinel-1 data. Landslides, v. 15, p. 123–133, doi:10.1007/s10346-017-0915-7.

Iverson RM (1997) The physics of debris flows: Reviews of Geophysics, v. 35, p. 245–296, doi:10.1029 /97RG00426.

Iverson RM, George DL, Allstadt K, Reid ME, Collins BD, Vallance JW, Schilling SP, Godt JW, Cannon CM, Magirl CS, Baum RL, Coe JA, Schulz WH, and Bower JB (2015) Landslide mobility and hazards: Implications of the 2014 Oso disaster. Earth and Planetary Science Letters, v. 412, p. 197–208, doi:10.1016/j.epsl.2014.12.020.

Jakob M (1996) Morphometric and geotechnical controls on debris flow frequency and magnitude, southern Coast Mountains, British Columbia. Ph.D. thesis, Vancouver, University of British Columbia, 242 p.

Jakob M (2005) A size classification for debris flows. Engineering Geology, v. 79; p. 151–161.

Jakob M, McDougall S, Weatherly H, and Ripley N (2013) Debris-flow simulations on Cheekye River, British Columbia. Landslides, v. 10, p. 685–699, doi:10.1007/s10346-012-0365-1.

James MR, and Robson S (2012) Straightforward reconstruction of 3D surfaces and topography with a camera: Accuracy and geoscience application. Journal of Geophysical Research, v. 117, p. 1–17, F03017, doi:10.1029 /2011JF002289.

James MR, Robson S, d'Oleire-Oltmanns S, and Niethammer U (2017a) Optimising UAV Topographic Surveys Processed with Structure-from-Motion: Ground Control Quality, Quantity and Bundle Adjustment. Geomorphology, v. 280(1), p. 51-66, doi:10.1016/j.geomorph.2016.11.021.

James MR, Robson S, and Smith MW (2017b) 3-D Uncertainty-Based Topographic Change Detection with Structure-from-Motion Photogrammetry: Precision Maps for Ground Control and Directly Georeferenced Surveys. Earth Surface Processes and Landformsl v. 42(12), p. 1769-1788, doi:10.1002/esp.4125.

Jellinek AM, Manga M, and Saar MO (2004) Did melting glaciers cause volcanic eruptions in eastern California? Probing the mechanics of dike formation. Journal of Geophysical Research: Solid Earth, v. 109, p. 1–10, doi:10.1029/2004JB002978.

Jordan P (1994) Debris Flows in the Southern Coast Mountains, British Columbia: Dynamic Behavior and Physical Properties. Ph.D. thesis, University of British Columbia, Vancouver, BC. 272 p.

Jordan P, and Slaymaker O (1991) Holocene sediment production in Lillooet River basin, British Columbia: a sediment budget approach. Géographie physique et Quaternaire, v. 45, p. 45–57.

Kampes BM (2006) Radar Interferometry – Persistent Scatterer Technique, Springer, Dordrecht, p. 43–69.

Keiler M, Knight J, and Harrison S (2010) Climate change and geomorphological hazards in the eastern European Alps. Philosophical Transactions. Series A, Mathematical, Physical, and Engineering Sciences, v. 368, p. 2461–2479, doi:10.1098/rsta.2010.0047.

Kelfoun K (2011) Suitability of simple rheological laws for the numerical simulation of dense pyroclastic flows and long-runout volcanic avalanches. Journal of Geophysical Research, v. 116, B08209, doi:10.1029/2010JB007622.

Kelfoun K, and Druitt TH (2005) Numerical Modeling of the Emplacement of Socompa Rock Avalanche, Chile. Journal of Geophysical Research, v. 110, B12202, doi:10.1029/2005JB003758.

Kennedy D, and Bouchard R (2010) The Lil'Wat World of Charlie Mack. Talonbooks, Vancouver, 288 p.

Kilburn CRJ, and Petley DN (2003) Forecasting giant, catastrophic slope collapse: Lessons from Vajont, Northern Italy. Geomorphology, v. 54, p. 21–32, doi:10.1016/S0169-555X(03)00052-7.

Koch J, Menounos B, and Clague JJ (2009) Glacier change in Garibaldi Provincial Park, southern Coast Mountains, British Columbia, since the Little Ice Age. Global and Planetary Change, v. 66, p. 161–178, doi:10.1016/j.gloplacha.2008.11.006.

Kolzenburg S, Favalli M, Fornaciai A, Isola I, Harris AJL, Nannipieri L, and Giordano D (2016) Rapid updating and improvement of airborne LIDAR DEMs through ground-based SfM 3-D modeling of volcanic features. IEEE Transactions on Geoscience and Remote Sensing, v. 54, p. 6687–6699, doi:10.1109/TGRS.2016.2587798.

Krautblatter M, Funk D, and Gunzel FK (2013) Why permafrost rocks become unstable: a rock ice-mechanical model in time and space. Earth Surface Processes Landforms, v. 38(8), p. 876-887, doi:10.1002/esp.3374.

Lane SN, James TD, and Crowell MD (2000) Application of digital photogrammetry to complex topography for geomorphological research. The Photogrammetric Record, v. 16(95), p. 793–821, doi:10.1111/0031-868X.00152.

Lane SN, Westaway RM, and Hicks MD (2003) Estimation of Erosion and Deposition Volumes in a Large, Gravel-Bed, Braided River Using Synoptic Remote Sensing. Earth Surface Processes and Landforms, v. 28(3), p. 249–271, doi:10.1002/esp.483.

Leroi E, Bonnard CH, Fell R, and McInnes R (2005) Risk assessment and management. Proceedings of the International Conference on Landslide Risk Management, Vancouver, BC, p. 159–198.

Liggins F, Betts RA, and McGuire B (2013) Projected future climate changes in the context of geological and geomorphological hazards. In McGuire B, Maslin M (eds.), Climate Forcing of Geological Hazards. Wiley-Blackwell, Oxford, p. 34–55.

Linder W (2009) Digital Photogrammetry: A Practical Course. Springer, Berlin, 235 p.

Loew S, Gschwind S, Gischig V, Keller-Signer A, and Valenti G (2017) Monitoring and early warning of the 2012 Preonzo catastrophic rock slope failure. Landslides v. 14(2), p. 141-154, doi:10.1007/s10346-016-0701-y.

Lowe DG (1999) Object Recognition from Local Scale-Invariant Features. Proceedings of the Seventh IEEE International Conference on Computer Vision, v. 2, p. 1150-1157, doi:10.1109/ICCV.1999.790410.

Maccaferri F, Richter N, and Walter TR (2017) The Effect of Giant Lateral Collapses on Magma Pathways and the Location of Volcanism. Nature Communications, v 8 (1), p. 1–11, doi:10.1038/s41467-017-01256-2.

Major JJ, and Newhall CG (1989) Snow and Ice Perturbation during Historical Volcanic Eruptions and the Formation of Lahars and Floods-A Global Review. Bulletin of Volcanology, v. 52 (1), p. 1–27, doi:10.1007/BF00641384.

Manconi A, Longpré MA, Walter TR, Troll VR, and Hansteen TH (2009) The effects of flank collapses on volcano plumbing systems. Geology, v. 37, p. 1099–1102.

Mathieu L, van Wyk de Vries B, Pilato M, and Troll VR (2011) The Interaction between Volcanoes and Strike-Slip, Transtensional and Transpressional Fault Zones: Analogue Models and Natural Examples. Journal of Structural Geology, v. 33 (5), p. 898–906, doi:10.1016/j.jsg.2011.03.003.

Matthews JA, and Briffa KR (2005) The “Little Ice Age”: Re-evaluation of an evolving concept. Geografiska Annaler: Series A. Physical Geography, v. 87, p. 17–36, doi:10.1111/j.0435-3676.2005.00242.x.

Mathews WH, and McTaggart KC (1969) The Hope landslide, British Columbia. Proceedings of the Geological Association of Canada, v. 20, p. 65–75.

McColl ST, Davies TRH, and McSaveney MJ (2010) Glacier retreat and rock-slope stability: Debunking debuttressing. 11th Congress of the International Association for Engineering Geology and the Environment, Auckland, Aotearoa, 5-10 September 2010, Auckland, New Zealand, p. 467-474.

McColl ST, Davies TRH (2013) Large Ice-Contact Slope Movements: Glacial Buttressing, Deformation and Erosion. Earth Surface Processes and Landforms, v. 38 (10), p. 1102–1115, doi:10.1002/esp.3346.

Mertes J R., Gulley JD, Benn DI, Thompson SS, and Nicholson LI (2017) Using Structure-from-Motion to Create Glacier DEMs and Orthoimagery from Historical Terrestrial and Oblique Aerial Imagery. Earth Surface Processes and Landforms, v. 42 (14), p. 2360–2364, doi:10.1002/esp.4188.

Micheletti N, Chandler JH, and Lane SN (2015) Section 2.2. Structure from Motion (SfM) photogrammetry. In Cook SJ, Clarke LE, Nield JM (eds.), Geomorphological Techniques (Online Edition). British Society for Geomorphology, London, UK, Chapter 2, Section 2.2, 12 p.

Mokievsky-Zubok O (1977) Glacier caused slide near Pylon Peak, British Columbia. Canadian Journal of Earth Sciences, v. 15, p. 1039–1052.

Mölg N, and Bolch T (2017) Structure-from-Motion Using Historical Aerial Images to Analyse Changes in Glacier Surface Elevation. Remote Sensing, v. 9(10), p. 1021-1039, doi:10.3390/rs9101021.

Moretti L, Allstadt K, Mangeney A, Capdeville Y, Stutzmann E, and Bouchut F (2015) Numerical modeling of the Mount Meager landslide constrained by its force history derived from seismic data. Journal of Geophysical Research: Solid Earth, v. 120, p. 2579–2599, doi:10.1002/2014JB011426.

Moro M, Saroli M, Stramondo S, Bignami C, Albano M, Falcucci E, Gori S, Doglioni C, Polcari M, Tallini M, Macerola L, Novali F, Costantini M, Malvarosa F, and Wegmüller U (2017) New Insights into Earthquake Precursors from InSAR. Scientific Reports, v.7 (1), p. 1–11, doi:10.1038/s41598-017-12058-3.

Mullen EK, and Weis D (2013) Sr-Nd-Hf-Pb Isotope and Trace Element Evidence for the Origin of Alkalic Basalts in the Garibaldi Belt, Northern Cascade Arc. Geochemistry, Geophysics, Geosystems, v. 14 (8), p. 3126–3155. doi:10.1002/ggge.20191.

Mullen EK, Paquette J-L, Tepper JH, and McCallum IS (2018) Temporal and Spatial Evolution of Northern Cascade Arc Magmatism Revealed by LA–ICP–MS U–Pb Zircon Dating. Canadian Journal of Earth Sciences, v. 55 (5), p. 1–20. doi:10.1139/cjes-2017-0167.

Neri M, Casu F, Acocella V, Solaro G, Pepe S, Berardino P, Sansosti E, Caltabiano T, Lundgren P, and Lanari R (2009) Deformation and Eruptions at Mt. Etna (Italy): A Lesson from 15 Years of Observations. Geophysical Research Letters, v. 36 (2), p. 1–6, doi:10.1029/2008GL036151.

NSBG (Nevin Sadlier-Brown Goodbrand Ltd) (1980) Meager Mountain Geothermal Project Status of Environmental Studies Baseline Data Collection Program. Report gt14 for B.C. Hydro and Power Authority, 176 p.

NSBG(Nevin Sadlier-Brown Goodbrand Ltd) (1981) Meager Mountain Geothermal Project Status of Environmental Studies Baseline Data Collection Program 1980. Report gt20 for B.C. Hydro and Power Authority, 202 p.

NSBG (Nevin Sadlier-Brown Goodbrand Ltd) (1985). Multielement Geochemistry of the Meager Creek Geothermal System. Report gt22 for B.C. Hydro and Power Authority, 122p.

NRCan (Natural Resources Canada) (2013) Digital Elevation Model: Product Specifications, Edition 1.1. Government of Canada, Natural Resources Canada, Map Information Branch, GeoGratis Client Services,11p.

Onsel E, Donati D, Stead D., and Chang O (2018) Applications of virtual and mixed reality in rock engineering. ARMA, 52nd US Rock Mechanics/Geomechanics Symposium, 17-20 June 2018 Seattle.

Paguican EMR, van Wyk de Vries B, and Lagmay AMF (2014) Hummocks: How they form and how they evolve in rockslide-debris avalanches. Landslides, v. 11, p. 67–80, doi:10.1007/s10346-012-0368-y.

Palmer BA, and Neall VE (1989) The Murimotu Formation: 9500 year old deposits of a debris avalanche and associated lahars, Mount Ruapehu, North Island, New Zealand. New Zealand Journal of Geology and Geophysics, v. 32, p. 477–486, doi:10.1080/00288306.1989.10427555.

Petrie G, and Toth CK (2010) Introduction to Laser Ranging, Profiling, and Scanning. In Shan J and Toth CK (eds.), Topographic Laser Ranging and Scanning: Principles and Processing. Taylor and Francis, Boca Raton, USA, 2009, 574 p.

Pinel V, Jaupart C (2005) Some consequences of volcanic edifice destruction for eruption conditions. Journal of Volcanology and Geothermal Research, v. 145, p. 68–80, doi:10.1016/j.jvolgeores.2005.01.012.

Pioli L, Erlund E, Johnson E, Cashman K, Wallace P, Rosi M, and Delgado Granados H (2008) Explosive Dynamics of Violent Strombolian Eruptions: The Eruption of Parícutin Volcano 1943-1952 (Mexico). Earth and Planetary Science Letters, v. 271(1–4), p. 359–368, doi:10.1016/j.epsl.2008.04.026.

Plafker G, and Ericksen GE (1978) Nevado Huascarán avalanches, Peru. In Voight B (eds) Rock-slides and Avalanches: Natural Phenomenon. Elsevier, Amsterdam, v. 1, p. 277–314, doi:10.1016/B978-0-444-41507-3.50016-7.

Pola A, Crosta GB, Fusi N, Barberini V, and Norini G (2012) Influence of alteration on physical properties of volcanic rocks. Tectonophysics, v. 566–567, p. 67–86, doi:10.1016/j.tecto.2012.07.017.

Pola A, Crosta GB, Fusi N, and Castellanza R (2014) General characterization of the mechanical behaviour of different volcanic rocks with respect to alteration. Engineering Geology, v. 169, p. 1–13, doi:10 1016/j.enggeo.201311.011.

Pudasaini SP (2011) Some exact solutions for debris and avalanche flows. Physics of Fluids, v. 23, 043301, doi:10.1063/1.3570532.

Pudasaini SP (2012) A general two-phase debris flow model. Journal of Geophysical Research, v. 117, F03010, doi:10.1029/2011JF002186.

Pudasaini SP, and Hutter K (2003) Rapid shear flows of dry granular masses down curved and twisted channels. Journal of Fluid Mechanics, v. 495, p. 193–208, doi:10.1017/S0022112003006141.

Pudasaini SP, and Krautblatter M (2014) A two-phase mechanical model for rock-ice avalanches. Journal of Geophysical Research: Earth Surface, v. 119, p. 2272–2290, doi:10.1002/2014JF003183.

Pudasaini SP, Wang Y, and Hutter K (2005) Modelling debris flows down general channels. Natural Hazards and Earth System Sciences, v. 5, p. 799–819, doi:10 .5194/nhess-5-799-2005.

Raspini F, Bianchini S, Ciampalini A, Del Soldato M, Solari L, Novali F, Del Conte S, Rucci A, Ferretti A, and Casagli N (2018) Continuous, Semi-Automatic Monitoring of Ground Deformation Using Sentinel-1 Satellites. Scientific Reports, v. 8 (1). p. 1–11, doi:10.1038/s41598-018-25369-w.

Rampino MR, Self S, and Fairbridge RW (1979) Can rapid climatic change cause volcanic eruptions? Science, v. 206(4420), p. 826–829.

Read PB (1977) Meager Creek volcanic complex, southwestern British Columbia. In Current Research, Part A: Geological Survey of Canada Paper 77–1A, p. 277–281.

Read PB (1978) Geology of Meager Creek Geothermal Area, British Columbia. Geological Survey of Canada Open File 603, map, 1 sheet, scale 1:20.000.

Read PB (1990) Mount Meager complex, Garibaldi Volcanic Belt, southwestern British Columbia. Geoscience Canada, v. 17, p. 167–170.

Reid ME, and Brien DL (2006) Assessing massive flank collapse at stratovolcanoes using 3-D slope stability analysis. In Evans SG, et al. (eds.), Landslides from Massive Rock Slope Failure. Dordrecht, Springer, p. 445–458, doi:10.1007/978-1-4020 -4037-5_24.

Reid ME, Sisson TW, and Brien DL (2001) Volcano collapse promoted by hydrothermal alteration and edifice. Geology, v. 29, p. 779–782.

Remondino F, Spera MG, Nocerino E, Menna F, and Nex F (2014) State of the art in high density image matching. The Photogrammetric Record, v. 29, p. 144–166.

Roberti G, Friele P, van Wyk de Vries B, Ward B, Clague JJ, Perotti L, and Giardino M (2017a) Rheological evolution of the Mount Meager 2010 debris avalanche, southwestern British Columbia. Geosphere, v. 13(2), p. 1–22, doi:10.1130/GES01389.1.

Roberti G, Ward B, van Wyk de Vries B, Falorni G, Perotti L, and Clague JJ (2015) Mount Meager volcano, Canada: A case study for landslides on glaciated volcanoes. Abstract, American Geophysical Union, Fall Meeting, 14-18 December 2015, San Francisco, California, U.S.A.

Roberti G, Ward B, van Wyk de Vries B, and Perotti L (2017b) Structure from Motion and landslides: The 2010 Mount Meager collapse from slope deformation to debris avalanche deposit mapping. Geotechnical News, v. 35, p. 20–22.

Roberti G, Ward B, van Wyk de Vries B, Friele PA, Perotti L, Clague JJ, and Giardino M (2017c) Precursory slope distress prior to the 2010 Mount Meager landslide, British Columbia. Landslides, v. 15(4), p. 637–647, doi:10.1007/s10346-017-0901-0.

Roche AD, Guthrie RH, Roberts NJ, Ellis E, and Friele P (2011) Once more into the breach: A forensic analysis of the August 2010 landslide dam outburst flood at Meager Creek, BC. In Proceedings of 5th Canadian Conference on Geotechnique and Natural Hazards, Kelowna, British Columbia, 15–17 May, Canadian Geotechnical Society, 10 p.

Rose ND, and Hungr O (2007) Forecasting potential rock slope failure in open pit mines using the inverse-velocity method. International Journal of Rock Mechanics and Mining Sciences, v. 44, p. 308–320.

Roverato M, Capra L, Sulpizio R, and Norini G (2011) Stratigraphic reconstruction of two debris avalanche deposits at Colima Volcano (Mexico): Insights into pre-failure conditions and climate influence. Journal of Volcanology and Geothermal Research, v. 207, p. 33–46, doi.org/10.1016/j.jvolgeores.2011.07.003.

Roverato M, Cronin S, Procter J, and Capra L (2014) Textural features as indicators of debris avalanche transport and emplacement, Taranaki volcano. Geological Society of America Bulletin, v. 120, p. 3–18, doi:10.1130/B30946.1.

Russell JK, Edwards BR, Porritt L, and Ryane C (2014) Tuyas: A Descriptive Genetic Classification. Quaternary Science Reviews, v. 87, p. 70–81. doi:10.1016/j.quascirev.2014.01.001.

Schenk T (2005) Introduction to Photogrammetry, GS400.02, The Ohio State University, 100 p.

Schiefer E, Menounos B, and Wheate R (2007) Recent volume loss of British Columbian glaciers, Canada. Geophysical Research Letters, v. 34, 6 p., L16503, doi:10.1029/2007GL030780.

Scott KM, Macias JL, Vallance JW, Naranjo JA, Rodriguez-Elizarraras SR, and McGeehin JP (2002) Catastrophic debris flows transformed from landslides in volcanic terrains: Mobility, hazard assessment, and mitigation strategy: U.S. Geological Survey Professional Paper 1630, 59 p.

Semyonov D (2011) Algorithms used in Photoscan, PhotoScan Forum, http://www.agisoft.com/forum/index.php?topic=89.0.

Shea T, and van Wyk de Vries B (2008) Structural analysis and analogue modeling of the kinematics and dynamics of rockslide avalanches. Geosphere, v. 4, p. 657–686, doi:10.1130/GES00131.1.

Shea T, and van Wyk de Vries B (2010) Collapsing volcanoes: The sleeping giants' threat. Geology Today, v. 26, p. 72–77, doi:10.1111/j.1365-2451.2010.00750.x.

Shepherd EC (1965) Laser to watch height. New Scientist, 33 p.

Shulmeister J, Davies TR, Evans DJA, Hyatt OM., and Tovar DS. (2009) Catastrophic Landslides, Glacier Behaviour and Moraine Formation - A View from an Active Plate Margin. Quaternary Science Reviews, v. 28(11–12). p. 1085–1096, doi:10.1016/j.quascirev.2008.11.015.

Shugar DH, and Clague JJ (2011) The Sedimentology and Geomorphology of Rock Avalanche Deposits on Glaciers. Sedimentology, v. 58, p. 1762–1783, doi:10.1111/j.1365-3091.2011.01238.x.

Shugar DH, Rabus BT, Clague JJ, and Capps DM (2012) The response of Black Rapids Glacier, Alaska, to the Denali earthquake rock avalanches. Journal of Geophysical Research, v. 117, F01006, doi:10.1029/2011JF002011.

Siebert L (1984) Large volcanic debris avalanches: Characteristics of source areas, deposits and associated eruptions. Journal of Volcanology and Geothermal Research, v. 22, p. 163–197.

Siebert L (2002) Landslides resulting from structural failure of volcanoes. Reviews in Engineering Geology, v. 15, p. 209–235, doi:10.1130/REG15-p209.

Simpson KA, Stasiuk M, Shimamura K, Clague JJ, and Friele P (2006) Evidence for catastrophic volcanic debris flows in Pemberton Valley, British Columbia. Canadian Journal of Earth Sciences, v. 689, p. 679–689, doi:10.1139/E06-026.

Smellie JL (2013) Quaternary Vulcanism: Subglacial Landforms. In Elias S and Mock CJ (eds), Encyclopedia of Quaternary Science: Second Edition., Elsevier, Amsterdam, p 780–802, doi:10.1016/B978-0-444-53643-3.00074-1.

Smith MV, Carrivick JL, and Quincey DJ (2015) Structure from motion photogrammetry in physical geography. Progress in Physical Geography: Earth and Environment v. 40, p. 247–275, doi:10.1177/0309133315615805.

Snavely N, Seitz SN, and Szeliski R (2008) Modeling the world from internet photo collections. International Journal of Computer Vision, v. 80, p. 189–210, doi:10.1007/s11263-007-0107-3.

Soil Survey Division Staff (1993) Soil survey manual: U.S. Department of Agriculture Soil Conservation Service Agricultural Handbook 18, https://www.nrcs.usda.gov /wps /portal/nrcs/detail/soils/ref/?cid=nrcs142p2_054262.

Stasiuk MV, Hickson CJ, and Mulder T (2003) The Vulnerability of Canada to Volcanic Hazards. Natural Hazards, v. 28 (2–3), p. 563–589, doi:10.1023/A:1022954829974.

Stasiuk MV, Russell JK, and Hickson CJ (1996) Distribution, nature, and origins of the 2400 BP eruption products of Mount Meager, British Columbia; linkages between magma chemistry and eruption behaviour. Geological Survey of Canada, Bulletin 486, 33p.

Statistics Canada (2017) Pemberton [Population Centre], British Columbia and British Columbia [Province] (table). Census Profile. 2016 Census. Statistics Canada Catalogue no. 98-316-X2016001. Ottawa, ON. Released November 29, 2017.

Stewart M (2002) Dacite block and ash avalanche hazards in mountainous terrain: 2360 yr BP eruption of Mount Meager, British Columbia. Thesis (MSc). University of British Columbia, 120 p.

Szeliski R (2011) Computer Vision–Algorithms and Applications. Springer, Heidelberg, Germany. 812 p.

Takahashi T (2007) Debris Flow: Mechanics, Prediction and Countermeasures. New York, Taylor and Francis, 440 p, doi:10.1201/9780203946282.

Takarada S, Ui T, and Yamamoto Y (1999) Depositional features and transportation mechanism of valley-filling Iwasegawa and Kaida debris avalanches, Japan. Bulletin of Volcanology, v. 60, p. 508–522, doi:10.1007/s004450050248.

Terlien MTJ (1998) The determination of statistical and deterministic hydrological landslide-triggering thresholds. Environmental Geology, v. 35(2–3), p. 124–130, doi:10.1007/s002540050299.

Torres R, Snoeij P, Geudtner D, Bibby D, Davidson M, Attema E, Potin P, Rommen B, Floury N, Brown M, Navas Traver I, Deghaye P, Duesmann B, Rosich B, Miranda N, Bruno C, L'Abbate M, Croci R, Pietropaolo A, Huchler M, and Rostan F (2012) GMES Sentinel-1 mission. Remote Sensing of Environment, v.120, p. 9–24.

Tormey D (2010) Managing the Effects of Accelerated Glacial Melting on Volcanic Collapse and Debris Flows: Planchon-Peteroa Volcano, Southern Andes. Global and Planetary Change, v. 74 (2), p. 82–90. doi:10.1016/j.gloplacha.2010.08.003.

Tost M, Cronin SJ, Procter JN, Smith IEM, Neall VE, and Price RC (2014) Impacts of catastrophic volcanic collapse on the erosion and morphology of a distal fluvial landscape: Hautapu River, Mount Ruapehu, New Zealand. Geological Society of America Bulletin, v. 127, p. 266–280, doi:10.1130/B31010.1.

TRE-Altamira (2018) UK InSAR map. TRE-Altamira website, http://tre-altamira.com/news/land-motion-uk-mapped-unprecedented-accuracy/.

Ui T, Takarada S, and Yoshimoto M (2000) Debris avalanches. In Sigurdsson H, (eds.), Encyclopedia of Volcanoes. San Diego, Academic Press, p. 617–626.

Ullman S (1979) The Interpretation of Structure from Motion. Proceedings of the Royal Society of London. Series B. Biological Sciences v. 203 (1153), p 405-426.

Valderrama P, Roche O, Samaniego P, van Wyk de Vries B, Bernard K, and Mariño J (2016) Dynamic implications of ridges on a debris avalanche deposit at Tutupaca volcano (southern Peru). Bulletin of Volcanology, v. 78(14), p. 1-11, doi:10.1007/s00445-016-1011-x.

Vallance W, and Scott KM (1997) The Osceola mudflow from Mount Rainier: Sedimentology and hazard implications of a huge clay-rich debris flow. Geological Society of America Bulletin, v. 109, p. 143–163, doi:10.1130/0016-7606(1997)109<0143:TOMFMR>2.3.CO;2.

van der Kooij M, and Lambert A (2002) Results of processing and analysis of large volumes of repeat-pass InSAR data of Vancouver and Mount Meager (BC). Geoscience and Remote Sensing Symposium, IGARSS '02, 2002 IEEE International.

van Wyk de Vries B, and Davies T (2015) Landslides, debris avalanches, and volcanic gravitational deformation. In Sigurdsson H, Houghton B, Rymer H, Stix J, and McNutt S (eds.), Encyclopedia of Volcanoes (second edition). London, Academic Press, p. 665–685, doi:10.1016/B978-0-12-385938-9.00038-9 .

van Wyk de Vries B, and Delcamp A (2015) Volcanic debris avalanches. In Davies, T, (eds.) Landslide Hazards, Risks, and Disasters. Amsterdam, Elsevier, p. 131–157, doi:10.1016/B978-0-12-396452-6.00005-7.

van Wyk de Vries B, and Francis PW (1997) Catastrophic collapse at stratovolcanoes induced by gradual volcano spreading. Nature, v. 387, p. 387–389, doi:10.1038/387387a0.

van Wyk de Vries B, Self S, Francis PW, and Keszthelyi L (2001) A gravitational spreading origin for the Socompa debris avalanche. Journal of Volcanology and Geothermal Research, v. 105, p. 225–247.

Venugopal S, Moune S, William-Jones G, Druitt T, Vigouroux N, Wilson A, and Russel K (In press) Two distinct mantle sources beneath the Garibaldi Volcanic Belt: Insight from olivine-hosted melt inclusions. Earth and Planetary Science Letters.

Venugopal S, Moune S, William-Jones G, Wilson A, and Russel K (2017) Gas emissions and magma source of the Mount Meager Volcanic Complex, Garibaldi Volcanic Belt, BC. IAVCEI Scientific Assembly Abstracts, August 14-18, 2017, Submission 244, Portland, OR.

Voight B (1990) The 1985 Nevado Del Ruiz Volcano Catastrophe: Anatomy and Retrospection. Journal of Volcanology and Geothermal Research, v. 42 (1–2), p 151–88, doi:10.1016/0377-0273(90)90075-Q.

Voight B, Glicken H, Janda RJ, and Douglass PM (1981) Catastrophic rockslide avalanche of May 18. In Lipman W, Mulineaux DR (eds.), The 1980 Eruptions of Mount St. Helens, Washington. U.S. Geological Survey Professional Paper 1250, p. 347–377.

Voight B, Komorowski JC, Norton GE, Belousov A, Belousova M, Boudon G, Francis PW, Franz W., Heinrich P, Sparks RSJ, and Young SR (2002) The 26 December (Boxing Day) 1997 sector collapse and debris avalanche at Soufriére Hills Volcano, Montserrat. In Druitt TH, Kokelaar P (eds.), The Eruption of Soufriere Hills Volcano, Montserrat, from 1995 to 1999.Geological Society of London Memoir 21, p. 363–407.

Wolf PR, and Dewitt, BA (2000) Elements of Photogrammetry with Applications in GIS (3rd Edition). McGraw-Hill, Boston, 624 p.

Wood NJ, and Soulard CE (2009) Community exposure to lahar hazards from Mount Rainier, Washington. U.S. Geological Survey Scientific Investigations Report 2009-5211, 26 p.

Watt SFL, Pyle DM, and Mather TA (2013) The volcanic response to deglaciation: Evidence from glaciated arcs and a reassessment of global eruption records. Earth Science Reviews, v. 122, p. 77–102, doi:10.1016/j.earscirev.2013.03.007.

Waythomas CF (2012) Landslides at stratovolcanoes initiated by volcanic unrest. In Clague JJ and Stead D (eds.), Landslides: Types, Mechanisms and Modeling. Cambridge University Press, doi:10.1017/CBO9780511740367.005.

Waythomas CF (2014) Water, Ice and Mud: Lahars and Lahar Hazards at Ice-and Snow-Clad Volcanoes. Geology Today, v. 30 (1), p. 34–39, doi:10.1111/gto.12035.

Westoby MJ, Brasington J, Glasser NF, Hambrey MJ, and Reynolds JM (2012) 'Structure-from-Motion' photogrammetry: A low-cost, effective tool for geoscience applications. Geomorphology, v. 179, p. 300–314, doi:10.1016/j.geomorph.2012.08.021.

Wilson AM, and Russel JK (2017) Lillooet Glacier Basalts, Southwestern British Columbia, Canada: Products of Quaternary Glaciovolcanism. Canadian Journal of Earth Sciences, v. 54(6), p. 639-653, doi:10.1139/cjes-2016-0201.

Wilson AM, and Russel JK (2018) Quaternary glaciovolcanism in the Canadian Cascade volcanic arc—Paleoenvironmental implications. In Poland M, Garcia M, Camp V, Grunder A (eds.), Field Volcanology: A Tribute to the Distinguished Career of Don Swanson, GSA Special Publication 538.

Wilson AM, Russell JK, Kelman MC, and Hickson CJ (2016) Geology of the Monmouth Creek Volcanic Complex, Garibaldi Volcanic Belt, British Columbia. Geological Survey of Canada, Current Research 2 (January), 16 p, doi:10.4095/298798.

Wohletz K, and Heiken G (1992) Volcanology and Geothermal Energy. Berkeley, University of California Press, 432 p, http://ark.cdlib.org/ark:/13030/ft6v19p151/.

Wyering LD, Villeneuve MC, Wallis IC, Siratovich PA, Kennedy BM, Gravley DM, and Cant JL (2014) Mechanical and physical properties of hydrothermally altered rocks, Taupo Volcanic Zone, New Zealand. Journal of Volcanology and Geothermal Research, v. 288, p. 76–93, doi:10.1016/j.jvolgeores.2014.10.008.

Zahibo N, Pelinovsky E, Talipova T, and Nikolkina I (2010) Savage-Hutter model for avalanche dynamics in inclined channels: Analytical solutions. Journal of Geophysical Research, v. 115, B03402, doi: 10.1029/2009JB006515.

Zurek J, Williams-Jones G, Trusdell F, and Martin S (2015) The Origin of Mauna Loa's Ninole Hills: Evidence of Rift Zone Reorganization. Geophysical Research Letters, v.42 (20), p. 8358–8366, doi:10.1002/2015GL065863.

APPENDIX A.

Supplemental Files to Chapter 2

Table A1 Airphotots and digitization specifications

Year	n° of photos	Estimated flight height above the ground [Z] (m)	Estimated focal length [c] (m)	Scale factor of the frame [mb]	Expected map scale factor [Δr]	Graphic error[e] (m)	Frame side size [l] (m)	Frame side size on the ground[D] (m)	Distance between frame centers [b] (m)	Distance between frame centers on the ground [B] (m)	Precision coefficient [E]	Precision coefficient [K]	Acceptable error (half pixel) mm	Necessary pixel size (image)	Minimum DPI scan	σ(xy) m	σ(z) m	DPI scan	Estimated pixel size on the ground
				mb = Z/c	Δr = (mb/k)^2	e = [Δr]*0,2mm		D = l-mb		B = mb-b	E = Z/B	K = B/Z				σ(xy) = [(mb * E) * (pixel/2)]/1000	σ(z) = √2 * σ(xy)		D/ (DPI scan * (l/2,54))
2006	114	4025	0.303	13287	4414	0.883	0.23	3056	0.085	1129	3.564	0.281	441	0.033	764	0.786	1.108	800	0.42
1990	89	4025	0.306	13169	4336	0.867	0.23	3029	0.085	1119	3.596	0.278	433	0.032	771	0.779	1.099	800	0.42
1981	51	6000	0.305	19666	9669	1.934	0.23	4523	0.085	1672	3.589	0.279	966.	0.049	516.	1.735	2.446	800	0.62
1973	116	4025	0.306	13173	4338	0.868	0.23	3030	0.077	1014	3.968	0.252	433	0.032	771	0.860	1.213	800	0.42
1964	29	3915	0.153	25533	16298	3.260	0.23	5873	0.079	2017	1.941	0.515	1629	0.063	397	1.581	2.230	800	0.81
1962	108	4355	0.300	14516	5268	1.054	0.23	3339	0.094	1365	3.191	0.313	526	0.036	699.	0.840	1.185	800	0.46
1951	11	9398	0.153	61428	94335	18.867	0.23	14128	0.087	5344	1.759	0.569	9433	0.153	165	8.294	11.695	800	1.95
1947	50	6000	0.300	20000	10000	2.000	0.23	4600	0.069	1380	4.348	0.230	1000	0.050	508	2.173	3.065	800	0.64

APPENDIX B

Supplemental Files to Chapter 3

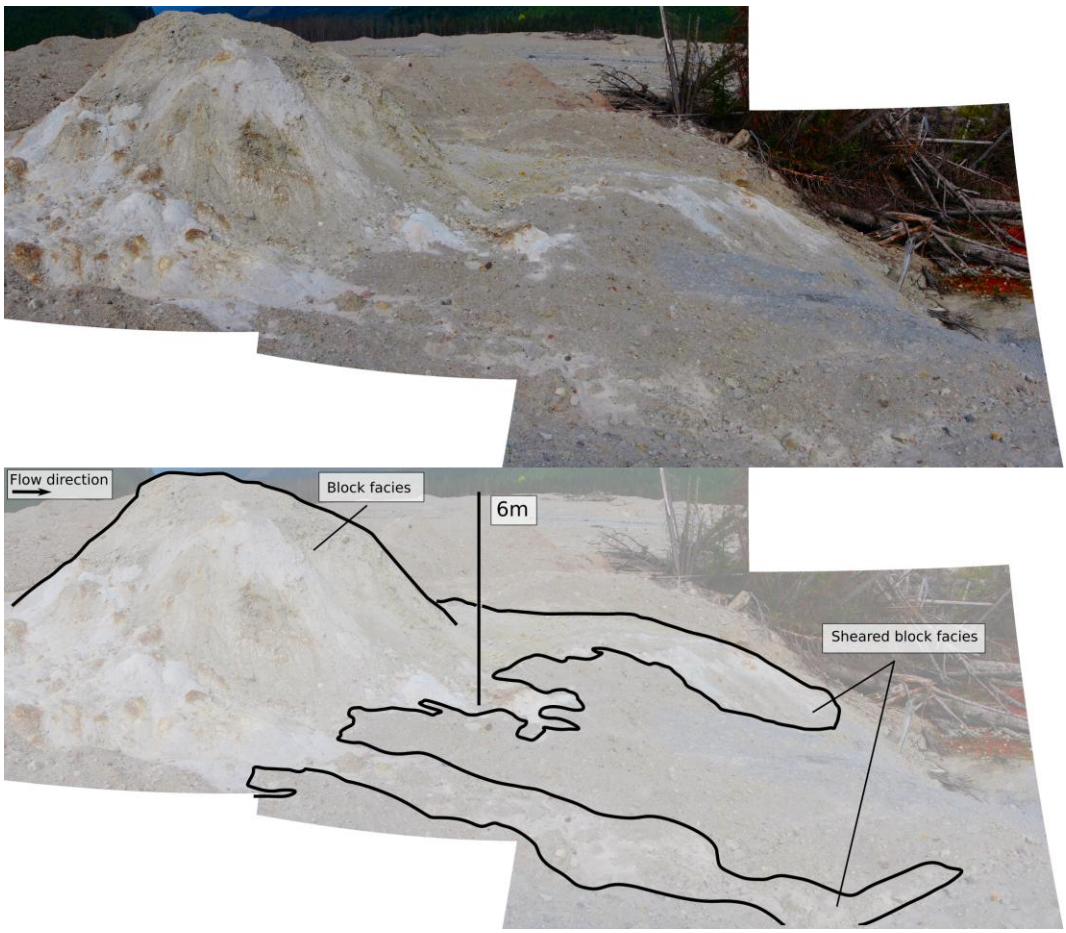

Figure B1. Photo of a block forming a hummock with related streaks of sheared block facies in area 3

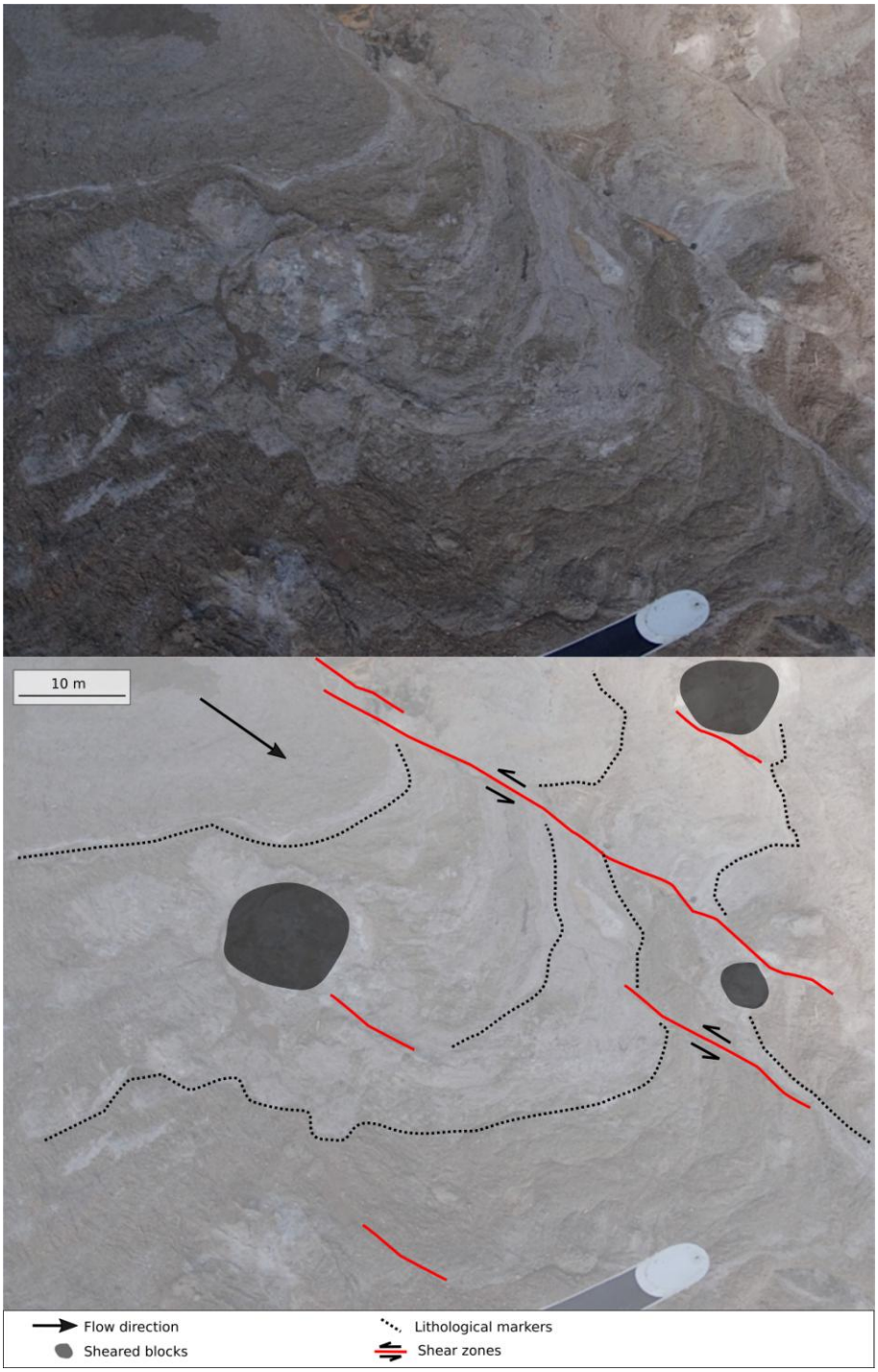

Figure B2. Helicopter view of the debris avalanche surface before the dam breach. Shearing and lithological markers are evident.

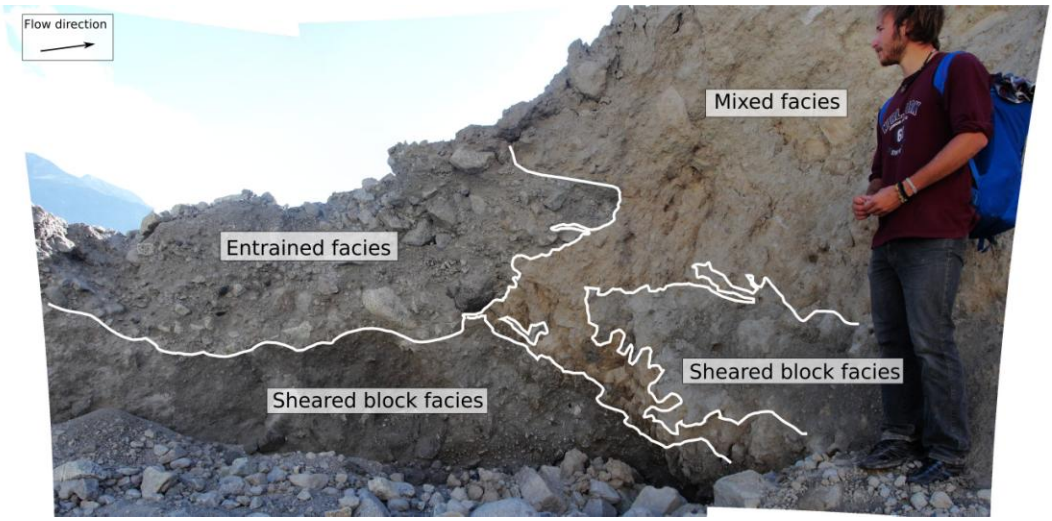

Figure B3. Photo of an outcrop showing relations among facies in area 1

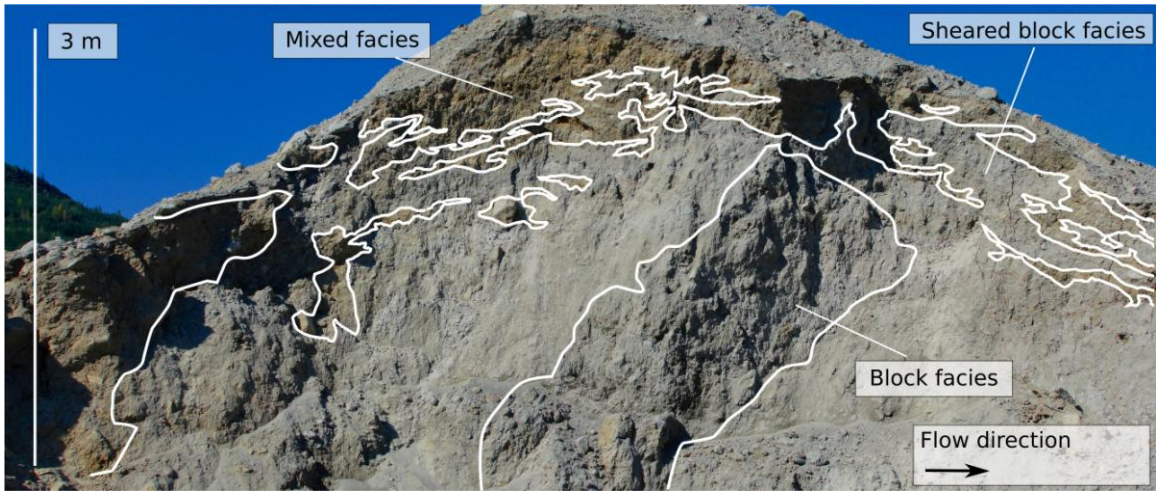

Figure B4. Photo of an outcrop section through a hummock showing facies relations in area 3

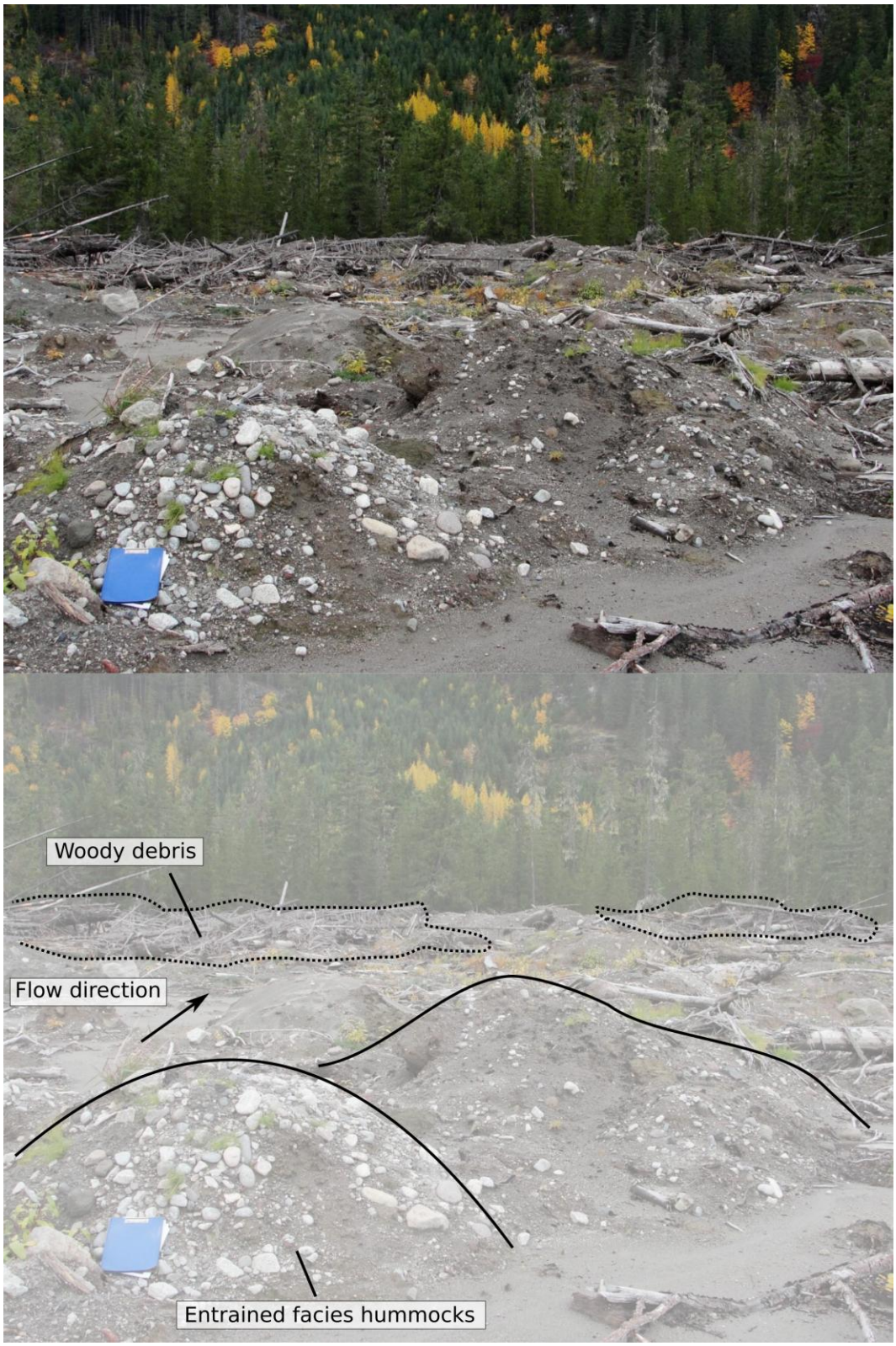

Figure B5. Photo of entrained-facies hummocks in the water-rich phase of the deposit, area 4

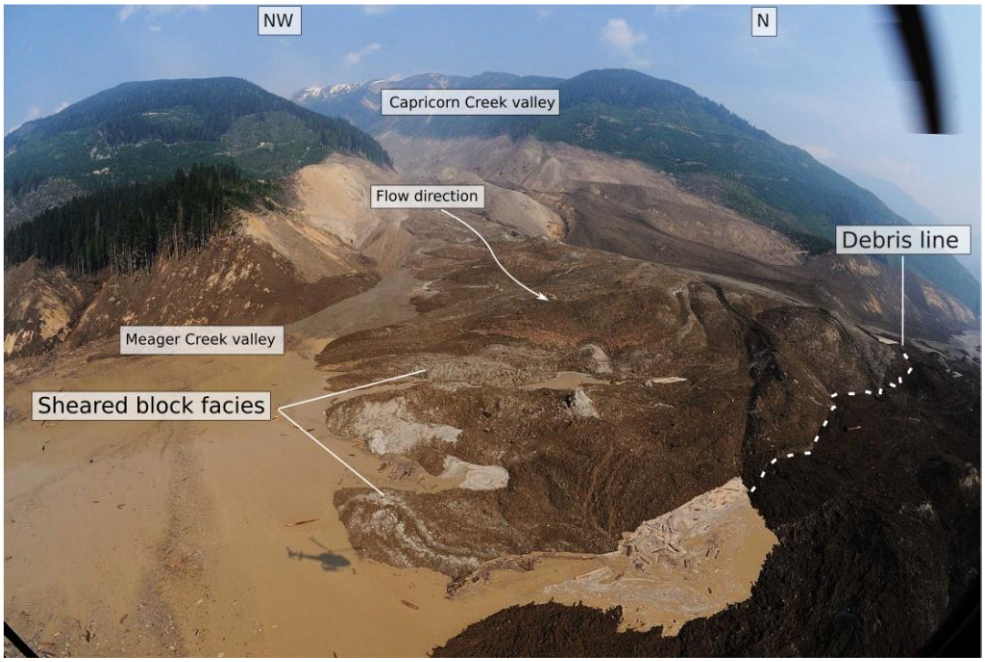

Figure B6. Helicopter view of the Mea- ger barrier before the dam breach. Photo courtesy of D.B. Steers.

Figure B7. Helicopter view of the Meager barrier after the dam breach. Photo courtesy of D.B. Steers.

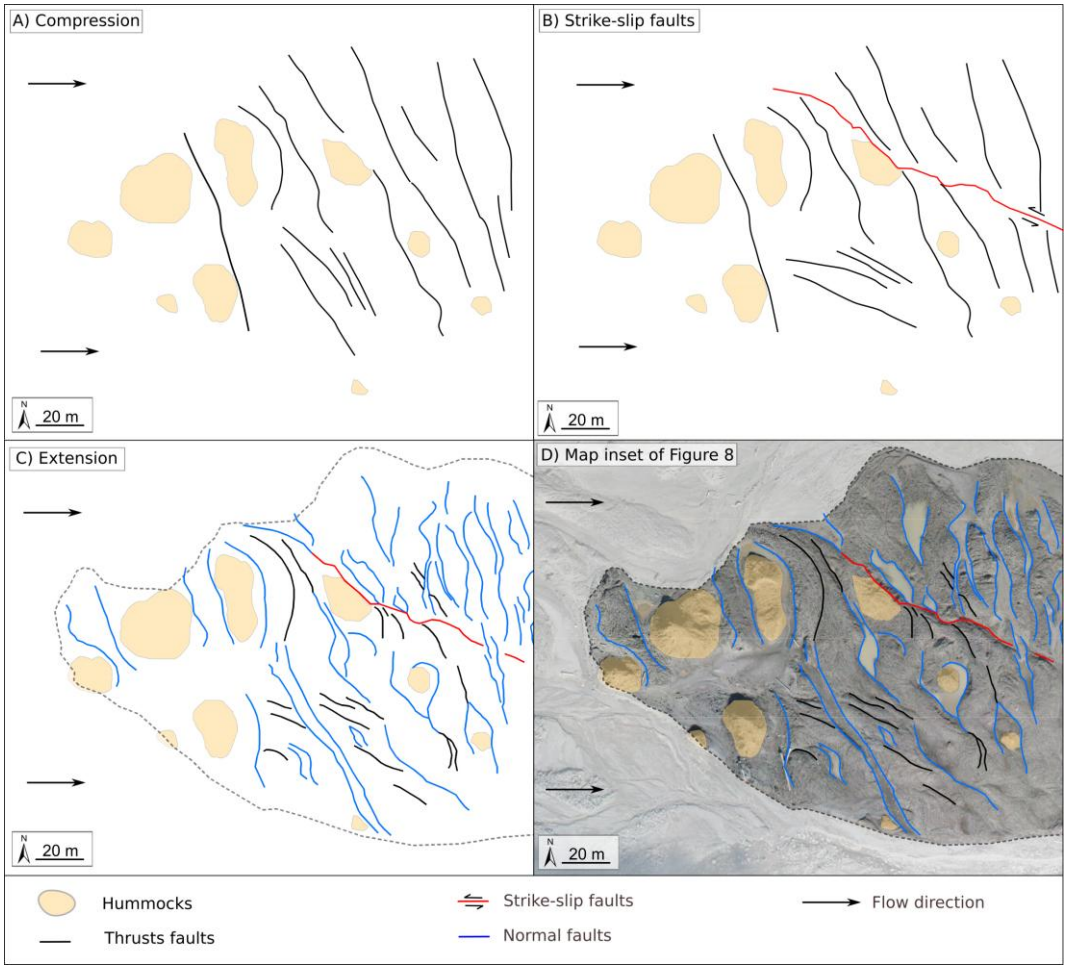

Figure B8. **Sketch showing the inferred structural evolution of the west end of the plug. (A) First compressional ridges formed as the front started to decelerate. (B) The debris divided into different lobes, and strike-slip faults accommodated the differential motion. (C) This area stopped while the front was still moving. Normal faults accommodated the con- sequent extension. (D) Inset map of the west end of the plug.**

APPENDIX C.

Supplemental Files to Chapter 4

Table C1. Airphotos and digitization specifications

Flight	Date	Picture number	n° of photos	Estimated flight height above the ground [Z] (m)	Camera	Estimated focal length [c] (m)	Scale factor of the frame [mb] mb = Z/c	Expected map scale factor [Δr] Δr = (mb/k)^2	Graphic error[e] (m) e = [Δr]*0,2mm	Frame side size [l] (m)	Frame side size on the ground[D] (m) D = l-mb	Distance between frame centers [b] (m)	Distance between frame centers on the ground [B] (m) B = mb-b	Precision coefficient [E] E = Z/B	Precision coefficient [K] K = B/Z	Acceptable error (half pixel) mm	Necessary pixel size (image)	Minimum DPI scan	DPI scan	Estimated pixel size on the ground D/ (DPI scan * (l/2,54))
BCC06084	Jul. 26, 2006	55-65	11	4025	Wild 30/4 NAT-S No 17118	0.302923	13287.2	4413.745	0.882749	0.23	3056.057	0.085	1129.412	3.5638	0.280599	441.3745	0.033218	764.6454	800	0.421874261
BCC06084	Jul. 26, 2006	86-90	5	4025	Wild 30/4 NAT-S No 17118	0.302923	13287.2	4413.745	0.882749	0.23	3056.057	0.085	1129.412	3.5638	0.280599	441.3745	0.033218	764.6454	800	0.421874261
bcc06169	Aug. 19, 2006	83-89	7	4025	Wild 30/4 NAT-S No 17118	0.302923	13287.2	4413.745	0.882749	0.23	3056.057	0.085	1129.412	3.5638	0.280599	441.3745	0.033218	764.6454	800	0.421874261
bcc06169	Sep. 2, 2006	117-126	10	4025	Wild 30/4 NAT-S No 17118	0.302923	13287.2	4413.745	0.882749	0.23	3056.057	0.085	1129.412	3.5638	0.280599	441.3745	0.033218	764.6454	800	0.421874261
bcc06169	Sep. 2, 2006	158-173	16	4025	Wild 30/4 NAT-S No 17118	0.302923	13287.2	4413.745	0.882749	0.23	3056.057	0.085	1129.412	3.5638	0.280599	441.3745	0.033218	764.6454	800	0.421874261
bcc06169	Sep. 2, 2006	188-204	17	4025	Wild 30/4 NAT-S No 17118	0.302923	13287.2	4413.745	0.882749	0.23	3056.057	0.085	1129.412	3.5638	0.280599	441.3745	0.033218	764.6454	800	0.421874261
BCC06170	Sep. 2, 2006	19-37	19	4025	Wild 30/4 NAT-S No 17118	0.302923	13287.2	4413.745	0.882749	0.23	3056.057	0.085	1129.412	3.5638	0.280599	441.3745	0.033218	764.6454	800	0.421874261
BCC06170	Sep. 2, 2006	52-72	21	4025	Wild 30/4 NAT-S No 17118	0.302923	13287.2	4413.745	0.882749	0.23	3056.057	0.085	1129.412	3.5638	0.280599	441.3745	0.033218	764.6454	800	0.421874261
BCB90052	Jul. 16, 1990	208-218	11	4025	Nr110399	0.30564	13169.09	4335.622	0.867124	0.23	3028.89	0.085	1119.372	3.595765	0.278105	433.5622	0.032923	771.5037	800	0.418123992
BCB90053	Jul. 16, 1990	9-20	12	4025	Nr110399	0.30564	13169.09	4335.622	0.867124	0.23	3028.89	0.085	1119.372	3.595765	0.278105	433.5622	0.032923	771.5037	800	0.418123992
BCB90113	Aug 28, 1990	239-252	14	4025	Nr122520	0.30509	13192.83	4351.268	0.870254	0.23	3034.351	0.085	1121.39	3.589294	0.278606	435.1268	0.032982	770.1154	800	0.418877764
BCB90114	Aug	45-59	15	4025	Nr122520	0.30509	13192.83	4351.268	0.870254	0.23	3034.351	0.085	1121.39	3.589294	0.278606	435.1268	0.032982	770.1154	800	0.418877764

BCB90114	28, 1990 Aug 28,																		
BCB90114	1990 Aug 28,	74-86	13	4025	Nr122520	0.30509	13192.83	4351.268	0.870254	0.23	3034.351	0.085	1121.39	3.589294	0.278606	435.1268	0.032982	770.1154	800	0.418877764
BCB90114	1990 Aug 28,	161-175	15	4025	Nr122520	0.30509	13192.83	4351.268	0.870254	0.23	3034.351	0.085	1121.39	3.589294	0.278606	435.1268	0.032982	770.1154	800	0.418877764
BC81085	1990 Ju 27,	191-199	9	4025	Nr122520	0.30509	13192.83	4351.268	0.870254	0.23	3034.351	0.085	1121.39	3.589294	0.278606	435.1268	0.032982	770.1154	800	0.418877764
BC81085	1981 Ju 27,	154-159	6	6000	Nr122520	0.30509	19666.33	9669.111	1.933822	0.23	4523.255	0.085	1671.638	3.589294	0.278606	966.9111	0.049166	516.6191	800	0.624414058
BC81095	1981 Aug 1,	204-213	10	6000	Nr122520	0.30509	19666.33	9669.111	1.933822	0.23	4523.255	0.085	1671.638	3.589294	0.278606	966.9111	0.049166	516.6191	800	0.624414058
BC81095	1981 Aug 1,	18-31	14	6000	Nr110398	0.30556	19636.08	9639.389	1.927878	0.23	4516.298	0.085	1669.067	3.594824	0.278178	963.9389	0.04909	517.4149	800	0.623453609
BC81095	1981 Aug 1,	48-61	14	6000	Nr110398	0.30556	19636.08	9639.389	1.927878	0.23	4516.298	0.085	1669.067	3.594824	0.278178	963.9389	0.04909	517.4149	800	0.623453609
BC81095	1981 Aug 1,	92-106	20	6000	Nr110398	0.30556	19636.08	9639.389	1.927878	0.23	4516.298	0.085	1669.067	3.594824	0.278178	963.9389	0.04909	517.4149	800	0.623453609
BC7550	1981 Sept 4,	122-125	4	6000	Nr110398	0.30556	19636.08	9639.389	1.927878	0.23	4516.298	0.085	1669.067	3.594824	0.278178	963.9389	0.04909	517.4149	800	0.623453609
BC7550	1973 Sept 4,	200-211	12	4025	Nr110398	0.30556	13172.54	4337.892	0.867578	0.23	3029.683	0.077	1014.285	3.968312	0.251996	433.7892	0.032931	771.3018	800	0.418233463
BC7551	1973 Sept 4,	230-243	14	4025	Nr110398	0.30556	13172.54	4337.892	0.867578	0.23	3029.683	0.077	1014.285	3.968312	0.251996	433.7892	0.032931	771.3018	800	0.418233463
BC7551	1973 Sept 4,	53-70	18	4025	Nr110398	0.30556	13172.54	4337.892	0.867578	0.23	3029.683	0.077	1014.285	3.968312	0.251996	433.7892	0.032931	771.3018	800	0.418233463
BC7551	1973 Sept 4,	83-101	19	4025	Nr110398	0.30556	13172.54	4337.892	0.867578	0.23	3029.683	0.077	1014.285	3.968312	0.251996	433.7892	0.032931	771.3018	800	0.418233463
BC7551	1973 Sept 4,	209-225	17	4025	Nr110398	0.30556	13172.54	4337.892	0.867578	0.23	3029.683	0.077	1014.285	3.968312	0.251996	433.7892	0.032931	771.3018	800	0.418233463
BC7555	1973 Sept 4,	241-254	14	4025	Nr110398	0.30556	13172.54	4337.892	0.867578	0.23	3029.683	0.077	1014.285	3.968312	0.251996	433.7892	0.032931	771.3018	800	0.418233463
bc5104	1973 Jul.	22-33 259missing)260-	12 9	4025 3915.23	Nr110398 15Ag108	0.30556 0.15334	13172.54 25533	4337.892 16298.35	0.867578 3.25967	0.23 0.23	3029.683 5872.59	0.077 0.079	1014.285 2017.107	3.968312 1.941013	0.251996 0.515195	433.7892 1629.835	0.032931 0.063833	771.3018 397.9164	800 800	0.418233463 0.810683324

	26, 1964	268(269missing)																	
bc5104	1964-65	206-208	3	3915.23	15Ag108	0.15334	25533	16298.35	3.25967	0.23	5872.59	0.079	2017.107	1.941013	0.515195	1629.835	0.063833	397.9164	800	0.810683324
bc5141	1964-65	25-34	10	3915.23	15Ag108	0.15334	25533	16298.35	3.25967	0.23	5872.59	0.079	2017.107	1.941013	0.515195	1629.835	0.063833	397.9164	800	0.810683324
bc5149	1964-65	(44missing)45-51	7	3887.399	15Ag269	0.15225	25533	16298.35	3.25967	0.23	5872.59	0.079	2017.107	1.927215	0.518883	1629.835	0.063833	397.9164	800	0.810683324
BC684	1948	39-58	20	4025	?	0.15225	26436.78	17472.59	3.494517	0.23	6080.46	0.085	2247.126	1.791176	0.558292	1747.259	0.066092	384.313	800	0.839378765
BC684	1948	73-85	13	4025	?	0.15225	26436.78	17472.59	3.494517	0.23	6080.46	0.085	2247.126	1.791176	0.558292	1747.259	0.066092	384.313	800	0.839378765